Quantum Transport Phenomena in Magnetic Molecules

Gaudenzi, Rocco

DOI
10.4233/uuid:c9667e59-a7f9-45f1-a975-32c6dfe2d95d

Publication date
2017

Document Version
Final published version

Citation (APA)
Gaudenzi, R. (2017). *Quantum Transport Phenomena in Magnetic Molecules*. [Dissertation (TU Delft), Delft University of Technology]. https://doi.org/10.4233/uuid:c9667e59-a7f9-45f1-a975-32c6dfe2d95d

QUANTUM TRANSPORT PHENOMENA IN MAGNETIC MOLECULES

QUANTUM TRANSPORT PHENOMENA IN MAGNETIC MOLECULES

Proefschrift

ter verkrijging van de graad van doctor
aan de Technische Universiteit Delft,
op gezag van de Rector Magnificus prof. ir. K. C. A. M. Luyben,
voorzitter van het College voor Promoties,
in het openbaar te verdedigen op maandag 26 juni 2017 om 15:00 uur

door

Rocco GAUDENZI

Master of Science in Physics, Swiss Federal Institute of Technology (ETH), Zürich, Switzerland
geboren te Bologna, Italië

Dit proefschrift is goedgekeurd door de promotor:

Prof. dr. ir. H.S.J. van der Zant

Samenstelling promotiecommissie:

Rector Magnificus,	voorzitter
Prof. dr. ir. H.S.J. van der Zant,	Technische Universiteit Delft, promotor
Onafhankelijke leden:	
Prof. dr. T. M. Ihn,	ETH Zurich
Prof. dr. M. R. Wegewijs,	RWTH Aachen University
Dr. E. Burzurí,	IMDEA Nanoscience Institute Madrid
Prof. dr. A. Cornia,	University of Modena and Reggio Emilia
Dr. M. Ternes,	Max-Planck Institute for Solid State Research
Prof. dr. ir. T. M. Klapwijk,	Technische Universiteit Delft
Prof. dr. ir. L. M. K. Vandersypen,	Technische Universiteit Delft, reservelid

Keywords: Molecular magnetism, quantum transport, molecular electronics, radicals, Landauer principle, superconductivity

Printed by: Gildeprint, Enschede

Front & Back: *Netwon: Pesonification of Man limited by reason*, Colour print, ink and watercolour on paper, William Blake, 1795. A commentary in the last section of the first chapter details the significance of the choice.

Casimir PhD Series, Delft-Leiden 2017-21

ISBN 978-90-8593-305-2

An electronic version of this dissertation is available at
`http://repository.tudelft.nl/`.

To those I will never know

CONTENTS

SUMMARY

In this work, we investigate a series of physical phenomena resulting from the confinement of electrons in those localised charge and spin quantum boxes generically called *molecules*.

The journey begins with a laud of the molecular world where we humbly attempt to justify why life has, long ago, chosen for matter made of molecules rather than for its inorganic and crystalline form; and why, in a world of nuclei, we would not be here, writing these words. We identify the reasons in a number of facts concerning the energy scales of the electronic processes, the combinatorial possibilities, the information content and its distribution. We then describe scattering from a layman's prospective; with which tools and how to contact single molecules and ensembles; the crosses and blessings of the transport and non-transport based techniques relevant to this work. As the world is not all round, challenges and pitfalls accompanying this investigation on molecules inevitably follow in the description.

Chapter 2 introduces transport through a generic molecular object from a more quantitative prospective. The real and virtual transport pictures are briefly distinguished and their nomenclature, in the various communities' jargon, spelled out with the purpose of stimulating a mutual understanding between the different electron transport communities. The "traditional" master equation approach is laid out didactically for the real-only and virtual-only regimes and combined into one comprehensive form encompassing real *and* virtual. This leads to the appearance of an intermediate regime in the stability diagram – called COSET – that includes and emerges from the non-trivial interplay of these two regimes with important repercussions on the system's relaxation dynamics. This "extension" of the traditional model is more and more relevant as the intrinsic relaxation rate decreases – i.e. for "good" devices – and, in fact, can be used to estimate it. The whole theoretical treatment is substantiated by experimental data on a high-spin molecular system of high-quality where COSET and, concurrently, spin-pumping manifest.

In Chapters 3, 4 and 5, we use some of the tools detailed in the introductory chapter to explore three molecular species from the same radical family and increasing spin complexity. The simplest features a shelled, radical electron in its neutral state exhibiting a Kondo effect, which we completely characterize as a function of bias, temperature and magnetic field in electromigrated break junctions and electrode separations in mechanically-controlled break junctions. This analysis is performed on a significant number of samples and reveals a good sample-to-sample consistency in the Kondo energy scales and a high robustness against mechanical and electrostatic variations of the surrounding environment.

The chemical unit at the base of the mono-radical is then assembled to form di- and tri-radical species with two and three coupled spins, respectively. These are investigated with inelastic electron tunneling spectroscopy as a function of gate voltage. The di-radical can be reversibly and controllably charged using the gate electrode while preserving its radical character. This allows to switch from the original

two-spin to a three-spin system where the added electron asymmetrically couples to the two radical centres. This magnetic parallel "path", switchable electrically in sub-picosecond timescales, can be thought of as changing the time evolution of the two-spin system and, in fact, is at the base of one of the implementations of the $\sqrt{\text{SWAP}}$ gate. The tri-radical, a triangular spin system exhibiting a robust quartet ground state in crystals and frozen solutions, shows instead, when in a molecular junction, a sample-to-sample reversal of the exchange interactions from ferro- to antiferromagnetic while keeping its radical character intact. We attribute this inversion to mechanical distortions induced by the substrate and we back this hypothesis with a density functional theory model describing the magnetic couplings as a function of mechanical torsion. We find that small torsions act strongly on the electron delocalization, resulting in an inversion for relatively small angles. These two examples illustrate the effect of the solid-state electrodes' when a magnetic molecular system interfaces with them and show, in turn, the role they play in stabilizing certain magnetic configurations as a result of electronic and mechanical interactions.

From the investigations on high-spin radicals, in Chapter 6 we take an excursion into basic thermodynamics and information theory. This inquire is not carried out with transport, but rather armed with a susceptometer and a SQUID; nor realized targeting a single molecule, but a *crystal*. In this sense, this chapter is the "isolate" of the present dissertation. Yet, what justifies its presence and location is the use of molecules one step higher in magnetic complexity compared to the radicals, i.e. authentic nano-magnets whose distinctive element is an axial anisotropy. At sufficiently low temperatures, this feature renders the molecules comparable to Ising-like spins in which information can be encoded. On a crystalline ensemble of such spins, we perform a Landauer erasure-storage cycle exploiting the quantum tunneling of magnetization induced by a transverse magnetic field. Through a *macroscopic* measurement of the ensemble's magnetization, we estimate the work needed for this operation. The result *per spin* is consistent with the Landauer limit $k_{\text{B}}T\ln 2$ and implies that each molecule behaves as an ideal and isolated single spin, i.e. non-dissipatively. Owing to the quantum-annealing dynamics, the relaxation time of the system is very short and thus permits to couple the Landauer limit with fast operation. Viewing the energy-time action as the real global cost of a computation, our systems performs several orders of magnitude better than other existing memory devices.

After the digression of the previous one, Chapter 7 reverts to the use of transport as the investigation tool. It is not, though, the single electron transport the reader is by now accustomed to, rather an extension of it to "electron pairs". These are produced by placing two superconducting slabs (S) in series with the gold electrodes (N) of the molecular junction (c) thus forming an SN-c-NS junction. The device that results reveals a soft superconducting gap persisting up to above 4 K and high magnetic fields while maintaining the virtues of gold electromigration and the customary gold-molecule chemistry. The demonstration of this is provided by a working superconducting molecular transistor.

The last chapter freely discusses the more promising and intriguing possibilities sprouting from the subjects of the previous chapters as well as the limitations and the possible improvements based on a critical analysis of the accumulated successes and failures.

SAMENVATTING

In dit werk onderzoeken we verschillende fysische fenomenen die voortkomen uit het opsluiten van elektronen in gelokaliseerde lading- en spin-kwantumdoosjes, genaamd *moleculen*.

Onze reis in de wondere wereld van de moleculen begint met de vraag waarom leven zich lang geleden heeft gevormd uit moleculen, in plaats van uit anorganische, kristallijne structuren; en waarom wij in een wereld bestaande uit alleen atoomkernen niet zouden bestaan en niet deze woorden zouden kunnen schrijven. We geven onze bescheiden kijk op deze vraag op basis van een aantal feiten met betrekking tot de energieschalen van de elektronische processen, de combinatoriek, en de inhoud en verdeling van informatie. Vervolgens beschrijven we het begrip *verstrooiing* in lekentaal; op welke manier we enkele moleculen en verzamelingen van moleculen kunnen aansluiten, en wat de haken en ogen zijn van de op transport gebaseerde en niet op transport gebaseerde technieken die relevant zijn voor dit werk. Onderzoek naar moleculen is niet zonder uitdagingen en valkuilen, dus we ontkomen er niet aan om deze ook te noemen in de beschrijving.

In hoofdstuk 2 introduceren we transport door een generiek moleculair object vanuit kwantitatief oogpunt. De reële en virtuele transportmechanismes worden bondig vergeleken en de wetenschappelijke terminologie uit verschillende vakgebieden wordt toegelicht om zo tot een gemeenschappelijk begrip te komen. Het traditionele *master equation* formalisme wordt didactisch uitgelegd voor het reële regime en het virtuele regime, waarna beide regimes gecombineerd worden tot één geheel met zowel reële als virtuele processen. In dit intermediaire regime van het *stability diagram* – genaamd COSET – vindt een niet-triviale wisselwerking tussen de twee regimes plaats die belangrijke gevolgen heeft voor de ontspanningsdynamica. Voor kleiner wordende intrinsieke ontspanningssnelheden – dat wil zeggen, voor 'goede' systemen – wordt het uitbreiden van het traditionele model des te meer relevant; hiermee kunnen schattingen van deze waarden worden gemaakt. De theoretische uiteenzetting wordt aangevuld met experimentele data van een moleculair systeem met een grote spin waarin zowel effecten van COSET als van *spin-pumping* te zien zijn.

In hoofdstukken 3, 4 en 5 gebruiken we de concepten uit het eerste hoofdstuk om drie soorten moleculen uit dezelfde familie van radicaalmoleculen te bestuderen, met toenemende spin-complexiteit. Het simpelste molecuul bevat een enkel radicaalelektron in zijn neutrale toestand dat een Kondo effect laat zien dat we volledig karakteriseren als functie van *bias*-voltage, temperatuur en magnetisch veld in geëlektromigreerde breekjuncties en mechanische breekjuncties. De analyse, uitgevoerd op een significant aantal samples die robuust zijn tegen mechanische en elektrostatische variaties van de omgeving, laat een goede consistentie in Kondo-energieën zien.

De chemische eenheid die de basis vormt van de mono-radicaal kan gebruikt worden voor de synthese van di- en triradicalen met respectievelijk twee en drie ge-

koppelde spins. Deze radicaalmoleculen worden bestudeerd met behulp van *inelastic electron tunneling spectroscopy* als functie van gate voltage. Het diradicaal kan reversibel en gecontroleerd geladen worden door de gate elektrode, waarbij de radicaalelektronen intact blijven. Dit maakt het mogelijk om te schakelen tussen het originele systeem met twee spins en een systeem met drie spins, waarin het toegevoegde elektron asymmetrisch gekoppeld is met de twee radicaalelektronen. Dit parallelle magnetische 'pad', wat elektrisch te schakelen is binnen picoseconden, kan gezien worden als de tijd-evolutie van het systeem met twee spins en vormt de basis van een implementatie van een SWAP gate. Het triradicaal, een driehoekig spinsysteem dat een robuuste *quartet* grondtoestand heeft in kristallen en bevroren oplossingen, laat in verschillende moleculaire juncties een variatie zien in uitwisselingsinteracties; van ferromagnetisch tot antiferromagnetisch, waarbij in alle gevallen de radicaalelektronen behouden blijven. We dichten de inversie van de uitwisselingsinteracties toe aan de mechanische verstoringen die het substraat veroorzaakt en onderbouwen deze hypothese met behulp van een *density functional theory* model dat de magnetische koppelingen beschrijft als functie van mechanische torsie. Hieruit blijkt dat lichte torsie een groot effect heeft op de delocalisatie van de elektronen wat resulteert in een inversie van de koppeling. Deze twee voorbeelden illustreren het effect van de elektrodes op een magnetisch moleculair systeem en laten de rol zien die ze spelen bij het stabiliseren van magnetische toestanden via de elektronische en mechanische interacties.

Van de radicaalmoleculen met grote spins, nemen we in hoofdstuk 6 een uitstapje naar basis thermodynamica en informatietheorie. Dit deel van het onderzoek wordt niet uitgevoerd met behulp van transportmetingen, maar met een susceptometer en een SQUID; en niet met een enkel molecuul, maar met een *kristal*. In die zin staat dit hoofdstuk los van de rest van de dissertatie. Maar de aanwezigheid en de plaats van het hoofdstuk past toch in het verhaal door het gebruik van moleculen met grotere magnetische complexiteit, namelijk nano-magneten met een kenmerkende axiale magnetische anisotropie. Bij voldoende lage temperaturen, maakt deze eigenschap de moleculen als Ising-spins waarin informatie kan worden opgeslagen. Op een kristallijne verzameling van deze spins voeren we een Landauer cyclus van informatie wissen en opslaan uit, waarbij we gebruik maken van de kwantumtunneling van de magnetisatie door een transversaal magnetisch veld. Door een *macroscopische* meting van de magnetisatie schatten we de benodigde arbeid voor deze operatie. Het resultaat *per spin* komt overeen met de Landauer limiet $k_B T \ln 2$ wat impliceert dat ieder molecuul zich gedraagt als een ideale, geïsoleerde enkele spin, dat wil zeggen, zonder dissipatie. Door de kwantum-*annealing*-dynamica is de ontspanningstijd van het systeem heel kort waardoor het mogelijk is de Landauer limiet te combineren met snelle operaties. Als we de energie-tijd actie beschouwen als de daadwerkelijke globale kosten voor een berekening, presteren onze systemen ordes van grootte beter dan andere bestaande opslagapparaten.

Na het uitstapje in het vorige hoofdstuk, keren we in hoofdstuk 7 terug naar het gebruik van transportmetingen als onderzoeksmiddel, al bespreken we niet het transport van enkele elektronen zoals in het voorgaande, maar breiden we uit naar *paren* van elektronen. Deze worden gemaakt door twee supergeleiders (S) die we in serie plaatsen met de gouden elektrodes (N) van de moleculaire junctie (c); in de vorm van een SN-c-NS-junctie. De verkregen supergeleidende junctie laat een *soft*

gap zien die blijft bestaan boven 4 K en in een groot magnetisch veld, terwijl de voordelen van de elektromigratie van goud en de gebruikelijke goud-molecuul-chemie behouden blijven. We demonstreren dit aan de hand van een werkende supergeleidende moleculaire transistor.

In het laatste hoofdstuk bespreken we de veelbelovende en intrigerende mogelijkheden die voortkomen uit de onderwerpen van de vorige hoofdstukken, en ook de beperkingen en mogelijke verbeteringen op basis van een kritische analyse van behaalde successen en mislukkingen.

1

A TALE OF MOLECULES

In science one tries to tell people, in such a way as to be understood by everyone, something that no one ever knew before. In the case of poetry, it is the exact opposite!

Paul Dirac

Si sta
come d'autunno
sugli alberi
le foglie

Giuseppe Ungaretti

This chapter is intended as a bird's-eye roaming on molecules and molecular electronics, the thrill of measuring a single-molecule and the challenges encountered by the various experimental methods. It is in the aim of the author to stretch, here and there, the scientific language and add some colour in the attempt of fascinating the laymen and the scientist into the molecular world wunderkammer.

1

1.1. THE BEAUTY OF MOLECULES

In my first approach to chemical and physical sciences, long ago, I distinctively remember of being fascinated by a peculiar definition of the molecule as the smallest chemical-physical quantity a given substance can be divided into still preserving the composition and properties of that substance. Put in this way, the molecule is the "atom of chemistry" – from *a-tomos*, non-divisible. A molecule, like an atom, can certainly be divided in more elementary constituents, but the moment this occurs, it transforms into something whose function is irremediably altered. Differently than for atoms, it is not only its chemical composition – as it can be written down in letters and subscripts – that determines its function, but also its arrangement in space, i.e. its "stereochemistry". So it goes that some beneficial substances become poisonous by a chiral transformation and that enzymes selectively catalyse *only one* of the many possible reactions, as one key enters one lock.

This carrying the information in the structure is called stereo-specificity and is fascinatingly placed by the biochemist Jacques Monod at the source of the complexity of life and its ability to "defeat" thermodynamics [1]. It is the fabric of this complexity what molecules constitute and they do it through their distinct combinatorial, thus informational, possibilities. Protons and neutrons can be combined into about a hundred of distinct atomic species, but atoms can be combined in an uncountable number of molecules: the incommensurability of the this ratio is almost as beautifully terrifying as a $\sqrt{-1}$![1] At the root of the bewildering variety is the diversity of types and shapes of the valence electronic orbitals that the *aufbau* guarantees and the ease of losing and accepting charge. This is ultimately due to the fact that molecules are governed by low-energy, electron-mediated laws while atoms by the high-energy strong forces. These "low energies" happen to range from below to above room temperature and the solar spectrum energy span, so that stability and stillness (strong, covalent bonds) can be combined with manipulation, transformation and recycling (weak, non-covalent bonds). This relative weakness is a strength – and a necessity – when it comes to mean flexibility in many aspects of life and in physics, since it allows a multiplicity of states close in energy and yet *distinguishable*. An exquisite instance of this multiplicity are the isomers of a molecule that, differing by a bond rotation only, carry a different information and can, like Maxwell's demoniacal gatekeepers, allow or block a chemical reaction.

In addition to the astounding variety, another interesting aspects of the molecular world is the prominent relation between structure and function. A single defect in a crystal cannot determine a dramatic change of the band structure, as this is a result of, i.e. "emerges" from, the whole lattice and is therefore a *delocalized* property (Bloch's theorem). For analogous reasons, chemical doping as we know it nowadays would lose its meaning when applied to the handful of atoms in the nanometer-square-size transistors of our future computers. A molecule is instead an object that wholly encodes its function in its self-contained structure: A single defect in a protein will render it ineffective as a catalyst. This connection between the structure and the function is a result of the molecule containing its information *locally*, as an independent and well characterised unit. This is allowed by the fact that molecules

[1] E. Zamjatin, in "We" his politico-satirical book about a rational totalitarianism, considers that the most ungraspable object.

self-assemble with *atomic precision*, wherein the ultimate atomic control over physical properties is reached [2].

For what we have discussed and other reasons, nature chooses a molecular life and molecules enjoy a rock-star "popularity" as far as living beings are concerned. The world of molecules is a world in which our bodies can be creative factories of matter and reactions and a deft chemist's hand, with the help of affordable temperatures and pressures, can potentially synthesise anything. Doing that in a nuclear-based world would require a large up-shift of the energy range we live in to match the sizes and forces characteristic of the large scales of the Universe. It is not a chance that, for now, the only furnaces of the incredibly stable atoms are the stars[2]. From these finite set of "given" atoms, molecules assembly and that is what life utilises to build itself.

In this tale of molecules, nuclei play the dormant, heavy and phlegmatic characters (Born-Oppenheimer approximation) always shrouded by a buzzing and restless cloud of electrons. These electrons are the main players in the game of exchange and binding and therefore the exchange currency of most of the transactions that take place in nature at the physiological level. For this reason, nature has a fully-fledged molecular electronics which has existed already for a number of millennia in, among others, catalysis, photosynthesis, metabolism and of which we actually *are* a result. The purpose of our modest version of molecular electronics is to exploit, for our scientific as well as technological needs, some of the properties and riches we have listed. One of the ways of implementing that passes through the incorporation of a molecule into a solid-state device. In this fusion of the molecular bottom-up and top-down worlds, to the complexity of the former, the degree of freedom of the latter is added, creating a vast landscape of possibilities.

1.2. CONDUCTANCE IS SCATTERING: THROWING CHARGED PEBBLES AT MOLECULES

The question of how to measure the properties of an individual object that is about a hundred millions times smaller than our human hands would scare most of the profanes. The ones that attended with some wonder a biology class, after few seconds of initial baffling, will tell you: "with a microscope, right?" Others, more insightfully, would say: "with a ruler that has a similar or smaller size". Behind the apparent difference, the two answers are facets of the same underlying principle: some particles "hit" the (similarly-sized or larger) object of interest, i.e. they interact with it, and they come back to you with an answer[3]. Everyone is familiar with this concept and has had fun with it as a kid, in one way or another. In fact, this extremely natural way of measuring is the essence of what physicists call "the scattering problem": An ingoing, initial state interacts with the system of investigation by exchanging energy, linear and angular momentum and results in a final, outgoing state containing some information on the system. In this work, the electrons in the source (drain) correspond to the ingoing (outgoing) state and the amount of electron flow (conductance) carries the information. What can be exactly gained through this electron *scattering spectroscopy*? Information on the *availability* of electronic states in the localised

[2] Given the results of artificial nuclear fusion, I dare to say that that *now* will extend far into the future.
[3] The absence of an answer is, of course, an answer itself.

object embedded between the electrodes: depending on the context, this would be called the cross section, the density of states, the discrete spectrum or the transmission (transparency) of the object. In all cases, it describes the probability with which an electron goes from an initial state characterised by an energy and angular momentum to a final state with (different) characteristics as a consequence of the interaction with the object. In the case of a spinful molecule, the quantisation of energy and angular momentum generate a discrete spectrum which, by varying voltages and magnetic field, can be thoroughly explored and characterised.

As a result of the rich landscape of the molecular world, the spectrum of a molecule can be arbitrarily complex and reflect the many degrees of freedom available. A good number of those are accessible by transport spectroscopy. To facilitate the enumeration, it is helpful to consider two large sets of phenomena divided according to whether they carry information on the statics (time-independent response) or dynamics (time-dependent response) of the system:

- **Statics**

  Elastic electronic currents provide information on the molecular orbitals: their energy, shape, delocalisation, hybridisation with the electrodes as well as whether they exhibit quantum interference and correlations; inelastically exchanging energy and/or angular momentum with the molecule, the electron can *probe* vibrational and spin states.

- **Dynamics**

  By increasing their current and/or polarizing their spin, electrons can *pump* the molecular system or induce conformational changes and probe its relaxation properties.

Despite sharing the same scattering idea, we will see later that different techniques are needed to access all these phenomena/information. Given electron transport in molecules is defined by *local* properties – much differently than in solids –, what binds all the techniques described in the next paragraph is the attempt of getting as close as possible to measuring conductance through a *single* molecule.

Contacting a single molecule The idea of contacting and passing current through a single molecule is likely to have appeared as something close to folly even to the scientists of half a century ago. That idea might have started becoming more of a reality with the invention of the scanning tunneling microscope (STM), in 1981. In spite of that, the first "contact" between an STM tip and a molecule did not occur until 1995, when the current through a fullerene on a gold substrate was recorded and the transparency of this "unusual" tunnel barrier estimated. Two years later, the previously existing mechanically-controlled break junction architecture was employed to measure a single molecule self-assembled between source and drain contacts. The limitation of this technique, as stated by the authors, is that "a third proximal probe cannot be placed near the molecule"; such a probe would allow, for instance, "a definitive demonstration of Coulomb blockade". A notable stepping stone was posed in 2000 with the invention of the electromigration break junction. The same process at the base of integrated circuit failures was cleverly turned into the opportunity of producing nanometer-size gaps in gold nanowires [3]. In this configuration, the addition of

a third electrode under the gap and sufficiently close to the molecule provided the "lever" to shift the molecular levels, acting like a gate in a solid-state transistor.

The three techniques briefly described have continued to be used successfully throughout the years with some conceptual modifications and great technological refinement. Given their relevance to this work, it is worthwhile to dwell on the advantages and limitations of each one, following the same chronological line.

As seen in Table 1.1, one of the prominent advantages of the scanning tunneling microscope over the break junctions lies in its capability of imaging in real space. Being a scanning technique, it allows to measure the molecule site-by-site, probing its orbitals (shape, localization) and associating them to the respective transport characteristics. This has yielded a body of noteworthy literature on, among others, Kondo effect and Shiba physics [4] and allowed to beautifully image molecular orbitals [5] as well as the formation of chemical bonds [6]. The freedom to adjust the molecule-tip distance allows to tune the current through the sample and, with that, the study of the molecule's dynamics[4]. This tunability comes at the price of a relatively limited junction stability in time (drift) at room temperature. Other limitations are the absence of a gate electrode, the ultra-high vacuum and all the "requirements" that contribute to make it a bulky apparatus, hardly conceivable in places other than a laboratory. As far as molecular electronics is concerned, the compatibility with high-vacuum restricts the choice of deposition techniques to vacuum sublimation and, more recently, electro-spraying, thus reducing the set of available molecules.

Given the similar underlying concept, mechanically-controlled break junctions (MCBJ) share some of the characteristics of STMs like the molecule-electrodes distance adjustability and the practical difficulties of building in a gate electrode. On their side, they boast a good electrode's mechanical stability [7] which allows long averaging and very large statistics at room temperature. For this reason over the years, they have emerged, on the one hand, as a robust characterization tool to explore the conduction mechanisms in molecules, the various anchoring groups [8], quantum interference effects and vibrational states [9, 10]. As far as the dynamics is concerned, single MCBJ traces can reveal the transient behaviour of a molecule – in relation to the electrodes or one of its internal degrees of freedom – upon electrodes' pushing and pulling.

Finally, we come to electromigration break junctions (EMBJ) – thanks to which most of this work is realized. The major difference, and advantage, over the two other techniques is the presence of the gate electrode, which allows the modulation of the molecular levels independent of the bias voltage. With this knob, a regime where the molecule gets charged and discharged periodically is accessible. This regime, called sequential electron tunneling, goes beyond the pure scattering character of elastic and inelastic transport in that any intermediate state between initial and final is not *virtual*, but rather characterised by a real reduction/oxidation of the molecular species. As it can be driven in and out, the charge can also be stabilised on the molecule, thereby changing its electrochemical state. This can affect, and thus be used to manipulate, its magnetic parameters and ground state (Chapter 4) as well as, for instance, its vibrational spectrum [11]. The relaxation properties of this new

[4] In turn, the strong molecule-substrate coupling intrinsic to this technique renders the presence of a decoupling layer necessary when substrate-substrate scattering are to be suppressed and appreciable dynamics is wanted.

Technique	Advantages	Limitations
STM	Real-space imaging	No "energy-space" imaging
	Mechanical manipulation	Bulkiness (vacuum, room-T instability)
MCBJ	Adjustable & stable distance	No gate electrode
	Large statistics	No real-space imaging
EMBJ	Electrochemical change	No manipulation
	Compactness (low-T, low noise)	Limited statistics

Table 1.1: A simple-minded list of the main advantages and limitations of scanning tunneling microscopy, mechanically-controllable and electromigrated break junctions (see text for details).

state, the starting state and all the shades between them can be studied as a function of gate voltage (Chapter 2). Other winning aspects of electromigration junctions are the electrodes' stability and the *on-chip* compactness which allows low-noise measurements at mK temperatures. The major drawback of this technique, especially when it comes to building an hypothetical device out of it, is the limited degree of control on the electrodes' fine structure and molecule's arrangement between them. This implies that acquiring a large statistics (and trends) on molecular behaviours is challenging, if not impracticable. Interesting progress has been made in this sense by studying the electromigration dynamics *in vivo* under a transmission electron microscope [12].

Since each of these techniques is complementary to the others and visits this or the other corner of the large landscape of molecular transport, an effort to combine them yields almost always a more complete picture (Chapter 3). In prospective, there is a concrete possibility that these methods will appear medieval, not to say prehistoric, to the future reader of this work, when advanced and compact "tweezers" might be able to manipulate molecules as we handle bolts and nuts.

Let us now briefly touch upon two other sets of methods that are not based on the single-molecule scheme.

Contacting many molecules: ensemble measurements As we wrote above, a unique property of molecules is their ability to self-assemble. On the right surface and with the right chemistry, molecules will self-assemble into an ordered monolayer film. Besides its extensive use in the coating industry, nanofabrication, sensing and so on, this can be thought as a platform to measure an ensemble of molecules with coherent orientation and composition when an electrode is placed "on top" of this layer. In this *vertical* arrangement, a voltage can be applied to the electrodes and a current through the ensemble results. Experiments with a variety of electrode materials, deposition methods and molecules have been performed, ranging from gold to eutectic gallium-indium alloys. Average information on the conduction mechanism, semiconducting properties, charge traps have been extracted. Given the relative "softness" of the molecular layer, the metal's tendency to intercalate through it and the roughness of the electrodes at the atomic level, some of the first results are disputable in their claim that transport really occurs through the molecule and not via metallic low resistance paths.

Alternative methods: non-transport based Methods that are not based on transport are innumerable. Without the purpose of being exhaustive, here we will briefly mention the few which are used to investigate the spin properties of molecules.

Electron paramagnetic resonance (EPR) is a spectroscopic method based on setting unpaired electron spins of an molecules' ensemble in resonance with a fixed microwave field and measuring the absorbance as a function of magnetic field. With this method, information on the anisotropy parameters, gyromagnetic ratios and hyperfine couplings with a resolution of about 10 MHz (0.5 mK) can be obtained – provided the sample consists of a sufficiently high number of spins. As ultimately the results are magnetic energies, this technique can be partly thought of as a many-molecule counterpart of inelastic electron transport spectroscopy, with the former exhibiting higher energy resolution but a smaller excitation-energy range as compared to the latter. It is worth mentioning that a pulsed version of the continuous wave EPR permits, through sequences of microwave pulses, to perform various spin rotations/qubit operations. This constitutes an important characterization (and manipulation) tool to measure the dynamical and relaxation behaviour – respectively quantified by phase-memory and spin-lattice relaxation time – of spins in molecules.

Superconducting quantum interference devices (SQUIDs) and ac-susceptibility coils directly measure magnetization and its derivative (magnetic susceptibility). When applied to molecules, the two techniques reveal their magnetic ground state, hysteretic phenomena and spin relaxation dynamics. Traditionally applied to samples with a large number of spins, SQUIDs have lately reached sensitivities allowing the measurements of few spins [13, 14]. In Chapter 6, we use the two techniques on a crystal of Fe_8 molecular magnetic bits to measure the work necessary to carry out a Landauer erasure-storage cycle.

After this brief journey through the virtues and vices of experimental techniques, we would like to come back to the single-molecule junction setting and address, a bit more closely, the challenges and non-idealities that this paradigm still poses.

1.3. THE CHALLENGES

So far we have assumed that the investigation and use of molecules in single-molecule junctions come at no price, i.e. the way we contact them has little or no influence on their properties. The truth is that, in the attempt of investigating these rich quantum boxes, we inevitably affect them – even for the simple fact that the contacts modify their symmetry. In fact, considering the molecule and the solid-state device (or substrate) as two independent objects does not reflect the reality of transport experiments on molecules. More appropriate is to consider the two as entangled into one molecular junction. This issue – both a bless and a curse – is well-exemplified by STM experiments where single atoms acquire additional/distinctive properties as a result of their interaction with the substrate and, sometimes neglected, vice versa. The bless is that this constitutes "a sort of extended periodic table" [15] for both atom and substrate; the curse lies in that some of the resulting effects might be undesired and/or difficult to model and thus predict.

In the field of molecules, an analogous reasoning applies with the difference that the structural complexity is higher. Well-known examples of this "dressing" – borrowing the concept from quantum field theory – occurring when in contact to a

solid-state substrate are the renormalization of the "bare" HOMO-LUMO gap and variations of level alignment (See Ref. [16] and references therein), the stabilization of added charges on the ligands [17], the formation of spinterfaces in spintronics [18] and the radical changes in quantum spin dynamics and relaxation [19]. Major factors here are electrostatic effects in the form of charge transfer through the molecule-electrode interface – and image charges – and, in particular for the spin dynamics and relaxation, the presence/absence of relaxation channels (electrons, phonons) via the substrate. Due to the sensitivity to the electronic configuration over relatively small energy scales, magnetism is affected by any of the mentioned factors. As exemplified in Chapter 4 and Chapter 5, large variations in the magnetic properties can also occur as a consequence of mechanical distortions. Some of the listed effects will depend on the substrate/electrode material – and thus be more controllable – and others on the specific arrangement of the molecule between the electrodes or the electrodes' shape.

All the aforementioned elements, and especially the latter, add an intrinsic stochasticity to the molecular junction formation and constitute probably the major challenge of molecular electronics. This stochasticity renders the systematic study difficult and ultimately may prevent the real-world exploitation/integration of single molecules in electronic devices (memory, logic circuits, transistors, sensors, etc.).

A way to attack the issue would be ensuring a reproducible anchoring of single molecules to electrodes and, eventually, their stability at room temperature and pressure. Notable attempts in this direction have been made. One of the most intriguing ones [20] makes use, on the one hand, of an antibody molecule trained in a living mice body to recognize and bind to gold nanoparticles and, on the other, of source-drain electrodes on each of which two gold nanoparticles are placed with the help of an atomic force microscope. The antibody is then deposited on the patterned structure in a liquid solution and allowed to bind to the nanoparticles through self-assembling. The site-specific characteristic of the antibody provides reproducible contacts at room temperature. The caveat is that the method applies to proteins of about 10 nm in size.

When wanting to scale down to the few nanometer size, fewer biologically-inspired methods are available. At that scale, a potentially promising approach makes use of graphene electrodes. Carbon-carbon, carbon-sulphur covalent bonds would be strong and "directional" enough to ensure reproducible contacts. When a process similar to electromigration is used (electroburning), the difficulty lies in producing clean electrode edges ("clean gaps") and avoid the appearance of unwanted quantum dots during the burning process. Alternatives to this method would be the direct patterning of the electrodes by means of very stable and high-resolution electron-beam lithography or He-milling.

1.4. PROSPECT OF THIS WORK

The present work treats quantum phenomena arising from magnetic, i.e. spinful, molecules. All but one chapter (Chapter 6) use electron transport as investigation – and pumping – tool. Moving from an initial chemical compound, the magnetic properties of which are tailored from a chemical prospective, we investigate the effects arising from these intrinsic properties and from their integration into a solid-state

device in the form of a molecular quantum dot. The different topics, hinted at in the present chapter, are organized as follows:

Chapter 2 details the different regimes of electron transport expected in a molecular junction with a particular focus on phenomena occurring at the crossover between the well-characterized cotunneling and resonant electron transport regimes. These phenomena are treated and analysed starting from experimental data collected on a magnetic molecule.

Chapter 3 is the first of the series of three following chapters integrating organic radical molecules in junctions. There we address the Kondo physics arising from the unpaired electron of a neutral monoradical molecule and shows the relatively high robustness of the Kondo feature against perturbations of the mechanical and electrostatic environment.

Chapter 4 goes one step higher in the ladder of chemical complexity by discussing results of transport through a di-radical molecule and shows an example of *electric* control of its magnetic properties. Such control allows to switch on and off the exchange interaction between the added electron and the radical pair.

Chapter 5 explores the effects of mechanical torsions on the exchange coupling and ground state inversion in a tri-radical neutral molecular species. The transition from ferromagnetic to anti-ferromagnetic coupling is attributed to the interaction of the molecule with the electrodes and supported by DFT calculations.

Chapter 6 is an excursion into the territory of fundamental thermodynamics and information theory. In it, we use a molecular magnet as a magnetic bit to perform an erasure-storage operation at the Landauer limit. We discuss the result in terms of the energy-time complementarity of a computation and show that the quantumness of the system employed allows us to operate at the thermodynamics limit without compromising the speed of operation.

Chapter 7 describes an extension of the three-terminal solid-state junction used in the previous chapters to superconducting transport exploiting the proximity-effect. A measurement of a magnetic molecule in this setting is shown as a proof of concept.

Conclusion and outlook contain an open discussion – free from the formal constraints of scientific publication imposed on the other chapters – of a number of, more or less audacious, developments of the experiments previously described.

1.5. COMMENTARY ON THE COVER

The man you see depicted on the cover crouched on a rock, deeply absorbed in geometrically dividing and "rationalizing" in what seems to be the obscure depths of the sea, surrounded by lichens and algae, is Sir Isaac Newton. The executor of this watercolour monotype print – this choice gives the representation its peculiar bluriness – is the poet, artist, visionary "madmen" William Blake, who portrays Newton in this pose about seventy years after death had taken him. The two Englishmen had evidently antipodal visions of the universe and that is what brought the latter to subtitle the print "Personification of Man limited by reason". More specifically, the problem that this visionary figure, classifiable, if you like, as early romantic, had with the other visionary figure of science was that the latter, according to the former, based his speculations on a single rational vision, where the second considered essential a

four-folded vision of reality which would accompany and complement reason with emotion, imagination and instinct. In the atmosphere of scientific materialism of the Europe of his time, on the one hand, and oppressive obedience to a moral code on the other, he exhorts to the humanitarian goal of achieving personal wholeness of body and spirit – *energy* and *reason* in his language –, openly already recognizing in their dichotomy the source of the hypocritical nature of the moral principles and the consequent inauthenticity of communication. But we all know that Newton was a strong believer, to the point of deducing the existence of a God starting from his observation of the "delicate balance" of the solar system[5]. Why then should he be used as a symbol of the "Man limited by reason"? In fact, it is not religion that Blake, and we here, refer to. He rather takes Newton as a metonymy of the human attempt of understanding *all* the aspects of reality only through the glasses of the active reason. Today, in an epoch wherein scientists and laymen are enthused by the indisputable and empowering material success of the *Western* scientific view, the former should be aware of their share of responsibility in maintaining alive the plurality of approaches by not enforcing inadvertently a hubristic *colonization* of the forms of *knowledge* at the root of these approaches: anything attempting to reduce everything to a single point – even with the best of the intentions – is pitifully impoverishing as much as it is empowering.

[5] In one of his letters [21] he lists his "arguments for a deity": "[...] To make this system therefore, with all its motions, required a Cause which understood and compared together the quantities of matter in the several bodies. [...] that Cause to be not blind and fortuitous but very well skilled in mechanics and geometry." I cannot not mention here that this makes me think of Newton as the first of the physicists (among which, for instance, Barrow and Tipler [22]) who endorse that subtle form of intelligent design that goes under the name of anthropic principle.

2

AN INTRODUCTION TO TRANSPORT IN MAGNETIC MOLECULES

Géométrie est l'art de bien raisonner sur des figures mal faites

Henri Poincaré

At the single-molecule level, the two major complementary ways to explore molecules' properties are molecular quantum-dot structures and scanning probes. This chapter outlines comprehensive principles of electron-transport spectroscopy relevant to both these approaches and presents a high-resolution experiment on a high-spin single-molecule junction exemplifying these principles. In this joint experimental and theoretical analysis, particular focus is put on the crossover between resonant *regime [single-electron tunneling (SET)] and the* off-resonant *regime [inelastic electron (co)tunneling (IETS)]. We show that the interplay of these two processes leads to unexpected* mirages *of resonances not captured by either of the two pictures alone. Combined with nonequilibrium IETS – four-electron pump-probe excitations – these mirages provide crucial information on the relaxation of spin excitations. The resulting encompassing physical picture is supported by a master-equation approach that goes beyond weak coupling.*

Parts of this chapter have been published in J. Chem. Phys. **146**, 092330 (2017) by R. Gaudenzi, M. Misiorny, E. Burzurí, M. R. Wegewijs, H.S.J. van der Zant.

2.1. INTRODUCTION

Both the fundamental and applied studies on transport phenomena in electronic devices of molecular dimensions have bloomed over the past decade [23–26]. An interesting aspect of this development is that it has increasingly hybridized the diverse fields of chemistry, nanofabrication and physics with the primary ambition of accessing properties like high spin and large exchange couplings, vibrational modes, large charging energies and long electronic/nuclear spin coherence times, subtle electronic orbital interplay, self-organisation [27, 28] and chirality [29, 30]. This is rendered possible by the higher energy scales of the molecular systems – a direct consequence of their size – and their complex, chemically tailorable, inner structures which have proven to be effective in addressing, for instance, the spin-phonon [11, 31], Shiba [4, 32] and Kondo physics [33], quantum interference effects [34] and nuclear spin manipulation [35].

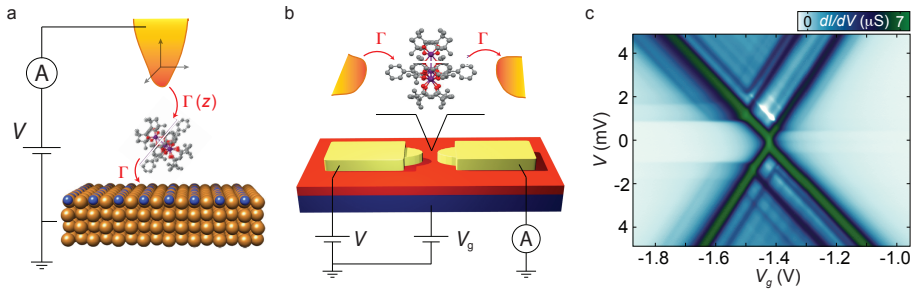

Figure 2.1: **High-spin single-molecule junctions.** (a) Vertical approach: the metallic tip of a scanning tunneling microscope (STM) allows one to scan laterally in real space and acquire transport spectra as a function of the bias V at specific molecular sites. The vertical position z controls the tip-molecule coupling $\Gamma(z)$, while the molecule-substrate coupling is fixed. (b) Planar approach: by embedding a bottom-up synthesized magnetic molecule into a solid-state device, one can control its energy levels through a gate-voltage V_g. This *scanning in energy space* grants access to both regimes of real (redox) charging and virtual charging (scattering) and their nontrivial crossover. (c) Conductance map showing a range of features in the resonant regime (center), off-resonant regimes (far left and right) as well as the crossover regime. These are analyzed in detail in Fig. 2.11 and Fig. 2.16.

In most of the works, in particular those concerning molecular *spin* systems, two complementary approaches have contributed to explore these effects. On the one hand stands off-resonant transport spectroscopy, which is the major tool of choice in the scanning-tunneling microscopy (STM) approach to nanoscale spin systems [36–47], depicted in Fig. 2.1(a). Off-resonantspectroscopy is also dominant in the field of mechanically-controlled break junctions (MCBJ) [48, 49] to study vibrations [11, 50–53] and, less often, spin effects [33, 54, 55]. On the other hand, resonant transport spectroscopy, originating in the multi-terminal fabrication of quantum dots (QDs, Fig. 2.1(b)) [56], is a well-developed tool applied to a broad range of excitations in nanostructures, [57–66] including spin [67–77]. The key difference between resonant and off-resonant approaches is the former's reliance on energy-level control *independent* of the transport bias, i.e., true *gating* of the molecular levels [78–82], which should be distinguished from the capacitive level shift in STM which is *caused* by the bias. In terms of physical processes, this difference corresponds to resonant spectroscopy relying on real charging of the molecule and off-resonant transport involv-

Regime	Section	QD community	STM / MCBJ community
Resonant	Sec. 2.2.1	Single-electron tunneling (SET) Sequential / incoherent tunneling	Resonant tunneling
Off-resonant	Sec. 2.2.2	(In)elastic co-tunneling (COT)	(In)elastic electron tunneling spectroscopy (EETS/IETS)
		Coherent tunneling Schrieffer-Wolff (transformation)	Appelbaum (Hamiltonian)
	Sec. 2.2.2		Pump-probe (co)tunneling spectroscopy
Crossover	Sec. 2.2.3	Cotunneling-assisted single-electron tunneling (COSET, CAST)	

Table 2.1: **Nomenclature of off-resonant and resonant spectroscopy in different communities.**

ing only virtual charging.

In this contribution we discuss a comprehensive picture of transport applicable to a large family of nanoscale objects. This is motivated by the experimental spectrum of a molecular junction depicted in Fig. 2.1(c). Such a conductance map is so full of detail that it warrants a systematic joint experimental and theoretical study. In particular, we discuss several effects which are often overlooked despite their importance to electron transport spectroscopy and despite existing experimental [53, 83, 84] and theoretical works [85–90]. For instance, it turns out that inelastic / off-resonant transport is *not* simply equivalent to the statement that "resonant processes play no role". In fact, we show that generally less than 55% of the parameter regime of applied voltages that nominally qualified as off-resonant is actually described by the widely used inelastic (co)tunneling (COT or IETS) picture. Although in many experiments to date this has not been so apparent, our experimental evidence suggests that this needs consideration. In theoretical considerations, resonant and off-resonant transport regimes are often taken as complementary. Our measurements illustrate how this overlooks an important class of relaxation processes. The breakdown of the COT picture in the off-resonant regime presents, in fact, new opportunities for studying the relaxation of molecular spin-excitations which are of importance for applications. Interestingly, these resonances are qualitative indicators of a device of high quality, e.g., for applications involving spin-pumping. We illustrate *experimentally* the ambiguities that the sole modeling of off-resonant conductance curves can run into. For instance, we show that this may lead one to infer quantum states that do not correspond to real excitations, but are simply *mirages* of lower lying excitations, including their Zeeman splittings. Although elaborated here for a spin system, our conclusions apply generally, for example to electronic [83] and vibrational excitations in nano electro-mechanical systems (NEMS) [53, 84].

The outline of this chapter is as follows: In Sec. 2.2 we review the physical picture of electron tunneling spectroscopy and outline how a given spectrum manifests itself in resonant [Sec. 2.2.1] and off-resonant [Sec. 2.2.2] transport spectra. In Sec. 2.2.3 we discuss how these two spectra continuously transform into each other as the energy levels are varied relative to the bias voltage. With this in hand, we put together a physical picture capturing all discussed effects which will be subsequently applied

to describe the experiment in Sec. 2.3.

In Sec. 2.3 we follow the reverse path of experimental transport spectroscopy: We reconstruct the excitation spectrum of a high-spin molecular junction based on the feature-rich transport spectra as a function of bias voltage, magnetic field, and gate voltage. Starting from the off-resonant analysis, we use the boundary conditions imposed by the resonant spectrum to resolve a number of ambiguities in the off-resonant state-assignment. With the full model in hand we highlight two informative transport features: (i) *nonequilibrium COT*, i.e., a pump-probe spectroscopy using the electronic analog of Raman transitions and (ii) *mirages* of SET resonances that occur well inside the off-resonant regime. We conclude with an outlook in Sec. 2.4.

Since we aim to bring the insights from various communities together, we summarize in Table 2.1 the different but equivalent terminology used. For clarity reasons we set $k_B = \hbar = e = 1$ for the rest of this discussion.

2.2. PHYSICAL PICTURES OF TRANSPORT - REAL VS. VIRTUAL CHARGING

The two prevalent conceptual approaches to transport through molecular electronic devices are characterized by the simple physical distinction, sketched in Fig. 2.2, between real charging – chemical reduction or oxidation – and virtual charging – electrons scattering between contacts through a molecular bridge. Theoretically, the distinction rests on whether the physical processes appear in the leading or next-to-leading order in the tunnel coupling strength, Γ, relative to the thermal fluctuation energy T. Experimentally, this translates into distinct applied voltages under which these processes turn on. These conditions are the primary spectroscopic indicators, allowing the distinction between real and virtual transport processes, and take precedence over line shape and lifetime broadening. For reviews on theoretical approaches to molecular transport see Refs. [25, 91–93].

2.2.1. RESONANT TRANSPORT SPECTROSCOPY

Real charging forms the starting point of what we will call the resonant picture of transport (see Table 2.1 for other nomenclature). Its energy resolution is limited by the Heisenberg lifetime set by the tunnel coupling $\mathscr{H}^T$

$$(\mathscr{H}^{\mathrm{T}})^2 \propto \Gamma, \tag{2.1}$$

allowing for sharp transport spectroscopy of weakly coupled systems. This relation has a prominent place in the field of QDs which covers structures such as artificial atoms and artificial molecules with redox spectra [56] very similar to real atoms [94] and simple molecules [62, 75, 95–97]. Resonant transport also plays a role in STM although its energy resolution is often limited by the strong coupling typical of the asymmetric probe-substrate configuration.

Given sufficient weak coupling/energy resolution, much is gained when the energy-level dependence of these transport spectra, can be mapped out as function of *gate-voltage*. This dependence allows a detailed model to be extracted involving just a few electronic orbitals [95, 98], their Coulomb interactions [99] and their interaction with the most relevant degrees of freedom (e.g., isotropic [72] and anisotropic

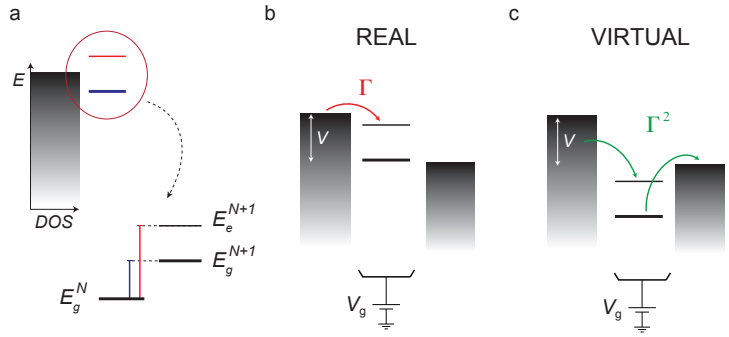

Figure 2.2: **Real and virtual transport processes.** (a) Electrochemical potential (μ) picture (top) and corresponding molecular energy level picture (bottom). Each discrete "level" in the top panel stands for an *electrochemical potential* of the molecule, i.e., a *difference* between two energies sketched in the lower panel, $E_g^{N+1} - E_g^N$ (dark blue) and $E_e^{N+1} - E_g^N$ (red). The energies E_i^N depend on the charge N and further quantum numbers denoted by i. Due to the capacitive coupling to a gate electrode these energy differences can be tuned to be (b) on-resonance and (c) off-resonance with the electrode continuum indicated by the gray shaded boxes. (b) Real charging: absorption of an electron, reduces the molecule for real, $(N,g) \to (N+1,e)$, going from the ground state g for charge N to an excited state e with charge $N+1$. Since this is a one-step process, the rate scales with Γ, the strength of the tunnel coupling. The applied voltage V equals the difference between the electrochemical potentials of the electrodes. (c) Virtual charging: the scattering of an electron off or through the molecule proceeds via a virtual intermediate state, for example, starting from the ground state g and ending in a final excited state e, $(N+1,g) \to (N,g) \to (N+1,e)$. The rate of such a two-step process scales as Γ^2. In this case charging is considered only virtual, as no redox reaction takes place: although energy and angular momentum are transferred onto the molecule, the electron number remains fixed to $N+1$.

spins [67, 100], quantized vibrations [11, 101], and nuclear spins [35, 102–104]). In particular electronic [57, 59, 60, 62, 63, 77, 79, 105], spin-orbit [82, 106] structure as well as electro-mechanical coupling [53, 64, 84, 107] of CNTs have been very accurately modeled this way.

In molecular electronics transport spectroscopy takes a prominent role since imaging of the device is challenging. By moving to molecular-scale gated structures one often compromises real-space imaging. Here we highlight the advantages that such structures offer. Nevertheless, electrical gates that work simultaneously with a scanning tip [108] or a MCBJ [109] have been realized, but with rather low gate coupling. Notably, mechanical gating [110, 111, 111–114] by lifting a single molecule from the substrate has been demonstrated, resulting in $\mathrm{d}I/\mathrm{d}V$ stability diagrams where the role of V_g is taken over by the tip-height z in Fig. 2.1. A scanning quantum-dot [115] has also been realized using a single-molecule [116].

RESONANT EXCITATIONS - GATE DEPENDENCE

In the resonant transport regime one considers processes of the leading order in the tunnel coupling Γ, cf. Eq. (2.1). Although most of this is in principle well-known, we review this approach [92, 117] since some of its basic consequences for the *off-resonant regime* – discussed below – are often overlooked.

Typically, analysis of resonant spectra requires a model Hamiltonian $\mathscr{H}$ that involves at most tens of states in the most complex situations [72, 90, 118–121]. Its energies E_i^N are labeled by the charge number N and a further quantum numbers

(orbital, spin, vibrational) collected into an index i. Crucial for the following discussion is the voltage-dependence of this energy spectrum. We assume it is uniform, i.e., $\propto N$, independent of further quantum numbers i. This can be derived from a capacitive description of the Coulomb interactions between system and electrodes referred to as the *constant interaction model* [91, 92, 99, 117, 122]. In this case, $E_i^N(V_g, V_L, V_R) = E_i^N - N(\alpha_g V_g + \alpha_L V_L + \alpha_R V_R)$ where E_i^N are constants and V_L (V_R) is the potential applied at source (drain) electrode. Here, $\alpha_x = C_x/C$ for x = L, R,g are capacitive parameters of which only two are independent since $C := \sum_x C_x$. In Sec. 2.2.4 we discuss corrections to this – often good – assumption [123]. Unless stated otherwise, we will set for simplicity $\alpha_g = 1$, i.e., the negative shift of the energy levels equals the gate voltage. The bias is applied to the electron source, $V_L = -V$, and the drain is grounded, $V_R = 0$, giving $E_i^N(V_g, V) = E_i^N - N\alpha_g V_g + N\alpha_L V$ and $\mu_L = \mu_R + V$ with constant μ_R. Unless stated otherwise, schematics are drawn assuming $\alpha_L = 1/2$, corresponding to symmetric and dominant source-drain capacitances $C_L = C_R \gg C_g$.

The Hamiltonian for the complete transport situation takes the generic form $\mathscr{H}^{tot} := \mathscr{H} + \mathscr{H}^{res} + \mathscr{H}^{T}$ where $\mathscr{H}^{T}$ is a sum of tunneling Hamiltonians that each transfers a single electron across one of the junctions to either metal electrodes. The electrodes, labeled by r =L(left), R(right), are described by $\mathscr{H}^{res}$ – essentially through their densities of states – and by their electrochemical potentials μ^r and temperature T. For the present purposes this level of detail suffices, e.g., see Ref. [90] for details. For a tunneling process involving such a transfer of precisely one electron, one of the electrochemical potentials has to fulfill

$$\mu^r \geq E_f^{N+1} - E_i^N \quad \text{for} \quad r = \text{L, R}, \tag{2.2}$$

in order for the electron to be injected into an N-electron state i, resulting in the final $N+1$-electron state f. Below this threshold the state $(N+1, f)$ is unstable, i.e., it decays back to (N, i) by expelling the electron back into the electrode. The rate for the injection process, $W_{f,i}^{N+1,N}$, is given by familiar Golden Rule expressions and depends on the difference of both sides of Eq. (2.2) relative to temperature T. When the process turns on by changing V, it gives rise to a peak in the differential conductance, $\mathrm{d}I/\mathrm{d}V$, corresponding to a sharp step in current, of width T and height $\sim \Gamma/T \ll 1$ (in units of e^2/h) since we are assuming weak coupling and high temperature.

If the total system conserves both the spin and its projection along some axis (e.g., the B-field axis), the rate involves a selection-rule-governed prefactor. This prefactor is zero unless the change of the molecular spin and its projection satisfy

$$|\Delta S| = 1/2 \quad \text{and} \quad |\Delta M| = 1/2. \tag{2.3}$$

These conditions reflect the fact that only a single electron is available for transferring spin to the molecule.

Incidentally, we note that this picture is very useful even beyond the weak couplings and high temperatures assumed here. Close to the resonance defined by condition (2.2) the transport still shows a peak which is, however, modified by higher-order corrections. The width of the current step becomes broadened $\propto \Gamma$, giving a conductance peak ~ 1 in units of e^2/h. Its energy position may shift on the order of Γ.

It is now clear in which regime of applied voltages the above picture applies. In Fig. 2.3 this is sketched in the plane of applied bias (V) and gate voltage (V_g). Here,

we call such a (schematic) $\mathrm{d}I/\mathrm{d}V$ intensity plot – also known as stability diagram or Coulomb-diamond – a *transport spectrum.* The indicated vertical line cuts through this diagram correspond to $\mathrm{d}I/\mathrm{d}V$ traces measured in STM or MCBJ experiments. Applied to the ground states of subsequent charge states – labeled by g – , Eq. (2.2) gives the two inequalities

$$\mu^L \geq E_g^{N+1} - E_g^N \geq \mu^R. \tag{2.4}$$

These define the shaded bias window in Fig. 2.3(a), delimited by the cross. Here, a single electron entering from the left can exit to the right, resulting in a net directed current.

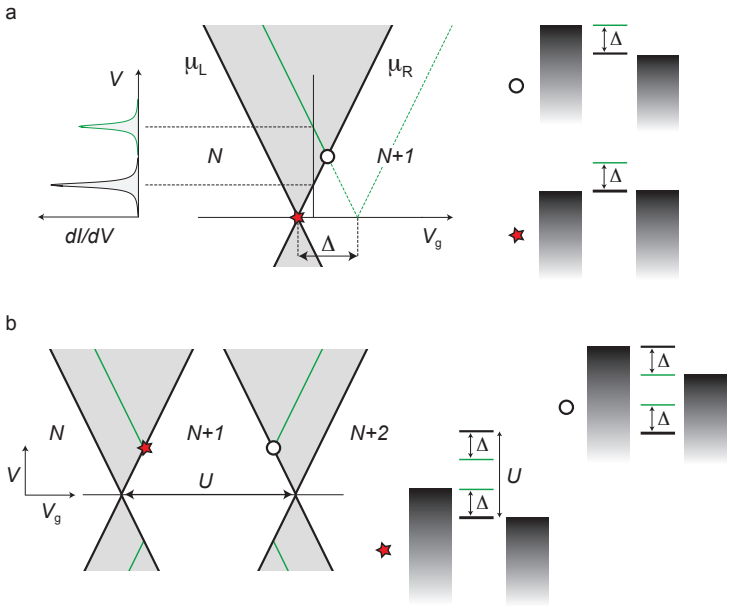

Figure 2.3: **Resonant regime: main features** (a) Current flows in the bias window set by Eq. (2.4) (shaded) for two charge states N and $N+1$. The boundary lines (bold), where $\mu_r = E_g^{N+1} - E_g^N$ for $r = \mathrm{L,R}$, have slopes $-\alpha_\mathrm{g}/(1-\alpha_\mathrm{R})$ and $\alpha_\mathrm{g}/\alpha_\mathrm{R}$, respectively, allowing the capacitive parameters to be determined. The green lines, offset horizontally by $\Delta = E_e^{N+1} - E_g^{N+1}$, indicate the window of accessibility of the excited state E_e^{N+1} and are defined by $\mu_r = \Delta + E_g^{N+1} - E_g^N$. (b) Similar to figure (a), for three charge states N, $N+1$ and $N+2$. This adds a copy of the bias window of (a) that is horizontally offset by the energy U [Eq. (2.6)] with boundaries $\mu_r = E_g^{N+2} - E_g^{N+1}$ for $r = \mathrm{L,R}$. The excitation lines on the right (green) are mirrored horizontally, $\mu_r = -\Delta + E_g^{N+2} - E_g^{N+1}$ for $r = \mathrm{L,R}$, since electron processes relative to $N+1$ have become hole processes.

It is now tempting to naively define the *off-resonant regime* as the complement of the grey resonant regime in Fig. 2.3(a), i.e., by moving across its boundaries by more than T or Γ. However, this simple rationale is not correct even for a small finite bias matching some excitation at energy Δ, indicated by green lines in Fig. 2.3(a). Only in the linear-response regime [122] around $\mu = \mu_\mathrm{L} = \mu_\mathrm{R}$ the off-resonant regime can be defined as the complement of the resonant regime:

$$|E_g^{N+1} - E_g^N - \mu| \gg \max\{\Gamma, T\}. \tag{2.5}$$

In subsequent charge states analogous considerations apply: transitions between charge states $N+1$ and $N+2$ give rise to a shifted copy of the bias window as shown in Fig. 2.3(b). The shift – experimentally directly accessible – is denoted by:

$$U := (E_g^{N+2} - E_g^{N+1}) - (E_g^{N+1} - E_g^{N}). \tag{2.6}$$

This includes the charging energy of the molecule, but also the magnitude of orbital energy differences and the magnetic field. For example, for a single orbital level with charging energy $u > 0$ and magnetic field B one finds $U = u + |B| > u$ due to the opposite spin-filling enforced by the Pauli principle.

STATIONARY STATE AND RESONANT TRANSPORT CURRENT

The above rules are substantiated by a simple master equation for the stationary-state occupations P_i^N of the states with energy E_i^N that can be derived from the outlined model, see, e.g., Ref. [90]. This approach is used in Sec. 2.3.3 to model part of our experiment. For the $N \leftrightarrow N+1$ resonance regime the stationary-state equation reads (for notational simplicity we here set $N = 0$)

$$\frac{\mathrm{d}}{\mathrm{d}t}\begin{bmatrix}\mathbf{P}^0\\ \mathbf{P}^1\end{bmatrix} = 0 = \begin{bmatrix}\mathbf{W}^{0,0} & \mathbf{W}^{0,1}\\ \mathbf{W}^{1,0} & \mathbf{W}^{1,1}\end{bmatrix}\begin{bmatrix}\mathbf{P}^0\\ \mathbf{P}^1\end{bmatrix}. \tag{2.7}$$

Here, $\mathbf{W}^{1,0}$ is the matrix of transition rates $W_{f,i}^{1,0}$ between states $(0,i)$ and $(1,f)$, and analogously for $\mathbf{W}^{0,1}$. For example, one of the equations,

$$\frac{\mathrm{d}}{\mathrm{d}t}P_f^1 = \sum_i W_{f,i}^{1,0}P_i^0 + W_{f,f}^{1,1}P_f^1, \tag{2.8}$$

describes the balance between the gain in occupation probability due to all transitions $(0,i) \to (1,f)$, and the leakage $-W_{f,f}^{1,1}$ from the state $(1,f)$. The entries of the diagonal matrices $\mathbf{W}^{0,0}$ and $\mathbf{W}^{1,1}$ have negative values $W_{f,f}^{0,0} = -\sum_i W_{i,f}^{1,0}$ and $W_{f,f}^{1,1} = -\sum_i W_{i,f}^{0,1}$, respectively, such that probability normalization $\sum_i P_i^0 + \sum_j P_j^1 = 1$ is preserved in Eq. (2.7). In the leading order in Γ, the rate matrix has separate contributions from the left ($r = \mathrm{L}$) and right ($r = \mathrm{R}$) electrode: $\mathbf{W} = \mathbf{W}^{\mathrm{L}} + \mathbf{W}^{\mathrm{R}}$. These allow the stationary current to be computed by counting the electrons transferred by tunnel processes through the r-th junction,

$$I^r = \sum_{N_f,N_i}{}' \sum_{f,i} \left(N_f - N_i\right) \times [W^r]_{f,i}^{N_f,N_i} P_i^{N_i}, \tag{2.9}$$

where stationarity guarantees $I^{\mathrm{L}} = -I^{\mathrm{R}}$. We note that, because we are considering only single-electron tunneling processes (first order in Γ), the primed sum is constrained to $N_f = N_i \pm 1$ by charge conservation.

2.2.2. OFF-RESONANT TRANSPORT SPECTROSCOPY

We now take the opposite point of view and consider transport entirely due to virtual charging or scattering through the molecule. The resulting off-resonant transport spectroscopy, alternatively called cotunneling (COT) or IETS spectroscopy, dates back to Lambe and Jacklevic [124]. The discussion of the precise conditions under

which the off-resonant picture applies is postponed to Sec. 2.2.3. Throughout we will denote by the label COT– unless stated otherwise – *inelastic* cotunneling.

The attractive feature of off-resonant relative to resonant spectroscopy is the higher energy resolution as we explain below [Eq. (2.18) ff.]. Exploiting this in combination with the STM's imaging capability has allowed chemical identification [43, 46, 47, 116, 125–132]. This in turn has enabled atomistic modeling of the junction using *ab-initio* calculations [133–136], also including strong interaction effects [112, 137, 138], giving a detailed picture of transport on the atomic scale [139–145].

In recent years, off-resonant spectroscopy has been also intensively applied to spin systems [38, 43, 45, 146–148] in more symmetric [5] STM configurations. However, it is sometimes not realized that the same off-resonant spectroscopy also applies to gated molecular junction, and more generally to QDs [82, 149–151]. In fact, motivated by the enhanced energy resolution, spectroscopy of discrete spin-states was introduced in gate-controlled semiconductor QDs [149, 152, 153] before it was introduced in STM as spin-flip spectroscopy [38], see also [154, 155]. COT spectroscopy is also used to study molecular properties other than spin, e.g., vibrational states [156–161].

OFF-RESONANT EXCITATIONS – NO GATE DEPENDENCE

In the off-resonant picture, one considers transport due to next-to-leading order processes, i.e. of order Γ^2 in the tunnel rates. This involves elastic (inelastic) processes involving two electrons from the electrodes and a zero (net) energy transfer of energy. When the maximal energy supplied by the electrons – one electron coming in from, say, $r = \mathrm{L}$ at high energy μ_L, and the other outgoing to $r = \mathrm{R}$ at low energy μ_R – exceeds a discrete energy difference of the molecule,

$$\mu_\mathrm{L} - \mu_\mathrm{R} = V \geq \Delta^{N+1}_{f,i} := E^{N+1}_f - E^{N+1}_i, \tag{2.10}$$

transport may be altered with V. Importantly, on the right hand side, all V and V_g dependences of the energies cancel out [cf. Sec. 2.2.1] since we assumed that the applied voltages *uniformly* shift the excitation spectrum for fixed charge [16, 123].

The occurrence of such a process depends on whether the initial state i is occupied or not by another already active process. It thus depends on whether we are in the "equilibrium" or "nonequilibrium" regime, both of which are accessible in our experiment in Sec. 2.3. The spectroscopy rules require the following separate discussion.

"Equilibrium" inelastic COT Already in the linear transport regime, $V \lesssim T, \Gamma$ (assuming no excitations lie below T and Γ), here is scattering through the molecule in a fixed stable charge state in the form of *elastic* COT [154, 155, 162], see Table 2.1 for the varied nomenclature. This gives rise to a small current scaling $\propto \Gamma^2$. With increasing bias V, this mechanism yields a nonlinear background current which is, however, featureless.

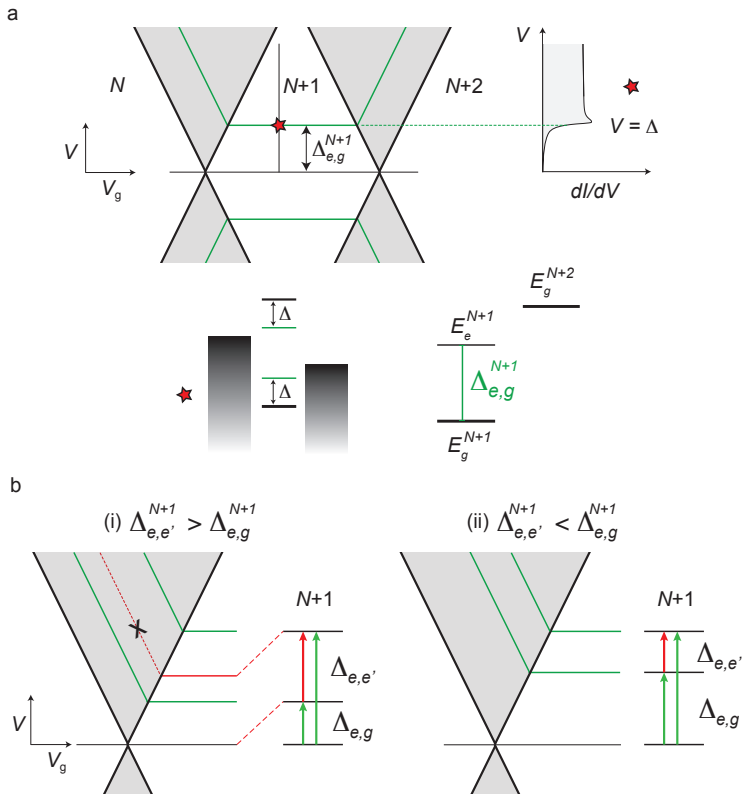

Figure 2.4: **COT transport conditions.** (a) Same as Fig. 2.3(b), now indicating the "equilibrium" resonance (green horizontal line) at which the excitation $(N+1,e)$ is reached from the *ground* state $(N+1,g)$ by a COT process. This horizontal line always connects to a SET resonance $(N,g) \to (N+1,e)$ on the left [$(N+2,g) \to (N+1,e)$ on the right] (green tilted lines). At the point where the COT and SET resonance line meet two conditions are simultaneously satisfied: one for the onset of SET, *electrochemical potential* $= \mu_{\rm L} = E_g^{N+1} - E_g^N$ [$\mu_{\rm R} = E_g^{N+2} - E_g^{N+1}$], and one for onset of inelastic COT, *bias* $= \mu_{\rm L} - \mu_{\rm R} = E_e^{N+1} - E_g^{N+1}$ = excitation at fixed $N+1$. This is depicted in Fig. 2.3(b) where the chemical potential diagrams are sketched for these two crossing points, marked $\circ$ and $\star$ in that figure. (b) "Nonequilibrium" COT resonance corresponding to a transition $(N+1,e) \to (N+1,e')$ starting from an *excited state e for* $N+1$ *electrons*. Case (i) and (ii) are discussed in the text. This resonance (red horizontal line) does not connect to some SET resonance (crossed-out dashed red line) since there is no single-electron transition $(N,e) \to (N+1,e')$: the state e is an excitation for $N+1$ electrons, *not* for N electrons. This should be contrasted with "equilibrium" COT resonances in (a).

When the voltage provides enough energy to reach the lowest excitation e of the $N+1$-electron ground state g, the transition $(N+1,g) \to (N+1,e)$ is enabled, cf. Fig. 2.2(c). This occurs when the *gate-voltage independent* criterion set by Eq. (2.10) with $i = g$ and $f = e$ is satisfied:

$$V \geq \Delta_{e,g}^{N+1}. \tag{2.11}$$

The above energy condition is the tell-tale sign of an off-resonant process: as sketched in Fig. 2.4(a), this allows for a clear-cut distinction from resonant processes with a gate dependent energy condition (2.2). Importantly, such a COT feature always

connects to the gate-dependent SET resonance corresponding to excitation $\Delta_{e,g}^{N+1}$. As in the resonant regime, we stress that criterion (2.11) uses the peak position in the (V_g, V) plane as a primary indicator. The line shape along a vertical cut in the figure, as measured in STM, may be less clear. In theoretical modeling the line shape is also not a unique indicator. The line shape is a good secondary indicator of the nature of a process.

"Nonequilibrium" inelastic COT: electronic pump-probe spectroscopy. The above "equilibrium" picture of off-resonant transport has been successfully applied in many instances. However, as the first excited state $(N+1, e)$ is accessed, the rules of the game change. If the relaxation induced by sources other than transport is weak enough [163], the occupation of the excited states can become non-negligible. In such a case, as illustrated in Fig. 2.4(b), a secondary inelastic COT process from the excited state e to an even higher excited state e' should be considered. Such secondary processes, with the generic condition:

$$V \geq \Delta_{e'e}^{N+1} = \Delta_{e'g}^{N+1} - \Delta_{eg}^{N+1}, \tag{2.12}$$

indicate a device with an intrinsic relaxation rate small compared to COT rates $\propto \Gamma^2$. As discussed in Fig. 2.4(b), such excitations *never* connect to a corresponding SET excitation in the transport spectrum. At this point, two cases have to be considered, both of which are relevant to the our experiment in Sec. 2.3.4.

(i) If $\Delta_{e'e}^{N+1} > \Delta_{eg}^{N+1}$ – i.e., the gaps in the energy spectrum grow with energy – an extra *"nonequilibrium" inelastic COT* resonance at bias $V = \Delta_{e'g}^{N+1} - \Delta_{eg}^{N+1}$ appears, as illustrated in panel (i) of Fig. 2.4(b). This extra resonance is very useful since it provides a further consistency check on the excitations Δ_{eg}^{N+1} and $\Delta_{e'g}^{N+1}$ observed independently in the SET. (If the SET transition to e' is not allowed by a selection rule, the secondary COT resonance may be the only evidence of this state.) Clearly, the intensity of such secondary "nonequilibrium" COT resonances is generally expected to be lower than the primary ones that start from the ground state. In Sec. 2.3.4 we will experimentally control this sequential COTelectronic pump-probe excitations by tuning a magnetic field.

(ii) In the opposite case, $\Delta_{e'e}^{N+1} < \Delta_{eg}^{N+1}$, no *extra* COT excitation related to e' appears: there is no change in the current at the lower voltage $\Delta_{e'e}^{N+1}$ because the initial state $(N+1, e)$ only becomes occupied at the *higher* voltage Δ_{eg}^{N+1}. This is illustrated in panel (ii) of Fig. 2.4(b). Examples of both these cases occur in the off-resonant spectra of molecular magnets due to the interesting interplay of their easy-axis and transverse anisotropy, see the supplement of Ref. [68].

STATIONARY STATE AND OFF-RESONANT TRANSPORT CURRENT

Similar to the resonant case, the conditions (2.10)-(2.12) are incorporated in a simple stationary master equation for off-resonant transport whose derivation we discuss further below. In particular, the occupation probabilities $\mathbf{P}^{N+1}$ in the stationary transport state are determined by (as previously, we put $N = 0$)

$$\frac{\mathrm{d}}{\mathrm{d}t}\mathbf{P}^1 = 0 = \mathbf{W}^{1,1}\mathbf{P}^1. \tag{2.13}$$

Here, $\mathbf{W}^{1,1}$ is a matrix of rates $W^{1,1}_{f,i}$ for transitions between states $i \to f$. Since in the off-resonant regime charging is only virtual, these transitions now occur for a fixed charge state. The matrix takes the form $\mathbf{W}^{1,1} = \sum_{rr'} \mathbf{W}^{1,1;r,r'}$, including rate matrices $\mathbf{W}^{1,1;r,r'}$ for back-scattering from the molecule (to the same electrode, $r = r'$) and scattering through it (between electrodes $r \neq r'$). The current is obtained by counting the net number of electrons transferred from one electrode to the other:

$$I^{\mathrm{L}\to\mathrm{R}} = \sum_{f,i} (W^{1,1;\mathrm{R},\mathrm{L}}_{f,i} - W^{1,1;\mathrm{L},\mathrm{R}}_{f,i}) P^1_i. \tag{2.14}$$

The inclusion into this picture of the above discussed "non-equilibrium" COT effects depends whether one solves the master equation (2.13) or not. To obtain the simpler description of "equilibrium" inelastic COT [case (i) above] one can insert *by hand* equilibrium populations $P^1_i = e^{-E^1_i/T}/\mathcal{Z}^1$ directly into Eq. (2.14). Solving, instead, Eq. (2.13) without further assumptions gives the "nonequilibrium" inelastic COT case [45, 164] discussed above [case (ii)]. In practice, these two extreme limits – both computable without explicit consideration of intrinsic relaxation – are always useful to compare since any more detailed modeling of the intrinsic relaxation will lie somewhere in between'.

The electron tunneling rates in Eq. (2.13) are made up entirely of contributions of order Γ^2. There are two common ways of computing these rates, and we now present the underlying physics relevant for the discussion in Sec. 2.2.3.

Appelbaum-Schrieffer-Wolff Hamiltonian A conceptual connection between the off-resonantvirtual charging picture and the resonant picture of real charging in Sec. 2.2.1 emerges naturally when applying the unitary transformation [165] due to Appelbaum [166, 167], Schrieffer and Wolff [168–170] (ASW) to the transport *Hamiltonian* $\mathscr{H}^{\mathrm{tot}}$ [cf. Sec. 2.2.1]. The effective ASW model obtained in this way allows one to easily see the key features of the off-resonant spectroscopy.

In this approach, the one-electron tunneling processes described by the Hamiltonian $\mathscr{H}^T$, are transformed away and the charge state is fixed by hand to a definite integer. With that, also all the gate-voltage dependence of resonance *positions* [Eq. (2.11) ff.] drops out. This new ASW model is obtained by applying a specially chosen unitary transformation $\mathscr{U}$ to the original Hamiltonian such that:

$$\begin{aligned} \mathscr{H}^{\mathrm{tot}} &\to \mathscr{U}(\mathscr{H} + \mathscr{H}^{\mathrm{R}} + \mathscr{H}^{\mathrm{T}})\mathscr{U}^\dagger \\ &\approx \mathscr{H} + \mathscr{H}^{\mathrm{R}} + \mathscr{H}^{\mathrm{A}} + \mathrm{O}(\Gamma^4). \end{aligned} \tag{2.15}$$

The single-electron coupling $\mathscr{H}^{\mathrm{T}} \propto \sqrt{\Gamma}$ is effectively replaced by $\mathscr{H}^{\mathrm{A}} \propto \Gamma$, which involves only two-electron processes. When restricted to fixed charge N on the molecule, $\mathscr{H}^{\mathrm{A}}$ exclusively represents scattering of electrons off and through the molecule. In many cases of interest it contains terms describing the potential (scalar) and exchange (spin-spin) scattering of electrons with amplitudes J and K, respectively. For example, for a single-orbital model

$$\mathscr{H}^{\mathrm{A}} = \sum_{r,r'} (J_{rr'} \mathbf{S}\cdot\mathbf{s}_{rr'} + K_{rr'} N n_{rr'}). \tag{2.16}$$

where the operators $\mathbf{s}_{rr'}$ ($n_{rr'}$) describe spin-(in)dependent intra- ([$r = r'$]) and inter-electrode ($r \neq r'$) scattering of electrons. See Ref. [117] for details, such as the energy-dependence of J and K ignored above.

Selection rules. The ASW coupling $\mathscr{H}^{\mathrm{A}}$ has selection rules that differ from the original single-electron tunnel coupling $\mathscr{H}^{\mathrm{T}}$. If the time-evolution in the virtual intermediate state conserves spin (M and S), then the selection rules for $\mathscr{H}^{\mathrm{T}}$ imply the following selection rules for transition rates obtained from $\mathscr{H}^{\mathrm{A}}$:

$$|\Delta S| = 0, 1 \quad \text{and} \quad |\Delta M| = 0, 1. \tag{2.17}$$

For this to be valid, both the molecule ($\mathscr{H}$) and electrodes ($\mathscr{H}^{\mathrm{R}}$) must be spin-isotropic. However, even when effects that break this spin-isotropy are present these selection rules may still hold to good approximation. This requires the magnetic field, magnetic anisotropy terms, etc., to have characteristic energies that are small relative to the distance to resonance. In these cases, the selection rules (2.17) reflect that the two [1] electrons involved in the scattering process have integer spin 0 or 1 available for exchange with the molecule. We will apply this in Sec. 2.3.1.

For the example case (2.16), the scattering is coupled to the molecule only through its charge (N, constant) and spin ($\mathbf{S}$). As a result, the rules (2.17) apply with $\Delta S = 0$ and $|\Delta M| = 0$ (if $S = 0$) or $|\Delta M| = 1$ (if $S = 1/2$), because [2] a single orbital does not support a triplet spin ($S = 1$). For more general situations $\mathscr{H}^{\mathrm{A}}$ contains additional terms [171] that change both spin and orbital occupations, see also Sec. 4.3 of Ref. [172]. These do allow for $|\Delta S| = 1$ while still larger changes are forbidden. Physically, one can understand that $|\Delta S| = 1$ is indeed possible [164, 173] for a two-orbital molecule: starting from a singlet $S = 0$ one can reach spin triplet $S = 1$ via a virtual intermediate state with spin $S'' = 1/2$, i.e., when, after exiting, an electron returns into a different orbital. This effectively moves an electron between the two orbitals, allowing for a singlet-triplet transition.

Lifetime. After transforming to this new effective picture, scattering becomes the leading order transport mechanism. The Golden Rule approach can be then applied analogously to the case of of the resonant regime, but now with respect to the ASW scattering $\mathscr{H}^{\mathrm{A}}$. In this way Eq. (2.13) is obtained together with an expression for the corresponding rate matrix $\mathbf{W}^{1,1}$. The $\mathrm{d}I/\mathrm{d}V$ given by Eq. (2.14) shows gate-voltage-independent *steps* at energies set by Eq. (2.10).

Although at high temperatures these steps get thermally broadened [124], at low enough T their broadening is smaller than that of the SET peaks. While calculation of this lineshape requires higher-order contributions to $\mathbf{W}^{1,1}$, the relevant energy scale (inverse lifetime) is given by the magnitude of the Golden Rule rates *for the effective*

[1] We note that to transfer a single electron *through* the molecule, two electrons are needed: one enters the molecule, creating a virtual intermediate state, and one exits the molecule, producing the final state. In general, these electrons not necessarily have to be added to the same spin and / or orbital state on the molecule.

[2] This result can be understood in more detail from Eq. (2.16) as explained in Refs. [45, 140]: The Golden-Rule applied to the new effective coupling $\mathscr{H}^{\mathrm{A}}$, gives transition rates which involve matrix elements, $\langle S'M', s'm|\mathscr{H}^{\mathrm{A}}|SM, sm\rangle$ where we omit further quantum numbers unrelated to spin. Due to the factorization of the states $|SM, sm\rangle = |SM\rangle \otimes |sm\rangle$ into molecule ($|SM\rangle$) and electrode part ($|sm\rangle$) in this approximation, the matrix element have factors $\langle S'M'|\mathbf{S}|SM\rangle$, which is zero unless $\Delta S = 0$ and $|\Delta M| = 0, 1$, and $\langle S'M'|N|SM\rangle$, which is zero unless $\Delta S = \Delta M = 0$.

coupling $\mathscr{H}^A$ scaling as

$$(\mathscr{H}^{\mathrm{A}})^2 \propto \Gamma^2. \tag{2.18}$$

This results in a much larger lifetime compared to the one from SET [cf. Eq. (2.1)] due to the role of the interactions on the molecule suppressing charge fluctuations. The smaller intrinsic broadening is a key advantage of COT vs. SET spectroscopy [149].

Line shape. Due to nonequilibrium effects – i.e., the voltage-dependence of the occupations obtained by solving Eq. (2.13) – a small peak can develop on top of the COT step [152, 153, 164, 174]. Moreover, processes beyond the leading-order in $\mathscr{H}^{\mathrm{A}}$, which is all the COT approach accounts for, can have a similar effect. These turn the off-resonant tunneling step into a $\mathrm{d}I/\mathrm{d}V$ peak and are in use for more precise modeling of experiments [45, 175, 176]. Spin-polarization [177] and spin-orbit effects [151, 176], however, also affect the peak shape and asymmetry.

At low temperatures and sufficiently strong coupling a nonequilibrium Kondo effect develops which has been studied in great detail [164, 178–181]. These works show that the peak amplitude is then enhanced nonperturbatively in the tunnel coupling, in particular for low lying excitations. This requires nonequilibrium renormalization group methods beyond the present scope and we refer to various reviews [182–187]. In particular, it requires an account of the competition between the Kondo effect and the current-induced decoherence [188] in the (generalized) quantum master equation for the nonequilibrium density operator [180, 181].

From the present point of view of spectroscopy, the Kondo effect can be considered as a limit of an inelastic COT feature at $V = \Delta$ as $\Delta \to 0$, see Fig. 2.4(a). Its position is simply $V = 0$ at gate voltages sufficiently far between adjacent SET resonances by criterion (2.5). In particular, for transport spectroscopy of atomic and molecular spin systems the Kondo effect and its splitting into COT features [33, 189–191] is very important especially in combination with strong magnetic anisotropy [192–204]. We refer to reviews on STM [44, 205–207] and QD [76] studies.

Golden Rule $\mathscr{T}$-matrix rates A second way of arriving at the master equation (2.13) and the rates in $\mathbf{W}^{1,1}$ is the so-called $\mathscr{T}$-matrix approach [208]. In essence, here COT is regarded as a scattering process: in the Golden Rule the next-to-leading order $\mathscr{T}$-matrix [117],

$$\mathscr{T}(E) \approx \mathscr{H}^{\mathrm{T}} \frac{1}{E - \mathscr{H} - \mathscr{H}^{\mathrm{res}}} \mathscr{H}^{\mathrm{T}} + \ldots, \tag{2.19}$$

is used instead of the coupling $\mathscr{H}^T$, where E is the scattering energy. The main shortcoming of this approach is that the $\mathscr{T}$-matrix rates so obtained are infinite. The precise origin of the divergences was identified in Ref. [209] to the neglect of contributions that formally appear in *first-order in* Γ but which effectively contribute only in second order to the stationary state [90]. These come from so-called secular contributions, involving *off-diagonal* elements of the density matrix in the energy basis, in addition to the diagonal elements, the probabilities. By taking these contributions consistently into account [209], finite effective rates[3] for the master equation for the

[3] These rates can be brought into a form similar to those obtained in the ASW and $\mathscr{T}$-matrix approach, allowing some of advantages of the latter to be exploited.

probabilities are obtained. In both the ASW and $\mathscr{T}$-matrix approach these contributions are ignored and, instead, finite expressions for the rates are obtained only after *ad-hoc* infinite subtractions [119, 210]. This regularization "by hand" can – and in practice does – lead to rates *different* from the consistently-computed finite rates, see Ref. [209] for explicit comparisons. These problems have also been related [211] to the fact that calculation of stationary transport using a density matrix (occupations) is *not* a scattering problem – although it can be connected to it [212] – in the following sense: the coupling to the electrodes is never adiabatically turned off at large times (i.e., there is no *free* "outgoing state").

As we discuss next, such a consistent first *plus* second order approach is not only technically crucial but this also leads to additional physical effects that we measure in Sec. 2.3.

2.2.3. RESONANT– OFF-RESONANT CROSSOVER

Having reviewed the two prominent, complementary pictures of transport due to real and virtual charging, we now turn to the crossover regime where these two pictures coexist. This has received relatively little attention, but our experiment in Sec. 2.3 highlights its importance. As we have seen, despite the fact that charging is only virtual, an energy exchange between molecule and scattering electrons can occur. Depending on the energy-level positions, this virtual tunneling can "heat" the molecule so as to switch on real charging processes even well *outside* the resonant regime. However, in contrast to real heating, which leads to smearing of transport features, this nonequilibrium effect actually results in sharp features in the transport as a function of bias voltage. It thus becomes a new tool for *spectroscopy*.

SET MIRAGES OF COT EXCITATIONS

We first consider the simple case of a single excited state at energy $E_e^{N+1} = E_g^{N+1} + \Delta$ for $N+1$ electrons. In Fig. 2.5(a) we see that the resulting COT resonance at $V = \Delta$ (red) connects to the excited-state SET resonance $\mu_L = \Delta + E_g^{N+1} - E_g^N$ (blue), see also Fig. 2.4(a). The other SET resonance condition for the excited state,

$$\mu_R = \Delta + E_g^{N+1} - E_g^N \tag{2.20}$$

defines the green line dividing the inelastic COT regime $V \geq \Delta$ into two regions shaded red and blue. In the one shaded blue, at the point marked with a circle, the excited state created by a COT process is stable, that is, it cannot decay by a single-electron process since $\Delta + E_g^{N+1} - E_g^N < \mu_R$. As shown in the right panel of Fig. 2.5(b), the relaxation of this stable state can then only proceed by another COT process – via virtual charging – and it is thus slow ($\propto \Gamma^2$). Essentially, this means that the molecule is not "hot" enough to lift the Coulomb blockade of the *excited* state.

In contrast, in the red shaded area, at the point marked with a star, this stability is lost as $\Delta + E_g^{N+1} - E_g^N > \mu_R$. Now the relaxation proceeds much faster through a single-electron process (order Γ) as sketched in the left panel of Fig. 2.5(b). The molecule gets charged for real (either N or $N+2$) and quickly absorbs / emits an electron returning to the stable $N+1$ electron *ground* state, where the system idles waiting for the next COT excitation. Notably, this quenching of the excited state takes place far away from the resonant transport regime in terms of the resonance width, i.e., violating the linear-response criterion (2.5) for being off-resonance.

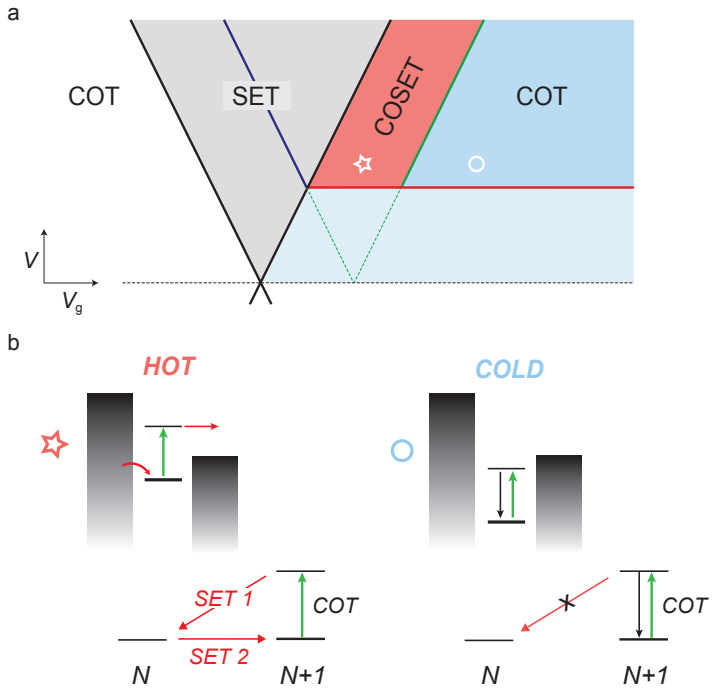

Figure 2.5: **Crossover regime between resonant and off-resonant transport.** (a) Same as Fig. 2.3(a), now indicating the regimes where the excited state $(N+1,e)$ relaxes by COT (darker blue area) to $(N+1,g)$ or by SET (red area) to (N,g). Only such "equilibrium" COT resonances, i.e., involving the *ground* state $(N+1,g)$ can exhibit such a COSET mirage. The reason is that only such a type of COT resonance connects to a SET resonance as explained in Fig. 2.4(b) for the case of *exciting* the molecule while charging it, $(N,g) \to (N+1,e)$. The COSET resonance corresponds to the SET transition between the same two states but in the reverse direction, *relaxing* the molecule $(N+1,e) \to (N,g)$, while discharging it. (b) Two relaxation mechanisms after excitation by COT: *Left panel*: relaxation in two steps (red) via real occupation of charge state N. *Right panel*: when the process "SET 1" is energetically not allowed excitation (green) and relaxation (black) proceeds in a single step by COT, using charge state N only virtually. (Since here process "SET 2" irrelevant it is not indicated.)

The enhanced relaxation induced by first-order tunneling, occurring when moving from the circle to the star in Fig. 2.5(a), leads to a change in current if no other processes (e.g., phonons, hyperfine coupling, etc.) dominate this relaxation channel ($\propto \Gamma$). As a results, the presence of such a resonance signals a "good" molecular device, i.e., one in which the intrinsic relaxation is small compared to the transport coupling Γ. We refer to this resonance, first pointed out in Refs. [85, 149, 152] and studied further [83, 86, 88–90], as cotunneling-assisted SET or COSET.

The COSET resonance has both COT and SET character. On the one hand, the geometric construction in Fig. 2.5(a) and Fig. 2.6 shows that it stems from *the same* excitation as the COT step at $V = \Delta$. However, its position V^* has the same strongly gate-voltage dependence as a SET resonance, in contrast to the original COT resonance at $V = \Delta$. Yet, the COSET peak requires COT to appear and its amplitude is relatively weak, whereas the SET peak is strong and does not require COT. For this reason, the COSET peak can be seen as a *mirage* of the COT excitation and a mirror

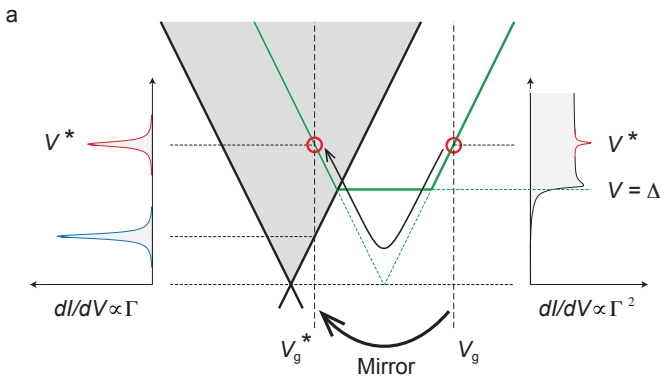

Figure 2.6: **Identifying a resonance as a COSET mirage.** Same situation as Fig. 2.5(a). The vertical $\mathrm{d}I/\mathrm{d}V$ cut on the right shows a COT resonance at $V = \Delta$ and its *mirage* at some bias $V^* > \Delta$. To identify the latter as such, a corresponding SET resonance must be present at the mirrored gate voltage V_g^*, as in the vertical cut shown on the left. Note that the indicated construction works for nonsymmetric capacitive coupling. For symmetric coupling, one can literally mirror the gate-voltage position relative to Δ on the horizontal axis.

image of the $(N, g) \rightarrow (N+1, e)$ SET peak, as constructed in Fig. 2.6(a). The resulting mirrored energy conditions can easily be checked in an experiment – cf. Fig. 2.14 – and impose constraints on spectroscopic analysis: if $\mathrm{d}I/\mathrm{d}V$ shows a resonance as a function of bias *outside* the SET regime, a resonance at the mirrored position *inside* the SET regime should be present.

CONNECTING OFF-RESONANT AND RESONANT ANALYSES

Besides the appearance of COSET mirages, the crossover regime provides further important pieces of spectroscopic information by constraining how SET and COT spectra continuously connect as the gate voltage is varied. This is discussed in Sec. 2.2.1, 2.2.2 and later on in Sec. 2.3.3, but we summarize the rules here. First, only "equilibrium" COT transitions can exhibit a COSET mirage as explained in Fig. 2.5. Second, excited-excited COT transitions (i.e., for the same charge state $N+1$) *never* connect to a corresponding SET feature, as we illustrated in panel (i) of Fig. 2.4(b). Finally, transitions between excited states with different charge – visible in the SET regime – *never* connect to a COT feature as will be illustrated in Fig. 2.12. These are strict consistency requirements when analyzing the transport spectra in the SET-COT crossover regime.

WHEN IS TRANSPORT "OFF-RESONANT" ?

We are now in the position to determine the region in which the physical picture of off-resonant scattering through the molecule of Sec. 2.2.2 applies. This is illustrated in Fig. 2.7.

The key necessary assumption of the COT approach – often not stated precisely – is that all excited states $(N+1, e)$ that are *accessible* from the ground state $(N+1, g)$ must be stable with respect to *first-order* relaxation processes:

$$W_{g,e}^{N,N+1} = 0 \quad \text{and} \quad W_{g,e}^{N+2,N+1} = 0. \tag{2.21}$$

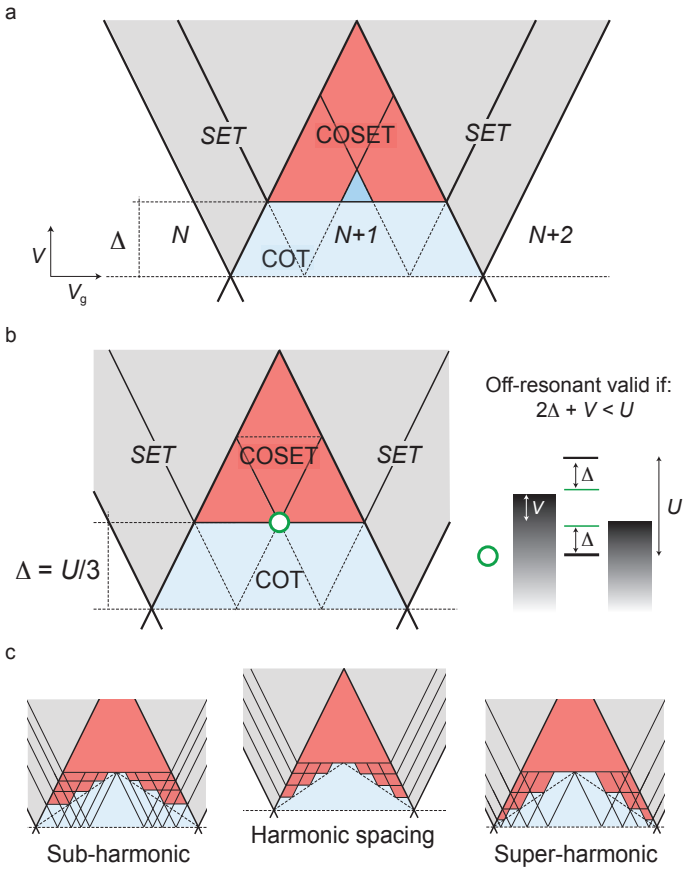

Figure 2.7: **Shape and size of the off-resonant regime as Δ is varied relative to U.** (a) Off-resonant regime for an excitation $\Delta < U/3$ as in Fig. 2.4(a). As in Fig. 2.5 the regions where the off-resonant approach is valid (fails) are colored blue (red). In the light blue region where $V < \Delta$ there is only elastic COT (dashed black construction lines are not resonances), but for $V \gtrsim \Delta$ inelastic COT does excite the molecule. The off-resonant approach only applies when both excitation *and relaxation* proceed by virtual charging. This is the case in the darker blue triangle which is restricted from both sides by Eq. (2.22) and shrinks in size with increasing $\Delta \to U/3$. (b) *Left panel:* For an excitation with $\Delta = U/3$ the off-resonant picture *no longer* works for the inelastic COT excitation at $V = \Delta$. Thus, the excitations $\Delta < U/3$ for which the off-resonant picture works lie in the blue area of this figure, which amounts to $5/9 \approx 55\%$ of the *nominal* off-resonant regime (blue plus red area). *Right panel:* To see why $\Delta = U/3$ is the threshold value we consider the best-case scenario for the off-resonant picture to work, i.e., at fixed gate voltage horizontally at the center while varying V vertically, traversing the point $\circ$. The diagram shows that there is no relaxation by SET as long as the bias satisfies $2\Delta + V < U$. Requiring this to hold at the onset of inelastic excitation by COT, $V = \Delta$, gives the threshold value. (c) Several excitations from a superharmonic (left), harmonic (center) and subharmonic (right) spectrum for charge $N+1$. In the limit of vanishing harmonic energy spacing, the blue region where the COT picture works approaches $1/3 \approx 33\%$ of the nominal off-resonant regime.

This is the case if the SET condition (2.2) additionally holds for the *excited* states, i.e., for $i = e$ in Eq. (2.2):

$$\mu_r < E_e^{N+1} - E_g^N \quad \text{and} \quad \mu_r > E_g^{N+2} - E_e^{N+1} \tag{2.22}$$

for both $r = \mathrm{L}, \mathrm{R}$. We note that in theoretical considerations, it is easy to lose sight

of condition (2.22) when "writing down" an ASW Hamiltonian model (or only $\mathscr{T}$-matrix rates for COT) [Sec. 2.2.2] and assuming the couplings to be fitting *parameters* of the theory. (In fact, in addition to condition (2.22) one needs to check that all excited states that are accessible via nonequilibrium cascades of COT transitions – "nonequilibrium COT" – are stable. We will not discuss this further complication.)

In Fig. 2.5(a) we already shaded in light blue the region bounded by the first condition (2.22) where the COT picture applies. In Fig. 2.7(a) we now show that the full restrictions imposed by both virtual charge states N and $N+2$ in (2.22) strongly restrict the validity regime of the COT approach for states with real occupations and charge $N+1$. In Fig. 2.7(b) and its caption we explain that for any individual excitation $\Delta > U/3$ the off-resonant picture *always* breaks down in the sense that it works only for *elastic* COT, i.e., for $V < \Delta$. For $\Delta = U/3$, this amounts to 55% of the *nominal* off-resonant regime.

When accounting for several excited states below the threshold $U/3$, a sizeable fraction of this region must be further excluded. In Fig. 2.7(c) we construct the regime of validity (blue) for some example situations. The shape and size of this validity regime (light blue) depends on the details of the excitation spectrum. The center panel illustrates that for a harmonic spectrum the COT picture in fact applies in only $\sim 33\%$ of the nominal off-resonant regime (i.e., obtained by taking the complement of the resonant regime). The left and right panel in Fig. 2.7(c) show how this changes for anharmonic spectra characteristic of quantum spins with positive and negative magnetic anisotropy, respectively.

In summary, resonant processes *always* dominate the relaxation of excitations at energy $\Delta > U/3$ populated by off-resonant excitation because they are "too hot": for such excitations there is no deep / far off-resonant regime where considerations based on the COT picture alone are valid. For lower-energy excitations, $\Delta \leq U/3$, there is a triangular-shaped region in which one is still truly far off-resonance and excitations are not quenched. The size of that region varies according to (2.22) and is much smaller than naively expected by extending the linear-response criterion (2.5). Although theoretical [85–90] and experimental [83, 149] studies on COSET exist, this point seems to have been often overlooked and is worth emphasizing. Experimentally, to be sure that the off-resonant picture applies to unidentified excitation one must at least have an estimate of the gap U and of the level position or, preferably, a map of the dependence of transport on the level position independent of the bias as in gated experiment discussed in Sec. 2.3 or STM situations allowing for mechanical gating [110–114].

STATIONARY STATE AND CURRENT AT THE RESONANT-OFF-RESONANT CROSSOVER

Due to their hybrid character, COSET mirages do not emerge in a picture of either real or virtual charging alone. In particular, SET processes are omitted when deriving the COT rates by means of the ASW transformation [Sec. 2.2.2], and, for this reason, that picture cannot account for these phenomena. Instead, a way to capture these effects is to extend Eqs. (2.7) and (2.13) to a master equation which simultaneously includes transition rates of leading (Γ) and next-to-leading order (Γ^2). This has been done using the $\mathscr{T}$-matrix approach [119, 210], requiring the *ad-hoc* regularization by hand mentioned in Sec. 2.2.2. A systematic expansion which avoids these problems is, however, well-known [162, 213, 214]. We refer to Refs. [90, 209, 215] for the calculation

of the rates and for a discussion [209] of how contributions beyond weak coupling account for correlations between molecule and electrodes.

Relevant to our experiment in Sec. 2.3 is that with the computed rates in hand, a stationary master equation needs to be solved to obtain the occupation of the states and from these the current. We stress that *even when far off-resonance* – where naively speaking the charge is fixed to, say, $N+1$ – a description of the transport requires a model which also includes *both the N and N* + 2 *charge states*, together with their relative excitations. This is essential to correctly account for the relaxation mechanisms that visit these states for real and not virtually. Note that keeping these states is *not* related to obtaining the correct strength of the couplings for scattering in the ASW Hamiltonian. Even with the correct values for J and K in Eq. (2.16), the COSET mirages are missed since $\mathscr{H}^{\mathrm{A}}$ only accounts for scattering processes. The minimal master equation required for off-resonant transport thus takes then the form:

$$\frac{\mathrm{d}}{\mathrm{d}t}\begin{bmatrix}\mathbf{P}^0\\ \mathbf{P}^1\\ \mathbf{P}^2\end{bmatrix} = 0 = \begin{bmatrix}\mathbf{W}^{0,0} & \mathbf{W}^{0,1} & \mathbf{W}^{0,2}\\ \mathbf{W}^{1,0} & \mathbf{W}^{1,1} & \mathbf{W}^{1,2}\\ \mathbf{W}^{2,0} & \mathbf{W}^{2,1} & \mathbf{W}^{2,2}\end{bmatrix}\begin{bmatrix}\mathbf{P}^0\\ \mathbf{P}^1\\ \mathbf{P}^2\end{bmatrix}, \tag{2.23}$$

where as before $N = 0$ for simplicity. Here the rates for the various processes change whenever one of the energetic conditions (2.2) and (2.10) is satisfied. Examination of the various contributions in the expression of the rate matrices [90] reveals that the following effects are included:

- $\mathbf{W}^{1,0}$ is a matrix of SET rates that change when condition (2.2) is met. It also includes Γ^2-corrections that *shift and broaden* the SET resonance.
- $\mathbf{W}^{1,1}$ is a matrix of both SET and COT rates. The latter change when condition (2.10) is met.
- $\mathbf{W}^{2,0}$ and $\mathbf{W}^{0,2}$ are matrices of *pair-tunneling* rates, e.g., $W^{2,0}_{f,i}$ for transitions between states differing by *two* electrons, $(N,i) \to (N+2,f)$. These lead to special resonances discussed in Sec. 2.2.4.

The solution of the full stationary master equation (2.23) requires some care [90, 209] due to the fact that it contains both small COT rates and large SET rates whose interplay produces the COSET mirages. Even though the *(first-order) SET rates* are large, they have a small – albeit non-negligible – effect since, in the stationary situation, the initial states for these transitions may have only small occupations. These occupations, in turn, depend on the competition between *all* processes / rates in the stationary limit. This is the principal reason why one cannot avoid solving the master equation (2.23) with both first and second order processes included.

To conclude, Eq. (2.23) captures the delicate interplay of resonant (SET) and off-resonant (COT) processes leading to mirages (COSET). The appearance of such mirages indicates that *intrinsic* relaxation rates are smaller than SET transport rates ($\propto \Gamma$). "Nonequilibrium" COT is also included in this approach and the appearance of its additional features in our experiment signals a molecular device with even lower intrinsic relaxation rates, i.e., smaller than the COT relaxation rates ($\propto \Gamma^2$).

2.2.4. BREAKING THE RULES OF TRANSPORT SPECTROSCOPY

The above account of the basic rules of transport spectroscopy, although extensive, is by no means exhaustive. The key conditions are Eq. (2.2) and (2.10), determining the *resonance positions* as a function of applied voltages. Readers interested mostly in the application of these rules to a high-resolution transport experiment can skip the remainder of this section and proceed directly to Sec. 2.3. Here, we give an overview of a variety of additional effects that bend or break these rules, found in experimental and theoretical studies. In Fig. 2.8 we sketch a number of transport spectra that cannot be understood from what we have learned in the previous discussion.

Nonuniform level shifts due to voltages The assumption made so far [Sec. 2.2.1] that all energy levels are uniformly shifted by applied gate and bias voltages may not be valid in case of local electric field gradients. In fact, this was already seen in the first experiment on gated COT spectroscopy of a single-triplet semiconductor dot [149] due to the change of the confining potential with gate voltage. In molecular junctions this has also been observed. Figure 2.8(a) schematizes how the transport spectrum in Refs. [216] displays such effects. In this case, the COT resonances can still be identified as weakly gate-dependent resonances, which is not a trivial issue as the experiments in Ref. [217] show. However, a qualitatively new and strongly gate-dependent resonance [216, 218] (red line) appears upon ground state change. Piecing together all the evidence, it was shown that this effect originates from a change in amplitude of the COT background, without requiring the introduction of any additional states into the model. These effects are included in Eq. (2.23), which was shown [218] to reproduce the experimental data of Ref. [216] in detail.

Pair tunneling In all the schematics so far we left out resonances that are caused by electron *pair tunneling*. These are described [90, 219] by the rates $\mathbf{W}^{2,0}$ and $\mathbf{W}^{0,2}$ included in the master equation (2.23). In Fig. 2.8(b) we sketch where these pair-tunneling resonances (red lines) are expected to appear: their positions are obtained by taking the *bias-averaged positions* of the two *subsequent SET resonances*. This condition follows by requiring the maximal energy of an electron pair in the electrode r to match a corresponding molecular energy change. For example, for a single orbital at energy ϵ one obtains $2\mu_r = E_g^{N+2} - E_g^N = 2\epsilon + u$ where u is the charging energy. This gives a bias window in which pair tunneling $N \leftrightarrow N+2$ can contribute to transport,

$$\mu_{\mathrm{L}} \geq \epsilon + \tfrac{1}{2}u \geq \mu_{\mathrm{R}},. \tag{2.24}$$

provided that the N and / or the $N+2$ state is occupied. The effective *charging energy* for each electron is *halved* since the energy u is available for both electrons together in a single process. Although small (comparable with COT) its distinct resonance position and shape clearly distinguish the pair-tunneling current from SET current Ref. [219] that dominates in the resonant regime where it occurs.

Electron attraction Clearly, pair tunneling effects are expected to become important if the effective interaction energy u is attractive [220, 221, 221–224]. Such attraction in fact appears in various systems. In molecular systems this is known as electrochemical potential-inversion [225]. In artificial QDs a negative u have been observed

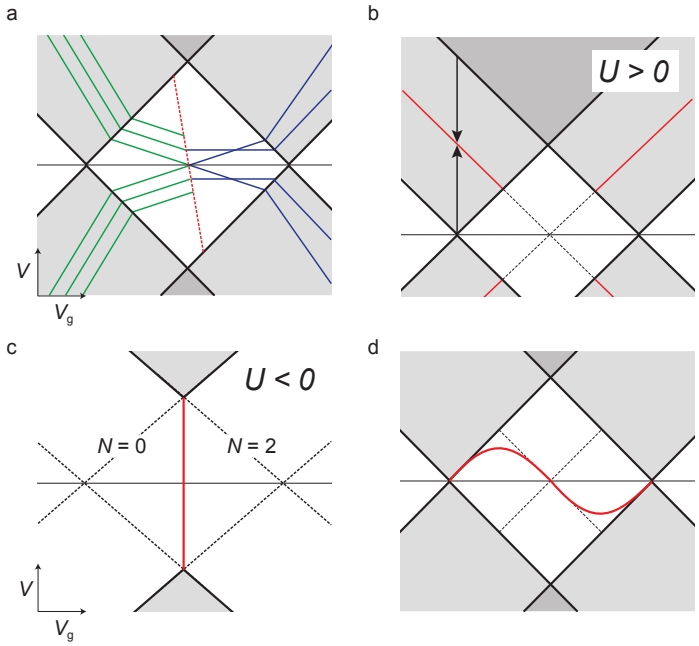

Figure 2.8: **Breaking the rules of transport spectroscopy.** (a) Effects of nonuniform gate and bias dependence sketched after Fig. 3 of Ref. [216]. Split singlet-to-triplet inelastic COT excitations (green) are tuned to degeneracy by a strong V_g-dependence. Upon crossing the red line, the ground state changes from singlet to triplet, see main text. (b-c) Electron-pair tunneling resonance (red) for (b) repulsive electron interaction $U > 0$ and (c) effectively attractive interaction $U < 0$. (d) Transport feature (red) due to coherent spin-dynamics on a single, interacting orbital coupled to nearly antiparallel ferromagnets. Although it looks like a resonance with anomalous gate and bias dependence it does not correspond to any state on the system. It is instead a sharp amplitude modulation caused by the *orientation* of the accumulated nonequilibrium spin relative to the electrode polarization vectors.

experimentally [226, 227] in transport spectra of the type sketched in Fig. 2.8(c), see also Ref. [228]. Interestingly, in this case the ground state has either N or $N+2$ electrons and never $N+1$ since starting from (N,g) the single-electron transition energies $E_g^{N+1} - E_g^N$ and $E_g^{N+2} - E_g^{N+1}$ are higher than electron-pair transition energy *per electron* $(E^{N+2} - E^N)/2$. This is also included in the approach (2.23), see Ref. [215].

"Coherence" effects Finally, we turn to the assumption used in Sec. 2.2.1 that the molecular state is described by "classical" occupation probabilities of the quantum states (statistical mixture). For instance, each degenerate spin multiplet is treated as an "incoherent" mixture of different spin projections (no quantum superpositions of spin-states states). Equivalently, the spin has no average polarization in the direction transverse to the quantization axis.

However, when in contact with, e.g., spin-polarized electrodes, such polarization does arise already in order Γ. In that case one must generalize Eq. (2.23) to include off-diagonal density-matrix in the energy eigenbasis. (The off-diagonal elements also come into play when going to order Γ^2, see discussion in Sec. 2.2.2.) In physical terms, this means that one must account for the coupled dynamics of charge,

spin-vector and higher-rank spin tensors [229, 230]. In the SET regime, such effects can lead to a nearly 100% modulation of the transport current [229, 231] due to quantum interference. This emphasises that [232] SET– the first order approximation in Γ – is not "incoherent" or "classical" as some of the nomenclature in Table 2.1 seems to imply.

Similar coherence effects can arise from orbital polarization in QDs [232–236] and STM configurations [237], from an interplay between spin and orbital coherence [98, 238, 239], or from charge superpositions of electron pairs. Finally, for high-spin systems coherence effects of tensorial character can arise. This leads to the striking effect that in contact with ferromagnets (vector polarization) they can produce a magnetic anisotropy (tensor) [230, 240], see also related work [241–244]. An extension of the approach (2.23) also describes these effects [230, 245].

The perhaps most striking effect of spin-coherence is depicted in Fig. 2.8(d): SET resonances can *split* for no apparent reason [240] and wander off deep into the COT regime [245] (red line). Depending on the junction asymmetry, this feature of coherent nonequilibrium spin dynamics can appear as a pronounced gate-voltage dependent current peak or as a feature close to the linear response regime, mimicking a Kondo resonance, see also Ref. [236].

2.3. SPECTROSCOPY OF A HIGH-SPIN MOLECULE

In this second part we present feature-rich experimental transport spectra as a function of gate-voltage and magnetic field. Their analysis requires all the spectroscopic rules that we outlined in the first part. We show how the underlying Hamiltonian model can be reconstructed from the transport data, revealing an interesting high-spin quantum system with low intrinsic relaxation.

The molecule used to form the junction is a Fe_4 single-molecule magnet (SMM) with formula $[Fe_4(L)2(dpm)6] \cdot Et2O$ where Hdpm is 2,2,6,6- tetramethyl-heptan-3,5-dione. Here, H3L is the tripodal ligand 2-hydroxymethyl-2-phenylpropane-1,3-diol, carrying a phenyl ring [246]. After molecular quantum-dot formation, the device showed interesting isotropic high-spin behavior and the clearest signatures of COSET to date [83, 149] for any quantum-dot structure. The device showed no significant anisotropy splittings of spin multiplets in transport, see discussion below. Before turning to the measurements and their analysis, we first discuss specific challenges one faces probing spin-systems using either COT or SET spectroscopy.

2.3.1. PRINCIPLES OF SPIN-SPECTROSCOPY.

Isotropic, *high-spin* molecules have molecular states labeled by the spin length S and spin-projection M. To detect them two types of selection rules are frequently used in STM and QD studies. Using these we construct the possible spectroscopic COT and SET fingerprints that we can expect to measure.

SPIN SELECTION RULES FOR COT

Spectroscopy using COT conductance as a function of magnetic field B (spin-flip spectroscopy [38]) has been a key tool in both STM and break-junction studies. This approach assumes that virtual charging processes dominate. These processes involve two electrons for which the selection rules (2.17) apply.

However, for high-spin molecules considered here, there can be multiple spin-spectrum assignments that fit the same COT transport spectrum. An indication for this is that in the present experiment some of the spectra are very similar to those of entirely different nanostructures [247].

To see how this comes about we construct in Fig. 2.9(a)-(c) the three possible different fingerprints that two spin-multiplets can leave in the COT transport spectrum based on selection rules (2.17) alone. For simplicity, we assume that all processes start from the ground state $(N+1, g)$, i.e., in the "equilibrium" COT approximation discussed in Sec. 2.2.2. This figure shows that one can determine only whether the spin value changes by 1 or remains the same upon excitation, but not on the *absolute* values of the spin lengths (unless the ground state has spin zero).

SPIN SELECTION RULES FOR SET– SPIN BLOCKADE

A second key tool in the study of spin effects is the transport in the SET regime [56, 67, 69–72]. This provides additional constraints that reduce the nonuniqueness in the COT spin-assignment.

In the SET regime, the linear-transport part is governed by the transition between the two ground-state multiplets with different charge, (N, g) and $(N+1, g)$, for which selection rules (2.3) hold. As sketched in Fig. 2.10, if linear SET transport is observed, then the ground-state spin values are necessarily linked by

$$|S_g^{N+1} - S_g^N| = \tfrac{1}{2}. \tag{2.25}$$

This constraint, used in Refs. [68, 69, 248], restricts the set of level assignments inferred through COT spectroscopy on each of the *two* subsequent charge states, by fixing the relative ground state spins S_g^N and S_g^{N+1}. Their absolute values remain, however, undetermined, unless one of two happens to be zero. Arguments based on the presence of the additional spin-multiplets can then be used to motivate a definite assignment of spin values.

Molecules for which Eq. (2.25) fails can be identified by a clear experimental signature: the SET transport is blocked up to a finite bias as explained in Fig. 2.10. Such *spin-blockade* has been well-studied experimentally [249–251] and theoretically [252–256] and finds application in spin-qubits (Pauli-spin blockade). It has been reported also for a molecular junction [248].

Clearly, when several excited spin multiplets/charge states are involved, both the SET and COT spin-spectroscopy become more complex. However, selection rules similar to Eq. (2.25) also apply to *excited* states and thus lock the two spin spectra together. In addition, the nonequilibrium occupations of the states contribute to further restricts[4] the set of possible spin-values as we will now illustrate in our experimental spectroscopic analysis.

[4] We note that if spin multiplets are internally split, for example, due to magnetic anisotropy, then the spectroscopy gives more information about the absolute value of S_g^{N+1}. This is exploited, e.g., in the gate-voltage spectroscopy of single-molecule magnets [69, 70]

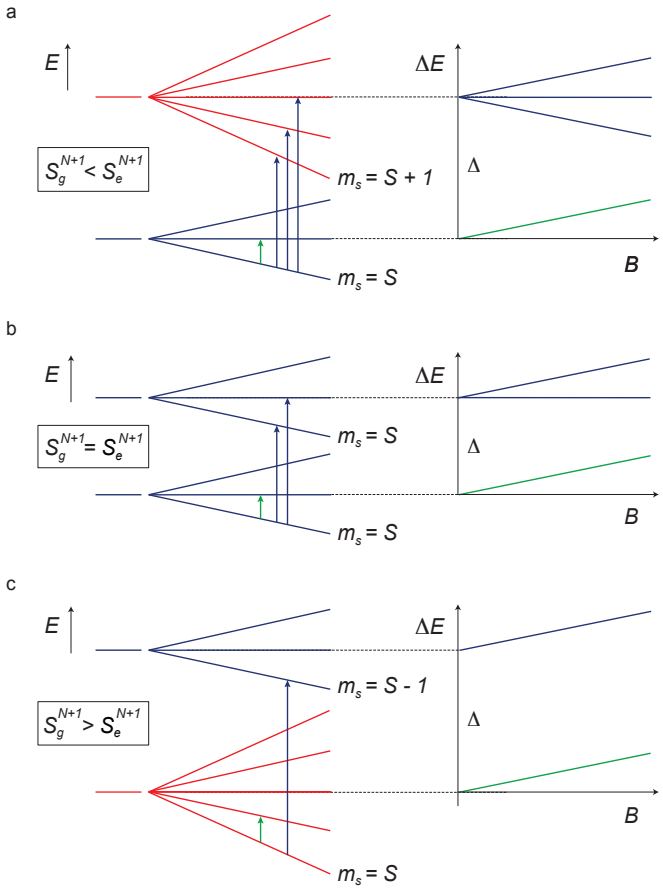

Figure 2.9: **COT spectroscopy of a high-spin molecule.** The left panels in (a)-(c) show COT transitions between energy levels (E) vs. a magnetic field B. The right panels show the corresponding transport spectra, i.e., the resonant bi0.8as positions in $\mathrm{d}I/\mathrm{d}V$ matching an energy difference (ΔE). (a) If the spin increases upon excitation, $S_e^{N+1} = S_g^{N+1} + 1$, there is a *three-fold* splitting of the transport-spectrum (blue) starting at $V = \Delta$ for $B = 0$ due to the transitions to the excited multiplet. The ground multiplet gives a line (green) starting at $V = 0$ and increasing with B if $S_g^{N+1} \geq 1/2$. Only for $S_g^{N+1} = 0$ this green line is *missing*. (b) If the spin length does not change upon excitation, $S_e^{N+1} = S_g^{N+1}$, the excited multiplet appears in the transport spectrum through a *double* line starting at $V = \Delta$. The ground multiplet gives a line (green) starting at $V = 0$ and increasing with B if $S_g^{N+1} \geq 1/2$. Clearly, for $S_g^{N+1} = 0 = S_e^{N+1}$ the B-dependent lines are *missing*. (c) If the spin length decreases upon excitation, $S_e^{N+1} = S_g^{N+1} - 1$, the excited multiplet appears in the transport spectrum through a single line (blue) starting at $V = \Delta$, increasing with B. Since in this case the ground spin S_g^{N+1} is always nonzero, there is an intra-multiplet line (green) starting at $V = 0$.

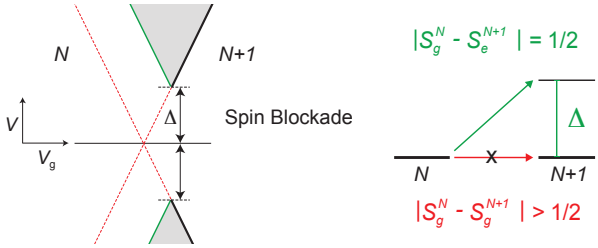

Figure 2.10: **SET spectroscopy of a high-spin molecule: spin blockade.** If ground state transitions are spin-forbidden, $|S_g^{N+1} - S_g^N| > 1/2$, then SET transport is suppressed (red dashed cross). Transport sets in only when a finite bias makes the lowest *spin-compatible* excitation energetically accessible. This can be either and $N+1$ state with $|S_e^{N+1} - S_g^N| = 1/2$ (shown) or an N electron state with $|S_g^{N+1} - S_e^N| = 1/2$ (not shown).

2.3.2. MOLECULAR JUNCTION FABRICATION

Molecular junctions are produced starting from a three-terminal solid-state device [257, 258] consisting of an oxide-coated metallic local gate electrode with a thin gold nanowire deposited on top. On such a device, a low-concentration solution of molecules (~ 0.1 mM) is drop-casted. The nanowire is then electromigrated at room temperature and allowed to self-break [257] so that a clean nanogap is formed, with a width of ≈ 1.5 nm. The solution is evaporated and the electromigrated junctions are cooled down in a dilution fridge ($T_{\text{base}} \approx 70$ mK) equipped with a vector magnet and low-noise electronics. All the measurements are performed in a two-probe scheme either by applying a DC bias V and recording the current I or by measuring dI/dV with a standard lock-in AC modulation of the bias.

A molecular junction as sketched in Fig. 2.1(b) is formed when a molecule physisorbs[5] on the gold leads, and thus establishes a tunneling-mediated electrical contact. The presence of the molecule in the junction is signaled by large SET transport gaps U exceeding 100 meV and low-bias inelastic COT fingerprints. Numerous molecular systems have been investigated in this configuration [33, 55, 67–71, 102, 216, 247, 248, 259–264].

As a side remark, the fact that we do not observe pronounced magnetic anisotropy effects is not unexpected: the formation of a molecular junction may involve surface interactions. In several cases previously studied clear spectroscopic signatures of the bare molecular structure (before junction formation), such as the magnetic anisotropy [55, 68, 262], were observed also in junctions. However, depending on the mechanical and electrical robustness of the molecule, this and other spin-related parameters may undergo quantitative [43, 71, 204, 265] or qualitative changes [46, 247] and sometimes offer interesting opportunities for molecular spin control [266]. Image-charge stabilization effects, for example, can lead to entirely new spin structure such as a singlet-triplet pair [16, 248] on opposite sides of a molecular bridge.

[5] Physisorption is the dominant binding mechanism for the molecular species used here, given no chemically-active linking groups are present. Chemisorption is the other common alternative used in molecular electronics where a chemical bond forms between the molecule and the electrode.

2.3.3. CHARACTERIZATION OF SPIN STATES IN ADJACENT REDOX STATES

We now turn to the analysis of the feature-rich transport spectrum anticipated in Fig. 2.1(c) and reproduced in Fig. 2.11. It consists of two off-resonant regimes on the left and right with fixed charge states – provisionally labeled N and $N+1$ – and a resonant regime in the center surrounded by a significant crossover regime.

OFF-RESONANT ANALYSIS

We first separately identify the electronic spectrum for each of the two accessible charge states N and $N+1$ using the off-resonant approach discussed in Sec. 2.2.2.

In Fig. 2.11 (a) we show the $\mathrm{d}^2I/\mathrm{d}V^2$ color map and the corresponding $\mathrm{d}I/\mathrm{d}V$ steps for fixed $V_\mathrm{g} = -1.25$ V as a function of magnetic field, B. Two steps (peaks in $\mathrm{d}^2I/\mathrm{d}V^2$) starting from $V \approx 0$ meV and $V = 0.78$ meV at $B = 0$ T shift upward in energy and parallel to each other as the magnetic field increases. In the standard COT picture each step signal to the opening of an inelastic transport channel through the molecule. Transport takes place via virtual charging involving a real spin-flip excitation with selection rules on spin-length $\Delta S = 0, 1$ and magnetization $\Delta M = 0, \pm 1$. The charge of the molecule remains fixed, and is labeled $N+1$. The shift in magnetic field of both steps indicates a nonzero spin ground state multiplet with spin S_g^{N+1}. According to Sec. 2.3.1, the presence of only one other finite-bias excitation shifting in magnetic field relates the spin-values as $S_g^{N+1} = S_e^{N+1} + 1$, but leaves their absolute values undetermined.

As we will see later, other spectroscopic information constrains the ground spin to be a triplet T, $S_g^{N+1} = 1$, with a singlet excited state labeled S. From the COT excitation voltage, a ferromagnetic (FM) interaction energy $J = 0.78$ meV can be extracted. Such type of excitation has been seen in other molecular structures [247, 248, 267, 268]. Spectra of this kind have also been obtained earlier in other quantum-dot heterostructures, such as few-electron single and double quantum dots, albeit typically characterized by smaller and antiferromagnetic couplings [149, 269].

We now change the gate voltage to more negative values so that the molecule is oxidized $N+1 \to N$, i.e., we extract exactly one electron from the molecule. This can be inferred from the SET transport regime that we traverse along the way. In this new charge state we perform an independent off-resonant spectroscopy. In Fig. 2.11(b) we show the $\mathrm{d}^2I/\mathrm{d}V^2$ for $V_\mathrm{g} = -1.81$ V as a function of the magnetic field B with corresponding $\mathrm{d}I/\mathrm{d}V$ line cuts. At $B = 0$ T two sets of peaks in $\mathrm{d}^2I/\mathrm{d}V^2$ appear at $V = 1.2$ meV and $V = 2.26$ meV and split each in three peaks at higher magnetic fields. A weak excitation shifting upwards in B from $V = 0$ V is also present. With the help of Fig. 2.9(a) the weak excitation and the first set of peaks are associated to $S_e^N = S_g^N + 1$, while the second set, corresponding instead to the spectrum depicted in Fig. 2.9(b), fixes the spin to $S_{e'}^N = S_g^N$. The crucial information provided by the clear absence of spin blockade in the intermediate SET regime eventually constrains S_g^N to 1/2 or 3/2 according to (2.25). The only two spin configurations compatible with the observations are therefore: a ground doublet D_1, an excited quartet Q and a second doublet D_2 or, alternatively, a ground quartet, an excited sextuplet and a quartet. As we will see in the next section, the latter can be rigorously ruled out by analyzing the SET spectrum.

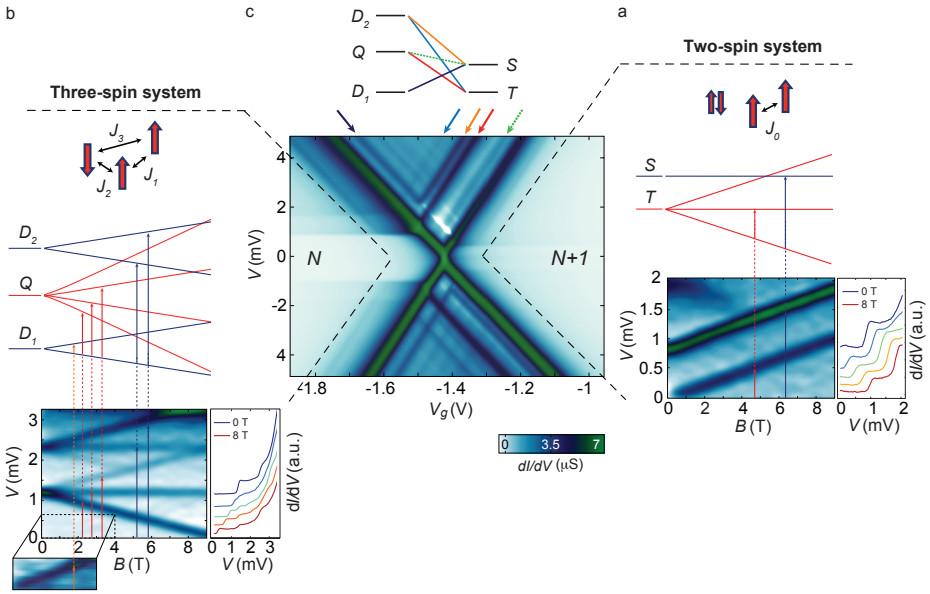

Figure 2.11: **The characteristics regimes of a complex molecular spin system.** $\mathrm{d}I/\mathrm{d}V$ color map (stability diagram) of a high-spin molecular dot. The gate electrode allows to electrostatically vary the dot's chemical potential. This scanning in energy space grants access to real charging (mixed-valence, middle) as well as the virtual cotunneling transport regimes (far left and right side, fixed charge). Between the two regimes, the hybrid COSET regime is visible where excitation (relaxation) is dominated by COT (SET). COT spectroscopy at $V_\mathrm{g} = -1.81$ V, in (b), ($V_\mathrm{g} = -1.25$ V, in (a)) in magnetic field reveals the presence of a three (two) spin system with specific ferro-/antiferromagnetic exchange couplings. The color-coded arrows indicate the transitions between the different spin multiplets of the three- and two-spin systems.

The presence of the excited quartet state Q implies that the charge state N is a *three-spin* system, $N = 3$, as sketched in the top panel of Fig. 2.11(b). The system with one extra electron in Fig. 2.11(a) is thus actually a $N+1 = 4$ electron system with one closed shell, as sketched in the figure. Upon extraction of an electron, the spectrum of the molecular device changes drastically, transforming from a ferromagnetic *high-low* spin spectrum for $N+1 = 4$ into a nonmonotonic *low-high-low* spin excitation sequence for $N = 3$. The spin-excitation energies extracted from the two independent COT analyses are:

$$\begin{cases} E_Q - E_{D_1} = 1.2 \text{ meV} \\ E_{D_2} - E_{D_1} = 2.26 \text{ meV} \end{cases} \quad \text{for} \quad N = 3, \tag{2.26}$$

and

$$E_S - E_T = 0.78 \text{ meV} \quad \text{for} \quad N+1 = 4. \tag{2.27}$$

These energy differences provide the starting point of a more atomistic modeling of the magnetic exchanges in the two charge states. We stress that for the transport spectroscopy this is not necessary and it goes beyond the present scope. We only note that while the $N+1 = 4$ state requires only one fixed ferromagnetic exchange coupling $J_0 = E_S - E_T$ [Fig. 2.11(a)] together with the assumption that two other electrons occupy a closed shell; the $N = 3$ spectrum requires, in the most general case, three

distinct exchange couplings between the three magnetic centers [Fig. 2.11(b)]. These relate to the two available energy differences through $E_Q - E_{D_1} = (J_1 + J_2 + J_3)/2 + X/2$ and $E_{D_2} - E_{D_1} = X$ to a complicated function $X(J_1, J_2, J_3)$. Since this involves three unknowns for two splittings, only microscopic symmetry considerations or detailed consideration of the transport current magnitude are needed to uniquely determine the microscopic spin structure.

This type of microscopic modeling has proven successful in many instances, see Ref. [45] and references therein. However, the underlying assumptions on localized spins and fixed charge occupations can only be made when sufficiently far away from resonance, i.e., such that COSET does not take place as expressed by conditions (2.21) and (2.22).

RESONANT ANALYSIS

Using the ability to control the energy levels with the gate, the COT analysis can be complemented by a SET spectroscopy in the central part of Fig. 2.11(c). Here, real charging processes dominate. For example, starting from the ground state D_1, addition of a single electron leads to occupation of the T ground state. This is evidenced by the clear presence of a SET regime of transport down to the linear-response limit. Inside the resonant regime additional lines parallel to the edges of the cross appear as well. As we explained in Fig. 2.3, these correspond to real charging processes where excess (deficit) energy is used to excite (relax) the molecule. These additional lines, schematized for our experiment in Fig. 2.12(a), fall into two categories according to the criteria:

1. Lines terminating at the boundary of the SET regime correspond to the *ground* N to excited $N \pm 1$ transitions or *vice versa*.

2. Lines that never reach the SET boundary, but terminate inside the SET regime at a line parallel to this boundary. These correspond to *excited* N to excited $N \pm 1$ transitions. Their earlier termination indicates that that the initial excited state must become first occupied through another process. The line *at which* it terminates corresponds to the onset of this activating process.

In Fig. 2.11(c) and Fig. 2.12(a) the SET transitions $D_1 \leftrightarrow S$, $Q \leftrightarrow T$ and $D_2 \leftrightarrow T$ fall into category (1), while the $D_2 \leftrightarrow S$ and $Q \leftrightarrow S$ transitions belong to (2). Due to the large difference in spin-length values of the spin-spectra the latter transition, marked in dashed-green, is actually forbidden by the selection rules (2.3). Following this line, we find that it terminates at a strong negative differential conductance (NDC) feature (white in the stability diagram in Fig. 2.11) marking the onset of the transition $D_1 \leftrightarrow S$.

To test our earlier level assignment based COT, we now compute the expected SET transport spectrum the first-order (Γ) master equations (2.7)-(2.9) and by adjusting the result, we extract quantitative information about the tunnel coupling. The model Hamiltonian is constructed from the energies (2.26)-(2.27) and their observed spin-degeneracies. Assuming that spin is conserved in the tunneling, the rates between magnetic sublevels are fixed by Clebsch-Gordan spin-coupling coefficients [192, 256] incorporating both the SET and COT selection rules Eqs. (2.3) and (2.17). The tunnel parameters in units of an overall scale Γ^* are adjusted to fit the

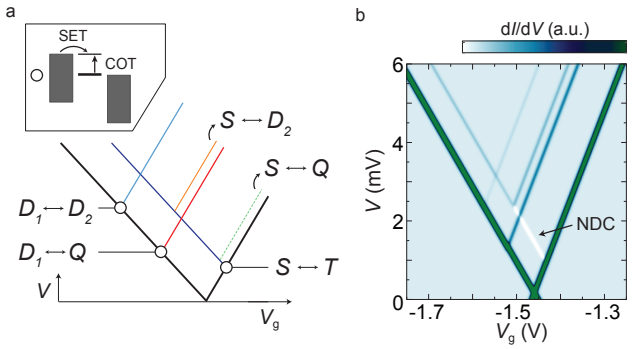

Figure 2.12: **Connecting the off-resonant and resonant analyses.** (a) Schematic of COT and SET excitations observed in Fig. 2.11. SET transitions between a *ground and excited* state (blue, red) reach the boundary of the resonant regime at the black circle from where they continue horizontally as a COT excitation. The inset depicts the chemical potential configuration at such a black circle where COT and SET connect. The SET transitions between *two excited* states (orange, green) do not connect to any COT excitation. (b) SET transport spectrum computed using the master equations (2.7)-(2.9). The energies are extracted independently from the two COT spectra in Fig. 2.11 and the capacitive parameters $\alpha_g = 0.012$, $\alpha_L = \alpha_g/0.6$ $\alpha_R = \alpha_g/0.4$ are fixed by the observed slopes of the SET lines [cf. Fig. 2.3(a)], leaving the tunnel rates (2.28)-(2.29) as adjustable parameters. The broadening of the dI/dV peaks in the experiment is due to tunneling, $\Gamma \approx 4.6$ K ~ 0.4 meV (FWHM), rather than temperature, $T \approx 70$ mK $\sim 6\,\mu$eV. Eq. (2.7)-(2.9) do not include this Γ-broadening and we crudely simulate it by an effective higher temperature $T^* = 270$ mK $\sim 23\,\mu$eV. The master equations (2.7)-(2.9) are valid for small effective tunnel coupling $\Gamma^* \ll T^*$, which only sets the overall scale of plotted SET current and not the relative intensities of interest. The caption to Fig. 2.16 explains that Γ^* should not be adjusted to match the larger experimental current magnitude.

relative experimental intensities:

$$\begin{cases} \Gamma_{D_1,T} = 1.0\,\Gamma^*, \\ \Gamma_{Q,T} = 1.0\,\Gamma^*, \\ \Gamma_{D_2,T} = 0.25\,\Gamma^* \quad \text{(weak intensity)}, \end{cases} \tag{2.28}$$

and

$$\begin{cases} \Gamma_{D_1,S} = 0.5\,\Gamma^*, \quad \text{(NDC)}, \\ \Gamma_{Q,S} = 0.0 \quad \text{(spin-forbidden)}, \\ \Gamma_{D_2,S} = 1.0\,\Gamma^*. \end{cases} \tag{2.29}$$

Their relative magnitudes provide further input the further microscopic modeling of the 3-4 spin system mentioned at the end of Sec. 2.3.3. As shown in Fig. 2.12(b), the *resonant (SET) part* of the experimental conductance in Fig. 2.11(c), as schematized in Fig. 2.12(a) is reproduced in detail. This includes transitions exciting the molecule from its ground states, but also a transition between excited states.[6] The NDC effect is explained in more detail later on together with the full calculation in Fig. 2.15.

CONNECTING THE OFF-RESONANT AND RESONANT ANALYSES

As discussed in Fig. 2.4-2.5 and indicated in Fig. 2.12(a) the SET excitations corresponding to the ground N to excited $N \pm 1$ transitions connect continuously to

[6] The dashed green line in (a) can also be included by allowing a slight breaking of spin-conservation, enabling the $S \leftrightarrow Q$ transition. This more detailed modeling goes beyond the level of detail required for the COSET and COT features on which we focus.

the COT excitations. Those corresponding to two excited states, each of a different charge state, has no corresponding COT excitation to connect to. In this sense, the SET spectrum effectively ties the two separately-obtained COT spin spectra and allows a consistency check on their respective level assignments, cf. Sec. 2.2.3.

For instance, from the fact that the $Q \leftrightarrow T$ transition is clearly visible – marked red in Fig. 2.11(c) – we conclude that the first excited multiplet of the N charge state *cannot* be a sextuplet ($S = 5/2$) since such SET transition would be spin-forbidden and thus weak. Another example is given by the presence of the $S \leftrightarrow D_2$ SET transition [orange in Fig. 2.11(c)], which implies that the second excited multiplet of the N charge state cannot be a quartet. The fact that this transition does not continue into any of the COT ones is also consistent with its excited-to-excited character.

These two exclusions considerations were anticipated in Sec. 2.3.3 and are crucial for our off-resonant assignment in the three-electron state and has now allowed us to reverse-engineer the effective many-electron molecular Hamiltonian. With this in hand, we turn to the main experimental findings and investigate the "nonequilibrium" COT through the molecule [Sec. 2.3.4] and the crossover regime where real and virtual tunneling nontrivially compete in the relaxation of spin excitations [Sec. 2.3.5].

2.3.4. PUMP-PROBE SPIN SPECTROSCOPY BY NONEQUILIBRIUM COT

We first investigate how COT spectrum evolves as we further *approach* the SET regime from either side. Fig. 2.13(a) shows the analogous of Fig. 2.11(a) but closer to the SET regime, at $V_g = -1.32$ V. A horizontal, B-field independent line appears (dotted green line in the center-panel schematic) that terminates at $B_c \approx 4.5$ T, precisely upon crossing the intra-triplet excitation (blue line). This indicates that the excited triplet (spin $S = 1$ perpendicular to the field, $M = 0$) lives long enough for a secondary COT process to excite the system to the singlet state (reducing the spin length to $S = 0$). Strong evidence for this is the termination of this line: once the initial state ($M = 0$ excited triplet) for this transition is no longer accessible for $B > B_c$, the "nonequilibrium" cascade of transitions is interrupted.

We consistently observe this effect, also when approaching the SET regime from the side of the other charge state ($N = 3$) with different spin. In Fig. 2.13(b) we show the magnetic field spectrum taken at $V_g = -1.75$ V. Here the lowest D_2 excitation gains strength[7] relative to Fig. 2.11(b). In this case, the excited D_1 state is the starting point of a "nonequilibrium" cascade. As for the previous case, it terminates when levels cross at $B \approx 4$ T for similar reasons: Once the Q state gains occupation for $B > B_c$ (since the $D_1 \leftrightarrow Q$ transition becomes energetically more favorable) the excited M-substates of the D_1 multiplet are depleted causing the line to terminate. In both charge states the observed "nonequilibrium" COT current gives an estimate for the spin-relaxation time, $\tau_{\mathrm{rel}} \gtrsim 10^{-9}$ s: to have any such pump-probe current, spin-relaxation after a pump process should not be complete before the probe process starts. The inverse of this measured current (in electrons/second) gives the above estimate.

Nonequilibrium transitions can thus give rise to clear excitations at *lower* energy than expected from the simple selection-rule plus equilibrium arguments of

[7] Since this enhancement of the excited D_1 state is small compared to that of the other "equilibrium" excitations it is not revealed by Fig. 2.11(b).

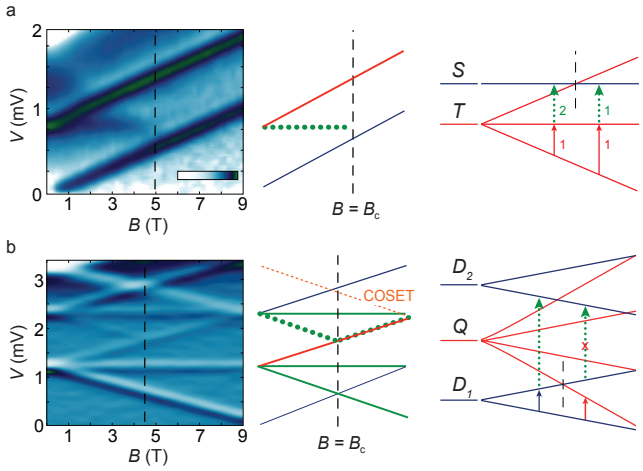

Figure 2.13: **Nonequilibrium spin pumping and locking mechanism.** In contrast to Fig. 2.11, we highlight here the transitions that are involved in the spin pumping process (green dotted lines). (a) $\mathrm{d}^2I/\mathrm{d}V^2$ spectra measured as a function of B-field at $V_g = -1.32$ V in the $N+1 = 4$ charge state. The $T \leftrightarrow S$ nonequilibrium spin-excitation shows up as a weak, field-independent step vanishing at higher field. For $B < B_c$ the intra-triplet transition (red arrow) requires lower energy than the "nonequilibrium" $T \leftrightarrow S$ transition. For $B > B_c$, the intra-triplet is unlocked (activated) at an energy higher than the $T \leftrightarrow S$ and only one transition of the cascade is visible. (b) $\mathrm{d}^2I/\mathrm{d}V^2$ spectra measured as a function of B-field at $V_g = -1.76$ V in the $N = 3$ charge state. Here the nonequilibrium excitation has a negative slope. For $B < B_c$ the excited state of the ground-state doublet D_1 is populated enough to promote a second, nonequilibrium excitation to the excited doublet D_2 (green dotted line). As $B > B_c$ the $D_1 \leftrightarrow Q$ transition crosses over, lowering, in consequence, the population of the spin-up state. This results into a quench of the nonequilibrium excitation. Due to the proximity to SET regime as compared to Fig. 2.11(a), a COSET feature (orange dotted line) appears as a mirage of a spin-excitation.

Sec. 2.3.1. In this type of process, two COT events ($\propto \Gamma^2$) happen in sequence, so that a total of four electrons are involved[8]. In this sense, the phenomena can be regarded as a single-molecule *electronic pump-probe* experiment, that is, the excess energy left behind by the first process (pump) allows the second process to reach states (probe) that would be otherwise inaccessible at the considered bias voltage. This has been successfully applied in STM studies [140, 266] for dynamical spin-control.

2.3.5. MIRAGES OF SPIN TRANSITIONS "FAR FROM RESONANCE"

Mirages We now further reduce the distance to resonance, again coming from either side, and *enter* the crossover regime discussed in Sec. 2.2.3. We are, however, still "far from resonance" by the linear-response condition (2.5).

In the upper panel of Fig. 2.14(a) we show $\mathrm{d}I/\mathrm{d}V$ traces taken at various magnetic fields for a constant gate voltage $V_g = -1.72$ V. At high bias voltage the $\mathrm{d}I/\mathrm{d}V$ steeply rises due to the onset of the main SET resonance. Below this onset, we note a step-like excitation at $V = 2.1$ meV (black arrow) which shifts up in magnetic field with the same g-factor (≈ 2) as the other lower-lying COT excitations[9]. If one adopts the

[8] Note that this is not a single Γ^4 processes, since the two Γ^2 steps occur in sequence. This is similar to the COSET which is not a Γ^3 process, but a sequence of two processes, one of the order of Γ^2 and the other of Γ.

[9] The downshifting partner excitation is visible at a different gate voltage in Fig. 2.13(b) (labeled as COSET)

off-resonant picture this excitation is attributed to the opening of an independent COT channel. This attribution proves to be erroneous: Keeping $B = 3$ T fixed and varying the gate voltage (Fig. 2.14(a), lower panel), we observe that the lower excitations are left unchanged, whereas the higher one under consideration *shifts linearly* with V_g, revealing that it is *not* a COT excitation.

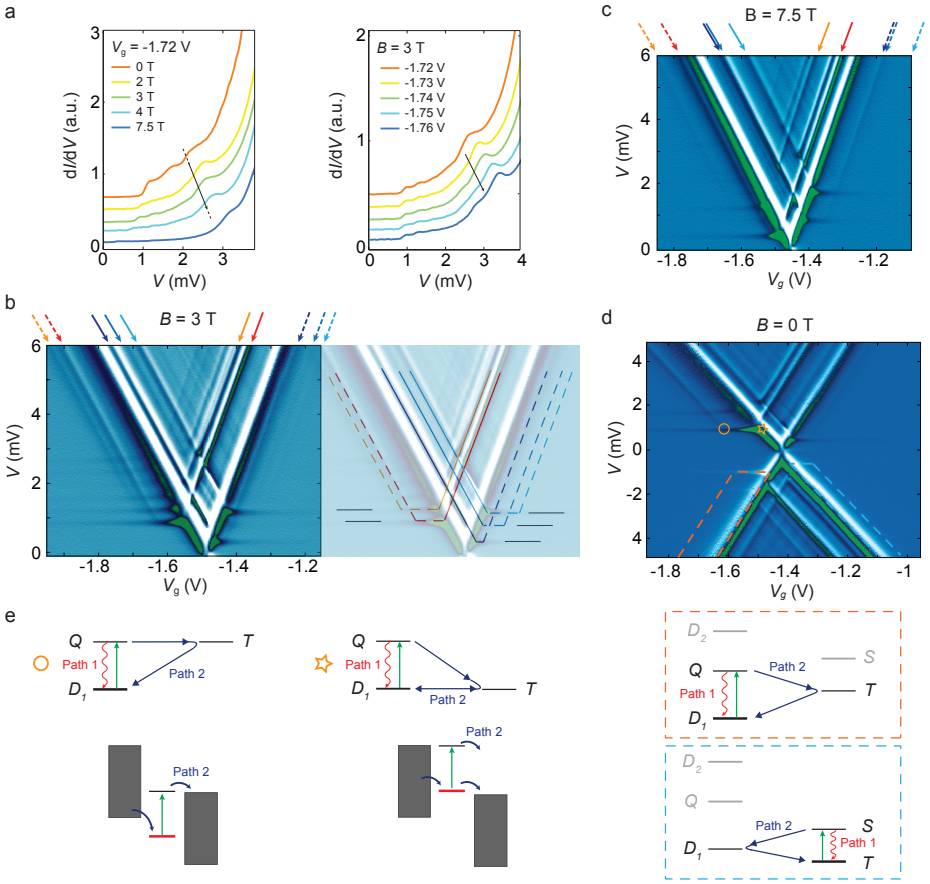

Figure 2.14: **Transport characteristics of spin COSET mirages**. (a) $\mathrm{d}I/\mathrm{d}V$ spectra taken at $V_g = -1.72$ V for different B-fields (upper) and at $B = 3$ T for different values of V_g (lower). The step indicated by the black arrow Zeeman-splits as a regular magnetic transition. The same step moves to higher energies as a function of gate voltage and fixed magnetic field. (b) $\mathrm{d}^2I/\mathrm{d}V^2$ color map at $B = 3$ T. Red (Blue) arrows and lines indicate the SET excitations that extend their mirror images into the COT regions of the N $(N+1)$ charge state. (c) $\mathrm{d}^2I/\mathrm{d}V^2$ color map at $B = 7.5$ T. The B-field evolution of the mirror lines follows that of their real counterparts. (d) $\mathrm{d}^2I/\mathrm{d}V^2$ of the plot in Fig. 2.11(c). The cotunneling-assisted SET transport bands are highlighted. As illustrated in the schematics, mirror images are created when two or more relaxation paths compete. One path (red) involves the intra-molecular relaxation rate characteristic of the COT regime. The second, alternative path (blue) requires a charge/spin fluctuation to the $(N \pm 1, S_{N\pm1})$ state. (e) Energy and chemical potential schematics at the boundaries of the COSET bands. SET and COT transport occur ($\star$). More negative gate voltages shift the T state higher in energy, forbidding SET and leaving only COSET and COT competing. At the position indicated by $\circ$ further gating finally quenches COSET.

and in the lower panel of Fig. 2.14(a).

This attribution to COT can be further ruled out by looking at the full gate-voltage dependence in the stability diagram shown in the left panel of Fig. 2.14(b). The excitation (red arrow) has the same gate dependence as the SET resonances, even though it is definitely not in the resonant regime by the linear-response criterion (2.5). In fact, it is a COSET mirage of the *same* lowest gate-voltage independent COT excitation as we explained in Fig. 2.6. Its bias (energy) position does not provide information about the excitation energy Δ: depending on the energy level position the mirage's excitation voltage V^* can lie anywhere above the COT threshold voltage $V = \Delta$, see Sec. 2.2.3.

In the stability diagram in the right panel of Fig. 2.14(b), we connect by dashed lines all the COSET resonances to their corresponding SET excitations according to the scheme in Fig. 2.6. We find that mirages appear for virtually all spin-related excitations of the molecule. The stability diagram in Fig. 2.14(c) [same color coding as in (b)] shows that at high magnetic field $B = 7.5$ T these mirages persist.

The clearly visible COSET resonances mark the lines where the relaxation mechanism changes from virtual (COT) to real (SET) charging. They indicate that any intrinsic relaxation is comparable or slower than SET. (If the intrinsic relaxation was much faster, compared to SET, it would dominate everywhere, giving a much smaller change in the current at COSET resonances.) Mirages are thus a signature of slow intramolecular relaxation, in particular they indicate that the intrinsic relaxation time is bounded from below by the magnitude of the observed SET currents $\tau_{\rm rel} \gtrsim \Gamma^{-1} \sim 10^{-11}$ s using the same estimation procedure as above. This is consistent with the sharper lower bound we obtained above from nonequilibrium COT spectroscopy.

Spin relaxation To shed light on what the relaxation mechanism by transport entails in our device, we return to the stability diagram for $B = 0$ T, which is shown as $\mathrm{d}^2 I/\mathrm{d}V^2$ in the right panel of Fig. 2.14(d). Highlighted at negative bias are the two crossover-regime bands within which COSET, rather than COT, dominates the relaxation. The left panel shows the different relaxation paths for these two bands.

Focusing on the orange band, we start out on the far left of Fig. 2.14(d) moving at fixed bias $V = 1.2$ meV along the onset of inelastic COT. Fig. 2.14(e) depicts the corresponding energies (left) and energy differences (right). Here, the molecule is in the spin-doublet D_1 ground state and is occasionally excited to the high-spin quartet Q by COT from where it relaxes via path 1 (10^{-9} s), again by COT.

When reaching the circle ($\circ$) in Fig. 2.14(d) the *relaxation* mechanism changes: path 1 is overridden by the faster relaxation path 2 (10^{-11} s) which becomes energetically allowed [Eq. (2.22)]. The top panel of Fig. 2.14(e) illustrates that although the ground state D_1 is off-resonant (highlighted in red), after exciting it by COT to Q – increasing the spin-length – the system has enough *spin-exchange* energy (green) to expel a single electron in a *real* tunneling processes leaving a *charged* triplet state behind.

At the star ($\star$) in Fig. 2.14(d) the *excitation* mechanism changes from off-resonant to resonant, leaving the relaxation path unaltered. Now the ground state D_1 becomes unstable with respect to real charging: there is enough energy to expel an electron to the right electrode and sequentially accept another one from the left. We thus have an resonant SET transport cycle, i.e., the stationary state is a statistical mixture of the

N and $N+1$ ground states.

The COSET regime is delimited by mirage resonances and situated between the two positions ∘ and ⋆. Failure to identify the difference between this "band" and the pure COT happening on the left of ∘, besides yielding a wrong qualitative spin multiplet structure, leads to an overestimation of the relaxation time: in the COSET regime the spin-excitations created by inelastic COT are *quenched*.

Quenching of spin-excitations We now assess this quenching in detail for the experimental situation by a calculation based on the master equation [90, 209] (2.23) that includes all Γ and Γ^2 processes using the model determined earlier [Eqs. (2.26)-(2.29)], simulating the broadening as before by an effective temperature [Fig. 2.12].

The computed conductance for $B = 0$ is shown in Fig. 2.15(a). Besides the SET excitations – including the NDC effect – obtained earlier in Fig. 2.12(c), we capture the main features of the experimental data in Fig. 2.12(c) and Fig. 2.14(d): the three horizontal COT excitations and two prominent COSET lines.

We can now explore the nonequilibrium occupations of the five spin-multiplets as the transport spectrum is traversed. These are shown in Fig. 2.15(b). The lowest panels show in the left (right) off-resonant regime the ground multiplet D_1 with N electrons (T with $N+1$ electrons) is occupied with probability 1 at low bias voltage (black regions). In contrast, in the resonant regime these two ground states are both partially occupied due to SET processes. We compare the occupations along three different vertical $\mathrm{d}I/\mathrm{d}V$ line cuts in Fig. 2.15(a).

(i) Increasing the bias voltage in the resonant regime, starting from $V_g = -1.46$ V, one first encounters in Fig. 2.15(a) a $\mathrm{d}I/\mathrm{d}V$ dip (NDC, white). This is caused by the occupation of the S state, as the S-panel in Fig. 2.15(b) shows. This drains so much probability from the T multiplet [with a higher transition rate to the D_1 multiplet, Eq. (2.28)-(2.29)] that the current goes down. Increasing the bias further depopulates the S state again, thereby restoring the SET current through a series of $\mathrm{d}I/\mathrm{d}V$ peaks.

(ii) Increasing the bias voltage starting from the right off-resonant regime the excited S-state becomes populated by COT decreasing the average spin-length of the molecule. When crossing the COSET resonance at higher bias this excitation is *completely quenched* (white diagonal band) well before reaching the resonant regime, *enhances* the molecular spin, restoring the triplet.

(iii) When starting from the left off-resonant regime, the population of the excited Q-state enhances the average spin-length of the molecule. As before, crossing the COSET resonance at higher bias *quenches* this excitation. Now this *reduces* molecular spin, restoring the doublet. Along the way, the D_2 state also becomes occupied by COT and subsequently quenched by COSET. Because of its higher energy, the white COSET band in the D_2-panel of Fig. 2.15(b) is much broader.

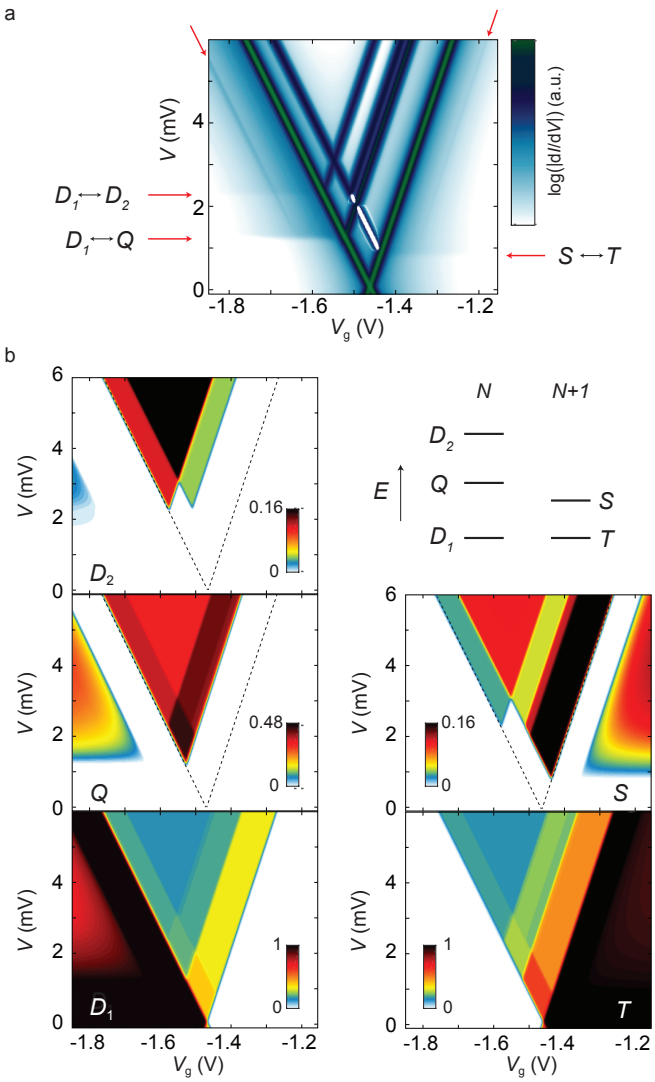

Figure 2.15: **Calculated stability diagram and multiplet occupations**. Result obtained from the full master equation (2.23) and its corresponding current formula (not shown, see Refs. [90, 209]) for the same parameters as in Fig. 2.12(b). (a) Transport spectrum for $B = 0$ corresponding to Fig. 2.11(c). (b) Corresponding color plots of the occupation probabilities of the five spin multiplets (probabilities summed of degenerate levels). The effective coupling Γ^* – merely an overall scale factor in Fig. 2.12(b) – now controls the magnitude of the COT and COSET current corrections *relative* to the SET current. Although elaborate, these corrections still neglect nonperturbative broadening effects and must kept small for consistency by explicitly setting $\Gamma^* = 2.2 \cdot 10^{-3}\, T^* = 0.6$ mK $= 5 \cdot 10^{-5}$ meV. More advanced master equation approaches based on renormalization-group [181, 270] (RG) or hierarchical [271, 272] (HQME) methods can deal with both this broadening and the corresponding larger currents.

2.3.6. HOW FAR IS "OFF-RESONANT" ?

The results show that the widths of the two bands where the COT excitations are quenched by COSET are unrelated to the width of the SET resonances, set by the

maximum of Γ and T. They are, instead, set by the *excitation spectrum* one wishes to probe.

In Fig. 2.16(a) we quantify how far the energy level has to be detuned from resonance in order avoid this quenching in our molecular QD device structure. When this detuning lies in the window $-1.5\Delta < \alpha_g V_g < -0.5\Delta$ one is sure to run into the COSET band with increasing bias. Only for $-\alpha_g V_g < 1.5\Delta$ there is a finite window where the excitation is not quenched. For the excitations T, Q, D_2 in our experiment, this amounts to 2.9, 4.5, and 8.5 times the SET resonance width.

In Fig. 2.16(b) we show the corresponding construction for strong capacitive asymmetry typical of STM setups. To avoid quenching for any bias polarity, one now needs to stay further away from resonance $-\alpha_g V_g < 2\Delta$. Interestingly, for $-2\Delta < \alpha_g V_g < -\Delta$ the COT excitation at forward $V = \Delta$ is not quenched, whereas at reverse bias $V = -\Delta$ it is. For asymmetric junctions, the COSET mechanism thus leads to a *strong bias-polarity dependence* of relaxation of excitations in the nominal off-resonant regime. For $-\Delta < \alpha_g V_g$ one is sure to run into the COSET band for forward bias.

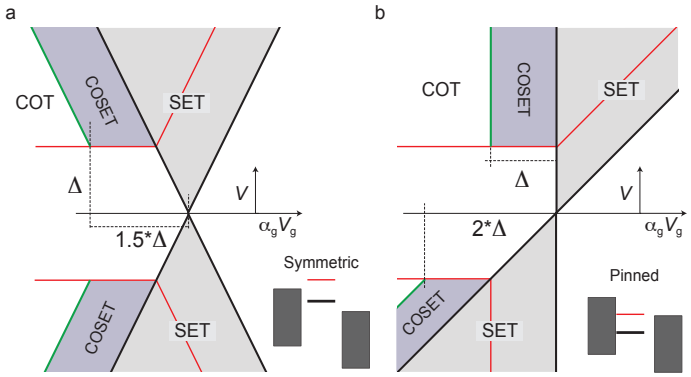

Figure 2.16: **How far is "off-resonant" ?** (a) Energy-energy stability diagram for symmetric capacitive coupling ($C_L = C_R \gg C_g$) characteristic of molecular QD devices. (b) Strongly asymmetric couplings, ($C_L \gg C_R$). This is typical for molecular STM junctions, where the energy levels pin to one electrode (substrate), leaving the tip electrode to act as a probe. In this case the energy $\alpha_g V_g$ represents the *level alignment* with the Fermi-energy.

Whereas in the present experiment we encountered relatively low-lying spin-excitations ($\Delta \sim$ few meV) atomic and molecular devices can boast such excitations up to tens of meV. To gauge the impact of COSET mirage resonances, consider an excitation at $\Delta \sim 25$ meV that we wish to populate by COT, e.g., for the purpose of spin-pumping [140, 266]. To avoid the quenching of this excitation $V = \Delta$ the distance to the Fermi-energy at $V = 0$ (level-alignment) needs to exceed *room temperature*, even when operating the device at mK temperatures. For vibrational and electronic excitations on the 100 meV scale the implications are more severe. Moreover, even for excitations that do satisfy these constraints, cascades of "nonequilibrium" COT excitations may – if even higher excitations are available (e.g., vibrations) – provide a path to excitations that do decay by SET processes. While all these effects can be phrased loosely as "heating", we have demonstrated their discrete, *in-situ* tuneability, and the

role they play as a spectroscopic tool.

2.4. SUMMARY

We have used electron transport on a single-molecule system to comprehensively characterize the spin degree of freedom and its interaction with the tunneling electrons. Three key points – applicable to a large class of systems – emerged with particular prominence:

(i) Combining SET and COT spectroscopy in a single stable device provides new tools for determining spin properties *within* and *across* molecular redox states. This is crucially relevant for the understanding of the different spin-relaxation mechanisms, even in a *single* redox state.

(ii) Nonequilibrium pump-probe electron excitation using two COT processes (four electrons) was demonstrated in our three-terminal molecular device and signals a substantial intrinsic spin relaxation time of about 1 ns, much larger than the transport times.

(iii) Mirages of resonances arise from the nontrivial interplay of SET and COT. These COSET resonances signal a sharp increase of the relaxation rate and can occur far away from resonance (many times the resonance width). This limits the regime where spin-pumping works by quenching nonequilibrium populations created by a COT current.

The appearance of a mirage of a certain COT excitation indicates that the relaxation of the corresponding molecular degree of freedom dominates over all possible unwanted, intrinsic mechanism. Thus, "good" devices show mirages and "even better" devices show nonequilibrium COT transitions.

Energy level control turns out to be essential for "imaging" in energy space which allows one to distinguish mirages from real excitations. Whereas real-space imaging seems to be of little help in this respect, the mechanical gating possible with scanning probes overcomes this problem. However, even when energy-level control is available, spectroscopy of molecular junctions still requires extreme care as we illustrated in Sec. 2.2.4 by several examples that break spectroscopic rules. Moreover, our work underlines that level alignment has to be treated on a more similar footing as as coupling (Γ) and temperature (T) broadening in the engineering of molecular spin structures and their spin-relaxation rates [140, 266].

Beyond electron charge transport, recent theoretical work [215, 273] has pointed out that importance of COSET is amplified when moving to nanoscale transport of *heat* [51]. Whereas in charge transport all electrons carry the same charge, in energy transport electrons involved in COSET processes effectively can carry a quite different energy from that acquired in a COT process only and therefore dominate energy currents [215, 273]. Thus, the sensitivity to spin-relaxation processes is dramatically increased in heat transport, indicating an interesting avenue [215] for a *spin-caloritronics* [274] on the nanoscale.

3

KONDO EFFECT IN A NEUTRAL AND STABLE ORGANIC RADICAL SINGLE-MOLECULE JUNCTION

Believe me, you will find more in the woods than in books.
Trees and stones will teach you what you cannot learn from the masters.

Saint Bernard of Clairvaux

Organic radicals are neutral, purely organic molecules exhibiting an intrinsic magnetic moment due to the presence of an unpaired electron in their ground state. This property, together with the low spin-orbit coupling and weak hyperfine interactions, make neutral organic radicals good candidates for molecular spintronics insofar the radical character is stable in solid state electronic devices. Here we show that the paramagnetism of the polychlorotriphenylmethyl (PTM) radical molecule in the form of a Kondo anomaly is preserved in two- and three-terminal solid-state devices and is robust under electrodes displacement and changes of the electrostatic environment. This, in concert with DFT calculations and measurements of the corresponding non-radical species, strongly indicates that a localized orbital in the radical is the source of magnetism. The results pave the way towards the use of all-organic neutral radical molecules in spintronics devices and demonstrate a reliable platform for further investigations into Kondo physics.

Parts of this chapter have been published in Nano Letters **15**, 3109 – 3114 (2015) by R. Frisenda*, R. Gaudenzi*, C. Franco, M. Mas-Torrent, C. Rovira, J. Veciana, I. Alcon, S. Bromley, E. Burzurí, H.S.J. van der Zant.

3.1. INTRODUCTION

Organic free radicals were first synthesized in the 1900 and recently have been explored as building blocks for magnetic materials [275–277]. Thanks to the unpaired electron, these molecules are paramagnetic in their neutral state and have low spin-orbit coupling and weak hyperfine interactions due to their all-organic composition. In virtue of these properties, absent in transition metal-based magnetic compounds, organic radicals have recently attracted attention for molecular spintronics applications [278, 279], where long spin coherence times are required to preserve the information encoded in the electronic spin.

A number of studies on transport through organic radicals have lately appeared both on assemblies as well as individual molecules. An example of the first type can be found in Ref. [280–282], where a self-assembled monolayer of radical molecules is studied employing a conductive AFM. At the single molecule level, investigations have been carried out in scanning tunneling microscopes and mainly focused on studies of the Kondo effect in π-extended organic radical molecules physisorbed on surfaces [283–285]. A demonstration that a neutral organic radical molecule can retain its magnetic moment when integrated in a solid-state device – a crucial step towards future spintronics applications – is so far absent, in contrast to analogous results reported for molecules containing transition metals [286].

Here, we report on the detection of the unpaired spin of a neutral and stable polychlorotriphenylmethyl (PTM) radical molecule in both two and three-terminal solid-state device settings. The detection is based on the observation of a Kondo resonance, arising from the many-body interaction between the conduction electrons and the magnetic impurity [287, 288]. Kondo temperatures T_K of about 3 K are extracted and found to be rather independent of the elastic/inelastic conductance background and mechanical displacement of the junction, in contrast with other molecular families [286, 289]. In addition, measurements on the non-radical PTM-αH counterpart show no Kondo signatures. These observations strongly support the picture that the magnetic impurity originates from the radical unpaired electron and is well-protected against variations of the molecular arrangement and weakly coupled to the electron bath in the leads.

Given the extended literature already present on Kondo physics, it is worth distinguishing this "intrinsic" Kondo effect from that observed in other organic compounds [248, 289–292] or in transition-metal based molecules [286, 293, 294]. In the first group of experiments, the magnetism is induced by a delocalized charge added with a gate voltage or by electron transfer from the leads in molecular systems that are not paramagnetic in their neutral state. In the second group, Kondo physics arises from $3d$ orbitals, which makes the Kondo temperature sensitive to "environmental" parameters like electrodes' displacement and microscopic shape [286] or voltage [294]. Moreover, for spintronics purposes, $3d$ orbitals of transition metals are expected to impact more negatively the spin decoherence of the flowing electrons compared to the p orbitals of organic radicals.

A schematic of the PTM radical molecule is presented in Fig. 3.1(a). The unpaired electron is mainly located in the trivalent central carbon atom, shielded by three chlorinated phenyl rings arranged in a propeller-like configuration which provide stability against chemical reactions ([295] and references therein). Two additional thiophene rings are bonded, through ethylene bridges, to the triphenylmethyl

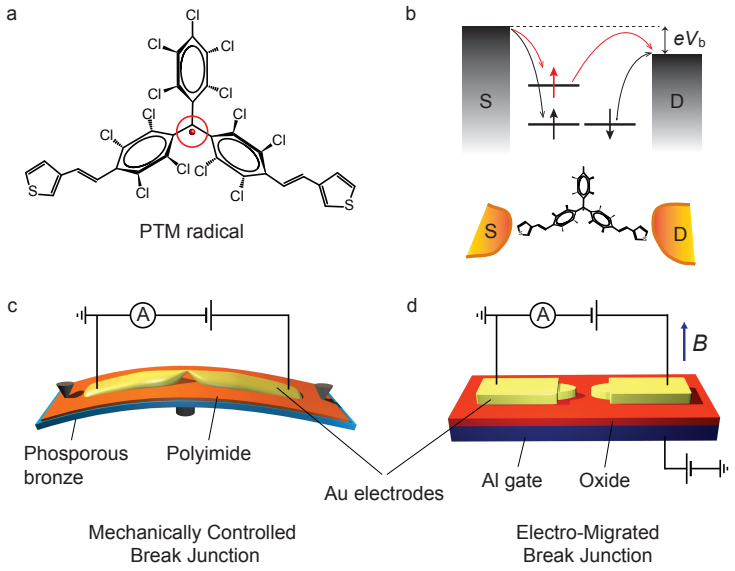

Figure 3.1: **Two and three-terminal PTM radical-based devices.** (a) Sketch of the neutral PTM radical molecule. The radical center lies in the carbon atom located in the middle of three chlorinated phenyl rings and is marked with a red circle. (b) Simple model of the energy levels/orbitals involved in the transport through the molecule. The HOMO orbital accounts for the spin-unpolarized background transport (black arrows), the radical-deriving SOMO orbital is the source of spin-correlated transport (red arrows). Below, the ideal arrangement of the molecule between source (S) and drain (D) electrodes is shown. (c) Two-terminal mechanically-controlled break junction device. (d) Three-terminal electro-migrated break junction transistor.

backbone and serve as linkers to the gold electrodes (Au-S bond). The ideal physical arrangement of the molecule between the source and drain electrodes and the associated off-resonant transport schematic are depicted in Fig. 3.1(b). As we will see later, we can identify a spin-unpolarized background transport channel (black arrows) through the Highest Occupied Molecular Orbital (HOMO) and a spin-flipping Kondo-mediated transport channel (red arrows). This additional channel arises from the Singly Occupied Molecular Orbital (SOMO) and is responsible for the paramagnetism.

Measurements on the molecule are performed with two "complementary" arrangements: the two-terminal mechanically-controlled break junction (MCBJ) and the three-terminal electro-migrated break junction (EMBJ), respectively depicted schematically in Fig. 3.1(c-d). MCBJs allow for a study of the Kondo feature on a large number of samples as a function of electrode displacement. More extended detailed measurements as a function of temperature, magnetic field and gate voltage are conducted with the EMBJs. In both cases, a *dc*-voltage bias V_b is applied to the source and drain electrodes and the corresponding current I is measured. Numerical derivative with respect to V_b allows to obtain the differential conductance $\mathrm{d}I/\mathrm{d}V$.

3.2. RESULTS

3.2.1. MECHANICALLY-CONTROLLED BREAK JUNCTIONS

The first experiments are carried in a low-temperature ($T \approx 6$ K) MCBJ setup. Here a large number of single-molecule junctions and different molecule-metal configurations can be studied by repeatedly breaking and making the electrodes. In this setting, we have measured in total 86 junctions in the presence of the PTM radical out of which 31 exhibited the signature of molecular junction formation. About 20% of the molecular junctions showed a zero-bias peak in the $\mathrm{d}I/\mathrm{d}V$.

In Fig. 3.2(a) we show the zero-bias conductance, extracted from $I-V$ traces, as a function of the inter-electrode separation for two different PTM radical junctions. Both conductance traces show a plateau at 1 G_0 due to transport through a single Au atom, indicating atomically-sharp electrodes. Upon further stretching, the conductance exhibit plateaus: this non-exponential decay with the inter-electrode distance is the main indicator of the presence of a molecule. At displacements of about 0.5 nm, both junctions exhibit an abrupt jump to conductance values below the noise level of 10^{-6} G_0, indicating the rupture of the molecular junction. The fluctuations observed in conductance around the $10^{-2}G_0$ value are to be assigned to atomic rearrangements at the metal/molecule interface or inside the molecule [296, 297]. Figure 3.2(b) shows three $\mathrm{d}I/\mathrm{d}V$ traces for each junction at the positions marked by the coloured arrows in Fig. 3.2(a). All traces show a zero-bias anomaly that persists along the stretching of the junction even if the average conductance background changes. Such mechanical stability shows that the origin of the zero-bias anomaly is not sensitive to stretching-dependent variations of the interface between the anchoring groups and the electrodes – in contrast to, for instance, Refs. [286, 289].

For reference, we have also measured 95 junctions in the presence of the non-radical αH counterpart. Molecular junctions are formed in 30 cases, yielding a junction formation probability of about 35%, approximately similar to the radical species. In contrast to the radical molecule, the non-radical one shows no zero-bias peak in all the cases, see Appendix A.2. In this way, we can ascribe the origin of the zero-bias resonance to an intrinsic property of the radical molecule, as compared to the non-radical one. Provided that the only difference between the two species lies in the open- or closed-shell electronic structure, it is reasonable to assign the zero-bias feature to the presence of the unpaired electron in the radical. In order to verify the Kondo character of this zero-bias resonance, measurements in temperature and magnetic field are carried out.

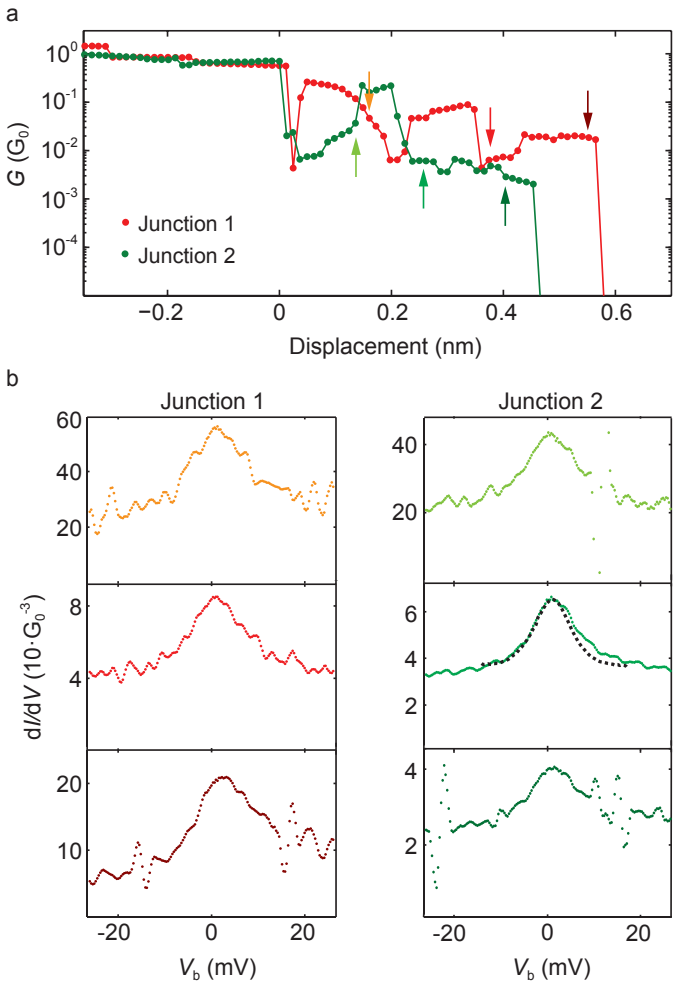

Figure 3.2: **Two PTM radical samples showing a Kondo resonance investigated with mechanically controlled break junctions** (color online) (a) Conductance versus displacement traces for two different junctions measured with MCBJ. Each data point is extracted from an individual I-V. (b) Differential conductance traces measured at displacements indicated by the arrows in (a). Measurements are taken at $T \approx 6$ K. The dashed line corresponds to a different measurement on a PTM radical in EMBJ at $T \approx 4.5$ K. The trace is offset vertically. The FWHM and the conductance levels are comparable with both techniques. The slight variations in the peak width and the noise level may be due to coupling fluctuations at the molecule/metal interface while stretching.

3.2.2. ELECTRO-MIGRATED BREAK JUNCTIONS

To investigate in more detail the zero-bias resonance we have employed the EMBJ setup. With this setup we perform low-noise measurements at temperatures ranging from $T \approx 30$ mK to $T \approx 4.5$ K, magnetic fields up to 8 T and gate voltage. Nanogaps are prepared following the electromigration method [3, 257] (see Methods).

We record the formation of 25 molecular junctions out of the 126 measured devices. From those, a zero-bias peak in $\mathrm{d}I/\mathrm{d}V$ appears in 11 samples. Differential conductance measurements as a function of the gate voltage showed off-resonant trans-

port throughout the entire accessible gate window (see Appendix A.3). This is a fingerprint of a substantial HOMO-LUMO gap. In Fig. 3.3 the temperature and magnetic field characterization for two of the measured junctions are presented. Figure 3.3(a-b) show dI/dV spectra at different temperatures. A zero-bias resonance is clearly visible. In Fig. 3.3(c-d) the corresponding conductance at $V = 0$, $dI/dV|_{V=0}$, is plotted as a function of temperature on a logarithmic scale. The typical dependence expected from a Kondo resonance is observed, ranging from the intermediate (weak coupling) $T \approx T_K$ to the low-energy (strong coupling) regime for $T \ll T_K$, where the asymptotic value of $dI/dV|_{V=0}$ is approached. For a direct comparison between traces shown here in the weak coupling regime and those measured with the MCBJ in Fig. 3.2, we refer the reader to the Appendix A.3. We notice here the three-order of magnitude difference in the conductance values of the two samples. In addition, in Fig. 3.3(b) two side shoulders weakly dependent on temperature are visible; such step-like features, occurring also at higher harmonically-spaced bias values, are observed in about 50 % of the measured samples. The harmonic spacing together with their non-exponential temperature dependence point to a vibrational origin [298, 299].

A fit to the formula describing the conductance G as a function of the temperature for spin-1/2 Kondo [300]:

$$G(T) = G_0 \left[1 + (2^{1/0.21} - 1) \left(\frac{T}{T_K} \right)^2 \right]^{-0.21} + G_b \tag{3.1}$$

yields $T_K = 3.6$ K and $T_K = 2.6$ K for the first and second samples respectively. In equation 3.1, G_0 is the conductance in the $T \to 0$ limit, G_b is the background contribution and T_K is defined so that $G(T_K) - G_b = G_0/2$. From the lower temperature spectra ($T \ll T_K$) of Fig. 3.3(a-b), i.e. the data points in the flat region of Fig. 3.3(c-d), an independent estimation of the Kondo temperature can be obtained. Fitting the Kondo peak with a Lorentzian, the Kondo temperature is extracted from the full width half-maximum (Γ_K) of the Lorentzian according to $\Gamma_K \approx 2\sqrt{2} k_B T_K$ [301]. The obtained values 3.0 K and 3.1 K are in agreement with those deduced from the fit to equation 3.1.

In Fig. 3.3(e-f) the magnetic field dependence of dI/dV in the strong coupling regime ($T \ll T_K$) is shown. Suppression and subsequent Zeeman splitting of the Kondo resonance are observed. An estimation of the g-factor from the Zeeman energy in magnetic field yields $g \approx 2.0 \pm 0.2$. Figure 3.3(g-h) display regularly-spaced ($\Delta B = 0.4$ T) linecuts extracted from Fig. 3.3(c-g). At $B_c \approx 1.2$ T and $B_c \approx 1.6$ T respectively, the onset of the Kondo resonance splitting is visible, as marked by the dashed lines in Fig. 3.3(e,f). These values are consistent with the expected critical magnetic field given by $B_c \approx 0.5 k_B T_K/(g\mu_B)$ [302], above which splitting of the Kondo peak should be observed. Particularly insightful is the field-dependence in Fig. 3.3(h), where the Kondo resonance is observed evolving on top of the two side shoulders in an independent way. This behaviour further supports the idea of a distinct origin for the two features.

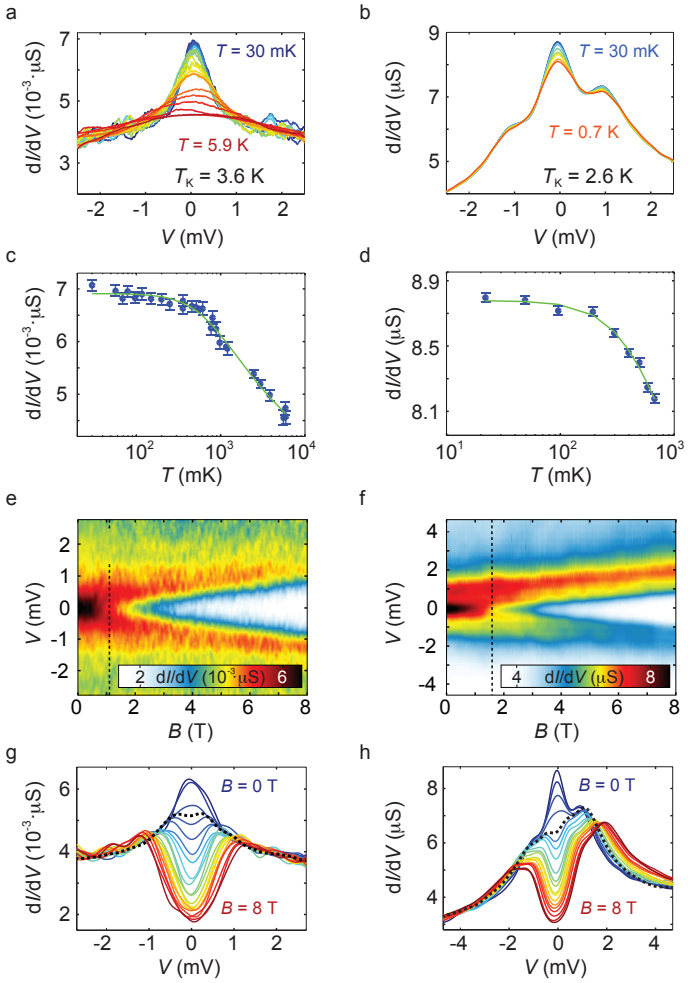

Figure 3.3: **Two PTM radical samples exhibiting Kondo resonance investigated with electro-migrated break junctions** (a,b) dI/dV traces ($1G_0 \approx 77\ \mu$S) of the radical for temperatures indicated in the panels. (c,d) Peak height ($dI/dV|_{V=0}$), extracted from (a,b), as a function of temperature on a logarithmic scale. The solid lines are fits to a spin-1/2 Kondo with parameters $G_0 = 3.8$ nS, $G_b = 3.1$ nS and $T_K = 3.6$ K for (c) and $G_0 = 3.1$ nS, $G_b = 5.6$ nS and $T_K = 2.6$ K for (d) (see text). (e,f) dI/dV color map measured as a function of the magnetic field B and bias voltage V at $T = 590$ mK and $T = 25$ mK respectively. Black dashed lines mark the onset of Kondo splitting. (g,h) dI/dV spectra extracted from (b) with a regular spacing of $\Delta B = 0.4$ T. The Kondo peak is seen splitting at $B_c \approx 1.2$ T and $B_c \approx 1.6$ T respectively, as black dashed traces indicate.

The measurements in the EMBJ setup feature a Kondo state that responds to the three different perturbations – increase in temperature, bias voltage and magnetic fields – in the expected way [284]. This provides a sound estimation of the Kondo energy scales involved and is consistent with the strong coupling regime. Worth noting that the aforementioned three-order of magnitude difference in conductance level is due to an increase of the background conductance G_b, with a similar G_0/G_b ratio in both cases.

3.3. DENSITY FUNCTIONAL THEORY CALCULATIONS

To corroborate the experimental findings, we carried out density functional theory (DFT) calculations to model the ground state electronic properties of the PTM radical.

Figure 3.4 shows the calculated energy level diagram of the valence orbitals of the PTM radical molecule for the two spin channels α and β. HOMO and LUMO exhibit spin degeneracy, while SOMO and LUMO-β are spin-polarized. The experimental Fermi energy of gold lies close to the middle of the SOMO-LUMO energy gap ($\approx 2eV$). The radical unpaired electron in the SOMO is therefore responsible for the magnetic properties of the system. The proximity of the Fermi level to the HOMO and SOMO occupied levels makes them the most relevant for transport, yielding an hole-mediated off-resonant conductance pathway. The large gap and the position of the Fermi energy are in agreement with the off-resonant transport experimentally observed in the whole gate voltage range (see Appendix A.2).

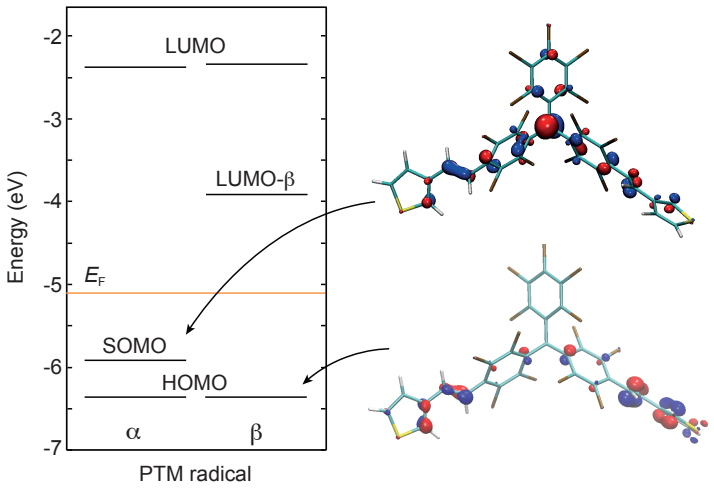

Figure 3.4: **Density functional theory calculations.** DFT energy level diagram for the two spin channels α and β of the PTM-radical molecule. The orange line indicates the theoretical Fermi energy of gold. HOMO and SOMO levels are depicted together with their relative iso-surfaces.

A comparison between the iso-surfaces of the SOMO and the HOMO shows the former as mostly localized on the radical carbon atom with a small component on the backbone and the latter as fully-delocalized over the molecular backbone with a considerable weight on the thiophene groups. Worth noticing is the two-lobed p-like shape of the SOMO, indicating a weak hybridization of the atomic orbital and its strong atomic character. Within this framework, we can propose a coherent picture to account for the transport through the PTM radical molecule observed in the experiments. The HOMO provides the spin-independent conductance background, while the SOMO is responsible for the Kondo-correlated phenomena. The strong localization of the SOMO in the carbon protected by the three chlorinated phenyl rings makes the Kondo resonance stable and reproducible in different samples and under

stretching. To complete the analysis, DFT calculations using the same model were conducted for the PTM-αH non-radical molecule and the stretched PTM-radical molecule. The energy diagram and isosurfaces of the relevant orbitals are reported in the Appendix A.4. The calculations for the PTM-αH non-radical reveal the presence of a fully-occupied HOMO with the absence of a SOMO level and its unpaired electron spin. These findings are again in accordance with the experimental absence of Kondo features in the PTM-αH-formed junctions. For the stretched PTM-radical molecule, one can observe that the energy of the SOMO varies only slightly throughout the stretching. This is in line with the localised character of the SOMO and the experimental findings (see Appendix A.4).

3.4. CONCLUSION

In summary, we contacted a neutral organic radical molecule in both two and three-terminal solid-state devices. We demonstrate that the magnetic moment of the PTM-radical open-shell system is preserved upon interaction with the metal electrodes and robust against mechanical/electrostatic changes at the electrode-molecule interface. We do this by measuring, in mechanically-controlled break junctions as well as electro-migrated break junctions, a statistically significant presence of fully-screened spin-1/2 Kondo features that are insensitive to the electrode displacement and background conductance. We attribute the source of the paramagnetism to the unpaired electron located in the radical carbon centre and we substantiate the picture with DFT calculations. Measurements on the closed-shell αH non-radical molecule show no Kondo correlations and therefore corroborate the relation between radical center and magnetic properties. The findings reported here open up the way towards the use of all-organic radical molecules in spintronics devices. From a more fundamental point of view, the overall stability of the unpaired electron of the radical molecule makes it an excellent platform for further investigation on Kondo physics.

A. APPENDIX

A.1. METHODS

Synthesis of PTM radical and PTM-αH The PTM-αH molecule has been synthesized using a Wittig-type coupling between polychlorinated triphenylmethane bisphosponate and the 1-thiophenecarboxaldehyde. Treatment of PTM-αH with tetrabutylammonium hydroxide promotes the removal of the acidic proton at the αH position to give the corresponding carbanion that was subsequently oxidized with p-chloranil giving the desired PTM radical.

The molecular solution is prepared in the glow-box dissolving 1.8 mg of polychlorotriphenylmethyl (PTM) radical powder into 2 ml of nitrogen-saturated dichlorobenzene solvent [1 mM].

MCBJ measurements The mechanically controlled break junctions experiments are performed in vacuum ($p = 1.0 \times 10^{-7}$ mbar) at $T \approx 6$ K. The molecular solution is drop-cast onto the MBCJ sample, whose fabrication is described elsewhere [303, 304], the setup evacuated and cooled down to liquid He temperature. Measurements begin with a metallic constriction, characterized by a conductance of 10 G_0. By bending the substrate, the junction can be stretched and broken in two aligned nano-electrodes which can eventually be bridged by a molecule. During the stretching of the wire, performed in steps of 10 pm, current-voltage characteristic can be measured at each position. The control of the bending is obtained with a feedback on the current/conductance.

EMBJ measurements Measurements in the electromigrated break junctions are carried out in the inner vacuum chamber ($p < 1.0 \times 10^{-3}$ mbar) of a dilution fridge with a base temperature of ≈ 30 mK. Magnetic fields up to 8 T can be applied to the sample. The molecular solution is drop-cast onto a Si/SiO_2 chip containing an array of 24 Au bridges 100-nm wide, 400 nm long and 12 nm thick with an Al/Al_2O_3 local gate underneath. A nano-gap is produced by feedback-controlled electromigration [3] of each of these bridges. As the bridge conductance reaches 3-4 G_0, electromigration is stopped and the wire is let self-break at room temperature [257, 305]. The molecular solution is evaporated while evacuating the chamber and the sample is cooled down. All measurements are performed in *dc*, with low-noise home-made electronics.

DFT calculations The molecular geometries of both the radical (spin unrestricted) and the H (closed shell) were optimized with no symmetry constraints using density functional theory as implemented in the Gaussian 09 code [306]. In all cases the B3LYP [307] hybrid exchange-correlation functional and a triple-zeta 6-311++G(d,p) basis set including polarization functions on all atoms was employed. Different configurations of the PTM molecule, corresponding to different possible orientations of the C=C-linked thyophene rings were tested in both its radical and αH forms. The lowest energy configurations were then used to extract the reported orbital energies. Optimizations of the PTM molecules with Au atoms placed near the two sulphur atoms to mimic the presence of gold contacts were found to very slightly stabilize all orbital energies by 0.05-0.1 eV. The significant dispersive contribution to the Au-S

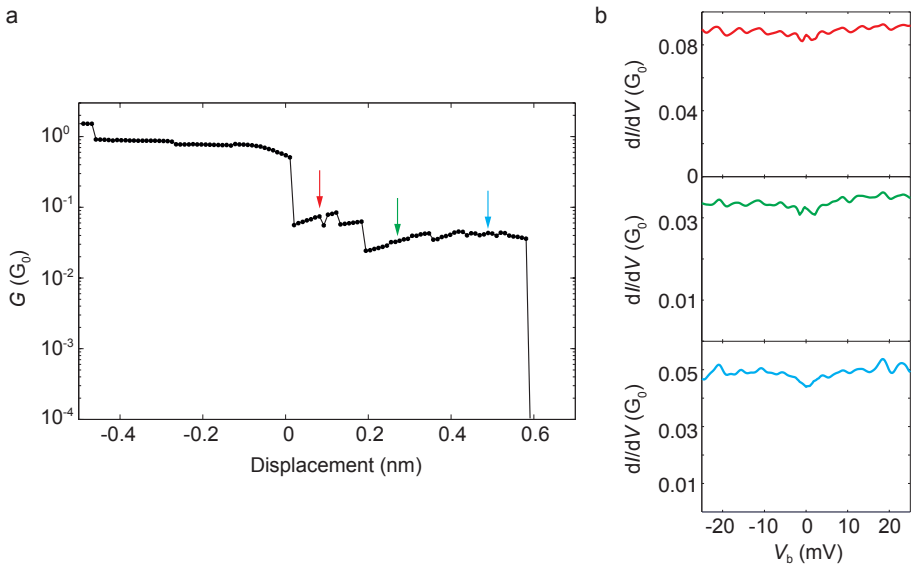

Figure 3.5: **Conductance trace and current-voltage of a non radical junction.** (a) Conductance versus displacement traces for a junction measured with MCBJ. Each data point is extracted from an individual IV. (b) Differential conductance traces measured at displacements indicated by the arrows in (a). Measurements are taken at a temperature of 6 K.

interaction was taken into account through use of the DFT-D2 method [308]. The interaction strength between a single Au atom and a S atom of the PTM was found to be 0.16 eV. Reported results are those from calculations without Au atoms.

A.2. MCBJ: MEASUREMENTS ON THE NON-RADICAL MOLECULE

Figure 3.5(a) reports the zero-bias conductance trace, extracted from the I-V characteristics, as a function of the electrode displacement for a PTM-αH molecular junction. Figure 3.5(b) shows three dI/dV versus V spectra measured at the positions indicated by the arrows. In contrast to the PTM radical, no zero bias peaks is observed. The pie charts in Fig. 3.6 summarize the molecular junction formation probability and the appearance of zero bias peaks in the dI/dV traces. The two investigated molecules show a similar junction formation probability but, while the PTM-radical molecular junctions exhibit a zero bias peak in 22% of the cases, the zero bias peak is completely absent in the PTM-αH non-radical counterpart.

How do we explain this relatively low occurrence (22%)? It is worth reminding that the observation of the Kondo effect in transport is especially sensitive to *(i)* the temperature, *(ii)* the molecule-electrode coupling and *(iii)* the level alignment to the electrodes' Fermi energy. A well-known mesoscopic-physics expression – see, for instance [309] – for the Kondo temperature T_K is: $k_B T_K \approx \sqrt{\Gamma U}\exp\left(\pi\frac{\epsilon(\epsilon+U)}{\Gamma U}\right)$, where Γ is the molecule/electrode coupling, ϵ is the level alignment and U is the charging energy. This formula shows that the Kondo temperature is strongly dependent on the combination of these parameters, which change from junction to junction. Some particular combinations of these prevents the observation of Kondo resonances at

the experimental temperature of the MCBJ setups.

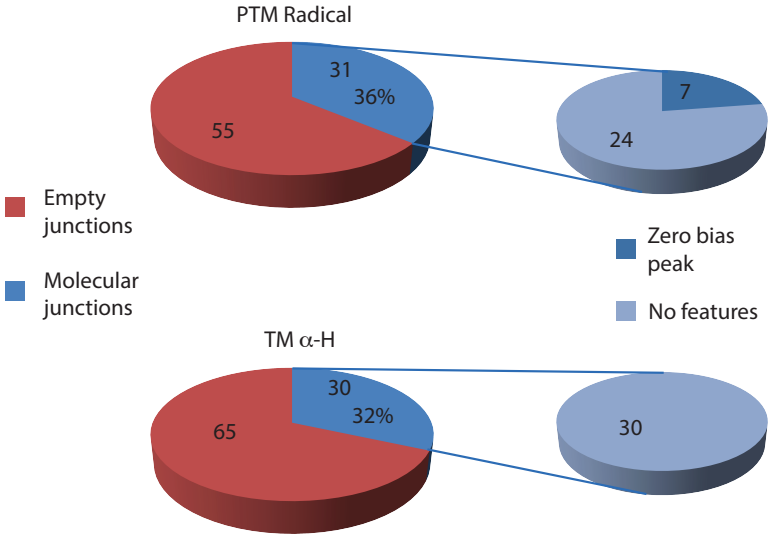

Figure 3.6: **Statistics of radical and non radical junctions.**

A.3. EMBJ: GATE DEPENDENCE AND COMPARISON TO MCBJ RESULTS

In order to verify the stability of the radical against charging, we have performed conductance measurements as a function of bias and gate voltages. Figure 3.7(a) shows the obtained differential conductance map related to the sample in Fig. 3.3. Varying the gate voltage value from $V_g = 0$ V towards positive (negative) values has the effect of increasing (decreasing) the Kondo peak height. However, from the symmetry point at $V_g \approx -0.25$ V the peak width is seen slowly increasing both for more positive and more negative gate voltages. Figure 3.7(b) shows a similar characterization for another sample in which Kondo effect is observed. An increase of peak width for negative gate voltages is observed. Worth remarking is that in both sample no signatures of resonant transport are visible for the whole gate and bias range. These measurements indicate that the Fermi level lies within a relatively large HOMO-LUMO gap and above an half-filled orbital SOMO orbital.

Here we also want to show how EMBJ traces compare with MCBJ traces. Figure 3.8 shows an exemplary trace measured with the former at temperatures $T \approx 4.5$ K against three traces obtained with the latter at $T \approx 6$ K for different displacements. The full width at half maximum of the EMBJ trace is comparable to, but slightly smaller than that of the MCBJ traces, consistently with the lower measuring temperature. Conductance levels are also comparable.

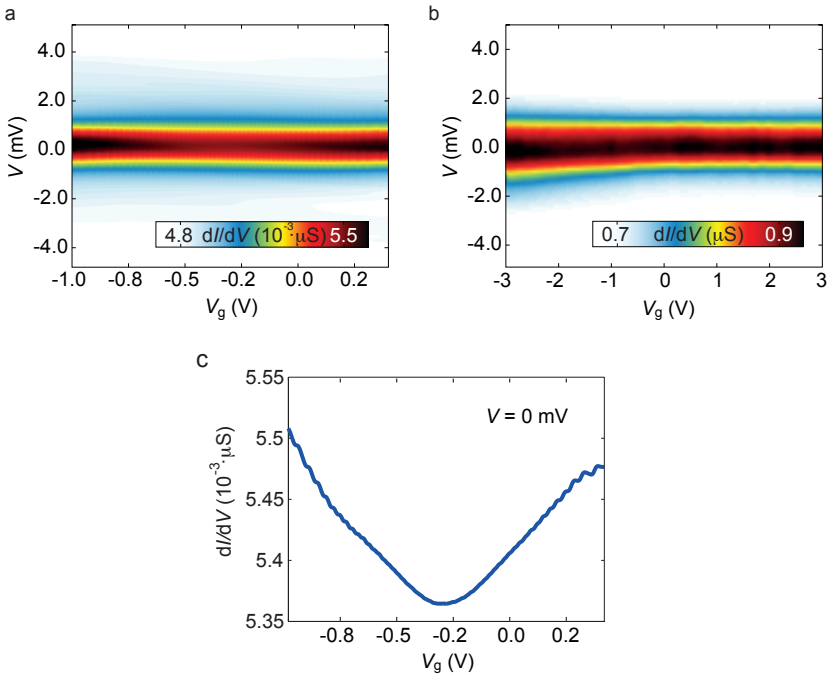

Figure 3.7: **Gate-dependent measurements on the PTM radical.** (a) Differential conductance map of the sample in Fig. 3.3 of the manuscript. The Kondo resonance can be seen to evolve with gate voltage. Peak height and width increase from $V_g \approx -0.25$ V towards both more positive and more negative gate voltages. No signatures of resonant transport and charging can be seen. (b) Differential conductance maps of another sample exhibiting Kondo correlations. Again the Kondo peak changes with gate voltage and no resonances are observed. (c) $\mathrm{d}I/\mathrm{d}V$ zero bias linecut as a function of gate voltage extracted from (a). The Kondo peak height is clearly seen increasing in both gate voltage directions from the symmetry point at $V_g \approx -0.25$ V.

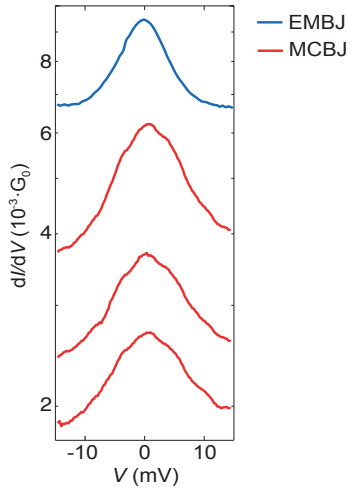

Figure 3.8: **Comparison between EMBJ and MCBJ measurements.** $\mathrm{d}I/\mathrm{d}V$ spectra of the PTM radical obtained in the three-terminal EMBJ at $T \approx 4.5$ K (blue) against the series of the three spectra obtained in the two-terminal MCBJ for three different displacements at $T \approx 6$ K (red). The $\mathrm{d}I/\mathrm{d}V$ is in a logarithmic scale.

A.4. DFT CALCULATIONS ON THE NON-RADICAL PTM-αH

Figure 3.9 compares the eigenvalues of PTM-αH non-radical and the PTM radical calculated with DFT. The orbitals of the HOMO are included.

We have also performed DFT calculations to study the effect of stretching on the SOMO as seen in Figure 3.10. Stretched conformations of the PTM molecule were obtained by performing constrained optimisations whereby the two S atoms of the molecule were separated by increasing fixed displacements from their fully relaxed positions from 0-0.24 nm. The structural change and the isosurface of the SOMO for the PTM molecule stretched by 0.2 nm is shown in Figure 3.10(a) and Figure 3.10(b). Incrementally stretching the PTM-molecule radical by up to 0.24 nm induces only very minor energy changes (0.02 eV) in the SOMO and LUMO, in line with their localised character and the experimental findings, see Figure 3.10(c) and Figure 3.10(d).

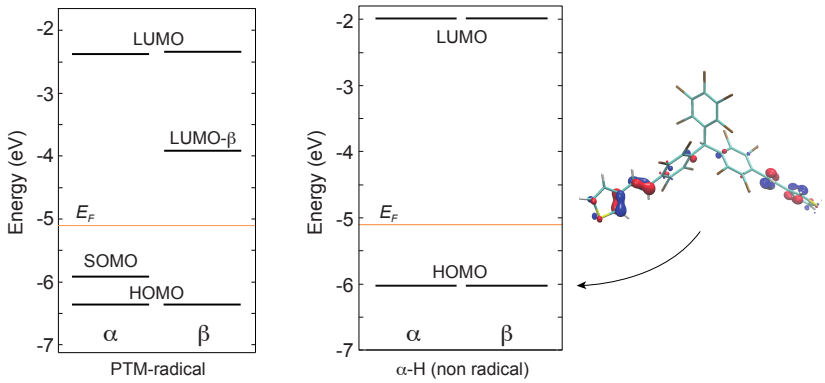

Figure 3.9: **DFT calculations.** Energy schemes for the PTM radical (left) and the PTM-αH (right).

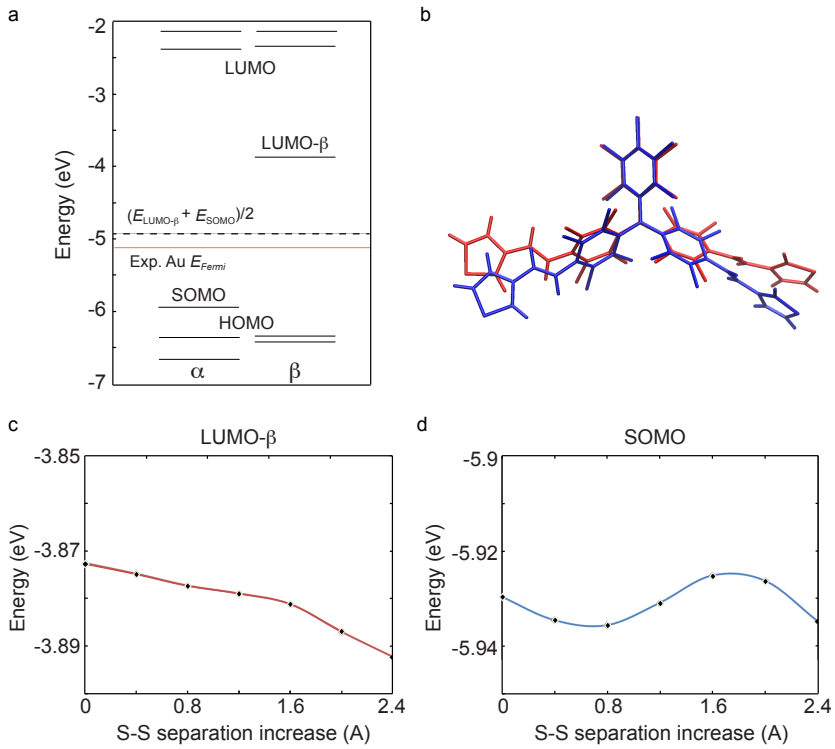

Figure 3.10: **DFT calculations.** (a) Energy level scheme of the molecule when mechanically stretched by 0.2 nm. (b) Comparison of the relaxed PTM radical molecule (blue) with the stretched configuration (red). (c) Variation of the LUMO-β orbital energy as a function of stretching. (d) Same as in (c), but for the SOMO orbital. Note that the molecule is stretched by increasing the separation of the two terminal S atoms of the thiophene anchoring groups from their original positions in the relaxed molecule. The structure of the modified molecule is then optimised while keeping fixed the new positions of the S atoms.

4

REDOX-INDUCED GATING OF THE EXCHANGE INTERACTIONS IN A SINGLE ORGANIC DIRADICAL

The usefulness of a pot is in its emptiness

Lao-Tzu

Embedding a magnetic electroactive molecule in a three-terminal junction allows for the fast and local electric field control of magnetic properties desirable in spintronic devices and quantum gates. In this chapter, we provide an example of this control through the reversible and stable charging of a single all-organic neutral diradical molecule. By means of inelastic electron tunnel spectroscopy (IETS) we show that the added electron occupies a molecular orbital distinct from those containing the two radical electrons, forming a spin system with three antiferromagnetically-coupled spins. Changing the redox state of the molecule therefore switches on and off a parallel exchange path between the two radical spins through the added electron. This electrically-controlled gating of the intramolecular magnetic interactions constitutes an essential ingredient of a single-molecule $\sqrt{SWAP}$ quantum gate.

Parts of this chapter have been published in ACS Nano, DOI: 10.1021/acsnano.7b01578, by R. Gaudenzi, J. de Bruijckere, D. Reta, I. de P.R. Moreira, C. Rovira, J. Veciana, H.S.J. van der Zant, E. Burzurí.

1. INTRODUCTION

Fast, reversible and local control of magnetic properties of molecular systems is sought for as a potential path for molecule-based spintronic devices [310–312] and quantum information processing [313–315]. The control of the intramolecular exchange coupling could allow, for instance, for the realization of a single-molecule quantum gate [316–319]. One way to achieve such control at the single-molecule level is to embed a magnetic electro-active molecule in a solid-state junction and use the gate electrode to change its magnetic properties through a form of spin-electric coupling [316, 320–326]. Traditional candidates are single-molecule magnets (SMMs), the magnetic parameters of which can be modulated with the addition of a charge [327–329] or through magnetoelectric effects [330].

A promising alternative to SMMs is offered by all-organic radical molecules [316] where the magnetism arises from the unpaired spins of carbon atoms [331, 332]. The simplicity of their spin structure and the absence of metal centers have proven to yield robust molecular junctions [33, 247, 333] and potentially allow to overcome the limitations inherent to SMMs owing to low spin-orbit coupling and hyperfine interaction. However, the existing experimental examples have shown either a relatively small electric control over the exchange coupling [247] or a reduction of the molecule to a closed-shell system with no unpaired spins [282].

Here, we report the reversible and stable reduction of a neutral diradical molecule in a three-terminal device, by means of a gate electrode. Inelastic electron tunneling spectroscopy (IETS) in the two stable redox states shows that the added electron magnetically couples to the two radical spins, preserving their open-shell character, while changing the magnetic state of the molecule from a singlet to a doublet state with three unpaired electrons. This ability to reversibly switch on the exchange couplings between the added electron and the two radical spins could form the base for a $\sqrt{\text{SWAP}}$ quantum gate [316, 334, 335].

2. RESULTS AND DISCUSSION

The molecule we use is a neutral 2,4,6-hexakis(pentachlorophenyl)mesitylene diradical molecule[336], hereafter PTM-based diradical, schematically shown in Fig. 4.1. It is made of three methyl carbon atoms connected *via* a central benzene ring. Two of these C atoms are methyl radicals with unpaired electrons, while the third binds a H that closes the electronic shell. The resulting molecule is a two-spin magnetic system. Two chlorinated phenyl rings attach and surround each methyl carbon in a propeller-like configuration as seen in Fig. 4.1. The single-molecule junction is formed when a single PTM-based diradical bridges the source and drain electrodes as illustrated in Fig. 4.1(a). The electric field produced by applying a gate voltage V_g to the third electrode is used to change the redox state of the molecule (Fig. 4.1(b)). In transitioning between the two states, a high-conductance peak is traversed, as shown in Fig. 4.1(c). On the right (left) of the peak, *i.e.*, at $V_{g,on}$ ($V_{g,off}$), the redox center has a stable spin $s = 1/2$ ($s = 0$). Additional details on the fabrication and molecule deposition can be found elsewhere [305, 337] and in Appendix A.1.

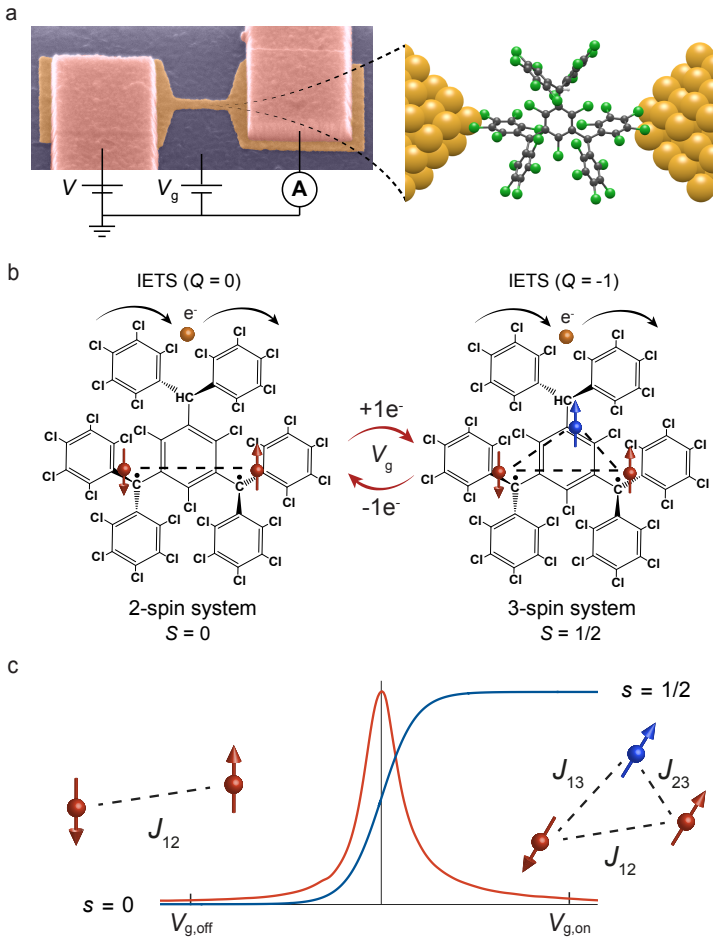

Figure 4.1: **The organic diradical spin system.** (a) Scanning Electron Microscope (SEM) false color image of a Au nanowire on top of an Al_2O_3/AuPd gate. (b) Structure and magnetism schematics of the neutral diradical and reduced form of the diradical. The red dots and the dashed lines mark the radical spins and the exchange interactions, respectively. A gate voltage allows to reversibly add a spin (blue dot) onto the redox center and, with that, switch on and off the magnetic couplings between the added electron and the two radical spins. For each state inelastic electron tunneling spectroscopy (IETS) is performed (yellow electron). (c) Differential conductance (red) and corresponding redox center spin value s (blue) as a function of V_g. Sweeping from $V_{g,off}$ to $V_{g,on}$, the site is progressively filled and s increases from 0 to 1/2. The value $V_{g,off}$ ($V_{g,on}$) marks the gate voltage at which the added spin stably resides off (on) the molecule.

We probe the excitation spectrum of an individual diradical molecule by measuring the *dc*-current I through the junction as a function of bias voltage V and extracting the differential conductance $\mathrm{d}I/\mathrm{d}V$. Each step in the $\mathrm{d}I/\mathrm{d}V$ spectrum signals the opening of an inelastic electron current channel *via* the excited state of the molecule with energy eV. Following the steps' energy as a function of magnetic field allows to read out the molecule's energy spectrum, providing a single-molecule analogue of electron-spin resonance spectroscopy. Figure 4.2(a) shows the $\mathrm{d}I/\mathrm{d}V$ spectra of a diradical junction at different magnetic fields B at fixed gate voltage $V_g = -2.3$ V. The spectrum taken at 0 T shows symmetric steps at ± 4.65 mV, which can be associ-

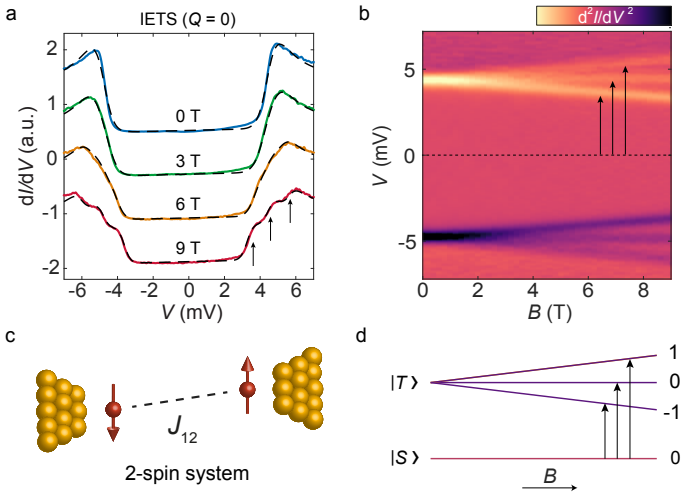

Figure 4.2: **Magnetic spectrum of the neutral diradical.** (a) Differential conductance (dI/dV) spectra of the neutral diradical molecular junction at different magnetic fields and at a fixed gate voltage V_g = -2.3 V. An excitation step at ±4.65 mV splits in three substeps under applied magnetic field. The superimposed dashed lines are fits using the model in Ref. [338]. (b) d^2I/dV^2 color map showing the splitting as a function of V and B. (c) Schematics of a two-spin system with exchange coupling J_{12}, confined between two gold electrodes. (d) Spin spectrum and allowed transitions for a two-spin system with antiferromagnetic J_{12}.

ated with transitions to excited spin states. The confirmation of the magnetic nature of the transitions is given by the evolution of the excitation energies as a function of the applied magnetic field B (see Fig. 4.2(b), where the second derivative, d^2I/dV^2, is shown for clarity). The excitation step splits in three substeps as B is increased. As shown in the level scheme of Fig. 4.2(d), this spectrum is consistent with the antiferromagnetically coupled two-spin system depicted in Fig. 4.2(c) with an open-shell singlet ($S = 0$) ground state $|S\rangle$ and a triplet ($S = 1$) excited state $|T\rangle$.

We compare the experimental spectra with numerical simulations based on the tunneling model of Ref. [338], commonly used in scanning tunneling spectroscopy. The dashed black lines in Fig. 4.2(a) show the results of these simulations. Within the framework of the model, we describe the diradical molecule by a model Hamiltonian with two spin-1/2 centers interacting through a Heisenberg exchange coupling J_{12}. For all magnetic field values, the data can be well fitted to this model with J_{12} = 4.65 meV. The preference for the singlet ground state is ascribed to the distortion of the molecule in the solid state device in analogy with previous studies on PTM-based neutral triradicals [247]. We have verified the plausibility of this scenario by DFT calculations (see Appendix A.3).

A similar measurement is conducted at fixed V_g = 3 V. Figure 4.3(a) shows the resulting dI/dV spectra for two different magnetic fields. At $B = 0$ T, excitation steps appear at $V = -22$ mV, -19 mV, +20 mV and +25 mV, together with a zero-bias peak ascribable to the Kondo effect [287, 293]. The asymmetry in bias-voltage positions with respect to $V = 0$ and the different step heights can be respectively explained by a bias-dependent tuning of the exchange coupling and contributions from resonant

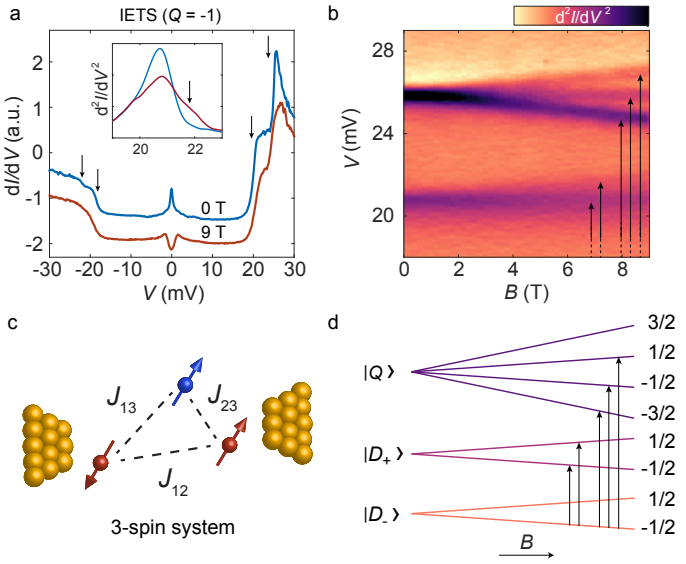

Figure 4.3: **Magnetic spectrum of the reduced diradical.** (a) Differential conductance ($\mathrm{d}I/\mathrm{d}V$) spectra of the diradical junction at different magnetic fields and fixed V_g = +3 V. Two excitation steps with energies +20 mV and +25 mV split in two and three, respectively, under applied magnetic field. Inset: $\mathrm{d}^2I/\mathrm{d}V^2$ linecuts taken from (b) showing the splitting of the doublet $|D_+\rangle$. (b) $\mathrm{d}^2I/\mathrm{d}V^2$ color map as a function of V and B. (c) Schematics of a three-spin system coupled *via* exchange interactions. The added electron, highlighted in blue, introduces two new exchange couplings, J_{13} and J_{23}, with the intrinsic radical spins. (d) Spin spectra and allowed transitions for a three-spin system with antiferromagnetic J_{12}.

transport with asymmetrically coupled electrodes. For increasing B, the zero-bias peak evolves into a dip and the excitation steps split into two (Fig. 4.3(a), inset) and three for the low and high energy value, respectively. The $\mathrm{d}^2I/\mathrm{d}V^2$ colour map of Fig. 4.3(b) shows this magnetic field evolution. From this set of excitations we deduce that the magnetic spectrum consists of a doublet ground state multiplet $|D_-\rangle$ – giving rise to the observed Kondo peak –, a doublet excited multiplet $|D_+\rangle$ and a quartet excited multiplet $|Q\rangle$, as shown in Fig. 4.3(d) (see Appendix A.2). The excitations at +20 mV and +25 mV correspond therefore to the transitions $|D_-\rangle \rightarrow |D_+\rangle$ and $|D_-\rangle \rightarrow |Q\rangle$, respectively.

The spectrum we obtain at this gate voltage can only be hosted by a system like the one depicted in Fig. 4.3(c), where the electrostatically-added electron occupies an empty orbital rather than either of the half-filled radical orbitals and couples to the two unpaired spins *via* the exchange interactions J_{13} and J_{23}. This type of charging, observed also in two other molecular junctions of the 13 measured (see Appendix A.1 for details on statistics), is in contrast to previously reported experiments on PTM monoradicals [282] and other neutral diradical molecules [339]. One of the possible explanations, explored by DFT calculations (see Appendix A.3), is that the structural distortions determining the preference for the singlet ground state lead also to a concomitant reduction of the HOMO-LUMO gap.

Differently than in the neutral state, the excitation spectrum of the reduced state does not provide a unique solution for J_{12}, J_{13} and J_{23}, but rather a subset of so-

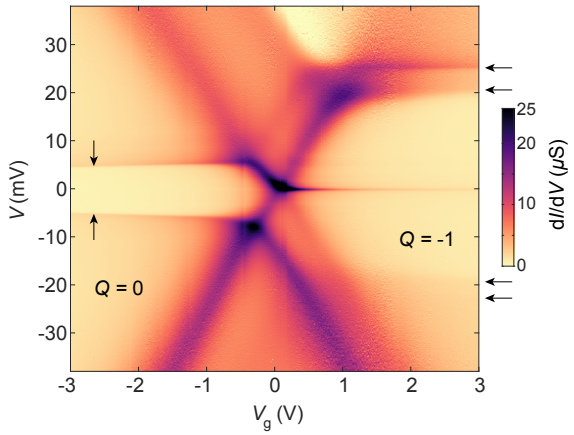

Figure 4.4: **The exchange-coupling gating mechanism.** Differential conductance ($\mathrm{d}I/\mathrm{d}V$) as a function of V and V_g at $B = 0$ T. Slanted high-conductance edges indicate resonant transport and separate two distinct, low-conductance regions where the charge state of the molecule is stable: a neutral charge state ($Q = 0$, left) and a reduced charge state ($Q = -1$, right). Excitations lines at ±4.65 mV (vertical arrows) are present in the $Q = 0$ state. In the $Q = -1$ state excitation lines appear at -19 mV, -22 mV, +20 mV and +25 mV (horizontal arrows), along with a zero-bias line of enhanced $\mathrm{d}I/\mathrm{d}V$.

lutions in the space of the three exchange couplings (see Appendix A.2). One scenario, obtained assuming that the coupling between the radical centers remains unchanged upon charging, yields for J_{13} and J_{23} the values 2 meV and 23 meV. In this scenario, the asymmetry between J_{13} and J_{23} suggests that the added spin resides in the proximity of one of the radical centers. Gas-phase DFT calculations indicate that the added electron may be delocalised over the central phenyl ring (see Section 3.4 in the Supp info).

The transport characteristics of Fig. 4.2 and Fig. 4.3 are connected as can be seen when varying the gate voltage V_g in a continuous way. Figure 4.4(a) shows a $\mathrm{d}I/\mathrm{d}V$ map as a function of V and V_g. The high-conductance slanted edges crossing into a zero-bias peak at $V_\mathrm{g} \approx 0$ V define a resonant electron transport region separating two areas of low conductance. These features signal the presence of a single molecule in the junction whose stable charge states, labelled by $Q = 0$ and $Q = -1$, differ by one electron. The two lines in $Q = 0$, marked by vertical arrows, correspond to the singlet-to-triplet excitation steps of Fig. 4.2, while the arrows on the right-hand side indicate the excitations discussed in Figure 4.3.

The gate electrode provides thus a path to reversibly switch between the neutral and the reduced state of the diradical molecule. Along a horizontal path around zero bias, the high-conductance peak of width $\Gamma \approx 5$ meV is traversed. In the proximity of the peak, the molecule is in a fully mixed-valence state – electrons from the electrodes are hopping on and off the redox center on a timescale $\tau = \hbar/\Gamma \approx 0.1$ ps. Upon application of a gate voltage $V_\mathrm{g} = +3$ V ($V_\mathrm{g} = -3$ V), within a time τ the redox center acquires a discrete occupation number and a stable spin $s = 1/2$ ($s = 0$). The presence of the spin on the redox center turns on two of the three magnetic couplings, J_{13} and J_{23}, which, in turn, influence the time evolution of the two-spin sys-

tem. This fast, electrically-controlled switching of the intramolecular magnetic interactions constitutes the essential ingredient of the quantum $\sqrt{\text{SWAP}}$ gate detailed in Refs. [318, 319, 334] where two alternative read-out mechanisms are also proposed.

3. CONCLUSIONS

In summary, we show that incorporating an organic neutral diradical molecule in a three-terminal device allows for reversible and stable charging from the neutral state to its reduced state by means of a gate voltage. By performing IETS on both redox states, we find that the electron added onto the redox center magnetically couples to the radical spins, thereby driving the two-spin singlet into a three-spin doublet ground state (with three exchange couplings). In this way, by controlling the occupation of the redox center, the exchange interactions between the two radical spins and the added electron are switched on and off. Due to the large coupling to the leads, this switching takes place within sub-picosecond timescales.

A. APPENDIX

A.1. EXPERIMENTAL METHODS

Molecule synthesis The investigated molecule is a neutral 2,4,6-trichloro-$\alpha,\alpha,\alpha',\alpha',\alpha'',\alpha''$-hexakis(pentachlorophenyl)mesitylene diradical prepared as previously reported [336]. Electron Spin Resonance spectroscopy in frozen solutions containing the molecules show a $S = 1$ high-spin ground state, indicative of ferromagnetic exchange interactions between the two radical carbons in the molecule.

Junction preparation and statistics The molecular solution is prepared in a water-free glove-box environment. A small amount of molecular powder is dissolved in nitrogen-saturated dichlorobenzene to a concentration of 0.5 mM approximately. Details on the fabrication and junction preparation are the same as in Appendix A.1 of the previous chapter.

A total of 160 junctions were measured, 13 of which showed signatures characteristics of spin-dependent molecular transport. Eleven of these 13 showed clear singlet-triplet excitations with antiferromagnetic coupling ranging from 0.1 meV to about 11 meV; one showed triplet-singlet characteristic with a ferromagnetic coupling of 2 meV. Four out of the 11 exhibited a degeneracy point and thus charging within the available gate voltage window. In 3 of the 4, the added charge modulates the magnetic properties.

Experimental conditions All the measurements reported in this chapter are performed in a high-vacuum chamber ($p < 5 \cdot 10^{-4}$ mbar) of a dilution refrigerator ($T \approx 70$ mK). A built-in superconducting magnet can be used to apply magnetic fields up to 9 T.

Electrical current I measurements are performed applying a DC bias voltage V to the source and drain gold electrodes and/or a DC gate voltage V_g while recording I. The differential conductance $\mathrm{d}I/\mathrm{d}V$ is obtained by numerically differentiating I with respect to V.

A.2. MODELLING OF THE MAGNETIC EXCITATION SPECTRA

Spin exchange coupling in a 2-spin system: the neutral diradical In Fig. 4.2(a) we show fits of the $\mathrm{d}I/\mathrm{d}V$ excitation spectra in the 2-spin state of the PTM diradical molecule. These fits are obtained using the tunneling model introduced in Ref. [338]. Within the framework of this model we describe the system by two magnetic centers with $S = 1/2$ interacting through a Heisenberg exchange coupling J_{12}. Depending on the sign of J_{12} this 2-spin system can host two distinct ground states: a singlet $|S\rangle$ and a triplet $|T\rangle$. From the excitation spectra we find the triplet to be the excited state, which implies that the exchange coupling is antiferromagnetic (positive J_{12}). The excitation energy for the transition $|S\rangle \rightarrow |T\rangle$ equals the exchange coupling J_{12}, which we determine by the fit to be 4.65 meV. In order to account for the broadening of the excitations steps, we take an effective temperature of 1.4 K. The splitting of the steps with increasing magnetic field is well reproduced by a Zeeman interaction with a g-factor of 2. A small added linear slope corrects for a possible non-flat density of states in the electrodes.

The peaks on top of the excitation steps around ±5 mV can be reproduced in the model by two distinct mechanisms. The first being third-order tunneling processes, which yield peaks at bias voltages corresponding to the energy of the intermediate state in the scattering process (as described in ref. [338]). Alternatively, the peaks can be reproduced by including non-equilibrium effects, which follow from non-zero occupations of the excited states [338]. Upon including these effects, the height of the excitation peaks decreases with increasing energy, which is in accordance with the observed decreasing height of the split excitation steps towards higher bias. In contrast, third-order tunneling processes yield equal peak heights for the three split excitation steps. We conclude that the best agreement with the data is found by including scattering processes of second order only.

Spin-exchange couplings in a 3-spin system: the reduced diradical The excitation spectrum of the 3-spin state in the reduced diradical (see Fig. 4.4(a)) shows additional features which cannot be captured within the framework of the employed tunneling model. A zero-bias peak and a sharply peaked excitation step at 25 mV signal the presence of Kondo correlations, for which more involved theoretical treatments are necessary [340]. In addition, the strong bias asymmetry for energies above the excitation energies cannot be explained by second-order co-tunneling processes. The bias asymmetry is a characteristic feature of sequential electron tunneling (SET) with asymmetrically coupled electrodes. Taking these processes into account is beyond the scope of this analysis. Still, we can extract valuable information from the spectrum within the framework of a simpler model in order to make reasonable estimates of the three spin-exchange couplings of this charge state.

For the analysis of the spin excitation spectra we model the 3-spin system by the phenomenological Heisenberg-Dirac-Van Vleck (HDVV) Hamiltonian

$$\hat{\mathscr{H}}^{\mathrm{HDVV}} = J_{12}\hat{\mathbf{S}}_1 \cdot \hat{\mathbf{S}}_2 + J_{13}\hat{\mathbf{S}}_1 \cdot \hat{\mathbf{S}}_3 + J_{23}\hat{\mathbf{S}}_2 \cdot \hat{\mathbf{S}}_3 \tag{4.1}$$

where J_{ij} represents the spin-exchange coupling between spins i and j, and $\hat{\mathbf{S}}_i$ the spin operator of spin i. This system can host three different spin multiplets: one quartet ($|Q\rangle$) and two doublets ($|D_+\rangle$ and $|D_-\rangle$), which can be written as

$$|Q\rangle = \begin{cases} |\uparrow\uparrow\uparrow\rangle & m = \frac{3}{2} \\ (|\uparrow\uparrow\downarrow\rangle + |\uparrow\downarrow\uparrow\rangle + |\downarrow\uparrow\uparrow\rangle)/\sqrt{3} & m = \frac{1}{2} \\ (|\uparrow\downarrow\downarrow\rangle + |\downarrow\uparrow\downarrow\rangle + |\downarrow\downarrow\uparrow\rangle)/\sqrt{3} & m = -\frac{1}{2} \\ |\downarrow\downarrow\downarrow\rangle & m = -\frac{3}{2} \end{cases} \tag{4.2}$$

and

$$|D_\pm\rangle = \begin{cases} (\alpha^\pm_{123}|\uparrow\uparrow\downarrow\rangle + \alpha^\pm_{132}|\uparrow\downarrow\uparrow\rangle + |\downarrow\uparrow\uparrow\rangle)/\sqrt{(\alpha^\pm_{123})^2 + (\alpha^\pm_{132})^2 + 1} & m = \frac{1}{2} \\ (\alpha^\pm_{321}|\uparrow\downarrow\downarrow\rangle + \alpha^\pm_{312}|\downarrow\uparrow\downarrow\rangle + |\downarrow\downarrow\uparrow\rangle)/\sqrt{(\alpha^\pm_{321})^2 + (\alpha^\pm_{312})^2 + 1} & m = -\frac{1}{2} \end{cases} \tag{4.3}$$

where the coefficients $\alpha^\pm_{ijk}$ depend on the values of the exchange couplings:

$$\alpha^\pm_{ijk} = \frac{J_{ij} - J_{jk} \pm X}{J_{ik} - J_{ij}} \tag{4.4}$$

with

$$X = \sqrt{J_{12}^2 + J_{13}^2 + J_{23}^2 - J_{12}J_{13} - J_{12}J_{23} - J_{13}J_{23}}. \tag{4.5}$$

These equations show that the coefficients of the doublet eigenstates are functions of the three exchange couplings. This is in contrast with the quartet eigenstate of the three-spin system (equation 4.2) and the singlet and triplet eigenstates of the two-spin system, which only involve numerical coefficients. The J-dependence disappears once a symmetry is imposed, like $J_{12} = J_{23}$ or any permutation of this equality. Here, we treat the most general case, which remains valid for $J_{12} \neq J_{13} \neq J_{23}$. The eigenenergies that correspond to the spin eigenstates are given by

$$E_Q = (J_{12} + J_{13} + J_{23})/4 \tag{4.6}$$

and

$$E_{D_\pm} = -(J_{12} + J_{13} + J_{23})/4 \pm X/2. \tag{4.7}$$

We note that $X \geq 0$, from which it follows that $|D_-\rangle$ is always the doublet with the lowest energy. Given that the quartet appears as an excited state in the spin spectroscopy measurements (see Fig. 4.4), we conclude that $|D_-\rangle$ is the ground state of the 3-spin system and the observed multiplet excitations correspond to $|D_-\rangle \rightarrow |D_+\rangle$ and $|D_-\rangle \rightarrow |Q\rangle$. The excitation energies of these transitions follow from equations 4.6 and 4.7:

$$\Delta_1 \equiv E_{D_+} - E_{D_-} = X, \tag{4.8}$$

$$\Delta_2 \equiv E_Q - E_{D_-} = (J_{12} + J_{13} + J_{23})/2 + X/2. \tag{4.9}$$

The experimental values we find for Δ_1 and Δ_2 are 20 meV and 25 meV, respectively (see Fig. 4.4). By equating these values with equations 4.8 and 4.9 we obtain a system of two equations with three unknown variables (J_{12}, J_{13} and J_{23}). This system of equations is undetermined and its solutions lie on an ellipse in the parameter space spanned by the three exchange couplings as represented in Fig. 4.5). Without additional knowledge about the system we cannot discern between these different solutions.

We can, however, conclude that no symmetric solution, i.e., $J_{12} \approx J_{13} \approx J_{23}$, is available. This suggests that the added electron in the reduced charge state does not go to the position of the third radical center in the structurally equivalent PTM triradical. Moreover, if we assume that the exchange coupling of the neutral charge state remains unchanged upon charging ($J_{12} \approx 5$ meV), the solution set reduces to a single solution in which the added electron is asymmetrically coupled to the two radical centers ($J_{13} \approx 2$ meV and $J_{23} \approx 23$ meV, green square in Fig. 4.5) and is therefore likely to be located on a ligand attached to one of the two radical centers. Two other characteristic scenarios within the solution set (red hexagon and orange circle) are highlighted in Fig. 4.5.

Additional information can be gained from the $\mathrm{d}I/\mathrm{d}V$ spectra by analyzing the relative step height of the two spin multiplet excitations. The intensity (step height) of a transition $|\psi_i\rangle \rightarrow |\psi_f\rangle$ in the $\mathrm{d}I/\mathrm{d}V$ spectrum is proportional to the modulus squared of its transition matrix element [338]:

$$|M_{if}|^2 = \frac{1}{2}|\langle\psi_f|\hat{S}_-^{(j)}|\psi_i\rangle|^2 + \frac{1}{2}|\langle\psi_f|\hat{S}_+^{(j)}|\psi_i\rangle|^2 + |\langle\psi_f|\hat{S}_z^{(j)}|\psi_i\rangle|^2. \tag{4.10}$$

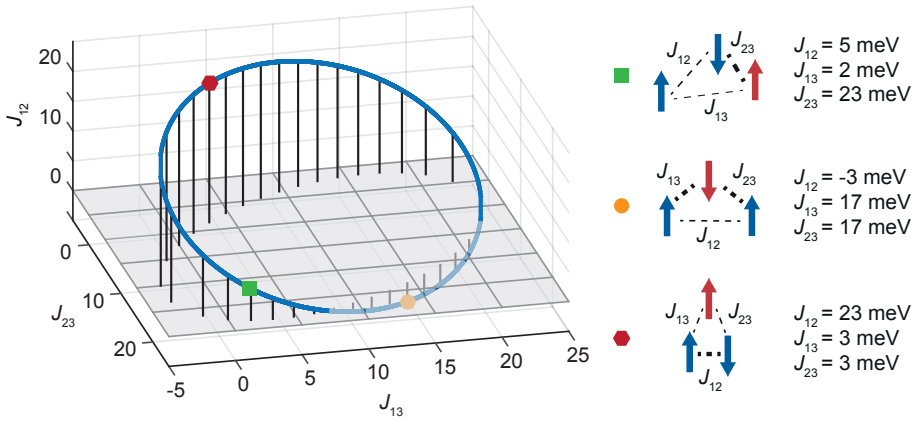

Figure 4.5: Solution set (blue ellipse) of equations 4.8 and 4.9 in the parameter space spanned by the exchange couplings J_{12}, J_{13} and J_{23} for the experimental values $\Delta_1 = 20$ meV and $\Delta_2 = 25$ meV. Three characteristic scenarios are highlighted: (1, green square) Coupling J_{12} remains unchanged upon charging and the added spin 3 couples asymmetrically to spins 1 and 2. (2, orange circle) One coupling is weakly ferromagnetic and the other two couplings are strongly antiferromagnetic and of similar strength. (3, red hexagon) Coupling J_{12} increases significantly upon charging and the added spin 3 is weakly coupled to both spin 1 and 2.

where $S_-^{(j)}$, $S_+^{(j)}$ and $S_z^{(j)}$ are the spin operators of spin j. In this expression, only spin-dependent second-order tunneling (co-tunneling) through spin j is taken into account. Given that the coefficients of the doublet eigenstates depend on the values of the three exchange couplings (see equations 4.3 to 4.5) we can express the matrix elements of the transitions $|D_-\rangle \rightarrow |D_+\rangle$ and $|D_-\rangle \rightarrow |Q\rangle$ in terms of J_{12}, J_{13} and J_{23}. Accordingly, we calculate the expected relative step height for the combinations of exchange couplings that give the observed excitation energies (the solutions shown in Fig. 4.5). Table 4.1 lists the relative step height for three combinations of exchange couplings.

J_{12}	J_{13}	J_{23}	$\lvert M_{D_-\rightarrow D_+}\rvert^2 / \lvert M_{D_-\rightarrow Q}\rvert^2$
5	2	23	2
-3	17	17	1.5
23	3	3	0.5

Table 4.1: Ratio of step heights $D_- \rightarrow D_+$ and $D_- \rightarrow Q$ excitations for different combinations of exchange couplings.

For the estimation of the step heights from the experimental spectrum we focus on the negative bias voltage side, where no contributions from Kondo correlations are visible and the flat excitation steps are indicative of second-order tunneling processes only. We estimate the ratio of the step heights of the two excitations to be ~2, for which the present analysis favors the first configuration in Table 4.1. Two spins are strongly coupled to each other (~23 meV), whereas the third spin is relatively weakly coupled (2-5 meV) to the former two. This is consistent with the scenario we proposed before, in which $J_{12} \approx 5$ meV as in the 2-spin state, $J_{13} \approx 2$ meV and $J_{23} \approx 23$

meV.

The contribution of elastic co-tunneling however, which we have neglected so far, is in this configuration one order of magnitude larger than the inelastic co-tunneling steps, which is not what we observe in the experimental spectrum. In fact, if we consider transport through only one spin there is no combination of exchange couplings that reproduces the measurements. Only by introducing an interfering channel through a second spin, both the ratio of the inelastic step heights, as well as the observed elastic co-tunneling contribution match the experimental spectrum. The transport through this three-spin system occurs therefore through at least two interfering channels.

A.3. DFT CALCULATIONS

Methods The calculations in this section are performed within the spin unrestricted Density Functional Theory (DFT) formalism, using the well-known B3LYP [341] hybrid functional and the Pople-type basis set 6-31G(d,p) [342–344]for all atoms, as implemented in the Gaussian09_*d* [306] suite of programs.

Throughout this work, we have assumed a model spin Hamiltonian defined as $\hat{H}^{HDVV} = \Sigma_{\langle i,j\rangle} J_{ij}\mathbf{S}_i \cdot \mathbf{S}_j$, where a negative J value indicates a ferromagnetic interaction of the unpaired electrons, whereas a positive J denotes an antiferromagnetic interaction. This corresponds with a situation in which both unpaired electrons are aligned parallel and antiparallel, respectively. The calculation of the magnetic coupling constants in the neutral diradical molecule have been done using the formula proposed by Yamaguchi [345–347], where the triplet (T) spin adapted state is approximated by a high-spin Kohn-Sham determinant with two unpaired electrons with parallel spins and the singlet (S) spin adapted state by a broken symmetry (BS) solution [348–350]. In this way, the vertical DFT triplet-singlet gap is approximately twice the energy difference between the high spin and the BS solutions,

$$\Delta_{vert} = E_S - E_T = \frac{2\,(E_{BS} - E_T)}{\langle S_T^2\rangle - \langle S_{BS}^2\rangle} \tag{4.11}$$

where E_S, E_T and E_{BS} are the energies of the singlet, triplet and broken symmetry states, respectively. The denominator contains the expectation value of the square of the total spin operator for the triplet and BS solutions (close to 2.000 and 1.000, respectively).

EXPLORATION OF DISTORTIONS LEADING TO GROUND STATE MULTIPLICITY REVERSAL

For the most extensively investigated sample, the ground state is a singlet state (see Fig. 4.2), as opposed to the triplet ground state of the same molecule in frozen solution [336]. Thus, it is reasonable to think that the reversal in the ground state multiplicity of the molecule comes from its interaction with the electrodes [247]. In the following, we study some sensible potential energy surfaces (PES) in order to check whether a torsion of the main dihedral angles also lead to a change in the sign of the magnetic exchange coupling of the molecule.

Definition of the D6 and D24 dihedral angles The z-matrix used to investigate the effect of the distortion on the electronic structure of the molecule is presented in Table 4.2. This matrix contains the coordinates of each element, the bond lengths, the

planar angles and the dihedral angles, respectively indicated in the table as Length, Angle and D-angle.

Table 4.2: Z-matrix corresponding to the PTM diradical.

Atom		Length		Angle		D-angle	
C							
C	1	B1					
C	2	B2	1	A1			
C	3	B3	2	A2	1	D1	0
C	4	B4	3	A3	2	D2	0
C	5	B5	4	A4	3	D3	0
C	6	B6	5	A5	4	D4	0
C	4	B7	3	A6	2	D5	0
C	7	B8	6	A7	5	D6	0
C	9	B9	7	A8	6	D7	0
C	9	B10	7	A9	6	D8	0
C	10	B11	9	A10	7	D9	0
C	11	B12	9	A11	7	D10	0
C	13	B13	11	A12	9	D11	0
C	7	B14	6	A13	5	D12	0
C	15	B15	7	A14	6	D13	0
C	15	B16	7	A15	6	D14	0
C	16	B17	15	A16	7	D15	0
C	17	B18	15	A17	7	D16	0
C	19	B19	17	A18	15	D17	0
C	8	B20	4	A19	3	D18	0
C	21	B21	8	A20	4	D19	0
C	21	B22	8	A21	4	D20	0
C	22	B23	21	A22	8	D21	0
C	23	B24	21	A23	8	D22	0
C	24	B25	22	A24	21	D23	0
C	8	B26	4	A25	3	D24	0
C	27	B27	8	A26	4	D25	0
C	27	B28	8	A27	4	D26	0
C	28	B29	27	A28	8	D27	0
C	29	B30	27	A29	8	D28	0
C	31	B31	29	A30	27	D29	0
Cl	5	B32	4	A31	3	D30	0
Cl	1	B33	2	A32	3	D31	0
Cl	3	B34	2	A33	1	D32	0
Cl	17	B35	15	A34	7	D33	0
Cl	16	B36	15	A35	7	D34	0
Cl	18	B37	16	A36	15	D35	0
Cl	20	B38	19	A37	17	D36	0
Cl	19	B39	17	A38	15	D37	0
Cl	10	B40	9	A39	7	D38	0
Cl	12	B41	10	A40	9	D39	0
Cl	14	B42	13	A41	11	D40	0
Cl	13	B43	11	A42	9	D41	0
Cl	11	B44	9	A43	7	D42	0
Cl	22	B45	21	A44	8	D43	0
Cl	24	B46	22	A45	21	D44	0
Cl	26	B47	24	A46	22	D45	0
Cl	25	B48	23	A47	21	D46	0
Cl	23	B49	21	A48	8	D47	0
Cl	29	B50	27	A49	8	D48	0

Cl	31	B51	29	A50	27	D49	0
Cl	32	B52	31	A51	29	D50	0
Cl	30	B53	28	A52	27	D51	0
Cl	28	B54	27	A53	8	D52	0
C	2	B55	1	A54	6	D53	0
H	56	B56	2	A55	1	D54	0
C	56	B57	2	A56	1	D55	0
C	58	B58	56	A57	2	D56	0
C	58	B59	56	A58	2	D57	0
C	59	B60	58	A59	56	D58	0
C	60	B61	58	A60	56	D59	0
C	61	B62	59	A61	58	D60	0
C	56	B63	2	A62	1	D61	0
C	64	B64	56	A63	2	D62	0
C	64	B65	56	A64	2	D63	0
C	65	B66	64	A65	56	D64	0
C	66	B67	64	A66	56	D65	0
C	68	B68	66	A67	64	D66	0
Cl	59	B69	58	A68	56	D67	0
Cl	61	B70	59	A69	58	D68	0
Cl	63	B71	61	A70	59	D69	0
Cl	62	B72	60	A71	58	D70	0
Cl	60	B73	58	A72	56	D71	0
Cl	65	B74	64	A73	56	D72	0
Cl	66	B75	64	A74	56	D73	0
Cl	68	B76	66	A75	64	D74	0
Cl	69	B77	68	A76	66	D75	0
Cl	67	B78	65	A77	64	D76	0

B1	1.41110046	B2	1.40623962	B3	1.41978805	B4	1.41343770
B5	1.41378455	B6	1.48223807	B7	1.48498927	B8	1.48361690
B9	1.41721731	B10	1.41670027	B11	1.40178991	B12	1.40189910
B13	1.40354201	B14	1.48368924	B15	1.41744118	B16	1.41673432
B17	1.40192059	B18	1.40187313	B19	1.40342067	B20	1.48525082
B21	1.41708194	B22	1.41726283	B23	1.40217844	B24	1.40189633
B25	1.40342291	B26	1.48306291	B27	1.41785776	B28	1.41636146
B29	1.40183323	B30	1.40153259	B31	1.40341220	B32	1.74831983
B33	1.75561754	B34	1.74516520	B35	1.74009318	B36	1.74212938
B37	1.73607710	B38	1.73232164	B39	1.73561129	B40	1.74188847
B41	1.73600249	B42	1.73222137	B43	1.73577108	B44	1.74115301
B45	1.74085784	B46	1.73592562	B47	1.73234834	B48	1.73601725
B49	1.74222854	B50	1.74094026	B51	1.73597741	B52	1.73221535
B53	1.73605932	B54	1.74195685	B55	1.54965667	B56	1.08968451
B57	1.54689301	B58	1.41219813	B59	1.40887951	B60	1.40232451
B61	1.40646844	B62	1.40122086	B63	1.54578100	B64	1.41279197
B65	1.40825787	B66	1.40241982	B67	1.40663455	B68	1.40125347
B69	1.74947567	B70	1.73562338	B71	1.73352162	B72	1.73644598
B73	1.74098254	B74	1.74947769	B75	1.73996828	B76	1.73617894
B77	1.73367965	B78	1.73568834	A1	116.15200149	A2	123.62176612
A3	116.42678592	A4	123.62912345	A5	121.96838752	A6	122.23683276
A7	120.18348452	A8	121.69331750	A9	121.67856645	A10	121.95451174
A11	122.01207771	A12	119.87916212	A13	120.75548851	A14	121.72892671
A15	121.70896091	A16	121.99637777	A17	122.04436666	A18	119.89860715
A19	119.38617092	A20	121.63791729	A21	121.72174332	A22	121.96117044
A23	121.96436358	A24	119.91786475	A25	121.71324089	A26	121.61284695
A27	121.89800608	A28	122.01062097	A29	122.11887953	A30	119.89600982
A31	117.95303377	A32	118.20814329	A33	119.05104219	A34	120.02776618
A35	120.16314170	A36	120.55129186	A37	120.19896052	A38	120.51927767

A39	120.14781038	A40	120.53217287	A41	120.20574392	A42	120.54829188
A43	120.03862873	A44	120.11485682	A45	120.52027907	A46	120.20842394
A47	120.54424116	A48	120.20302906	A49	119.97894621	A50	120.53866349
A51	120.22459957	A52	120.53526188	A53	120.15692109	A54	117.23526484
A55	100.40821185	A56	118.09905708	A57	117.20805526	A58	126.19194662
A59	122.66565118	A60	121.84346099	A61	119.52318213	A62	116.43697742
A63	117.17076063	A64	126.18522521	A65	122.53064102	A66	121.79272579
A67	120.19024546	A68	119.90034361	A69	120.74960101	A70	120.23794434
A71	120.47356697	A72	121.12888265	A73	120.02825037	A74	121.07499802
A75	120.46948734	A76	120.39302407	A77	120.72713711	D1	-0.95174211
D2	2.54533592	D3	-2.07628012	D4	-179.63885168	D5	-176.86447029
D6	48.61854578	D7	-129.82217583	D8	50.77587796	D9	-178.94574921
D10	179.91664749	D11	-0.97285620	D12	-131.34695591	D13	-130.13844772
D14	50.52473707	D15	-178.83247176	D16	179.84521993	D17	-1.00111356
D18	129.39427352	D19	-50.83335062	D20	129.88663290	D21	179.97133298
D22	179.13611280	D23	0.96700621	D24	-50.35746961	D25	130.29156719
D26	-50.54563294	D27	178.21636742	D28	-179.24456123	D29	0.89355281
D30	170.68688686	D31	175.06115726	D32	-179.78679052	D33	3.68286349
D34	5.05661448	D35	-179.92566475	D36	-179.51017760	D37	-179.88190289
D38	4.91389451	D39	-179.86300760	D40	-179.48979924	D41	-179.80027517
D42	3.84869270	D43	-4.17958274	D44	179.67908609	D45	179.60282890
D46	179.75251817	D47	-4.53343892	D48	-2.74541147	D49	179.84563170
D50	179.37868184	D51	-179.92244745	D52	-5.88960332	D53	-175.86468260
D54	35.85665666	D55	143.36326213	D56	-72.66062300	D57	113.04533645
D58	-174.83191476	D59	173.09710148	D60	1.15846333	D61	-71.55453258
D62	142.70510604	D63	-33.03611950	D64	-176.18360822	D65	174.70505986
D66	1.14056636	D67	4.92313696	D68	-179.54327640	D69	179.09651092
D70	-179.34785660	D71	-9.91628213	D72	3.38993554	D73	-7.92182933
D74	-179.58801802	D75	179.67427914	D76	-179.63358334		

The dihedral angles D6 and D24, as schematically drawn in Fig. 4.6, are used to perform the distortion. Note that the presented values correspond to the stationary point in the PES of the triplet state (the absolute minimum) and these dihedral angles define the relative position of the carbon-centered radical with the shared central ring.

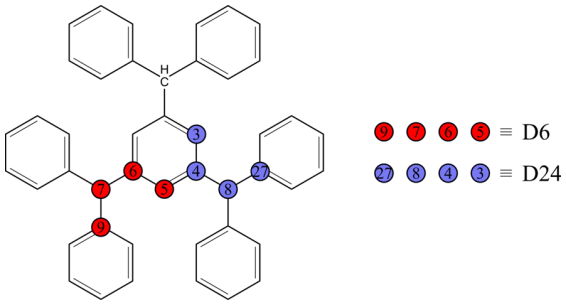

Figure 4.6: Graphical representation of structural parameters modified. The numbers correspond to the actual labels used in the z-matrix above. Note that the Chlorine atoms are omitted for the sake of clarity.

Now, in order to roughly simulate one of the possible impacts of the electrodes on these molecules, we undergo an investigation of the energies of the triplet and broken symmetry solutions at a series of distorted points. The strategy followed consists in modifying the D6 and D24 values, and allow a relaxation of the rest of structural

parameters for the triplet state. Once the restricted optimization has located a stationary point (keeping D6 and D24 fixed), this geometry is used to perform a single point calculation of the broken symmetry solution. With these two states and using Yamaguchi's formula, one can calculate the magnetic coupling constant at each geometry.

Energetic cost and magnetic coupling constant *vs* distortion The different points in the PES of the triplet, their corresponding absolute energies, the associated energetic cost to undergo the distortion from the absolute minimum and the extracted magnetic coupling constants are displayed in Table 4.3.

Table 4.3: Energy and magnetic coupling constants for different points in the PES of the triplet

D6, D24	State	Energy (a.u.)	$\langle S^2 \rangle$	ΔE (Kcal/mol)	J (meV)
35,-35	T	-16901.5716995	2.052	2.4	
	BS	-16901.5698462	1.0186		-97.6
40,-40	T	-16901.5738229	2.049	1.1	
	BS	-16901.5723603	1.0193		-77.3
45,-45	T	-16901.5751313	2.047	0.3	
	BS	-16901.5739896	1.0198		-60.5
48.62,-50.36	T	-16901.5755320	2.045	0.0	
	BS	-16901.5746406	1.020		-47.4
55,-55	T	-16901.5749341	2.043	0.4	
	BS	-16901.5743061	1.0206		-33.4
60,-60	T	-16901.5733634	2.042	1.4	
	BS	-16901.5729504	1.0209		-22.0
65,-65	T	-16901.5707591	2.041	3.0	
	BS	-16901.5705208	1.0212		-12.7
70,-70	T	-16901.5670913	2.040	5.3	
	BS	-16901.5669974	1.0220		-5.0
75,-75	T	-16901.5623530	2.040	8.3	
	BS	-16901.5623853	1.0231		1.7

The graphical representation of these values is presented in Fig. 4.7. We observe a similar tendency as in the previously reported PTM triradical [247]: a relatively low energy distortion of the molecule can invert the sign of the exchange coupling from ferro- to antiferromagnetic.

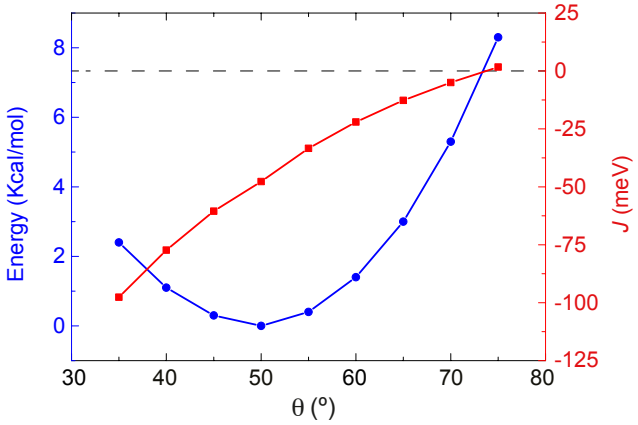

Figure 4.7: Graphical representation of the energetic cost and associated magnetic coupling constant at each restricted optimized geometry. Data points are extracted from Table S3.

Correlation between ground state reversal and HOMO-LUMO gap The experimental results discussed in the main text also indicate that the measured sample can be reversibly charged, passing from the neutral diradical to a reduced (anionic) diradical species which maintains the quartet and two doublet magnetic states in the low-lying region of the spectrum. This charging is in contrast to the monoradical [33] and triradical [247] suggests a lower HOMO-LUMO gap in the diradical case potentially induced by the distortion of the molecule as a consequence of the interaction with the electrodes. However, for both the triplet and BS solutions in each of the points discussed in Fig. 4.7, the HOMO-LUMO gap keeps a constant value of about 2 eV.

Thus, we performed a series of more extended distortions where the rest of the structural parameters were not relaxed. Again, we calculated the triplet and BS solutions for each geometry and investigated the impact on the HOMO-LUMO gap. We have found four differential behaviours (detailed in Table 4.4): first, one in which the distortions lead to a singlet ground state but leave intact the HOMO-LUMO gap; second, a situation in which the distortions reduce the HOMO-LUMO gap but result in even larger energy differences between the ground triplet and excited BS solutions; third, corresponding to the case that would explain the experimental results, where the distortion concomitantly stabilizes the BS state as the ground state and reduces the HOMO-LUMO gap. Finally, we have also observed that if the distortions are too large, to the point of having very close Cl···Cl or Cl···π-system interactions, the nature of the magnetic states is not maintained and the spin density is no longer dominated by the carbon-based radical centres (see Figure 4.8). In this case, the HOMO-LUMO gap of the much more stable BS solutions is reduced to 0.5 eV. However, since the experimental data clearly resolves the singlet-triplet spectrum, the latter case is discarded as a plausible explanation.

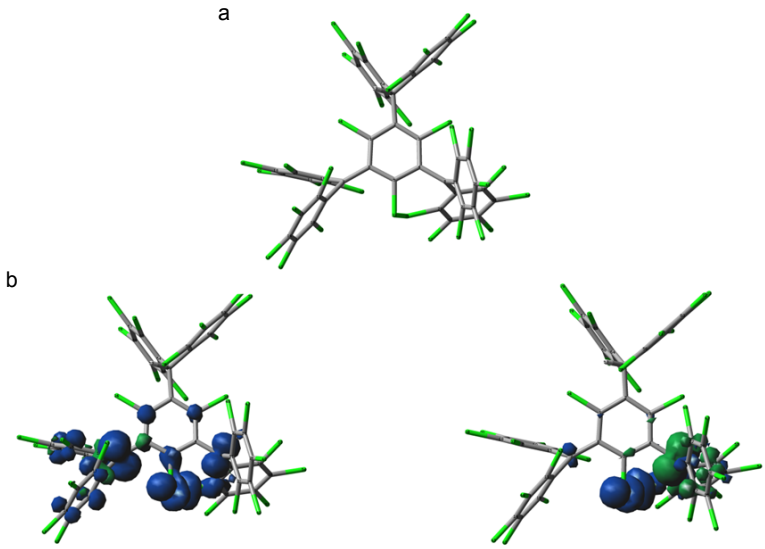

Figure 4.8: Representation of (a) structure and (b) spin densities of triplet and BS, respectively, in the situation where Cl···Cl destroys the nature of the magnetic states

Distortion along other dihedral angles Using the same definition of the z-matrix as the one presented in Table 4.2, we investigated several other PES by modifying a series of different structural parameters. Figure 4.9 depicts the new set of parameters that have been considered.

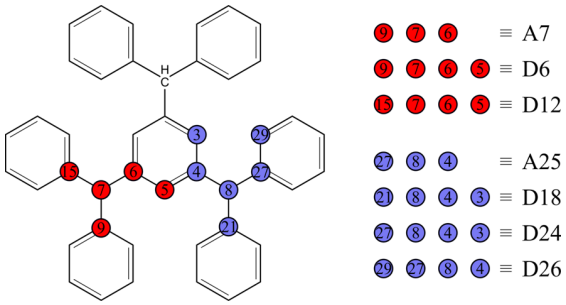

Figure 4.9: Graphical representation of structural parameters modified. The numbers correspond to the actual labels used in the z-matrix above. Note that the Chlorine atoms are omitted for the sake of clarity.

Magnetic coupling constant and HOMO-LUMO gap *vs* distortion Table 4.4 presents the different PES investigated with the corresponding values for each structural parameter modified, the energy difference between the triplet and BS solutions and the calculated HOMO-LUMO gap at each geometry. As evidenced above, a relationship between distortion and HOMO-LUMO gap is present, although it is not simple. The lowest value for the HOMO-LUMO gap that we have obtained is 1.5 eV for a BS ground state. Despite not being small enough to account for the capacity of

the sample to reversibly charge, these results clearly indicate that the HOMO-LUMO gap can be modified by simple structural distortions. And despite not having located the particular region in the PES of the molecule where that could happen, the presented results establish that this can indeed be achieved.

Table 4.4: Chart describing ΔE_{T-BS} (meV) and $\Delta E_{HOMO-LUMO}$ (eV) as a function of the structural parameters' label (according to Fig. 4.9) and values. Note that a positive value of ΔE_{T-BS} implies a more stable BS solution. The first and second entries in the $\Delta E_{HOMO-LUMO}$ column stand for the values calculated for triplet and BS, respectively. The last row indicates the values of modified parameters at the absolute minimum.

Label	Values	ΔE_{T-BS} (meV)	ΔE_{H-L} (eV)
D6, D24	10, -50.36	-39.4	1.9 / 2.1
	30, -50.36	-32.2	2.2 / 2.3
	50, -50.36	-22.8	2.3 / 2.4
	70. -50.36	-13.0	2.3 / 2.5
	90, -50.36	-5.1	2.3 / 2.4
	10, -90	-8.6	1.8 / 1.9
	30, -90	-2.6	2.1 / 2.2
	50, -90	+1.1	2.2 / 2.4
	70. -90	+2.9	2.2 / 2.4
	90, -90	+3.7	2.2 / 2.4
D6, D12, D18, D24	-180, 0, 90, -90	-5.1	1.1 / 1.1
	-150, 30, 90, -90	-2.1	1.6 / 1.6
	-120, 60, 90, -90	+14.5	1.7 / 1.8
	-90, 90, 90, -90	+43.2	1.9 / 2.2
	-0, -180, 90, -90	-4.7	1.1 / 1.1
A7, D6, D12, D18, D24	150, -48.6, -131.3, 90, -90	+9.5	1.7 / 1.7
	140, -48.6, -131.3, 90, -90	+9.2	1.7 / 1.8
	120, -48.6, -131.3, 90, -90	+7.3	1.7 / 1.7
	100, -48.6, -131.3, 90, -90	+2.2	1.5 / 1.5
	90, -48.6, -131.3, 90, -90	-6.7	1.3 / 1.3
A7, A25, D6, D12, D18, D24	150, 130, -48.6, -131.3, 90, -90	+4.2	2.0 / 2.1
	150, 140, -48.6, -131.3, 90, -90	+2.6	2.1 / 2.1
	150, 150, -48.6, -131.3, 90, -90	+1.6	2.1 / 2.1
	120, 90, -48.6, -131.3, 90, -90	-31.9	1.1 / 1.0
	120, 150, -48.6, -131.3, 90, -90	+0.3	2.2 / 2.3
	90, 90, -48.6, -131.3, 90, -90	-207	1.1 / 1.1
	90, 150, -48.6, -131.3, 90, -90	-4.6	2.1 / 2.1

A7 = 120.2; A25 = 121.7; D6 = 48.6; D12 = -131.3; D18 = 129.4; D24 = -50.4; D26 = -50.5

SPIN DENSITY AND GEOMETRY OF THE NEUTRAL AND REDUCED MOLECULE

We have also investigated the effect of charging on the spin and geometry of the gas-phase molecule.

Fixing the torsion angle to $\theta = 75°$, we calculate the spin densities of the neutral and reduced diradical. At this torsion angle, the former is in the singlet ground state (see Figure 4.7) while the latter in the doublet ground state. The result for the neu-

tral molecule is shown in Figure 4.10(a): one radical centre presents a majority of α-density (blue) and the other a majority of β-density (green) with both densities localised on their respective pairs of external phenyl rings. The result for the reduced form at the neutral geometry is shown in Figure 4.10(b). Here, both radical centres present the same density, and the inner phenyl ring presents a comparatively higher density than in the neutral case. This can be understood as a consequence of the spin-alternation rule [1] in the inner ring. According to these results, one would expect the extra electron to be located in the inner phenyl ring.

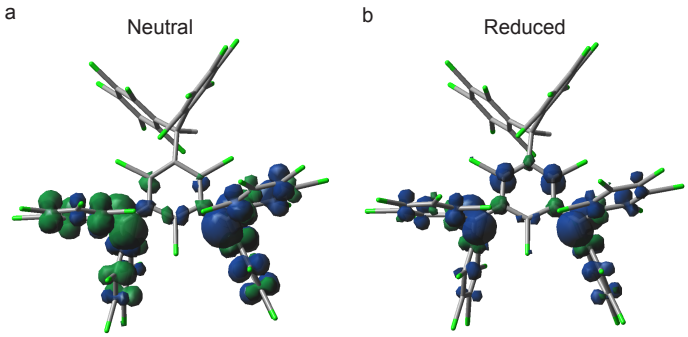

Figure 4.10: Spin density of the gas-phase neutral and reduced molecule at a torsion angle of 75°. According to this calculation, the added charge is located on the central phenyl ring.

In order to compare the geometry of the neutral and reduced diradical, we proceed by characterizing the stationary minima of both forms in gas phase. Figure 4.11 presents the overlapped structures after imposing one into another by ensuring that the rotation minimizes the RMSD value, following the algorithm proposed by Kabsch [351, 352], and implemented by Kroman and Bratholm [353]. The optimization

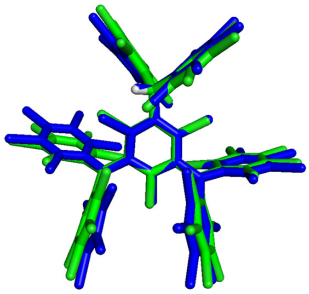

Figure 4.11: Structural comparison of optimized neutral (green) and anionic (blue) forms, as predicted by B3LYP.

of the reduced diradical (three spins) has been performed following the same method used to optimize the neutral diradical. An attempt to improve the basis set to include

[1] A consequence of Lieb theorem for non-alternating lattices according to which the configuration of lower energy would present an alternation of spins such that each centre with α-density is surrounded by centres of β-density, and vice versa

diffuse functions turned out not feasible due to memory problems(≈ 1700 basis functions).

The obtained Kabsch RMSD value is 0.674 Å which indicates that there is a significant difference between both structures. This is an indication that depending on how the molecule sits between the electrodes, it might favor the charging process just because the geometry is more similar to the one that the anion would adopt in the gas phase.

5

EXCHANGE COUPLING INVERSION IN A HIGH-SPIN TRIRADICAL MOLECULE

"What is time?" If no one asks me, I know;
but if I want to explain it to someone who asks, then I do not know[1].

Saint Augustine of Hippo

The magnetic properties of a nanoscale system are inextricably linked to its local environment. In ad-atoms on surfaces and inorganic layered structures the exchange interactions result from the relative lattice positions, layer thicknesses and other environmental parameters. In this chapter, we report on a sample-dependent sign inversion of the magnetic exchange coupling between the three unpaired spins of an organic triradical molecule embedded in a three-terminal device. This ferro-to-antiferromagnetic transition is due to structural distortions and results in a high-to-low spin ground state change in a molecule traditionally considered to be a robust high-spin quartet. Moreover, the flexibility of the molecule yields an in-situ electric tunability of the exchange coupling via the gate electrode. The findings open a route to the controlled reversal of the magnetic states in organic molecule-based nanodevices by mechanical means, electrical gating or chemical tailoring.

Parts of this chapter have been published in Nano Letters **16**, 2066 – 2071 (2016) by R. Gaudenzi, E. Burzurí, D. Reta, I. de P.R. Moreira, S. Bromley, C. Rovira, J. Veciana, H.S.J. van der Zant.

[1] Quid ergo est tempus? Si nemo ex me quaerat, scio; Si quaerente explicare velim, nescio.

1. INTRODUCTION

Magnetism at the nanoscale is often determined by the local environment: the sensitivity of the exchange coupling to the spatial arrangement and its dependence on the interactions between sandwiching layers, spin interfaces, ligands, neighbouring atoms or substrate is well-established. In most cases, these interactions lead to an increase or decrease of the strength of the local magnetism [46, 286, 305, 327, 354, 355]. Of special interest is the situation in which the sign of the exchange interaction reverses, leading to a transition from ferromagnetic to antiferromagnetic coupling (or vice versa). Altering the relative positions of the atoms in Fe dimers [356] or varying the thickness of the interlayer in Fe/Cr/Fe structures [357, 358] can, for instance, trigger such an inversion.

Owing to their intrinsic flexibility, single molecules form an interesting system to control this exchange reversal. In addition, as building blocks of molecule-based materials, knowledge on variations of the magnetic properties at the individual-molecule scale reveals effects that might go unseen in bulk. A previous work reports variations of the spin excitation energies in single molecules on metallic surfaces [46], but a ferro-to-antiferromagnetic exchange coupling inversion has never been demonstrated. In view of molecular spintronics applications, such a phenomenon is of particular interest in high-spin all-organic molecules - in which magnetism is not connected to the presence of metal ions [33, 283–285] - because of their favorable spin lifetimes [278].

Here, via inelastic electron tunneling spectroscopy (IETS), we map the magnetic states of individual neutral and stable organic triradical molecules. The all-organic molecule of our study exhibits, in solution, a strong ferromagnetic exchange interaction between its three unpaired electrons. Through the observation of distinct magnetic spectra in different samples, we infer that the exchange coupling significantly decreases in magnitude and can even turn antiferromagnetic when the molecule is embedded in a solid-state device. We attribute the reduction and the sign reversal to small deformations induced by the local environment of the junction and support this hypothesis with theoretical calculations. The analysis demonstrates that the distortions only modify the exchange but not the robust radical character of the three centers, in agreement with previous studies on monoradicals [33].

We use a 2,4,6-hexakis(pentachlorophenyl) mesityltriyl radical molecule [336, 359] sandwiched between two electromigrated [305] gold leads to construct our molecular junction, as schematically depicted in Fig. 5.1b (see Appendix A.1 for additional information on the molecule and the junction preparation). The molecule, shown in Fig. 5.1(a), is a neutral triradical with three unpaired electrons on the three methyl carbon atoms. Each one of these atoms, with three chlorinated phenyl rings surrounding it in a propeller-like conformation, forms one of the three elementary radical subunits. The central mesitylene ring is common to the three subunits and is used to magnetically interconnect them. Two of the propellers have the same sense of rotation while the third rotates with an opposite sense, conferring the molecule a C_2 symmetry. Owing to this architecture and particular orbital topology [360–362], the three radical electrons lie in three distinct non-disjoint, quasi-degenerate, non-bonding singly-occupied molecular orbitals (SOMOs) exhibiting a strong exchange interaction. Previous experiments [336] have demonstrated a robust high-spin quartet (S_Q = 3/2) ground state with a low-spin doublet (S_D = 1/2) excited state well-

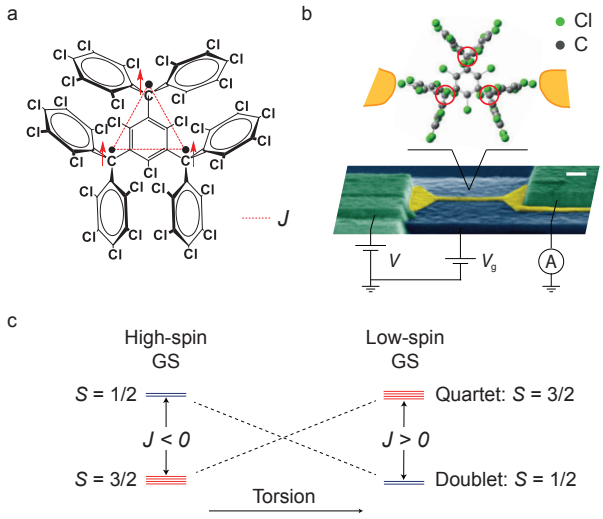

Figure 5.1: **The molecule, the device and the exchange coupling inversion mechanism.** (a) Molecular structure of a triradical organic molecule with a C_2 symmetry: the three radical centers, located on the three methyl carbon atoms, are each surrounded by three twisted perchlorinated phenyl rings. The three unpaired electrons are coupled through an exchange interaction, J, schematically represented by red dashed lines. (b) Scanning-electron-microscope micrograph (100-nm scale bar, false color) of the gold nanowire on a AuPd/Al_2O_3 gate. The molecular junction is created with the molecule bridging the nanogap formed during electromigration. (c) Schematics of the exchange coupling sign flipping mechanism: a torsion applied to the molecule increases the exchange coupling from negative (ferro-) to positive values (anti-ferromagnetic) through zero inducing a change from the $S = 3/2$ high-spin ground state (GS) to a $S = 1/2$ low-spin ground state.

separated in energy ($|E(|Q\rangle) - E(|D\rangle)| \gg k_B T$). This characterization is, however, performed in the solid state (crystal) and frozen solution, where the molecules adopt the thermodynamically most stable conformation with a C_2 symmetry.

2. RESULTS AND DISCUSSION

Electron transport spectroscopy on sample A is presented in Fig. 5.2 as a function of bias voltage and magnetic field B. Four well-defined conductance steps, symmetrically placed at positive and negative bias, are visible in the dI/dV color map of Fig. 5.2(a) and extracted spectra in Fig. 5.2(b.) The low- and high-energy steps are located around ±0.1 meV and ±2 meV at $B = 0$ T and shift linearly and parallel to each other as the magnetic field is increased. The small low-bias step visible at $B = 0$ T signals the presence of a small zero-field splitting (≈ 0.15 meV).

Each finite bias step is associated with the opening of an inelastic electron current channel via an excited state of the molecule. When spin excited states are involved, the steps' position in energy as a function of magnetic field provides a means to read out the molecule's energy spectrum. In the present case, the spectrum is composed of the eigenstates $|\mathbf{S}, S_z\rangle$ of the spin Hamiltonian:

$$\hat{\mathscr{H}} = \frac{J}{2}\left(\mathbf{S}^2 - \sum_{i=1}^{3}\mathbf{S}_i^2\right) + g\mu_B B_z S_z - D S_z^2, \tag{5.1}$$

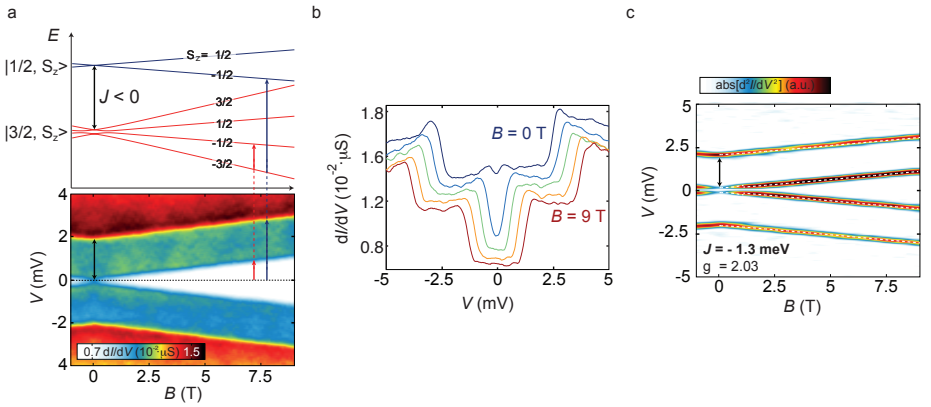

Figure 5.2: **Ferromagnetic exchange coupling J.** (color online) (a) $\mathrm{d}I/\mathrm{d}V$ map (below) measured on sample A as a function of bias voltage and magnetic field. The energy splitting between the low- and the high-energy step is constant in magnetic field and marked by a black double arrow. Above, the energy level scheme of a spin-3/2 system with a ferromagnetic exchange coupling ($J < 0$) and a small anisotropy parameter ($D = 0.06$ meV) as a function of magnetic field. Red and blue arrows indicate the allowed first-order spin-flip processes with $\Delta S_z = \pm 1$ to which the observed steps in $\mathrm{d}I/\mathrm{d}V$ are ascribed. (b) $\mathrm{d}I/\mathrm{d}V$ spectra extracted from the map in (a) with a spacing of $\Delta B = 1.8$ T starting from 0 T (offset for clarity). The low-energy excitation exhibits a zero-field splitting of about 0.1 meV. (c) Absolute value $|\mathrm{d}^2I/\mathrm{d}V^2|$ of the map in (a). The dashed lines superimposed to the experimental data are the fit to the Hamiltonian of equation(1) with $J = -1.3$ meV ($E(|Q\rangle) - E(|D\rangle) = 3/2J$) and $g = 2.03$. The zero-field spitting is clearly visible. All measurements are taken at $T \approx 70$ mK.

where $\mathbf{S}_i$ denotes the 1/2-spin vectors of the three radical electrons, $\mathbf{S} \equiv \sum_{i=1}^{3} \mathbf{S}_i$ and S_z the total spin and spin projection operators, respectively, and D the uniaxial anisotropy parameter. The second-order spin excitations induced by the tunneling electrons obey the selection rules $\Delta S_z = 0, \pm 1$. Within this framework, we can respectively assign the low- and high-bias steps seen in Fig. 5.2(a) (bottom) to the two spin transitions $|3/2, -3/2\rangle \rightarrow |3/2, -1/2\rangle$ and $|3/2, -3/2\rangle \rightarrow |1/2, -1/2\rangle$ between states of the molecular spectrum in Fig. 5.2(a) (top). The former transition takes place within the spin-3/2 ground state multiplet and approaches therefore zero energy at vanishing magnetic fields; the latter transition, on the other hand, involves an excited state belonging to the higher spin-1/2 multiplet and converges to a finite energy at $B = 0$ T.

In Fig. 5.2(c) the absolute value $|\mathrm{d}^2I/\mathrm{d}V^2|$ of the map in Fig. 5.2(a) is shown. The dashed line is a fit to the exchange Hamiltonian in Eq. (5.2) with an exchange coupling $J = -1.3$ meV and gyromagnetic ratio $g = 2.03$. This negative (ferromagnetic) J favors the high-spin quartet $|3/2, S_z = \pm 3/2, \pm 1/2\rangle$ over the low-spin doublet $|1/2, S_z = \pm 1/2\rangle$. The allowed transitions involve therefore $\Delta S_z = \pm 1$, giving rise to the two inelastic steps in the spectrum that increase linearly with magnetic field. A weak non-linearity of the low- and high-bias step evolution for fields $B < 0.5$ T is visible. This can be accounted for by setting a non-zero small anisotropy parameter to the spin Hamiltonian of Eq. (5.1).

On this sample gate-dependent measurements have also been performed and are shown in Appendix A.2. Throughout the entire accessible gate range no sign of resonant transport is seen. This suggests a large SOMO-SUMO (singly-unoccupied

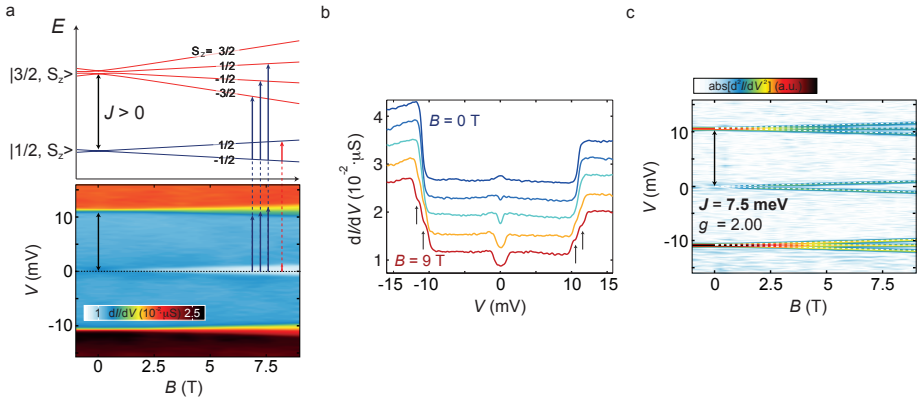

Figure 5.3: **Anti-ferromagnetic exchange coupling J.** (a) $\mathrm{d}I/\mathrm{d}V$ map measured on sample B as a function of bias voltage and magnetic field. A zero-bias peak and a step are visible at zero magnetic field. At high fields the high energy step is split into three smaller steps, with negative, zero and positive slopes. The upper panel shows the energy level scheme of a spin-3/2 system with an antiferromagnetic exchange coupling ($J > 0$) and a small anisotropy parameter ($D = 0.06$ meV). The colored arrows indicate the allowed processes with $\Delta S_z = 0, \pm 1$ associated with the observed spectrum. (b) $\mathrm{d}I/\mathrm{d}V$ spectra extracted from the map in (a) with a spacing of $\Delta B = 1.8$ T between 0 T and 9 T (offset for clarity). As the magnetic field increases, the zero-bias peak splits and the two additional steps appear in correspondence of the single step (black arrows). (c) Absolute value $|\mathrm{d}^2I/\mathrm{d}V^2|$ of the map in (a) with the fit to equation (1) superimposed (dashed lines). The splitting of the zero-bias peak and higher-energy excitation in three smaller staircase-like excitations is clearly visible. The extracted fitting parameters are $J = 7.5$ meV and $g = 2.0$. All measurements are taken at $T \approx 70$ mK.

molecular orbital) gap (also named SOMO-LUMO-β) and supports charge neutrality. While no resonant transport is visible, we observe that an increase in gate voltage results in a sizeable increase of the exchange coupling. This electric field-induced modulation of J amounts to a 9% of its total value.

We further note that two other measured samples show a similar set of transitions (see Appendix A.3). The extracted exchange coupling constants are in those cases $J = -2.2$ meV and $J = -2.3$ meV.

A second group of samples showed a markedly different set of spin transitions and magnetic field evolution. The characteristics are summed up for sample B in Fig. 5.3. The color map in Fig. 5.3(a) displays the $\mathrm{d}I/\mathrm{d}V$ as a function of bias voltage and magnetic field. A small zero-bias peak and two symmetric conductance steps at about ± 11 meV are visible at $B = 0$ T. The zero-bias peak evolves into two steps for increasing magnetic fields and the single high-bias step splits in three smaller steps. The three-fold excitation can be more readily seen in Fig. 5.3(b) (black arrows) and Fig. 5.3(c). This last feature is not compatible with the spin-3/2 ground state observed in sample A and indicates a ground state spin $S < 3/2$ together with a excited multiplet with $S + 1 \leq 3/2$ (either $S = 1/2$ or 0).

The presence of the zero-bias peak and its doublet-like magnetic field evolution indicate a $S = 1/2$ ground state. The energy spectrum corresponding to this case is displayed in Fig. 5.3(a) (top). The low-bias step is ascribed to the transition $|1/2, -1/2\rangle \rightarrow |1/2, 1/2\rangle$ within the spin-1/2 ground state multiplet; the high-bias ones are associated with the three allowed transitions to the spin-3/2 multiplet

$|1/2,-1/2\rangle \rightarrow |3/2,S_z\rangle$, with $S_z = \{-3/2,-1/2,1/2\}$, where the selection rule $\Delta S_z = 0$ also applies. Selected spectra extracted from Fig. 5.3(a) at different fields are displayed in Fig. 5.3(b). The zero-bias peak is clearly visible in the trace at zero magnetic field. The peak evolves into a dip at $B \approx 1.8$ T and opens up into two inelastic steps at higher fields. The observed weak zero-bias peak is consistent with the presence of Kondo correlations between one of the SOMO unpaired electrons of the spin-1/2 ground state and the electrons in the leads.

Taking the absolute value of the derivative of the map in Fig. 5.3(a), we obtain the $|\mathrm{d}^2I/\mathrm{d}V^2|$ map of Fig. 5.3(c). The splitting with magnetic field in two and three distinct steps of the low- and high-energy excitations respectively is clearly visible. Superimposed we show the result of a fit to Eq. (5.2), from which a magnetic exchange coupling $J = 7.5$ meV and $g = 2.0$ are extracted.

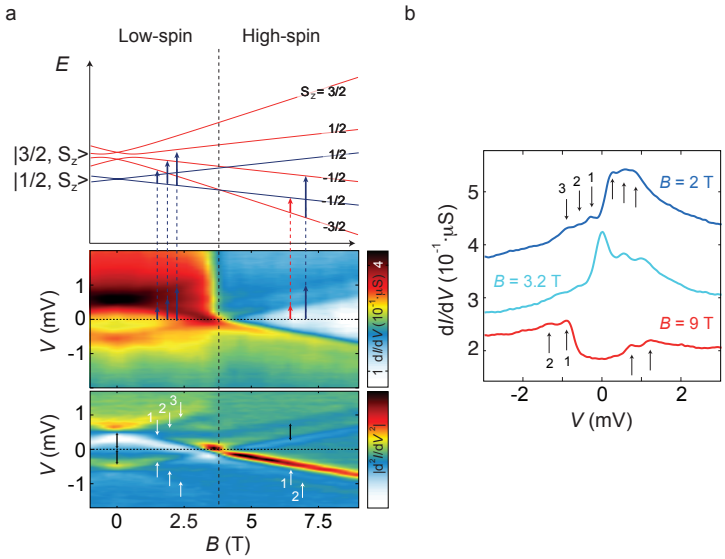

Figure 5.4: **Magnetic field control over the ground state.** (color online) (a) $\mathrm{d}I/\mathrm{d}V$ map (center) measured on sample C as a function of V and B. At low magnetic fields three conductance excitations (indicated by numbers) split in magnetic field. The positive and negative-bias ones numbered 1 cross at $B \approx 3.2$ T (black dashed line). For $B > 3.2$ T, the three lines merge into two steps. The constant energy splitting between the low- and high-energy step is marked by black arrows in the $\mathrm{d}^2I/\mathrm{d}V^2$ map (below). Above, the energy diagram of a spin-3/2 system with an antiferromagnetic exchange coupling ($J > 0$) and a small anisotropy parameter as a function of magnetic field. A negative but small J favors the low-spin doublet at low magnetic fields and the high-spin quartet at high magnetic fields. Red and blue arrows indicate the spin-flip processes with $\Delta S_z = 0, \pm 1$. (b) $\mathrm{d}I/\mathrm{d}V$ spectra extracted from the map in (a) at $B = 2, 3.2$ and 9 T (offset for clarity). The three steps (arrows 1, 2 and 3) present for values $B < 3.2$ T evolve into two steps (arrows 1 and 2) for $B > 3.2$ T.

We have observed a similar magnetic field dependence in two other samples with magnetic exchanges of $J = +3.0$ meV and $J = +0.4$ meV (sample C, shown in Fig. 5.4). Thus, In these samples, in contrast to sample A, the exchange coupling J is antiferromagnetic (positive) and stabilizes the low-spin doublet over the high-spin quartet.

Measurements in gate performed on sample B are shown in Appendix A.3. No sign of charging and resonant transport are present. Analogously to sample A, this

indicates a large gap and supports charge neutrality. The electric field-induced modulation of J amounts here to a 2% of its total value.

Figure 5.4 shows the results of a measurement on sample C displaying an intermediate scenario between the ones observed in sample A and B. The $\mathrm{d}I/\mathrm{d}V$ and corresponding $|\mathrm{d}^2I/\mathrm{d}V^2|$ color maps of Fig. 5.4(a) exhibit two conductance steps centered around $\approx \pm 0.55$ meV at $B = 0$ T. For magnetic fields below 3.2 T the steps at positive and negative bias split each into three excitations with positive, zero and negative slopes (numbered 1, 2 and 3 in the $|\mathrm{d}^2I/\mathrm{d}V^2|$ map and the $\mathrm{d}I/\mathrm{d}V$ linecut of Fig. 5.4(b)). The two excitations 1 in the positive and negative bias region intersect at $V = 0$ V and $B \approx 3.2$ T (dashed line in Fig. 5.4(a)). For $B > 3.2$ T only two of the three excitations survive. The zero-bias one emerges as a prosecution of excitation 1 with the same slope, while the finite-bias one continues from 2 with a different slope. The energy difference between the two steps is constant with magnetic field and amounts to ± 0.55 meV. It is important to notice that this value equals the energy of the excitation at zero magnetic field (black arrows in the map of Fig. 5.4(a)(bottom)). Following the energy level scheme of Fig. 5.4(a), the three excitations in the low-field region ($B < 3.2$ T) of the plot are associated with the transitions $|1/2,-1/2\rangle \rightarrow |3/2,S_z\rangle$, with $S_z = \{-3/2,-1/2,1/2\}$. The low- and high-bias ones in the high-field side ($B > 3.2$ T) are ascribed to the transitions $|3/2,-3/2\rangle \rightarrow |3/2,-1/2\rangle$ and $|3/2,-3/2\rangle \rightarrow |1/2,-1/2\rangle$ respectively. A change from low- to high-spin ground state thus occurs at the crossing point of the two regions ($B = 3.2$ T).

The set of transitions featured in this sample C can be explained with a positive, but small ($J \sim g\mu_B B$) exchange coupling J. This antiferromagnetic coupling favors the low spin state, but only up to a magnetic field equal to $\approx \frac{2}{3}J/g\mu_B$. For higher fields a spin-1/2 to spin-3/2 ground state flip occurs, with a consequent change in the excitation spectrum. Owing to the small J, the magnetic field provides thus a means to effectively control the magnetic ground state. Importantly, the spectra of samples A and B are therefore shown to be connected exclusively via a magnetic field change, with no need for oxidation/reduction of the molecule.

The data show that different samples of the same neutral individual triradical molecule in an electromigrated junction yield values of J spanning from -2.3 meV to $+7.5$ meV, in contrast to the robust value $J \leq -40$ meV obtained from the same molecule in frozen solution [336]. Excluding charging effects on the basis of the gate measurements and large calculated SOMO-SUMO (also named SOMO-LUMO-β) gap, we argue that the local environment of the junction is responsible for the reduction and sign change of J. The mechanism we propose relies on a molecular distortion induced on the molecule by the electrodes. In particular, we argue that the dihedral angle θ (Fig. 5.5(a) and Appendix A.4), which defines the relative position of the six peripheral rings with respect to the central one, determines the exchange and depends on the specific arrangement of the molecule between the electrodes, thus giving rise to the observed sample to sample variation. To test this hypothesis we perform unrestricted DFT-based calculations based on the broken symmetry approach [348–350, 363, 364] for different dihedral angles θ. The J-value at each step is extracted from the energy difference between the high-spin and the broken symmetry solution approaching the spin adapted doublet state (See Appendix A.4 for details on the calculations and explicit definition of the dihedral angle).

Spin-unrestricted molecular orbitals and magnetic exchange values resulting

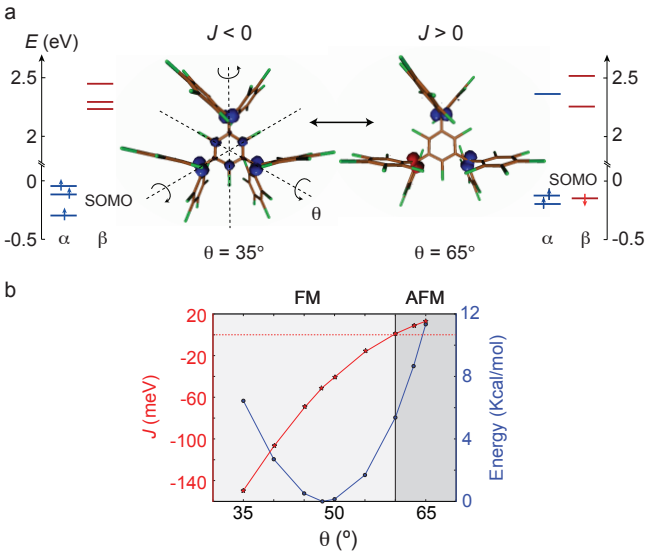

Figure 5.5: **Modelling orbitals energies and magnetic exchange coupling.** (color online) (a) Energy level diagram, molecular structure and spin density isosurfaces for two distinct torsion angles θ. A torsion applied to the three peripheral groups with respect to the central ring promotes the flip of one the spins (rightmost diagram) and a further concentration of the spin density onto the orbitals of methyl carbon atoms. (b) Energy and exchange coupling vs. angle θ plot. At the potential energy minimum ($\theta = 47°$) the ferromagnetic exchange energy exceeds room-T. Increasing (decreasing) the torsion angle results into an decrease (increase) of $|J|$ and ultimately to the reversal of its sign.

from the calculations are shown in Fig. 5.5. At low angles ($\theta = 35°$) the three spin-up SOMOs present a large energetic separation from the excited LUMO$-\beta$ orbitals. The non-disjoint [362] and near-degenerate character of these SOMOs is at the origin of the preferential high-spin GS. The spin density associated to this configuration is distributed on each of the three radical centers with a remarkable participation on the central phenyl ring. This through-bond delocalization of the unpaired electrons on the central ring determines the large exchange integral contributing to the stabilization of the high spin quartet. The delocalization over the central ring is progressively cut off as a torsion is applied and the dihedral angle increased. At high angles ($\theta = 65°$ is taken here as an example) the spin density on the central ring is completely suppressed and the orthogonality of the SOMOs compromised. The resulting large orbital overlap term favors electron pairing over the unpairing due to the exchange integral, yielding the observed positive (AFM) exchange coupling.

Energy cost and exchange coupling as a function of θ are reported in Fig. 5.5(b). The most thermodynamically stable conformation, obtained for $\theta = 47°$, is associated with a strong FM interaction. The calculated value ($|J| \approx 40$ meV $> k_b T$, with $T = 300$ K) is consistent with the high-spin ground state observed in room-T measurements on the molecule in frozen solution [336]. J monotonically increases for higher angles and the crossover to an AFM coupling is observed at $\theta = 60°$ at an energetic cost of only ~ 5 Kcal/mol[2]. The observed tunability of J with gate voltage can

[2]Given the approximate symmetry of the energetic cost as a function of torsion angle, one would expect

also be explained through this model. Provided unequal distances between the three radical electronic orbitals and the gate electrode, the electrostatic force can generate a net torque on the molecule. The torque can consequently result into a change in θ.

This model likely presents a simplified picture of the high complexity inherent to the molecule-electrodes coupled system where other kinds of distortions away from the thermodynamically most stable conformation may occur. Despite its simplicity, the model clearly demonstrates that non-destructive torsions applied to such polyradicals can lead to an inversion of the sign of the exchange coupling. Furthermore, the knowledge of this mechanism opens a pathway to the chemical, mechanical and electrical control of the reversal of magnetic states in individual as well as ensembles of these molecules. Such kind of direct control could be attained, for instance, by *in situ*-modifying the angle θ with the tip of a scanning tunneling microscope or a mechanically-controlled break junction. From the chemical point of view, the steric hindrance of the substituents can be engineered to stabilize the antiferromagnetic frustrated configuration in a single molecule.

3. CONCLUSIONS

In this chapter, we demonstrate that an individual high-spin all-organic triradical molecule in a junction exhibits changes in its exchange coupling between FM and AFM, while maintaining chemical integrity and charge neutrality. The change and sign inversion show, as supported by theory, that at the nanoscale the preference for the high-spin vs. low-spin ground state is not only dictated by the peculiar orbital topology arguments but also by molecular distortions imposed by the surrounding environment. Furthermore, external electric and magnetic fields may effectively control the J-value and the magnetic ground state. These results contribute to the understanding of the influence of the environment on the magnetic properties of molecule-based organic materials and open the way to the control of the magnetic ground states of flexible polyradicals for future molecular spintronics applications.

to observe also configurations with $|J| > 40$ meV. These configurations might go unseen in our measurements due to the fact that the bias window is limited to ± 30 meV to ensure the full stability of the gold nanogap.

A. APPENDIX

A.1. METHODS

Molecule synthesis The studied molecule is the diasteromeric form with a C_2 symmetry of 2,4,6-trichloro-α,α,α',α',α'',α''-hexakis(pentachlorophenyl)mesityltriyl radical, prepared as previously reported [336].

Junction preparation The molecular solution is prepared in the water-free glovebox dissolving the molecular powder in nitrogen-saturated dichlorobenzene solvent to reach a concentration of about 0.5 mM. Details on the fabrication and junction preparation are the same as in Appendix A.1 of Chapter 3.

Experimental conditions Measurements are performed in high vacuum ($p < 5 \cdot 10^{-4}$ mbar) in a dilution refrigerator ($\approx$ 70 mK) equipped with a superconducting magnet allowing magnetic fields up to 9 T. Current spectra are extracted applying a DC bias voltage V to the gold electrodes while recording current I. The differential conductance $\mathrm{d}I/\mathrm{d}V$ is then obtained by taking the numerical derivative.

Computational details All calculations in this chapter are performed within the spin unrestricted density functional formalism using the Gaussian-09 suite of programs [306]. The functional used was the popular B3LYP hybrid density functional and for all atoms, the basis set employed is the standard all electron 6-31G [341, 344, 365]. The exchange couplings exhibited in Fig. 5.5(b) are calculated within the broken symmetry (BS) approach [348–350], where the low S_z pure spin solution – in this case a doublet state – is described by means of a mono-determinant solution. The mapping procedure follows Ref. [364] and is further explained in Appendix A.4.

A.2. GATE MODULATION OF THE EXCHANGE COUPLING

In Figure 5.6 we show the $|\mathrm{d}^2I/\mathrm{d}V^2|$ color maps as a function of gate voltage V_g for samples A and B. These maps are taken sitting at $B = 0$ T in the maps of Fig. 2(c) and Fig. 3(c) and changing the gate voltage. The off-resonant character of transport is left unchanged by the gate voltage and does not exhibit any proximity to a charge degeneracy point. This is consistent with the large calculated SOMO-SUMO gap and supports charge neutrality. Noteworthy is the monotonic variation induced by the gate on the energy of the excitation: from -2.1 meV to -1.9 meV for sample A and from 11.1 V to -11.3 V for sample B in going from at $V_g = -2$ V to +2 V. The J-values are extracted by fitting the peak and translating the energy into the corresponding exchange coupling. We quantify the electric field-induced increase of J to be 9% and 2% for samples A and B respectively, thus showing a modest electrical control of the magnetic parameters.

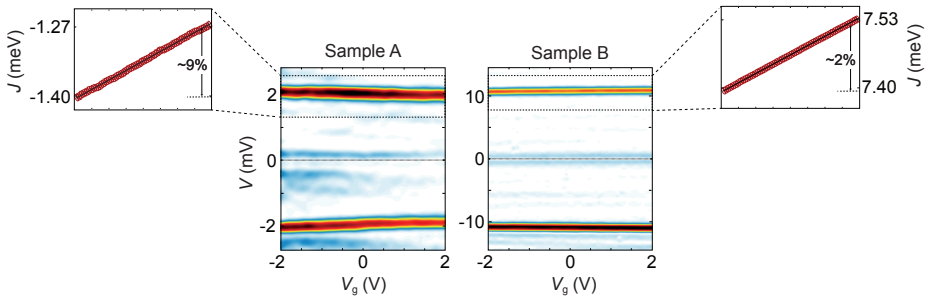

Figure 5.6: **Off-resonant transport and electric tunability of the exchange coupling.** $|\mathrm{d}^2I/\mathrm{d}V^2|$ color maps as a function of gate and bias voltage for samples A (left) and B (right). In the whole accessible gate range, no signs of resonant transport are visible. A fit of the peak positions reveals a tunability of J-value with applied electrostatic field. Modulations amount to 9% and 2% for A and B respectively. In both cases J increases in going from negative to positive gate voltages.

A.3. STATISTICS AND ADDITIONAL SAMPLES

In this study we have electromigrated and measured 120 junctions, none of which showed signs of resonant transport as expected from the energy level scheme of Fig. 5(a). For this reason, the presence of inelastic cotunneling is considered as the signature of the formation of a molecular junction. According to this criterion, 6 junctions were selected as containing the molecule. A summary of the main features of each of the six selected samples is given in Table 5.1.

SAMPLE	J (meV)	ZFS (meV)	Resonant transport
A	- 1.3 ± 0.1	0.15 ± 0.1	No
D	- 2.2 ± 0.1	0.15 ± 0.1	No
E	- 2.3 ± 0.4	0.05 ± 0.05	No
B	+ 7.5 ± 0.1	< 0.4	No
C	+ 0.4 ± 0.1	< 0.2	No
F	+ 2.6 ± 0.1	-	No

Table 5.1: Table of J-values and zero-field splittings (ZFS) relative to the measured samples. Samples exhibiting ferromagnetic and antiferromagnetic exchange couplings are grouped in the first and second block respectively. The last column indicates whether any sign of resonant transport is visible in the gate-dependent measurements.

In Fig. 5.7 we show the $\mathrm{d}I/\mathrm{d}V$ and $|\mathrm{d}^2I/\mathrm{d}V^2|$ color maps relative to the additional samples D and E. The presence of low- and high-bias steps shifting parallel to each other as the magnetic field is increased follows from the $S = 3/2$ high-spin ground state and $S = 1/2$ excited multiplet. This behaviour is analogous to the one observed in sample A and signals a ferromagnetic (negative) J-value. In Fig. 5.8 $\mathrm{d}I/\mathrm{d}V$ and $|\mathrm{d}^2I/\mathrm{d}V^2|$ color maps relative to sample F are displayed. The high-bias step split in three smaller steps at sufficiently high-magnetic fields and the low-bias step split in two steps. This behaviour results from a $S = 1/2$ low-spin ground state and a $S = 3/2$ high-spin ground state. In this case, the exchange interaction is antiferromagnetic (positive J-value) as in samples B and C of the main text.

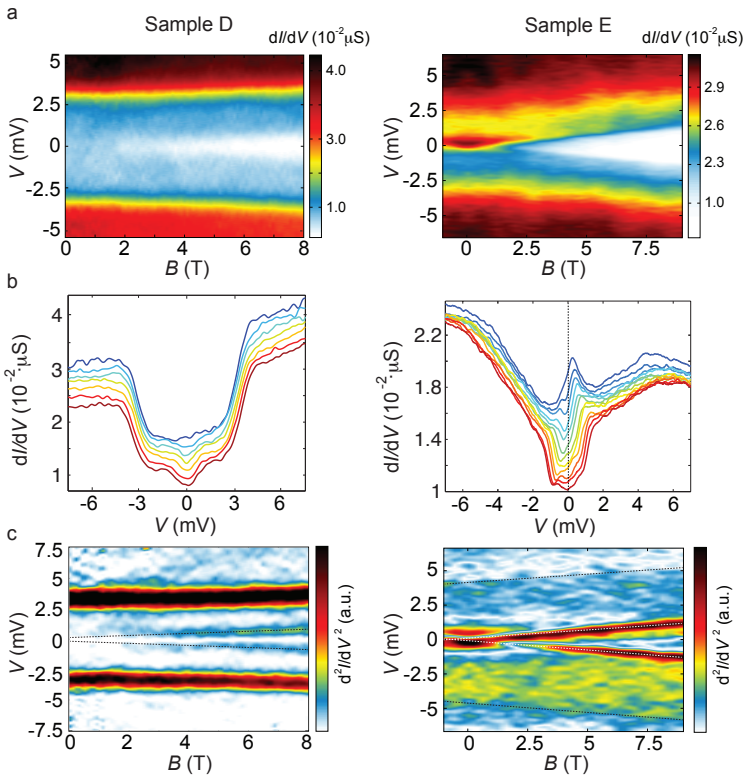

Figure 5.7: **Magnetic behaviour of additional samples D and E.** (a) $\mathrm{d}I/\mathrm{d}V$ color maps of samples D and E. In both samples, two steps in differential conductance shift linearly and parallel to each other in magnetic field. (b) $\mathrm{d}I/\mathrm{d}V$ linecuts extracted from the color maps in (a). (c) Corresponding $|\mathrm{d}^2I/\mathrm{d}V^2|$ color maps. This behaviour signals a high-spin ground state and is analogous to the one observed in sample A (ferromagnetic interaction), shown in the main text.

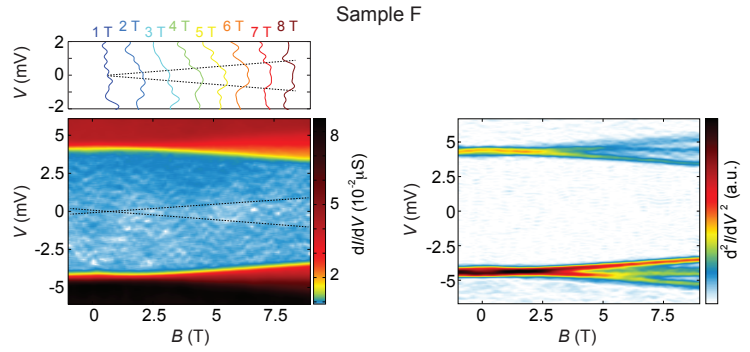

Figure 5.8: **Magnetic behaviour of additional sample F.** (below) $\mathrm{d}I/\mathrm{d}V$ and $|\mathrm{d}^2I/\mathrm{d}V^2|$ color maps (below) relative to sample F. Here the high-energy transition is seen splitting in three smaller steps, signalling a low-spin ground state. The transition $S_z = -1/2 \rightarrow 1/2$ within the ground state multiplet is very faintly visible and has been marked by the dashed line. (above) Linecuts extracted from the $\mathrm{d}I/\mathrm{d}V$ color map at the magnetic fields. This behaviour is analogous to that observed for sample B and C (antiferromagnetic interaction) in the main text.

A.4. THEORETICAL ANALYSIS

The strategy followed for the extraction of the exchange coupling constant as a function of the dihedral angle θ (as in Fig. 5.5(a) and more technically defined below) is analogous to the one in Appendix A.3 of the previous chapter and consists of the following steps: (i) modifying the value of the angle θ; (ii) performing a restricted optimization of the high-spin state – the quartet state in this case –, keeping fixed the angle while allowing a relaxation of the rest of the parameters; (iii) performing single point calculations for the BS solution at the local restricted minima found. The energy difference between the quartet and the BS doublet at each geometry yields the coupling constant.

Extraction of magnetic coupling constant through DFT: the mapping approach
From the magnetic point of view, the treatment we detail here follows the one in Appendix A.2 of the previous chapter. After briefly recalling it, we see now how to map that purely magnetic picture to states that can be described by DFT, in order to obtain a *numerical* value of the exchange coupling.

Starting from the Heisenberg Hamiltonian [366–369], with one $S = 1/2$ spin moment per each carbon sp^2 centre:

$$\hat{\mathscr{H}}^{\mathrm{HDVV}} = \sum_{<i,j>} J_{ij}\mathbf{S}_i \cdot \mathbf{S}_j = J_{12}\mathbf{S}_1 \cdot \mathbf{S}_2 + J_{23}\mathbf{S}_2 \cdot \mathbf{S}_3 + J_{13}\mathbf{S}_1 \cdot \mathbf{S}_3, \tag{5.2}$$

As previously seen, in the most general case, this spectrum involves the D_1, D_2 and Q states, which are pure spin states, meaning that they are eigenfunctions of the square of the total spin operator and of its z-component. These states can be expressed as a linear combination of the $|\alpha\alpha\beta\rangle$, $|\alpha\beta\alpha\rangle$ and $|\beta\alpha\alpha\rangle$ basis set elements which are eigenfunctions of the z-component of the total spin; the +1/2 component is chosen for convenience. By diagonalizing the matrix representation of the HDVV Hamiltonian in the above mentioned basis set, one obtains [370]:

$$|D_1\rangle = \frac{1}{\sqrt{2}}(|\alpha\alpha\beta\rangle - |\alpha\beta\alpha\rangle) \tag{5.3}$$

$$|D_2\rangle = \frac{1}{\sqrt{6}}(|\alpha\alpha\beta\rangle + |\alpha\beta\alpha\rangle - 2|\beta\alpha\alpha\rangle) \tag{5.4}$$

$$|Q\rangle = \frac{1}{\sqrt{3}}(|\alpha\alpha\beta\rangle + |\alpha\beta\alpha\rangle + |\beta\alpha\alpha\rangle) \tag{5.5}$$

and the corresponding eigenvalues are:

$$E_{D_1} = -1/4 \cdot (J_{12} + J_{13} + J_{23}) + 1/2 \cdot X \tag{5.6}$$

$$E_{D_2} = -1/4 \cdot (J_{12} + J_{13} + J_{23}) - 1/2 \cdot X \tag{5.7}$$

$$E_Q = -1/4 \cdot (J_{12} + J_{13} + J_{23}) \tag{5.8}$$

with

$$X = \sqrt{J_{12}^2 + J_{13}^2 + J_{23}^2 - J_{12} \cdot J_{13} - J_{12} \cdot J_{23} - J_{13} \cdot J_{23}} \tag{5.9}$$

from which the following expressions for the energy differences are obtained:

$$E_Q - E_{D_1} = 1/2(J_{12} + J_{13} + J_{23} - X) \tag{5.10}$$

5

$$E_Q - E_{D_2} = 1/2(J_{12} + J_{13} + J_{23} + X) \tag{5.11}$$

Now, the structural characteristics of the triradical studied permit a simplification of this spectrum, since the problem can be assumed to have the symmetry of an equilateral triangle. Thus, J_{12}, J_{23} and J_{13} are equal, the X term vanishes, the two doublet states D_1 and D_2 become degenerate and the relative position of the magnetic states is

$$E_Q - E_D = 3/2J \tag{5.12}$$

However, we are making use of the broken symmetry approach and therefore the functions that we are using to describe the doublet state are not eigenfunctions of the squared total spin operator, but functions that serve as basis set for the construction of the HDVV Hamiltonian, $|\alpha\alpha\beta\rangle$, $|\alpha\beta\alpha\rangle$ and $|\beta\alpha\alpha\rangle$. This procedure fits with the Ising Hamiltonian[371], and actually the diagonal elements of both matrices (HDVV and Ising) are the same. It is defined as:

$$\hat{\mathscr{H}}^{\text{Ising}} = \sum_{<i,j>} J_{ij} S_i^z \cdot S_j^z = J_{12} S_1^z \cdot S_2^z + J_{23} S_2^z \cdot S_3^z + J_{13} S_1^z \cdot S_3^z, \tag{5.13}$$

The difference is that HDVV has non-diagonal elements different from zero, while Ising does not. The advantage of the Ising picture is that we can directly access the diagonal elements of the matrix variationally minimizing the energy of the $|\alpha\alpha\beta\rangle$,$|\alpha\beta\alpha\rangle$ and $|\beta\alpha\alpha\rangle$ solutions, which is precisely what is done with density functional theory (DFT). Then, assuming the same equilateral triangle, the expressions for the energy of the quartet and broken symmetry doublet are:

$$E^{\text{Ising}}(|\alpha\alpha\alpha\rangle) = 3/4J \tag{5.14}$$

$$E^{\text{Ising}}(|\alpha\alpha\beta\rangle) = E^{\text{Ising}}(|\alpha\beta\alpha\rangle) = E^{\text{Ising}}(|\beta\alpha\alpha\rangle) = -1/4J \tag{5.15}$$

which implies:

$$E^{\text{Ising}}(|\alpha\alpha\alpha\rangle) - E^{\text{Ising}}(|\alpha\alpha\beta\rangle) = J \tag{5.16}$$

That is the expression that has been used in this work to extract the coupling constant from BS solutions.

Investigated potential energy surface and definition of the angle The reversal of the exchange coupling constant has been theoretically modelled following the torsion of the molecule along the collective angle θ, as defined in Fig. 5.9. The reported values in the main text refer to the angle defined as $\theta = (\theta_1 + \theta_2 + \theta_3 + \theta_4 + \theta_5 + \theta_6)/6$ where $\theta_1 - \theta_6$ are equal. The exact same profile is obtained when the restriction is less severe and the angle is defined as $\theta = (\theta_1 + \theta_3 + \theta_5)/3$.

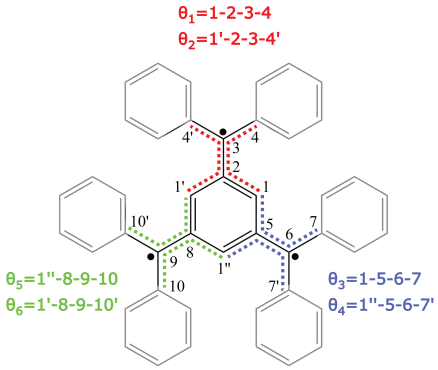

Figure 5.9: Schematic representation of the different angles used to performed the restricted optimizations.

6

QUANTUM-ENHANCED LANDAUER ERASURE AND STORAGE

The worse the republic,
The more numerous its laws[1]

Tacitus

The erasure of a bit of information encoded in a physical system is an irreversible operation bound to dissipate an amount of energy $Q = k_B T \ln 2$ [372]. As a result, work $W \geq Q$ has to be applied to the physical system to restore the erased information content [373–375]. This limit, called Landauer limit, sets a minimal energy dissipation inherent to any classical computation. In the pursuit of the fastest and most efficient means of computation, the ultimate challenge is to produce a memory device executing an operation as close to this limit in the shortest time possible. In this chapter, we use a crystal of molecular nanomagnets as a spin-memory device and measure the work needed to carry out a storage operation. Exploiting a form of quantum annealing, we border the Landauer limit while preserving fast operation. This result suggests a way to enhance classical computations by using quantum processes.

Parts of this chapter constitute a publication (arXiv:1703.04607; in peer-review, Nature Physics) by R. Gaudenzi, E. Burzurí, S. Maegawa, H.S.J. van der Zant, F. Luis.

[1] This can be invariably extended to any formal system.

1. INTRODUCTION

While a computation performed with an ideal binary logic gate (e.g. NOT) has no lower energy dissipation limit [376, 377], one carried out in a memory device does. The reason is that in the former the bit is merely *displaced* isentropically in the space of states, whereas in the latter the minimal operation comprises an entropy non-conserving erasure-storage cycle. In the *erasure* step, the bit is allowed to *explore* the two binary states and the phase space doubles with a consequent entropy increase of $\Delta S = k_B \ln 2$. A corresponding minimal dissipated heat $Q = k_B T \ln 2$, called the Landauer limit, results from this entropy change. In the *storage* step, a work $W \geq Q$ has to be applied to *reduce* the system's entropy and phase space to their initial values. In order to reach the $W = Q$ limit, *reversible* operation is required. This condition is fulfilled only when using a frictionless system in a quasi-static fashion, i.e., at timescales slower than its relaxation time τ_{rel}, so that unwanted memory and hysteresis effects are avoided. For this reason, slower (faster) operation is generally associated with a lower (higher) dissipation.

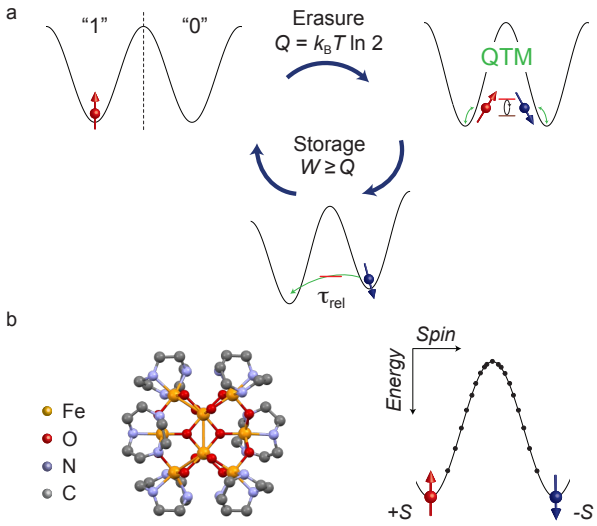

Figure 6.1: **Quantum-enhanced Landauer erasure and storage of a molecular bit.** (a) Schematics of the Landauer erasure process employing a quantum nanomagnet. In order to erase the spin bit, the effective barrier separating the two binary states is lowered by inducing quantum tunneling of magnetization (QTM). A small bias magnetic field is then used to initialise the spin in the desired state within a time τ_{rel} and store the new information. The Landauer principle fixes the minimal dissipated heat Q and work W involved in the cycle. (b) Sketch of the Fe_8 easy-axis molecular magnet. In the absence of magnetic field, the double-well potential favors the two $S_z = \pm 10$ easy-axis spin eigenstates.

This complementarity between work and time suggests considering the product $W \cdot \tau_{rel}$ – rather than either of the two – as the figure of merit assessing the energy-time cost of a computation. On one hand, driven by the demand for speed, effort has been put in pursuing fast-switching storage devices. This has successfully produced state-of-the-art systems with picosecond timescales, though operating far ($\gtrsim 10^6$) above the reversible limit [378–381]. On the other hand, reducing W down to the Landauer limit, at the expense of slow operation, has been beautifully demonstrated

using small particles in traps [382, 383] or single-domain nanomagnets [384] as envisioned by Landauer and Bennett [372, 373].

In our experiment, a crystal of Fe_8 molecular magnets (MM) is used as a spin memory to perform a quantum-enhanced erasure-storage protocol, shown in Fig. 6.1(a). We encode the bit in the "up" and "down" spin states of the MM (Fig. 6.1(b)) and measure the magnetic susceptibility along the erasure-storage cycle. We find that the net work applied to the spin system during this cycle reaches the Landauer limit. This minimal energy cost is retained up to high operation speeds thanks to the possibility of enhancing quantum tunneling of magnetization (QTM) via suitably oriented external magnetic fields.

2. RESULTS AND DISCUSSION

Each individual Fe_8 molecule represents a magnetic bit and is composed of eight spin-$\frac{5}{2}$ Fe^{3+}-ions coupled to each other by competing antiferromagnetic interactions to form a collective $S = 10$ ($20\mu_B$) giant-spin. By bottom-up chemical synthesis, arrays of these MMs, with perfectly aligned magnetic axes, are packed into a single crystal. Due to the relatively large intermolecular spacing, the exchange interactions between the molecules are negligible [385]. The giant-spin $S = 10$ multiplet of the single MM is described by the following Hamiltonian [386]:

$$\mathscr{H} = -DS_z^2 + E(S_x^2 - S_y^2) - g\mu_B \mathbf{S}\cdot\mathbf{B}. \tag{6.1}$$

The ligand field, parametrised by the anisotropy constants $D = 0.294$ K and $E = 0.04$ K, defines x, y and z as the hard, medium and easy magnetic axes, respectively, and creates an effective energy barrier with activation energy $U = 26.75$ K [387] separating the two $S_z = \pm 10$ ground eigenstates (Fig. (1b)). The relaxation over this barrier follows approximately Arrhenius' law $\tau_{\text{rel}} = \tau_0 \exp(U/k_B T)$, where $\tau_0 = 1.43 \cdot 10^{-8}$ s is the attempt time [387]. The action of the magnetic field reflects into the Zeeman term of Eq. (6.1) and is depicted in Fig. 6.2(a), where classical potential and quantum energy levels are represented. A magnetic field parallel to the easy axis, H_z, favours either of the two eigenstates $S_z = \pm 10$, i.e., increases the "up" or "down" polarization. Instead, magnetic fields along the medium axis, H_y, give rise to off-diagonal terms that mix "up" and "down" states [388]. This allows the spins to tunnel through the potential barrier via progressively lower levels, thus leading to a lower effective U and a consequent decrease in τ_{rel} [386]. After aligning to the principal magnetic axes of crystal (see Appendix A.2), we apply the sequence of magnetic fields depicted in Fig. 6.2(b) – comparable to that proposed in Ref. [376] for classical magnets – in order to carry out the erasure-storage operation on our MM. In step 1, the magnetic field along the medium axis of the MM (H_y) is ramped up to 2 T and the spin states are mixed so that the bit is erased. In step 2, H_z is ramped up to 210 mT in the constant H_y field to initialise the spin in the "up" state. In steps 3 and 4, both the magnetic fields are returned to zero in the same order, closing the cycle and completing the storage.

Throughout the cycle, the complex ac-susceptibility $\chi_z = \chi_z' + i\chi_z''$ along the easy axis is measured with an inductive susceptometer (see methods for details). χ_z is proportional to the derivative of the magnetization $\partial M/\partial H_{\text{ac}}$ and is function of the temperature T, frequency ω of the ac-field H_{ac} and magnetic field vector $\mathbf{H}$. Measur-

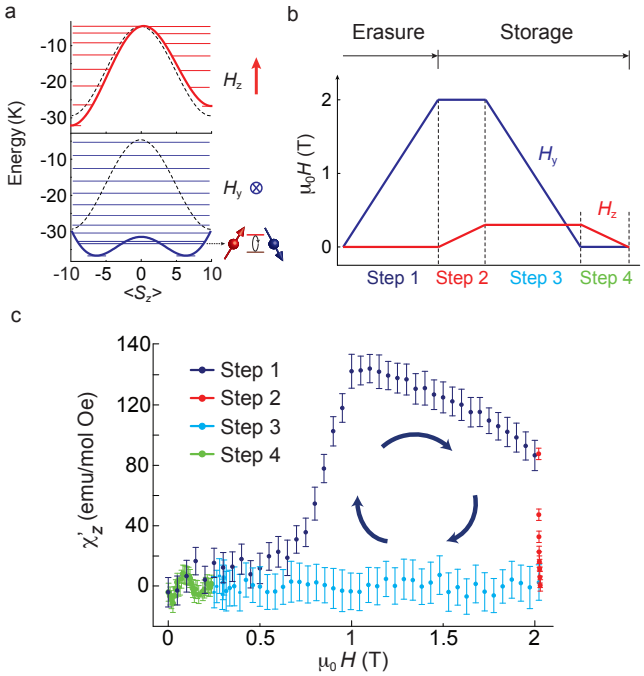

Figure 6.2: **Susceptibility of the quantum MM along the erasure-storage cycle.** (a) Magnetic energy of a Fe8 MM subject to a $\mu_0 H_z = 0.2$ T longitudinal magnetic field (top) and a $\mu_0 H_y = 2$ T transverse magnetic field (bottom). Thick solid lines show the classical potential landscape while thin horizontal lines give the quantum energy levels determined by numerical diagonalisation of Eq. (1). The dotted lines show the $H = 0$ potential. While H_z introduces an energy bias between up and down spin states, thus increasing the magnetic polarization along the easy axis, H_y keeps the symmetry of the potential intact but promotes QTM between these states. (b) The 4-step sequence of magnetic fields H_y (blue) and H_z (red) constituting the erasure-storage algorithm. The first step ($H_y : 0 \rightarrow 2$ T) consists of the Landauer erasure and the remaining 3 steps correspond to the storage protocol. (c) Real component of the longitudinal magnetic ac-susceptibility, χ'_z, as a function of the vector magnetic field's modulus, measured at 1K and a frequency of 333 Hz. The sequence of steps corresponds to the one in Fig. 6.2(b).

ing this quantity allows to track the dynamics of the spin system and its relaxation properties. In addition, from χ'_z the magnetization and work can be derived by integrating once and twice with respect to magnetic field. The work W obtained in this manner quantifies the heat dissipated during the erasure and measures how reversible the storage operation is [376, 384].

The experiment is conducted at $T = 1$ K and $\omega/2\pi = 333$ Hz. This temperature is low enough to store the spins for minutes with no field applied, and high enough to have them relaxing within hundreds of nanoseconds when in a transverse field. Furthermore, at this temperature the ferromagnetic ordering can be neglected since the dipolar interaction strength is about 0.6 K [385]. The results for the real component of the susceptibility, χ'_z, are shown in Fig. 6.2(c). The susceptibility, initially zero, steeply increases at $H_y \approx 0.6$ T, reaches a peak at $H_y \approx 1$ T and slowly decreases up to $H_y = 2$ T. As a small longitudinal field is applied (step 2), χ'_z sharply drops and reaches zero at $H_z \approx 0.19$ T. Upon retracting the fields in steps 3 and 4, χ'_z remains substantially zero.

At the beginning of step 1, the spins are all blocked in either of the potential wells and the wave-function is confined to the "up" or "down" spin eigenstate. Upon ramping up H_y, the admixture of the pure S_z eigenstates is enhanced and the wave-functions delocalised over the two potential wells [389]: χ'_z increases as the spin is free to tunnel between the two energetically equivalent spin states with the characteristic time $\tau_{\rm rel}$. In the presence of an ac-drive, the spins follow the oscillations of $H_{\rm ac}$ provided $\omega \lesssim 1/\tau_{\rm rel}$. At this point, the bit is erased. In step 2, a small H_z bias magnetic field is applied. The susceptibility decreases for increasing spin polarisation reaching zero upon saturation of the magnetization. At this point, the bits are initialised in the "up" configuration. In step 3, the admixing field is ramped down and thus QTM gradually turned off. This causes the spins to remain *frozen* (i.e., out of equilibrium) in the chosen configuration upon retraction of the bias polarizing field (step 4).

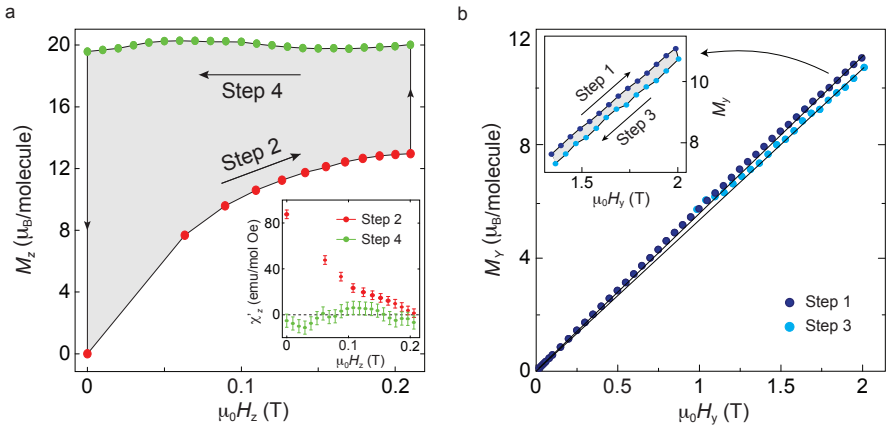

Figure 6.3: **Total bit storage work.** (a) Longitudinal magnetization per molecule M_z extracted by integrating χ'_z of steps 2 and 4 (zoom-in from Fig. 6.2(b) in the inset) with respect to H_z. The shaded area corresponds to the work done on the system by H_z. (b) SQUID magnetization per molecule M_y along the medium axis of the MM as a function of transverse field H_y at $T = 2$ K. The slope of step 1 is higher than that of step 3 due to the small applied bias H_z field (fits are guidelines to the eye). The area enclosed by these two curves (shaded area in the inset) corresponds to the work done by H_y. This work, summed to the one in (a), yields the energy needed for storing a bit of information.

By integrating the measured χ'_z with respect to H_z (inset of Fig. 6.3(a)), we calculate the easy axis magnetization M_z for steps 2 and 4 (see Appendix A.1). The result is plotted in Fig. 6.3(a). During step 2, M_z increases for increasing H_y before flattening out at about $13\,\mu_B$. Upon retracting H_y, M_z increases up to about its maximum value of $20\,\mu_B$ and remains approximately constant as H_z is also ramped to zero. The area enclosed by the magnetization loop amounts to the work made by the external magnetic field onto the molecular magnet. This yields the value $W_{2,4} \equiv W_4 - W_2 = (1.74761 \pm 0.28107) \cdot 10^{-16}$ erg/molecule, where the uncertainty corresponds to a 1σ confidence interval (see Appendix A.4 for the determination of molecules' number and Appendix A.3 for the uncertainties). To this quantity, the work $W_{1,3}$ done by the H_y in steps 1 and 3 needs to be added. This work cannot be extracted from the measured medium-axis susceptibility since, due to the strong magnetic anisotropy,

$\chi_y (\ll \chi_z)$ is below our detection limit. However, because χ_y is approximately independent of T and ω (see Appendix A.2), the magnetization can be invariably measured with a SQUID at $T = 2$ K. The result is shown in Figure 6.3(b). The transverse magnetization M_y is recorded as H_y is ramped up to 2 T (step 1) and subsequently ramped down in the small bias longitudinal field of 0.21 T (step 3). M_y increases during step 1 and decreases, with a slightly lower slope, during step 3. The net work is given by the difference between the works W_3 and W_1 done by H_y and amounts to $W_{1,3} \equiv W_3 - W_1 = (-5.6481 \pm 1.7712) \cdot 10^{-17}$ erg/molecule. The total dissipated energy, W, is then the sum $W = W_{1,3} + W_{2,4} = (1.1828 \pm 0.3322) \cdot 10^{-16}$ erg/molecule. Within the experimental uncertainty, this is equivalent to the theoretical Landauer limit at the experimental temperature of 1 K, equal to $k_B T \ln 2 = 0.9570 \cdot 10^{-16}$ erg/bit. This proves that the present system behaves effectively like an ideal "single-spin" bit [384].

We now discuss the extraction of the magnetic relaxation time. Ac-susceptibility measurements allow for an estimation of the dynamics of the spin relaxation processes. In particular, the ratio $\chi_z''/(\omega\chi_z')$ measures the magnetic relaxation time τ_{rel} or, alternatively said, the time the system takes to reach equilibrium [386]. In Fig. 6.4(a) we show the evolution of τ_{rel} as a function of H_y during step 1 in the range $0.7 \leq H_y \leq 1.15$ T for which $\chi_z'' \pm \sigma_{\chi''} \geq 0$ (Inset of Fig. 6.4(a)). We complement these data with τ_{rel} extracted from χ_z' measurements in temperature (see Appendix A.2). The relaxation time exponentially drops from 71.2 s at $H_y = 0$ T to 1.09 μs at $H_y = 1.7$ T. Extrapolation to $H_y = 2$ T leads to a relaxation time of 196 ns. This time is to be interpreted as the longitudinal response time of the phonon bath-and-molecule system upon a change in H_z and fixes the limit up to which quasi-static operation is retained and unwanted (dissipative) hysteresis are avoided.

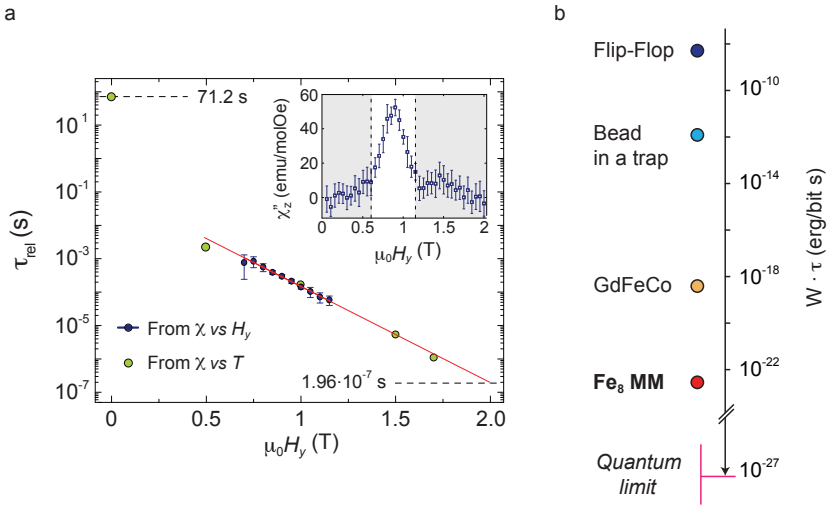

Figure 6.4: **Relaxation time and energy-time cost.** (a) Evolution of the spin relaxation time as a function of H_y during step 1. The blue data points are obtained from χ_z'' in the interval $0.7 \leq H_y \leq 1.15$ T (inset). The green data points are extracted from temperature sweeps (see Appendix A.2). The relaxation time reaches 196 ns at $H_y = 2$ T. This value sets the maximum speed up to which quasi-static operation is retained. (b) Chart comparing the energy-time cost of a storage operation performed with various systems at their respective operating temperature. The Fe_8 in this study is the closest to the quantum limit.

The product of the work and relaxation time, $W \cdot \tau_{rel}$, yields $2.31 \cdot 10^{-23}$ erg/bit·s. This figure quantifies the overall energy-time cost of a computation and its value can be compared to that of other storage devices, operating at room temperature ($T \approx 300$ K). As shown in Fig. 6.4(b) (see Appendix A.5 for the extended chart), the product $W \cdot \tau_{rel}$ for standard flip-flops – moderately fast but lossy – is $\sim 10^{-9}$ erg/bit·s; the optical trap system in Ref. [383] – slow but efficient – attains $\sim 10^{-12}$ erg/bit·s. Increased performances ($\sim 10^{-19}$ erg/bit·s) over these two system is given by the recent GdFeCo laser-driven ferromagnetic element in Ref. [381] owing to its tens of ps operation time. The Fe_8 MM performs about 10^4 times better than this system – reducing to 100 times when accounting for the lower operating temperature. Ultimately, the product $W \cdot \tau_{rel}$ is limited by the Heisenberg uncertainty relation [390, 391]. According to it, the evolution between two orthogonal, thus classically distinguishable, bit states separated by an energy Δ would take the minimal "relaxation" time $\tau_{rel} = \pi\hbar/(2\Delta)$ called quantum speed limit [392–394]. From it, the limit $W \cdot \tau_{rel} = \pi\hbar/2 = 1.65 \cdot 10^{-27}$ erg/bit·s is obtained as the best trade-off between speed and energy cost [395]. Although still far from this limit, the quantum dynamics of systems like the MM in this study proves to be the key to operate both fast and at the Landauer limit and can be used to explore the connection between this classical limit and the quantum speed limit.

A. APPENDIX

A.1. METHODS

Susceptibility measurements An ac-susceptometer thermally anchored to the mixing chamber of a dilution refrigerator in combination with a 3D vector magnet (9T, 1T, 1T, 0.001° accuracy) is used to measure the erasure-storage protocol. The complex susceptibility $\chi(T,\omega) = \chi'(T,\omega) + i\chi''(T,\omega)$ is measured with a standard lock-in technique with an ac excitation magnetic field of amplitude $H_{ac} = 0.01$ Oe parallel to the common easy axis of the molecules.

Magnetization measurements Magnetization is measured with a commercial SQUID magnetometer ($T \geq 1.8$ K) equipped with a rotating stage and an ac susceptibility option.

Calculations of magnetization and work The easy-axis magnetization M_z is obtained from the susceptibility χ'_z by making use of the integral:

$$M_z = \int \chi'_z \, dH_z.$$

The works done by H_z (steps 2 and 4) and H_y (steps 1 and 3) are calculated by performing an analogous integration on the resulting M_z and M_y, respectively:

$$W_{2,4} = \oint M_z \, dH_z, \quad W_{1,3} = \oint M_y \, dH_y.$$

These correspond to the loop shaded areas in Fig. 6.3 (a) and (b).

A.2. CHARACTERISATION IN TEMPERATURE AND TRANSVERSE FIELD

This section contains details on: the characterisation of the superparamagnetic behaviour of the MM crystal in temperature and frequency; the extraction of the relaxation time as a function of selected H_y fields; the determination of the crystal's magnetic easy and medium axes orientation with respect to the laboratory's reference system.

Temperature and frequency In Fig. 6.5, the real (in-phase) $\chi'(T,\omega)$ and imaginary (out-of-phase) $\chi''(T,\omega)$ components of the ac-susceptibility are shown as a function of temperature for the indicated frequencies in zero magnetic field. For each component, the longitudinal χ_z and transverse $\chi_\perp$ parts are plotted. For a fixed frequency, decreasing the temperature results in the increase of χ'_z accompanied by a constant $\chi''_z \approx 0$. This is the typical behaviour of a standard paramagnet, where the absence of an out-of-phase response signals equilibrium and a fast relaxation time $\tau_{\text{rel}} \ll 1/\omega$. However, as a frequency-dependent temperature is reached, χ'_z starts dropping to zero while χ''_z exhibits a peak. This temperature corresponds to the so-called blocking temperature, T_b, and it is characterised by a spin relaxation time $\tau_{\text{rel}} \simeq 1/\omega$. For $T < T_b$, the spin of the MM is increasingly driven out-of-equilibrium and τ_{rel} further increases. The observed behaviour is a fingerprint of the superparamagnetism

expected in a MM, where the potential barrier prevents fast spin relaxation at sufficiently low temperatures. The small temperature- and frequency-independent $\chi'_\perp$ and zero $\chi''_\perp$ further signal the strong spin polarisation along the easy-axis and negligible transverse (hard-plane) spin projection.

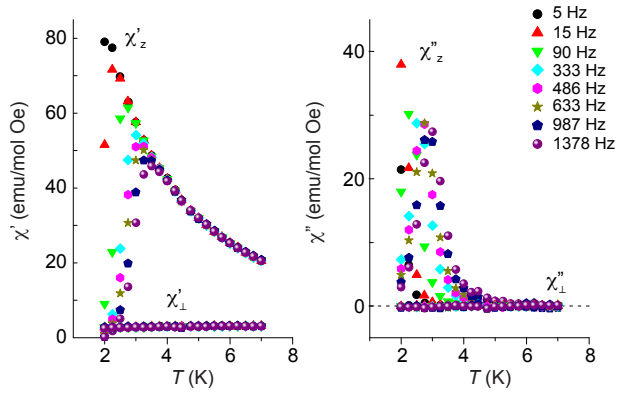

Figure 6.5: **Temperature and frequency characterization.** (a) Real (left) and imaginary (right) part of the susceptibility as a function of T and indicated frequency ω ranging from 5 Hz to 1378 Hz. The frequency-dependent departure from equilibrium signals the expected superparamagnetic behaviour.

Transverse magnetic field To extract the relaxation time data-points shown in Fig. 4 (and labelled "χ *vs* T data"), we use temperature-dependent complex susceptibility measurements for the different H_y fields at the frequency $\omega = 333$ Hz. Plotting the ratio $\chi''_z/\omega\chi'_z = \tau_{rel}$ as a function of the inverse temperature results in Fig. 6.6. At high temperatures, the relaxation time behaves according to Arrhenius' law $\log \tau_{rel} = U_{eff}/T + \tau_0$ with the effective barrier $U_{eff}(H_y)$ obtained by fitting the temperature-dependent part of the curves. Extrapolation of the fit to $T = 1$ K, yields $\tau_{rel}(H_y; T = 1\,\text{K})$ for the selected fields.

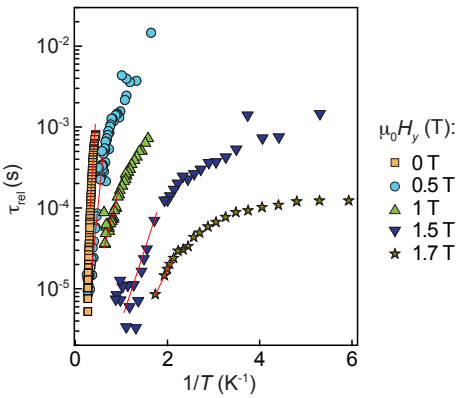

Figure 6.6: **Relaxation time for different transverse fields.** (a) τ_{rel} obtained from $\chi''_z/\omega\chi'_z$ as a function of inverse temperature. Fitting of the temperature-dependent side allows to obtain the desired $\tau_{rel}(H_y)$ at $T = 1$ K by extrapolation.

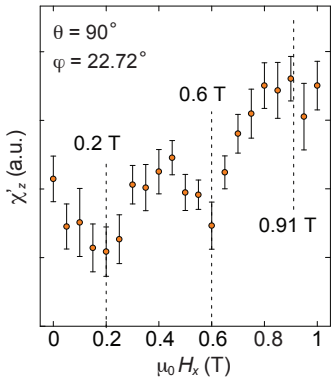

Figure 6.8: **Quantum interference pattern along the hard axis.** χ'_z as a function of magnetic field intensity along the hard axis (labelled by the subscript x). Oscillations signal the expected quantum interference pattern with minima at the indicated fields.

Alignment to principal axes In this subsection we describe the procedure used for finding the accurate orientation of the principal axes of the MM with respect to the X, Y and Z axes of the vector magnet. Provided this orientation is approximately known, the crystal is placed in the susceptometer with its easy, medium and hard axes about the Y, Z and X-axis of the magnet, respectively. Measurements are executed at $T = 3$ K and $\omega = 1333$ Hz. Under these conditions, the susceptibility is close to equilibrium (see Fig. 6.5) and thus strongly dependent on the magnetic field orientation. The first operation consists of rotating the magnetic field $\mu_0|H| = 0.1$ T on the XZ-plane by fixing $\phi = 0$ and sweeping θ.

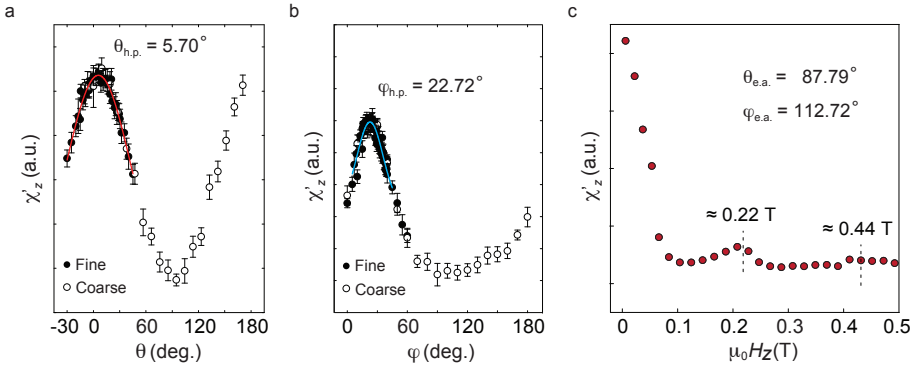

Figure 6.7: **Determination of the easy axis.** (a) χ'_z as a function of angle θ for fixed $\phi = 0°$ (XZ-plane). (b) Same as (a) for fixed $\theta = 90°$ (XY-plane). Maxima signal the two crossings with the hard plane from which the orientation of the easy axis is obtained. (c) χ'_z as a function of magnetic field intensity along the easy axis (labelled by the subscript z). The two peaks signal the expected magnetic level crossings.

As Fig. 6.7(a) shows, χ'_z exhibits a maximum (minimum), signalling a condition relatively closer to (further from) equilibrium. In correspondence of the maximum, for $\theta = 5.70°$, the magnetic field crosses the hard plane, while it is closest to the easy

axis in correspondence of the minimum. An analogous operation is conducted on the XY-plane (Fig. 6.7(b)), where the crossing with the hard plane occurs for $\phi = 22.72°$. The cross product between the two hard plane vectors yields an easy axis with angular coordinates $\theta = 87.79°$ and $\phi = 112.72°$. This axis is hereafter labelled by the subscript z. A confirmation of the accurate orientation of this axis is shown in Fig. 6.7(c). Sweeping the magnetic field along it gives rise to a peak at 0.22 T (0.44 T), in correspondence of the resonance between the spin eigenstates $S_z = 10$ and $S_z = -9$ ($S_z = 10$ and $S_z = -8$) expected at $B_n = \frac{D}{g\mu_B} n = 0.219\,\mathrm{T} \times n$, for $n = 1$ (2).

At this point, the magnetic field is swept on the hard plane for $\theta = 90°$ and $\phi = 22.72°$ (Fig. 6.8). The observed oscillatory behaviour in χ'_z, with minima at the indicated fields, is in accordance with the characteristic quantum interference pattern (see Ref. [17] of the main text) occurring in the proximity to the hard axis – labelled by x hereafter. A 90°-shift from this axis along the hard plane fixes the medium axis – labelled by y – and concludes the orientation procedure.

A.3. DETERMINATION OF THE NUMBER OF MOLECULES

We have determined the number of molecules (bits) in the crystal with two independent methods. The first and most straightforward is that of dividing the weight of the crystal, $m = 0.411$ mg, by the molecular weight, $P_m = 2262.45$ g/mol and multiply by the Avogadro constant. This yields a number of molecules $N = 1.094 \cdot 10^{17}$. The second method takes advantage of the fact that each molecule has a definite spin $S = 10$ ($20\mu_B$). By measuring the saturation magnetization, M_s, of the crystal in the SQUID setup and dividing by the spin of the single molecule yields:

$$N = \frac{M_s(\mathrm{emu})}{20\mu_B}\, 5.1883 \cdot 10^{20}\, \mu_B/\mathrm{emu}$$

Provided $M_s = (2.029 \pm 0.006) \cdot 10^{-2}$ emu (Fig. 6.9), $N = (1.09392 \pm 0.00326) \cdot 10^{17}$.

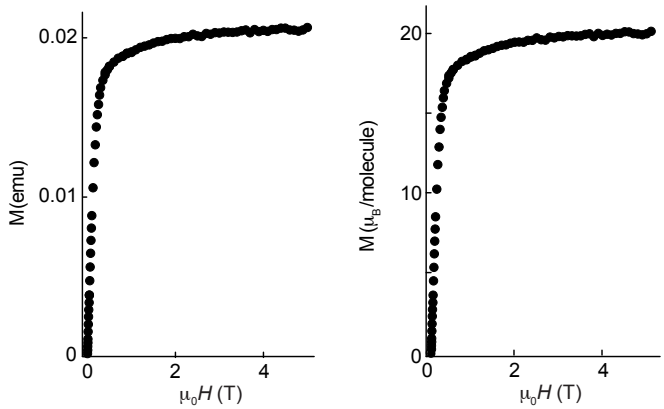

Figure 6.9: **Saturation of the magnetization.** (a) Raw magnetization M (emu) measured in the SQUID as a function of magnetic field. (b) Scaled magnetization $M(\mu_B/\mathrm{molecule})$ obtained normalizing the raw magnetization to the single-molecule value of 20 μ_B. The ratio between the two quantities yields the indicated estimate for the number of molecules in the crystal.

A.4. UNCERTAINTY ESTIMATION

The values of the susceptibility χ'_z given in Fig.2 at each magnetic field result from averaging over $n = 15$ samples. The uncertainty on the mean, σ_χ, is calculated as its standard deviation assuming a normal distribution. The magnetization per molecule M_z is a function of χ'_z and the number of molecules N and is therefore affected by an uncertainty $\sigma_M(H_z)$ given by the propagated uncertainties:

$$\sigma_M(H_z) = \sqrt{\left(\frac{\partial M_z}{\partial \chi'_z}\right)^2 \sigma_\chi^2 + \left(\frac{\partial M_z}{\partial N}\right)^2 \sigma_N^2}.$$

Since the work $W_{2,4}$ is calculated as:

$$W_{2,4} = \oint M_z(H_z)\, dH_z,$$

its upper (+) and lower (−) confidence bounds are given by:

$$W_{2,4}^{\pm} = \oint (M_z(H_z) \pm \sigma_M(H_z))\, dH_z,$$

So that its associated standard deviation $\sigma_{2,4}$ is:

$$\sigma_{2,4} = |W_{2,4} - W_{2,4}^{\pm}|.$$

The uncertainty, $\sigma_{1,3}$, on the work $W_{1,3}$ – obtained by integrating M_y – is calculated using an analogous procedure.

The total error affecting the work $W = W_{1,3} + W_{2,4}$ is then $\sigma = \sqrt{\sigma_{1,3}^2 + \sigma_{2,4}^2}$.

A.5. DETAILS ON THE ENERGY-TIME COST FOR DIFFERENT DEVICES

In Fig. 6.10 we report a more complete version of the chart in Fig. 4 of the main text where the quantities W and τ determining the product $W \cdot \tau$ are plotted on the Cartesian plane. Along the diagonal line, at the top-right corner of the plane sit slow and lossy devices whereas the fast and efficient ones are on the bottom-left. The devices belonging to this corner of the plane are bounded from below by the quantum limit $W \cdot \tau_{\text{rel}} = \pi\hbar/2 = 1.65 \cdot 10^{-27}$ erg/bit·s.

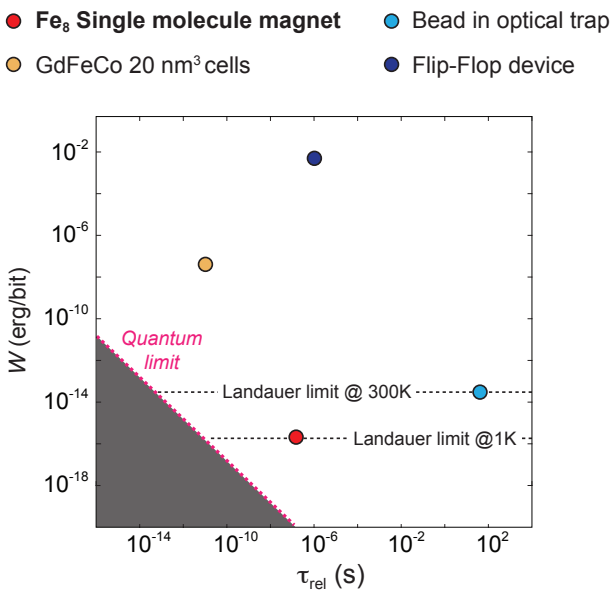

Figure 6.10: **Relaxation time and efficiency comparison.** (a) Chart comparing the energy-time cost of a storage operation performed with various systems. The Fe_8 is the closest to the quantum limit.

7

SUPERCONDUCTING ELECTRODES FOR SINGLE-MOLECULE TRANSPORT STUDIES

You will be part of the flavour of the fruit

René Char

We demonstrate that electronic transport through single molecules (or molecular ensembles), based on gold (Au) electrodes as used in the previous chapters, can be extended to superconducting electrodes by combining gold with molybdenum-rhenium (MoRe). This combination induces proximity-effect superconductivity in the gold to temperatures of at least 4.6 Kelvin and magnetic fields of 6 Tesla, improving on previously reported aluminum-based superconducting nanojunctions. As a proof of concept, we show three-terminal superconductive transport measurements through an individual Fe_4 single-molecule magnet.

Parts of this chapter have been published in Appl. Phys. Lett. **106**, 222602 (2015) by R. Gaudenzi, J. O. Island, J. de Bruijckere, E. Burzurí, T. M. Klapwijk, H.S.J. van der Zant.

1. INTRODUCTION

Recent advances in nanostructure fabrication have made possible to couple superconductivity (SC) with confined systems of electrons. From this interaction, interesting phenomena like Andreev reflections [396] and Yu-Shiba-Rusinov states [397–400] emerge where SC can be used alternatively as a probe to characterize the mesoscopic system [401] or as a tool to influence it [4, 402, 403].

When the confined system is an individual molecule or a nanocrystal, additional internal degrees of freedom like spin and vibrations are predicted to have an effect on the Cooper pair transport. For instance, supercurrent can be employed as a probe for isotropic and anisotropic spinful molecules [404, 405].

So far, only a handful of studies have investigated superconducting transport through individual molecules. Two recent examples are scanning tunneling microscopy studies using lead [4, 406] and two-terminal devices using tungsten [407]. However, due to the absence of a gate, these studies are limited to the off-resonant transport regime and a single fixed charge state. Further studies, involving a combination of resonant transport and SC, are based on electromigrated gold break junctions [408]. These junctions are equipped with a gate electrode in close proximity to the molecule thereby forming a single-molecule transistor. Due to the difficulty of electromigrating materials other than gold, SC is typically induced by proximity to a superconducting material like aluminum [409]. The small superconducting gap of aluminum ($\Delta \approx 0.18$ meV, $T_c \approx 1.2$ K, $B_c \approx 10$ mT), however, limits the range of operation in magnetic field and temperature. In particular, the conditions for attaining the intermediate coupling transport regime ($\Gamma \sim \Delta \sim k_B T_K$) restrict the range of molecular couplings Γ and Kondo energy scales $k_B T_K$. As a consequence limited room is left for the investigation of this intriguing regime where single-electron and many-body physics are directly competing [402, 403, 410, 411].

In this letter, we present a three-terminal hybrid electromigrated break junction, a SN-I-NS junction, that employs molybdenum-rhenium [412] (MoRe) as superconducting material (S) and gold as normal metal (N). Gold allows for the creation of nanogaps (I) by electromigration and is commonly used for contacting single molecules due to its nearly ideal Fermi gas-like density of states (DOS), as well as inertness and compatibility with organic ligand terminations. When in contact with MoRe (60/40 alloy, $\Delta_{BCS} \approx 1.4$ meV, $\xi \approx 20$ nm [412]), we find that the gold junction exhibits a proximitized gap of about 0.7 meV. We characterize transport through these hybrid electromigrated junctions as a function of temperature and magnetic field. We demonstrate superconducting behavior up to at least a temperature of 4.6 K and a magnetic field of 6T. We show preliminary transport measurements resulting from coupling a fabricated SC junction to an individual Fe_4 single molecule magnet (SMM).

2. FABRICATION OF THE PROXIMITY JUNCTIONS

The fabrication of the three-terminal device follows the procedure by O'Neill *et al.* [257] and only the relevant differences are described here. Conventional e-beam lithography and evaporation techniques are employed to fabricate the nanostructure. A scanning electron microscope (SEM) image of the device is shown in Fig. 7.1(a) and a corresponding side-view schematics is shown in Fig. 7.1(b). The

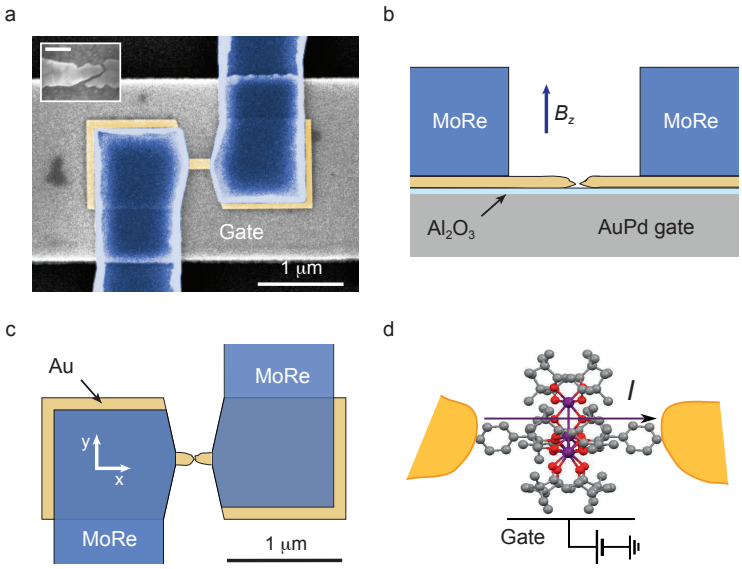

Figure 7.1: **The three-terminal hybrid MoRe-Au superconducting nanojunction.** (a) Scanning electron microscope micrograph of a three-terminal superconducting SNS junction (false colors) before electromigration. The two MoRe patches (purple), acting as source and drain superconducting reservoirs, are in contact with the Au nanoribbon (yellow). The narrow part of the nanoribbon forms the nanowire to be electromigrated. A micrograph of an electromigrated junction is shown in the inset (100 nm scale bar). The z-axis is along the out-of-plane direction. (b) Side view schematics of an electromigrated junction. (c) Top view of (b). The x and y-axis are indicated. (d) Ideal arrangement of Fe_4 molecule between source and drain electrodes forming the three-terminal superconducting molecular transistor.

stack consists of a 75 nm gold-palladium (AuPd) gate coated with 7 nm of atomic layer deposition-grown aluminum oxide (Al_2O_3) on top of which the thin gold wire is deposited. Two MoRe superconducting contacts (110 nm-thick) partially overlap the gold wire, leaving a narrow, rectangular portion uncovered. This 260 nm-long and 100 nm-wide bridge forms the nanowire in which a nanogap is subsequently produced by room-temperature electromigration [3] and self-breaking [257]. In this method, a real-time feedback-controlled current of electrons is passed through the nanowire and used to displace the gold atoms (for the electromigration curve of a characteristic device see Appendix A.1). This process allows the formation of the SN-I-NS junctions, where the vacuum nanogap corresponds to the insulator sandwiched between the two gold portions of the normal wire and the MoRe superconducting patches. In the inset of Fig. 7.1(a) a SEM image of an electromigrated nanowire is shown.

3. TEMPERATURE AND MAGNETIC FIELD CHARACTERIZATION

The electromigrated SN-I-NS junctions are cooled down in a dilution fridge ($T \approx 20$ mK) equipped with a vector magnet. Temperature and magnetic field measurements are performed in a two-probe voltage-bias scheme, i.e. by applying a source-drain

DC bias voltage (V) and recording the resulting current (I). The differential conductance spectrum $\mathrm{d}I/\mathrm{d}V$ versus V is then obtained by taking the numerical derivative. A three-terminal measurement as a function of gate voltage (V_{gate}) and bias voltage is carried out to check for the absence of any gating and/or Coulomb blockade effect, see Appendix A.1.

In Fig. 7.2(a) $\mathrm{d}I/\mathrm{d}V$ spectra as a function of temperature are shown. The low-temperature $\mathrm{d}I/\mathrm{d}V$ trace (T = 100 mK $\ll T_c$) shows a V-shaped dip between two symmetric peaks at bias voltages $2V_{\mathrm{gap}} = \pm 1.4$mV. At higher biases, the conductance smoothly decreases to a plateau value, which we interpret as the normal state resistance regime. Increasing the temperature up to about 1.2 K is seen to only slightly affect the conductance at low voltage. In contrast, an increase in temperature from 2 K up to 3.1 K and further, results in a softening of the dip and a lowering of the two peaks, leaving the higher bias conductance unchanged throughout. Prominently, a residual dip is maintained up to the highest measured temperature of 4.6 K.

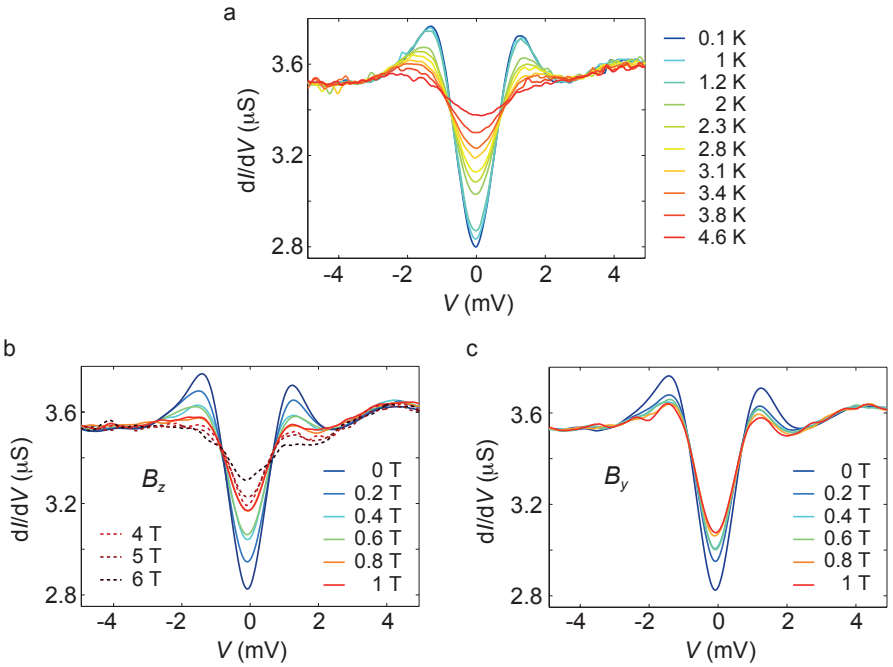

Figure 7.2: **Temperature and magnetic field voltage-bias characterization of the superconductivity.** (color online) (a) Differential conductance spectra measured as a function of temperature ranging from 100 mK to 4.6 K. The characteristic gapped structure of the superconductive DOS persists up to above liquid-He temperature. (b) Differential conductance traces measured as a function of the magnetic field along the z-axis at base temperature $T \approx 22$ mK. The dashed lines indicate the high magnetic field measurements. The signature of the superconducting gap is evident up to above a magnetic field $B_z = 6$ T. (c) Same as (b) but with the magnetic field pointing along the y-axis. The solid lines indicate magnetic fields ranging from $B_y = 0$ T to $B_y = 1$ T. The characteristic peaks and the gap softens comparatively slower than in (b). Note that the vector magnet that we employed is limited to a magnetic field of 1 T along the y-axis.

The presence of a reduced gap-like structure in bias voltage with characteristic energy $E_{\mathrm{gap}} < \Delta_{\mathrm{BCS}}$ is a well-known signature of proximity-induced superconductiv-

ity [413]. This effect has been already experimentally observed, among others, in Ref. [409, 414] and theoretically investigated in detail by several authors [415, 416]. In these previous experiments as well as in the one discussed here, the superconducting coherence length ξ compares with the characteristic lengths of the gold normal metal portion as $\xi, L \gg l_e \gg \lambda_F$, where L is the length of the bridge, l_e and λ_F are the elastic scattering length and Fermi wavelength respectively. This situation is called the quasi-classical diffusive limit for which the theory has been formulated by Usadel [417]. A spatially-dependent density of states along with a reduced gap $E_{gap}(L) < \Delta$ arises from an application of the model to a N film of finite length L connected to a superconductor. Within this framework, the peaks and the dip in the dI/dV spectra observed in this experiment result from the convolution of the superconducting peaks and the reduced gap in the proximity-induced DOS at the two N-I interfaces.

We also investigate the persistence of SC upon application of an external magnetic field for different spatial directions. Fig. 7.2(b) shows the differential conductance spectra as a function of a field along the z-axis, i.e. perpendicular to the plane of the nanostructure (see Fig. 7.1(c)). A gradual decrease of the characteristic features is observed up to 1T. For higher magnetic field values a further decrease is accompanied by a complete suppression of the peaks at ± 1.4 mV. A dip is present at the highest B-field value of 6 T signalling the presence of a residual superconducting DOS. Measurements with equivalent magnetic field intensities but along the y-axis, i.e. in-plane and perpendicular to the transport direction, are performed and the results displayed in Fig. 7.2(c). The softening of the dip and the coherence peaks for increasing magnetic fields is also observed. However, the spectra for the y-axis field maintain stronger superconducting features as compared to those of Fig. 7.2(b) for corresponding magnetic field values. Equivalently, the magnetic field B_y acts comparatively weaker than B_z in suppressing the proximity-effect SC. In analogy with the temperature-dependent measurements, we note that the high-bias regions ($eV > 2E_{gap}$) of the spectra are not affected by variations of the magnetic field.

The experimental magnetic field dependences can also be qualitatively explained within the diffusive Usadel framework. As shown in Belzig *et al.* [416], the applied magnetic field can be incorporated into an effective pair breaking rate Γ_{eff} that affects the magnitude of the coherence peaks and the reduced gap energy. This pair breaking mechanism is proportional to the intensity of the magnetic field vector, $|B|$, as well as the dimension of the nanowire transverse to it, W, ($\Gamma_{eff} \sim B^2W^2$). In the present situation, the transverse directions corresponding to the magnetic fields B_z and B_y are the nanowire width and thickness, respectively. This would result in a stronger pair breaking effect along the z-axis as compared to the y-axis ($\Gamma^z_{eff}/\Gamma^y_{eff} \sim 100$), qualitatively consistent with the experimental observations (for an additional sample see Appendix A.2). We note that the persistence to high-magnetic fields can be partially ascribed to junction shape and/or geometry effects.

4. THE SUPERCONDUCTING MOLECULAR TRANSISTOR

Envisioning the use of our hybrid junctions as a superconducting molecular transistor, we present here preliminary results obtained from coupling an individual Fe_4 single-molecule magnet [246] (SMM) to superconducting leads (schematically shown in Fig. 1(d)). Figure 7.3(a) displays the differential conductance map of an in-

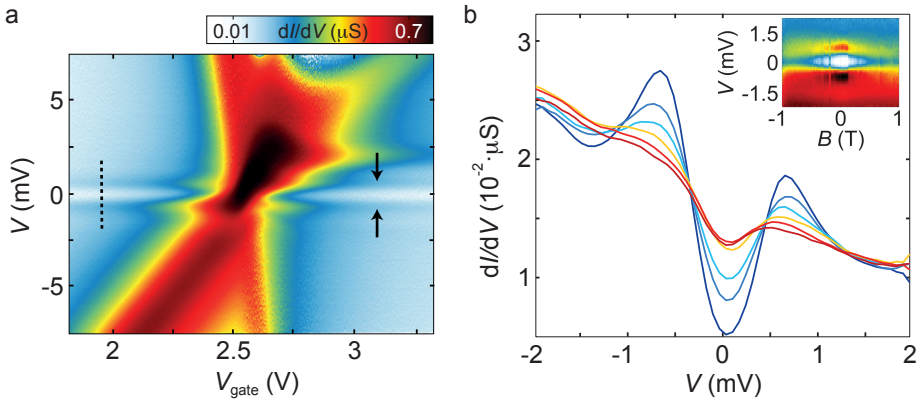

Figure 7.3: **The superconducting single-molecule transistor.** (color online) (a) Differential conductance map as a function of gate and bias voltages measured at $B = 0$ T and $T = 0.6$ K. Superconductivity and Coulomb blockaded transport superimpose in the two stable charged states. The horizontal lines of increased conductance (marked by black arrows) and the low-bias dip indicate the superconducting DOS of the leads. At the charge degeneracy point ($V_g \approx 2.5$ V) the superconducting gap is lifted and the conductance greatly increases. (b) Differential conductance spectra as a function of magnetic field and bias voltage at fixed gate voltage $V_{gate} = 1.95$ V (dashed line in the left stable charge state of (a)). The spectra are extracted from the map in the inset, starting from $B = 0$ T (blue line) to $B = 1$ T (red line) at a regular spacing $\Delta B = 0.2$ T. A weak trace of the gapped DOS is still visible at $B = 1$T.

dividual Fe_4-SMM as a function of gate and bias voltages for an external magnetic field $B = 0$ T. The standard features of sequential electron tunneling and Coulomb-blockade are seen. Each of the two low-conductance regions on either side of the charge degeneracy point ($V_{gate} \approx 2.5$ V, $V \approx 0$ V) corresponds to a stable charge state. Within these regions, the dip and the horizontal lines of increased conductance centered around zero-bias (black arrows) signal the expected SC density of states of the two leads. At the degeneracy point, the superconducting gap-like structure is lifted and a significant increase in zero-bias conductance occurs. In order to compare these observations with those on bare junctions, the differential conductance was measured as a function of magnetic field B_z, Fig. 7.3(b), at $V_{gate} = 1.95$ V, far into the off-resonant regime (dashed line in Fig. 7.3(a)). A reduced gap $2E_{gap} \approx 0.7$ meV appears. Gradual suppression of the superconducting features takes place from zero magnetic field to about 0.6 T, leaving a residual gap structure weakly evolving from 0.6 T to 1T. In the inset of Fig. 7.3(b) the differential conductance map from which the spectra are extracted is shown. The magnetic field ranges from -1 T to +1T. The smoothing of the superconducting features is symmetric for negative and positive field values.

In the present example the charging energy $U \geq 100$ meV and the tunneling rate $\Gamma \approx 1$ meV [1], characteristic energies of single-electron transport, are related to E_{gap} by $U \gg \Gamma \gtrsim E_{gap}$. The first condition, $U \gg \Gamma$, guarantees Coulomb blockade and single-electron-transistor behaviour [91]. The second condition, $\Gamma \gtrsim E_{gap}$, allows for the off-resonant inelastic quasiparticle tunneling and would theoretically enable the on-

[1] The value of Γ is extracted from the FWHM of the lorentzian fit of the Coulomb peak at a magnetic field of 8T, in order to minimize the influence of superconductivity on transport. The lower bound value for U is estimated from the full V vs V_{gate} conductance map (See also Appendix A.3).

resonant transport of both single electrons and Cooper pairs [418]. The off-resonant transport and the strong increase in zero-bias conductance observed in Fig. 7.3(a) are consistent with this picture and will be the subject of further study.

5. CONCLUSIONS

We have presented a three-terminal hybrid electromigrated break junction with high-critical field superconducting electrodes for single-molecule studies. In this SN-I-NS junction, superconductivity is induced in the gold by proximitizing it with MoRe. Gold as a normal metal allows for the creation of nanogaps by controlled electromigration and preserves the advantage of molecule-gold chemistry. The use of MoRe as a superconductor guarantees an induced gap larger than the previously reported Al-based designs. We characterize induced superconductivity as a function of temperature and magnetic field intensity and direction and demonstrate superconducting behaviour up to 4.6 K and a critical magnetic field of 6T. We finally show preliminary transport measurements through an individual Fe_4 single molecule magnet. Coexistence of Coulomb blockade and superconducting transport is observed. Low-bias on- and off-resonant conductance behaviour suggests that, owing to the relatively high gap energy E_{gap}, the condition $U \gg \Gamma \gtrsim E_{\mathrm{gap}}$ for intermediate coupling transport is satisfied. This intermediate coupling transport regime appears to be promising for investigating the interaction between confined electrons and superconductivity. Moreover, it constitutes the prerequisite - with the additional condition $k_{\mathrm{B}} T_{\mathrm{K}} \sim E_{\mathrm{gap}}$ - for the investigation of the interplay between Kondo screening and superconducting pairing.

A. APPENDIX

A.1. ELECTROMIGRATION AND THREE-TERMINAL MEASUREMENTS

The electromigration of the hybrid junctions described in this chapter does not qualitatively differ from the full gold junction described in Ref. [257, 305]. Nonetheless we describe it here to evidence that there are only some quantitative differences between the two.

As is the case with full gold junction, a feedback controlled software is used to monitor and adjust the voltage across the gold wire to steadily create a constriction at room temperature. Fig. 7.4(a) shows the typical current voltage characteristics recorded during the creation of a constriction. The voltage is ramped up to > 1V at which point the resistance of the junction starts to change and the feedback software decreases the voltage to arrest an avalanche breaking of the wire. This continues to create a final constriction which is left to self-break at room temperature leaving a few-nanometer gap.

Figure 7.4(b) shows a three terminal measurement of an SN-I-NS junction taken at 100 mK after the electromigration and self-breaking process. A numerical derivative is taken to plot dI/dV versus bias and gate voltage. The conductance does not change over the accessible gate voltage range (±6 V) indicating tunneling through a gate independent vacuum barrier.

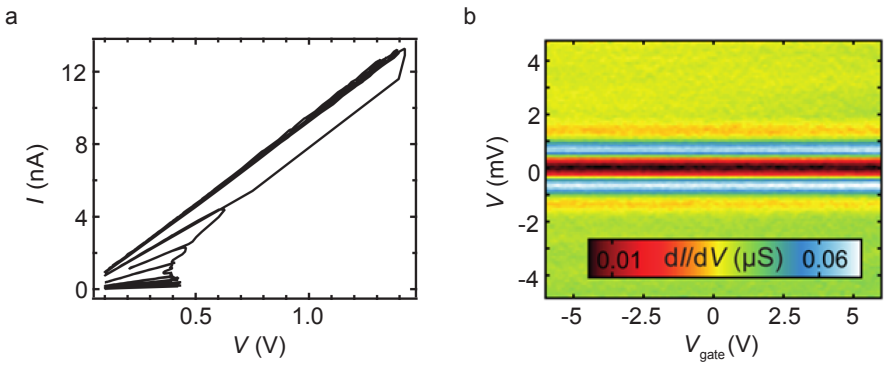

Figure 7.4: (a) Current-voltage characteristics for the electromigration of a typical device. (b) Three terminal measurement of an SN-I-NS junction at low temperature (100 mK). Current is measured as a function bias voltage and gate voltage. A numerical derivative is taken to plot $\mathrm{d}I/\mathrm{d}V$ as a function of V and V_{gate}.

A.2. TEMPERATURE AND FIELD DEPENDENCE FOR A SECOND DEVICE

Figure 7.5 shows the complete characterization for a second device. This SN-I-NS junction shows the same characteristics as the main text device. The softening of the proximity induced gap with temperature is shown in Figure 7.5(a). Again, a residual gap is still present at 4.5 K. Figure 7.5(b) and Fig. 7.5(c) for the magnetic field dependence in the z and y-axis. Greater modulation of the gap is found for fields in the z-axis direction.

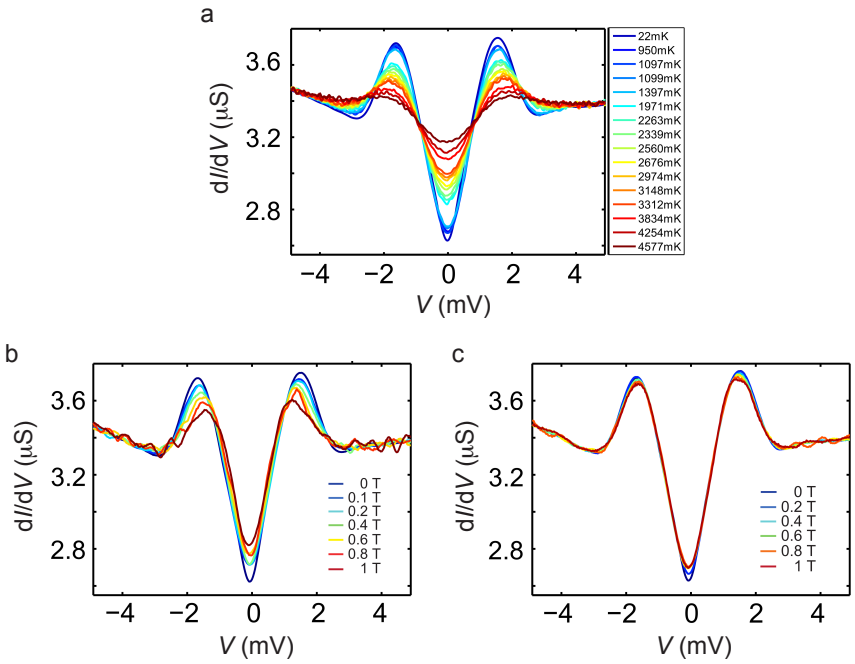

Figure 7.5: (a) Temperature dependence of the SN-I-NS junctions. The numerical derivative is plotted versus the applied bias voltage. (b) Magnetic field dependence of the junction with the external field in the z-axis direction. (c) Magnetic field dependence of the junctions with the external field in the y-axis direction.

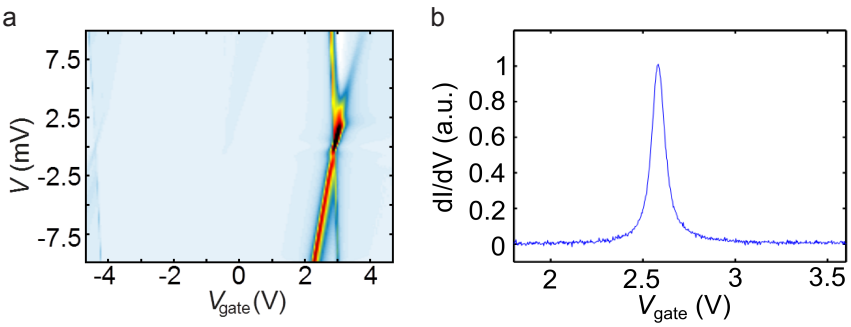

Figure 7.6: (a) Coarse differential conductance map of an individual Fe_4-SMM as a function of gate and bias voltages. The selected voltage range is the maximum allowed by the gate oxide. (b) Normalized differential conductance zero-bias trace (charge degeneracy point) as a function of gate voltage obtained at a magnetic field of 8 T. At this field superconductivity is completely lifted so that regular quasiparticle transport is restored. The molecule-electrode coupling constant is obtained by fitting the trace to a lorentzian.

A.3. ESTIMATION OF THE CHARGING ENERGY AND ELECTRODE COUPLING

As the superconducting molecular junction is formed, an estimation of the charging energy U can be obtained from the V *vs.* V_{gate} differential conductance map according to $U = \beta \Delta V_{\text{gate}}$, where β is the gate coupling, obtained from the slopes of the Coulomb edges of the same conductance maps, and ΔV_{gate} is the distance in gate voltage between two charge degeneracy points. From Figure 7.6(a), β = 13 mev/V and $\Delta V_{\text{gate}} \geq 7.5$ V, so that $U \geq 100$ meV.

The molecule-electrode coupling constant Γ is obtained from fitting the charge degeneracy peak ($V = 0$ V, $B = 8$ T) shown in Figure 7.6(b) to a Lorentzian function. The FWHM of the Lorentzian extracted from the fit multiplied by the gate coupling yields $\Gamma \approx 1$ meV. The high magnetic field ensures a negligible influence of superconductivity on transport.

8

CONCLUSION AND OUTLOOK

[...] He did not judge any new idea as foolish,
nor undisputable any established concept.

Michel Houellebecq

I have always believed
in the future of quantum technologies!

Galileo Galilei

This chapter contains a collection of conclusions from the previous chapters. In fact, starting from the principle that nothing ever *comes to a real conclusion* – in *life as well as in molecular electronics –, we are bound to seamlessly transform these conclusions into potential continuations in a free dialogue with the lacks, failures and open questions in our results. The discussion developing out of this liberty will inevitably be more informal and, as any* according-to-the-author *compilation, reflects an opinable view.*

In this work, we have addressed a collection of phenomena arising from the combination of two eminently quantum ingredients of reality: confinement of charged particles and the property of spin. Looking down on the landscape from the privileged viewpoint of the conclusion, we realize that this dissertation has brought us from the exploration of a pure paramagnetic system like the monoradical to a series of high-spin isotropic (Heisenberg-like) magnets, and further to fully-fledged nanomagnets with a giant and anisotropic (Ising-like) spin. Eventually, the last step of the path has provided us with a pair of "upgraded" (superconducting) glasses allowing the investigation of all these systems from the prospective of electron *pairs*. As we will see below, one such investigation has already been performed.

In the introductory chapter, we have explored with an experimental example the various forms of excitation and relaxation emerging from the interaction between the itinerant continuum of electrons in the leads and the few electrons confined discretely in the molecule. As mentioned in the last paragraph of the chapter, an extension of this analysis from charge to heat transport yields interesting results. To understand how things work from the prospective of heat and therefore offer a motivation to continue in that direction, let us see how relaxation influences the heat flow in a very simple instance. When inelastic cotunneling is involved, an energy transfer between the scattering electrons (electric energy) and the molecular spin system (magnetic energy) occurs. Upon regular relaxation[1], the energy gained by the system is equally dissipated into the two leads in the form of thermal energy, leading to a net electrical-to-thermal energy transformation. As we have seen, another form of relaxation can also take place where the "hot" electron is rapidly transferred to the low-energy lead. In this case, the distribution of the dissipated thermal energy is determined by the position of the energy level and can therefore be uneven between the two leads. The moral of this simple fact is that heat flow in not necessarily coupled from charge flow and constitutes thus a separate spectroscopic tool that can provide more, or different, information than charge-based spectroscopy.

Further in the dissertation, molecules from the same radical family have been proposed following the direction of increasing complexity. The simplest one featured a shelled, radical electron in its neutral state exhibiting a Kondo effect robust against mechanical and electrostatic variations of the surrounding environment. The chemical unit at the base of this radical is then assembled to form "triangular" di- and tri-radical species. The first shows the feasibility of electric control of the exchange interactions – at the base of one of the implementation of the $\sqrt{\text{SWAP}}$ gate –; the second shows that the same molecule can be found to exhibit a ferro- or antiferromagnetic exchange interactions between its radical spins as a function of mechanical torsion. These two examples illustrate the effect of the solid-state electrodes' when a magnetic molecular system interfaces with them and show, in turn, their role in stabilizing certain magnetic configurations as a result of electronic and/or mechanical interactions.

While the monoradical Kondo system exhibited an unprecedented robustness in virtue of its simplicity, the higher magnetic complexity of the two poly-radicals warn of the difficulty of incorporating high-spin molecules into solid-state devices without affecting their properties. On the other hand, as mentioned in Chapter 2, the

[1] i.e. not COSET, see Chapter 2

additional degrees of freedom arising from this complexity provide, opportunities to tune and "extend" these properties. In laying out an outlook in the form of future experiments for the three chapters treating the radicals, we should consider curses and blesses of each molecule.

The robustness of the Kondo effect in the monoradical species made us think of them as excellent candidates for introducing them across the proximitized superconducting electrodes of Chapter 7. The additional fact that the robustness is accompanied by a good consistency in the Kondo energy scales is particularly useful provided not much freedom is given for the reduced gap energy – constrained by the BCS gap of the superconducting electrodes and the distance between them. In this case, the Kondo strength, $k_B T_K \approx 1$ meV, approximately matches the superconducting energy scale $\Delta \approx 0.4 - 0.7$ meV. This has given us the possibility of studying the competition between the two effects [32], resulting into a mapping of the Shiba bound state for the two regimes where Kondo screening is stronger or weaker than the energy scale characterizing superconductivity.

The results obtained are encouraging, yet the coupling between molecule and electrodes is stochastic and thus sample-to-sample dependent. Although the "fixed-by-chemistry" electronic configuration of the radical – as compared to an electrically-added electron – greatly limits the range of variability of the Kondo coupling strengths, the fine tunability of the latter is still lacking. In scanning tunneling microscopy configurations, this limitation has been coped with using different absorption sites to tune the Kondo coupling [4]. Yet, in both cases, this aspect limits the complete mapping of the competition between Kondo and superconducting pairing and, ultimately, the possibility of driving the system *through* the Kondo singlet to superconducting doublet quantum phase-transition. Here, the gate electrode could come at rescue if combined with a molecule exhibiting electric tunability of the Kondo strength. The monoradical and diradical species have shown in few cases this tunability.

Regarding the di-radical and tri-radical species, an interesting direction is suggested by their "triangular" arrangement of the magnetic interactions and the "flexibility" of the magnetic ground state. Comparing the results obtained in Chapter 4 and Chapter 5 it is evident that, from the magnetic point of view, the tri-radical is a particular case of the reduced di-radical, i.e. the di-radical with an added electron: the first is obtained from the second when the three exchange couplings are set to be equivalent, which results into the degeneracy of the doublets $|D_{\pm}\rangle$ (see the analysis in Appendix A.2 of Chapter 4). This raises a question on the mechanism that seemingly conserves the symmetry of the tri-radical[2]. One hypothesis is the fact that the steric hindrance induced by the bulky chlorine atoms forces the same torsion angle to the three groups.

In both the di-radical and tri-radical systems, while the quartet ground state in the ferromagnetic configuration is not particularly interesting, the doublets generated by the antiferromagnetic interactions are *delocalised* and bear triplet components as can be seen from equation (4.3). These ingredients are at the origin of magnetic frustration, an interesting manifestation of which is ferromagnetic Kondo. This effect contrasts with the more usual (antiferromagnetic) Kondo in that it arises from

[2]This conclusion is based on the fact that no other doublet state is present *in the measured bias window* ($\approx \pm 30$ meV) although we cannot exclude the presence of a high-energy ($\gtrsim 30$ meV) doublet.

the interplay between the screening of one of the molecular spins and the local magnetic interactions that that spin entertains with the remaining two spins [419–421]. By increasing one of the interactions a pseudo-doublet, regularly Kondo screened, transforms into the delocalized doublet containing a triplet state, where the interaction between the conduction electrons and the impurity is ferromagnetic. This transition, occurring when the interactions are symmetric, is a quantum phase transition – Kosterlitz-Thouless in case of a imperfect symmetry – which quenches the Kondo screening, leaving a local moment asymptotically free[3]. Starting from one of our molecular species, such phenomenon could be observed upon mechanical manipulation of the exchange couplings with a break junction or the tip of an STM.

In Chapter 7 we have shown how to replace parts of the solid-state molecular device with the high-field superconductor alloy molybdenum-rhenium. The idea behind this hybridization was to maintain the existing gold-molecule bonding chemistry and electromigration ease while being able to measure superconducting transport through molecules. These constrains dictated the choice of proximity effect which, in our electromigrated SN-c-NS arrangement[4], is an interesting, and complex, phenomenon *per se*. The obtained results without and with molecules are a *proof of concept*, and thus not definitive. Concerning the empty gaps, modelling them with 1D Usadel diffusive equation results in qualitative agreement with the measured spectra [422], but cannot account for the anomalously large gap size and its relatively high softness in combination with the permanence up to high magnetic fields [422]. Despite the need for improvement and the open questions, interesting experimental observations have come out – besides the aforementioned investigation on Shiba states in combination with organic radicals. One of those, obtained with the Fe_4 single molecule magnet and briefly mentioned in Chapter 7, is displayed in Fig. 8.1. There, the degeneracy peak seems to be unaffected by the intragap quasiparticle depletion visible in the off-resonant region: the current in correspondence of the peak is enhanced rather than suppressed. As can be seen in Fig. 8.1(b), the enhancement sets in at the superconducting transition ($B \approx 1$ T). This is surprising because Andreev pairs are forbidden to occupy the resonant molecular energy level *in pairs* – the interaction energy U is by far the largest scale of the problem. A possible way out comes from the consideration that the electrons of the pair tunnel *one-by-one* on the molecule, without losing the coherence, and reform in the drain electrode. Such a mechanism is predicted to be possible if the tunneling ($\propto \Gamma$) happens faster than the pair decoherence ($\propto \Delta$) [418]. Provided $\Gamma \approx 1$ meV and the reduced gap[5] energy, $\Delta \approx 0.35$ meV, this effect should be contemplated.

All this said, in order to appreciate all the subtle effects deriving from the combination with magnetic molecules, an hard superconducting gap seems to be essential. Nano-fabrication work in the direction of reducing the spacing between the superconducting patches in the proximity setting as well as directly producing superconducting electrodes is ongoing. The former option requires a change in the design of

[3] The analogy to the asymptotic freedom comes from the zero-bias conductance behaviour in temperature: as opposed to regular Kondo, here increasing the Kondo energy scale ($T \to 0$) results in a weaker interaction.

[4] Electromigration allows to obtain constrictions/point contacts (for which 'c' stands) with different conductances or a tunnel barrier.

[5] We remind the reader that in the proximity-induced superconductivity, the BCS gap gets *reduced* in the normal metal.

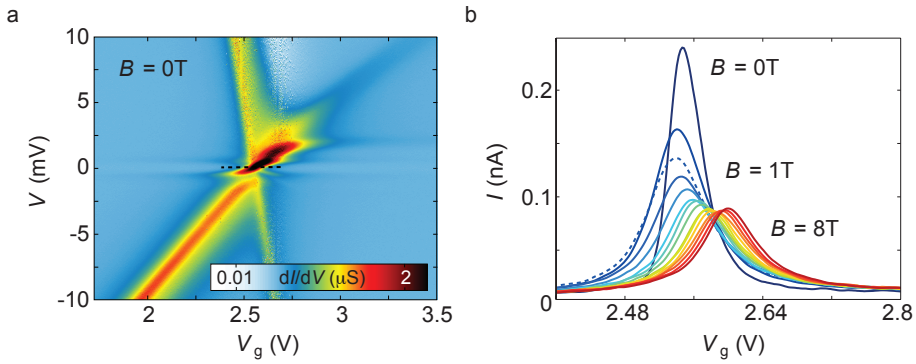

Figure 8.1: **Superconductivity-induced current enhancement at resonance.** (a) Bias-gate differential conductance diagram of a Fe_4 magnetic molecule at $B = 0$ T measured with the proximity-induced leads of Chapter 7. The superconducting gap around zero-bias is clearly visible in the off-resonant regime, but remarkably lifted near the degeneracy point. (b) Evolution of the degeneracy point (black dashed line in (a)) as a function of magnetic field (gate spectroscopy). For $B \lesssim 1$ T, in correspondence with the superconducting transition, the current is strongly enhanced.

the gold nanowire towards a bow-tie geometry. In this way, the higher current density at the constriction can compensate for the larger heat drainage to the more closely-spaced bulk leads. For the second alternative, among the large-gap pure materials, lead seems to be the most appropriate one: its high room temperature atomic mobility and low melting point allow the generation of "clean" gaps by electromigration[6]. Work on this material is currently under way and shows promising results [423].

At last, we move to the subject of Chapter 6. There we performed a test of the Landauer limit on a ensemble of molecular spin bits. This test differs from the two previous ones in literature in the fact that it is performed on a system of *single* quantum spins and not on single-domain magnetic dots (with $\gtrsim 10^4$ individual spins) [384] or with a micrometric bead [383]. Respectively due to their large number of spins and size, these two systems are classical in the sense that they have a continuum of possible states and are too large objects to exhibit quantum tunneling. Our Fe_8 system, as the name suggests, is made of only eight individual spins, the anisotropy and exchange interactions of which are created at the *molecular* level. The result is an Ising system with discrete magnetic levels exhibiting quantum tunneling of magnetization, which ultimately enables the annealing-like speed-up of the reset operation. The molecular nature of this system also enables the repetition and packing into a crystal of the single spins with negligible exchange interactions[7] and thus allows, quite uniquely, the macroscopic measurement of the thermodynamic work and relaxation time on a system whose dynamics is ruled by quantum mechanics. This last statement gives us the opportunity for an elucidating digression: as detailed in the relative chapter, the mixed states induced by the transverse magnetic field con-

[6] Repeated trials of electromigrating molybdenum-rhenium electrodes resulted in multiple unwanted quantum dots with small charging energies which render the measurements of molecules impossible. These quantum dots are presumably the result of the presence of grains of the material in the gap.

[7] The packing that guarantees negligible exchange interactions between the Ising giant spins also allows weak, but non-vanishing, dipolar interactions. Precisely this macroscopic manifestation of quantumness allows to traverse a quantum phase transition between ferromagnetic and paramagnetic.

sist of pairs of symmetric and antisymmetric combinations of the spin eigenstates $\pm m$ forming anticrossings split by energies Δ_m. Given the relatively short coherence time $\sim \hbar/\Delta_m \lesssim 1$ ns [389, 424], the spin effectively lives in an *incoherent* superposition of the split pair, rather than coherently oscillating. This incoherent quantum dynamics is a characteristics of the practical implementations of quantum annealers. Without opening the Pandora's box on their debated quantum speed-up that followed the claim of the D-wave computer [425, 426], the one experiment on annealing of a spin glass by Aeppli *et al.* [427] undeniably "indicate that quantum annealing hastens convergence to the optimum state", simply because as the transverse field grows "there is a spectacular increase of the relaxation". At all similar in this aspect[8], our experiment exploits, in essence, a quantum annealing process ending in an "optimum" – the ground state – constituted by the "trivial" configuration of all the spins aligned and where, equivalently, finding the ground state identifies with *initializing* the bits.

Despite the still unclear role of quantumness in annealing processes, what distinguishes an annealer from a quantum gate, or a combination of them, is the use of quantum *resources* like coherent superposition and/or entanglement. The topic just discussed constitutes thus a natural bridge to a closing comment – which, in the heydays of the Quantum Manifesto[9] (http://qurope.eu/manifesto), cannot be omitted – on the role and stand of molecules in the quantum computation contest. This boils down to the assessment of their characteristics in terms of *coherence* and scalability/addressability. In regard of the former, a consistent effort has been put in boosting the phase memory time of bulk molecular spins [428–431] to values which would render molecules promising qubits. Coherent manipulation has been shown also in single-molecule devices based on single-ion molecular magnets using nuclear and electronic spin for manipulation and read-out [35]. If coherence seems not to be the major issue, due to the wide possibilities of chemical synthesis, scalability and addressability still remain complementary challenges. To illustrate this, it is instructive to compare two implementations of the $\sqrt{\text{iSWAP}}$ quantum gate: the molecular modular design proposed in Ref. [319] and that discussed in the context of the di-radical of Chapter 4. In the first case, the chemistry has been demonstrated to be scalable, but the sharp redox switching needed for a proper working would require strong coupling to gates about 3 nm apart. In the second case, electric control is more readily implemented, but the scalability, in the absence of accurate control of the single molecule positioning, poses huge challenges. Paradigms like the cross-bar architecture shown in Ref. [432] could be viable platforms, but, in general, it should be kept in mind that these solutions will have to confront the already relatively high technology readiness level and the fast pace of the existing fully solid-state paradigms.

With the hope of having cast, through this work, a flash of light on the virtues of molecules for fundamental studies, the question that still remains is: will the unique attributes of molecules ever make them also the stars of quantum technologies?

You only, dear reader of the future, will know.

[8] Coincidentally, the random insertion of antiferromagnetic interactions would render the low temperature dipolar ferromagnetic ordering of our Fe_8 crystal analogous to that of the disordered magnet used in the mentioned experiment.

[9] A quick word search through it reveals, in case the bias were not already obvious, a 6/1 ratio of "solid-state" to "molecular" entries.

REFERENCES

[1] J. Monod, *Chance and necessity: an essay on the natural philosophy of modern biology* (Knopf, New York, 1971).

[2] J. R. Heath and M. A. Ratner, *Molecular electronics,* Physics Today **56**, 43 (2003).

[3] H. Park, A. K. L. Lim, A. P. Alivisatos, J. Park, and P. L. McEuen, *Fabrication of metallic electrodes with nanometer separation by electromigration,* Appl. Phys. Lett. **75**, 301 (1999).

[4] K. J. Franke, G. Schulze, and J. I. Pascual, *Competition of superconducting phenomena and kondo screening at the nanoscale,* Science **332**, 940 (2011).

[5] J. Repp, G. Meyer, S. M. Stojković, A. Gourdon, and C. Joachim, *Molecules on insulating films: Scanning-tunneling microscopy imaging of individual molecular orbitals,* Phys. Rev. Lett **94**, 026803 (2005).

[6] J. Repp, G. Meyer, S. Paavilainen, F. E. Olsson, and M. Persson, *Imaging bond formation between a gold atom and pentacene on an insulating surface,* Science **312**, 1196 (2006).

[7] R. Frisenda, S. Tarkuç, E. Galán, M. L. Perrin, R. Eelkema, F. C. Grozema, and H. S. van der Zant, *Electrical properties and mechanical stability of anchoring groups for single-molecule electronics,* Beilstein journal of nanotechnology **6**, 1558 (2015).

[8] Y. S. Park, A. C. Whalley, M. Kamenetska, M. L. Steigerwald, M. S. Hybertsen, C. Nuckolls, and L. Venkataraman, *Contact chemistry and single-molecule conductance: a comparison of phosphines, methyl sulfides, and amines,* Journal of the American Chemical Society **129**, 15768 (2007).

[9] D. Djukic, K. S. Thygesen, C. Untiedt, R. H. M. Smit, K. W. Jacobsen, and J. M. van Ruitenbeek, *Stretching dependence of the vibration modes of a single-molecule* Pt$-$h$_2-$Pt *bridge,* Phys. Rev. B **71**, 161402 (2005).

[10] R. Frisenda, M. L. Perrin, and H. S. van der Zant, *Probing the local environment of a single ope3 molecule using inelastic tunneling electron spectroscopy,* Beilstein journal of nanotechnology **6**, 2477 (2015).

[11] E. Burzurí, Y. Yamamoto, M. Warnock, X. Zhong, K. Park, A. Cornia, and H. S. J. van der Zant, *Franck–Condon blockade in a single-molecule transistor,* Nano Lett. **14**, 3191 (2014).

[12] T. Kozlova, M. Rudneva, and H. W. Zandbergen, *In situ tem and stem studies of reversible electromigration in thin palladium–platinum bridges,* Nanotechnology **24**, 505708 (2013).

[13] J.-P. Cleuziou, W. Wernsdorfer, V. Bouchiat, T. Ondarçuhu, and M. Monthioux, *Carbon nanotube superconducting quantum interference device,* Nature nanotechnology **1**, 53 (2006).

[14] M. Aprili, *The nanosquid makes its debut,* Nature nanotechnology **1**, 15 (2006).

[15] R. Sessoli, *Nanoscience: Single-atom data storage,* Nature **543**, 189 (2017).

[16] M. L. Perrin, C. J. O. Verzijl, C. A. Martin, A. J. Shaikh, R. Eelkema, J. H. van Esch, J. M. van Ruitenbeek, J. M. Thijssen, H. S. J. van der Zant, and D. Dulić, *Large tunable image-charge effects in single-molecule junctions,* Nature Nanotechn. **8**, 282 (2013).

[17] J. Fock, M. Leijnse, K. Jennum, A. Zyazin, J. Paaske, P. Hedegård, M. B. Nielsen, and H. Van der Zant, *Manipulation of organic polyradicals in a single-molecule transistor,* Physical Review B **86**, 235403 (2012).

[18] S. Sanvito, *Molecular spintronics: The rise of spinterface science,* Nature Physics **6**, 562 (2010).

[19] C. Cervetti, A. Rettori, M. G. Pini, A. Cornia, A. Repollés, F. Luis, M. Dressel, S. Rauschenbach, K. Kern, M. Burghard, *et al., The classical and quantum dynamics of molecular spins on graphene,* Nature materials **15**, 164 (2016).

[20] Y.-S. Chen, M.-Y. Hong, and G. S. Huang, *A protein transistor made of an antibody molecule and two gold nanoparticles,* Nature nanotechnology **7**, 197 (2012).

[21] I. Newton, *On the belief in a god,* in Letters to Dr. Bentley , (http://www.bartleby.com/209/603.html) (1756).

[22] J. Barrow and F. Tipler, *The Anthropic Cosmological Principle* (Oxford University Press, 1986).

[23] J. Bartolomé, F. Luis, and J. F. Fernández, eds., *Molecular magnets: Physics and applications* (Springer, Heidelberg, 2014).

[24] C. Huang, A. V. Rudnev, W. Hong, and T. Wandlowski, *Break junction under electrochemical gating: testbed for single-molecule electronics,* Chem. Soc. Rev. **44**, 889 (2015).

[25] K. Moth-Poulsen, ed., *Handbook of single-molecule electronics* (Pan Stanford Publishing Pte. Ltd, Singapore, 2016).

[26] M. L. Perrin, E. Burzurí, and H. S. J. van der Zant, *Single-molecule transistors,* Chem. Soc. Rev. **44**, 902 (2015).

[27] Y.-S. Chen, M.-Y. Hong, and G. S. Huang, *A protein transistor made of an antibody molecule and two gold nanoparticles,* Nature nanotechnology **7**, 197 (2012).

[28] N. C. Seeman, *Dna in a material world,* Nature **421**, 427 (2003).

[29] Z. Xie, T. Z. Markus, S. R. Cohen, Z. Vager, R. Gutierrez, and R. Naaman, *Spin specific electron conduction through dna oligomers,* Nano Lett **11**, 4652 (2011).

[30] R. Naaman and D. H. Waldeck, *Spintronics and chirality: spin selectivity in electron transport through chiral molecules,* Annu Rev Phys Chem **66**, 263 (2015).

[31] K. J. Franke and J. I. Pascual, *Effects of electron–vibration coupling in transport through single molecules,* J. Phys.: Condens. Matter **24**, 394002 (2012).

[32] J. O. Island, R. Gaudenzi, J. de Bruijckere, E. Burzurí, C. Franco, M. Mas-Torrent, C. Rovira, J. Veciana, T. M. Klapwijk, R. Aguado, and H. S. J. van der Zant, *Proximity-induced shiba states in a molecular junction,* Phys. Rev. Lett. **118**, 117001 (2017).

[33] R. Frisenda, R. Gaudenzi, C. Franco, M. Mas-Torrent, C. Rovira, J. Veciana, I. Alcon, S. T. Bromley, E. Burzurí, and H. S. J. van der Zant, *Kondo Effect in a Neutral and Stable All Organic Radical Single Molecule Break Junction.* Nano Lett. **15**, 3109 (2015).

[34] M. Koole, J. M. Thijssen, H. Valkenier, J. C. Hummelen, and H. S. van der Zant, *Electric-field control of interfering transport pathways in a single-molecule anthraquinone transistor,* Nano Lett **15**, 5569 (2015).

[35] S. Thiele, F. Balestro, R. Ballou, S. Klyatskaya, M. Ruben, and W. Wernsdorfer, *Electrically driven nuclear spin resonance in single-molecule magnets,* Science **344**, 1135 (2014).

[36] R. Meservey and P. Tedrow, *Spin-polarized electron tunneling,* Phys. Rep. **238**, 173 (1994).

[37] Z. Nussinov, M. Crommie, and A. Balatsky, *Noise spectroscopy of a single spin with spin-polarized STM,* Phys. Rev. B **68**, 085402 (2003).

[38] A. J. Heinrich, J. A. Gupta, C. P. Lutz, and D. M. Eigler, *Single-atom spin-flip spectroscopy,* Science **306**, 466 (2004).

[39] F. Meier, L. Zhou, J. Wiebe, and R. Wiesendanger, *Revealing magnetic interactions from single-atom magnetization curves,* Science **320**, 82 (2008).

[40] X. Chen, Y.-S. Fu, S.-H. Ji, T. Zhang, P. Cheng, X.-C. Ma, X.-L. Zou, W.-H. Duan, J.-F. Jia, and Q.-K. Xue, *Probing superexchange interaction in molecular magnets by spin-flip spectroscopy and microscopy,* Phys. Rev. Lett. **101**, 197208 (2008).

[41] R. Wiesendanger, *Spin mapping at the nanoscale and atomic scale,* Rev. Mod. Phys. **81**, 1495 (2009).

[42] K. Petukhov, M. S. Alam, H. Rupp, S. Strömsdörfer, P. Müller, A. Scheurer, R. W. Saalfrank, J. Kortus, A. Postnikov, M. Ruben, L. K. Thompson, and J.-M. Lehn, *Stm spectroscopy of magnetic molecules,* Coord. Chem. Rev. **253**, 2387 (2009).

[43] S. Kahle and *et al.*, *The quantum magnetism of individual manganese-12-acetate molecular magnets anchored at surfaces,* Nano Lett. **12**, 518 (2012).

[44] J.-P. Gauyacq, N. Lorente, and F. D. Novaes, *Excitation of local magnetic moments by tunneling electrons,* Prog. Surf. Sci. **87**, 63 (2012).

[45] M. Ternes, *Spin excitations and correlations in scanning tunneling spectroscopy,* New J. Phys. **17**, 063016 (2015).

[46] J. A. J. Burgess, L. Malavolti, V. Lanzilotto, M. Mannini, S. Yan, S. Ninova, F. Totti, S. Rolf-Pissarczyk, A. Cornia, R. Sessoli, and S. Loth, *Magnetic Fingerprint of Individual Fe4 Molecular Magnets under Compression by a Scanning Tunnelling Microscope.* Nat. Commun. **6**, 8216 (2015).

[47] B. W. Heinrich, L. Braun, J. I. Pascual, and K. J. Franke, *Tuning the magnetic anisotropy of single molecules,* Nano Lett. **15**, 4024 (2015).

[48] T. Böhler, J. Grebing, A. Mayer-Gindner, H. v Löhneysen, and E. Scheer, *Mechanically controllable break-junctions for use as electrodes for molecular electronics,* Nanotechnology **15**, S465 (2004).

[49] A. R. Champagne, A. N. Pasupathy, and D. C. Ralph, *Mechanically-adjustable and electrically-gated single-molecule transistors,* Nano Lett. **5**, 305 (2005).

[50] D.-H. Chae, J. F. Berry, S. Jung, F. A. Cotton, C. A. Murillo, and Z. Yao, *Vibrational excitations in single trimetal-molecule transistors,* Nano Lett. **6**, 165 (2006).

[51] M. Galperin, M. A. Ratner, and A. Nitzan, *Molecular transport junctions: vibrational effects,* J. Phys.: Condens. Matter **19**, 103201 (2007).

[52] J. Hihath, C. R. Arroyo, G. Rubio-Bollinger, N. Tao, and N. Agraït, *Study of electron-phonon interactions in a single molecule covalently connected to two electrodes,* Nano Lett. **8**, 1673 (2008).

[53] A. K. Hüttel, B. Witkamp, M. Leijnse, M. R. Wegewijs, and H. S. J. van der Zant, *Pumping of vibrational excitations in the Coulomb-blockade regime in a suspended carbon nanotube,* Phys. Rev. Lett. **102**, 225501 (2009).

[54] J. Parks, A. Champagne, G. Hutchison, S. Flores-Torres, H. Abruna, and D. Ralph, *Tuning the Kondo effect with a mechanically controllable break junction,* Phys. Rev. Lett. **99**, 026601 (2007).

[55] J. J. Parks, A. R. Champagne, T. A. Costi, W. W. Shum, A. N. Pasupathy, E. Neuscamman, S. Flores-Torres, P. S. Cornaglia, A. A. Aligia, C. A. Balseiro, G. K.-L. Chan, H. D. Abuña, and D. C. Ralph, *Mechanical control of spin states in spin-1 molecules and the underscreened Kondo effect,* Science **328**, 1370 (2010).

[56] R. Hanson, L. P. Kouwenhoven, J. R. Petta, S. Tarucha, and L. M. K. Vandersypen, *Spins in few-electron quantum dots,* Rev. Mod. Phys **79**, 1217 (2007).

[57] P. Jarillo-Herrero, S. Sapmaz, C. Dekker, L. Kouwenhoven, and H. van der Zant, *Electron-hole symmetry in a semiconducting carbon nanotube quantum dot,* Nature **429**, 389 (2004).

[58] F. H. L. Koppens, J. A. Folk, J. M. Elzerman, R. Hanson, L. H. W. van Beveren, I. T. Vink, H.-P. Tranitz, W. Wegscheider, L. P. Kouwenhoven, and L. M. K. Vandersypen, *Control and detection of singlet-triplet mixing in a random nuclear field,* Science **309**, 1346 (2005).

[59] P. Jarillo-Herrero, J. Kong, H. S. J. van der Zant, C. Dekker, L. P. Kouwenhoven, and S. De Franceschi, *Electronic transport spectroscopy of carbon nanotubes in a magnetic field,* Phys. Rev. Lett. **94**, 156802 (2005).

[60] S. Sapmaz, P. Jarillo-Herrero, J. Kong, C. Dekker, L. P. Kouwenhoven, and H. S. J. van der Zant, *Electronic excitation spectrum of metallic carbon nanotubes,* Phys. Rev. B **71**, 153402 (2005).

[61] A. K. Hüttel, S. Ludwig, H. Lorenz, K. Eberl, and J. P. Kotthaus, *Direct control of the tunnel splitting in a one-electron double quantum dot,* Phys. Rev. B **72**, 081310 (2005).

[62] M. R. Gräber, W. A. Coish, C. Hoffmann, M. Weiss, J. Furer, S. Oberholzer, D. Loss, and C. Schönenberger, *Molecular states in carbon nanotube double quantum dots,* Phys. Rev. B **74**, 075427 (2006).

[63] S. Sapmaz, P. Jarillo-Herrero, L. P. Kouwenhoven, and H. S. J. van der Zant, *Quantum dots in carbon nanotubes,* Semicond. Sci. Technol. **21**, S52 (2006).

[64] R. Leturcq, C. Stampfer, K. Inderbitzin, L. Durrer, C. Hierold, E. Mariani, M. G. Schultz, F. von Oppen, and K. Ensslin, *Franck–condon blockade in suspended carbon nanotube quantum dots,* Nature Phys. **5**, 327 (2009).

[65] S. Andergassen, V. Meden, H. Schoeller, J. Splettstoesser, and M. R. Wegewijs, *Charge transport through single molecules, quantum dots and quantum wires,* Nanotechnology **21**, 272001 (2010).

[66] F. Haupt, M. Leijnse, H. L. Calvo, L. Classen, J. Splettstoesser, and M. R. Wegewijs, *Heat, molecular vibrations, and adiabatic driving in non-equilibrium transport through interacting quantum dots,* Phys. Status Solidi B **250**, 2315 (2013).

[67] H. B. Heersche, Z. de Groot, J. A. Folk, H. S. J. van der Zant, C. Romeike, M. R. Wegewijs, L. Zobbi, D. Barreca, E. Tondello, and A. Cornia, *Electron transport through single Mn_{12} molecular magnets,* Phys. Rev. Lett. **96**, 206801 (2006).

[68] A. Zyazin, J. van den Berg, E. Osorio, H. van der Zant, N. Konstantinidis, M. Leijnse, M. Wegewijs, F. May, W. Hofstetter, C. Danieli, and A. Cornia, *Electric field controlled magnetic anisotropy in a single molecule,* Nano Lett. **10**, 3307 (2010).

[69] E. Burzurí, A. S. Zyazin, A. Cornia, and H. S. J. van der Zant, *Direct observation of magnetic anisotropy in an individual* fe_4 *single-molecule magnet,* Phys. Rev. Lett. **109**, 147203 (2012).

[70] M. Misiorny, E. Burzurí, R. Gaudenzi, K. Park, M. Leijnse, M. R. Wegewijs, J. Paaske, A. Cornia, and H. S. J. van der Zant, *Probing transverse magnetic anisotropy by electronic transport through a single-molecule magnet,* Phys. Rev. B **91**, 035442 (2015).

[71] E. Burzurí, R. Gaudenzi, and H. S. J. van der Zant, *Observing magnetic anisotropy in electronic transport through individual single-molecule magnets,* J. Phys.: Condens. Matter **27**, 113202 (2015).

[72] J. E. Grose, E. S. Tam, C. Timm, M. Scheloske, B. Ulgut, J. J. Parks, H. D. Abruña, W. Harneit, and D. C. Ralph, *Tunneling spectra of individual magnetic endofullerene molecules,* Nature Mater. **7**, 884 (2008).

[73] A. Kogan, G. Granger, M. Kastner, D. Goldhaber-Gordon, and H. Shtrikman, *Singlet–triplet transition in a single-electron transistor at zero magnetic field,* Phys. Rev. B **67**, 113309 (2003).

[74] N. Craig, J. Taylor, E. Lester, C. Marcus, M. Hanson, and A. Gossard, *Tunable nonlocal spin control in a coupled-quantum dot system,* Science **304**, 565 (2004).

[75] S. Moriyama, T. Fuse, M. Suzuki, Y. Aoyagi, and K. Ishibashi, *Four-electron shell structures and an interacting two-electron system in carbon-nanotube quantum dots,* Phys. Rev. Lett. **94**, 186806 (2005).

[76] S. Florens, A. Freyn, N. Roch, W. Wernsdorfer, F. Balestro, P. Roura-Bas, and A. Aligia, *Universal transport signatures in two-electron molecular quantum dots: gate-tunable Hund's rule, underscreened*

Kondo effect and quantum phase transitions, J. Phys.: Condens. Matter **23**, 243202 (2011).

[77] K. Grove-Rasmussen, S. Grap, J. Paaske, K. Flensberg, S. Andergassen, V. Meden, H. I. Jørgensen, K. Muraki, and T. Fujisawa, *Magnetic-field dependence of tunnel couplings in carbon nanotube quantum dots,* Phys. Rev. Lett. **108**, 176802 (2012).

[78] N. Mason, M. J. Biercuk, and C. M. Marcus, *Local gate control of a carbon nanotube double quantum dot,* Science **303**, 655 (2004).

[79] M. J. Biercuk, S. Garaj, N. Mason, J. M. Chow, and C. M. Marcus, *Gate-defined quantum dots on carbon nanotubes,* Nano Lett. **5**, 1267 (2005).

[80] J. Hauptmann, J. Paaske, and P. Lindelof, *Electric-field-controlled spin reversal in a quantum dot with ferromagnetic contacts,* Nature Phys. **4**, 373 (2008).

[81] H. Song, Y. Kim, Y. H. Jang, H. Jeong, M. A. Reed, and T. Lee, *Observation of molecular orbital gating,* Nature **462**, 1039 (2009).

[82] T. S. Jespersen, K. Grove-Rasmussen, J. Paaske, K. Muraki, T. Fujisawa, J. Nygard, and K. Flensberg, *Gate-dependent spin-orbit coupling in multielectron carbon nanotubes,* Nature Physics **7**, 348 (2011).

[83] R. Schleser, T. Ihn, E. Ruh, K. Ensslin, M. Tews, D. Pfannkuche, D. C. Driscoll, and A. C. Gossard, *Cotunneling-mediated transport through excited states in the coulomb-blockade regime,* Phys. Rev. Lett. **94**, 206805 (2005).

[84] A. K. Hüttel, M. Poot, B. Witkamp, and H. S. J. van der Zant, *Nanoelectromechanics of suspended carbon nanotubes,* New J. Phys. **10**, 095003 (2008).

[85] V. N. Golovach and D. Loss, *Transport through a double quantum dot in the sequential tunneling and cotunneling regimes,* Phys. Rev. B **69**, 245327 (2004).

[86] J. Aghassi, M. H. Hettler, and G. Schön, *Cotunneling assisted sequential tunneling in multilevel quantum dots,* Appl. Phys. Lett. **92**, 202101 (2008).

[87] M. C. Lüffe, J. Koch, and F. von Oppen, *Theory of vibrational absorption sidebands in the coulomb-blockade regime of single-molecule transistors,* Phys. Rev. B **77**, 125306 (2008).

[88] D. Becker and D. Pfannkuche, *Coulomb-blocked transport through a quantum dot with spin-split level: Increase of differential conductance peaks by spin relaxation,* Phys. Rev. B **77**, 205307 (2008).

[89] I. Weymann, *Effects of different geometries on the conductance, shot noise, and tunnel magnetoresistance of double quantum dots,* Phys. Rev. B **78**, 045310 (2008).

[90] M. Leijnse and M. R. Wegewijs, *Kinetic equations for transport through single-molecule transistors,* Phys. Rev. B **78**, 235424 (2008).

[91] J. M. Thijssen and H. S. J. van der Zant, *Charge transport and single-electron effects in nanoscale systems,* Phys. Status Solidi B **245**, 1455 (2008).

[92] D. Ferry, S. M. Goodnick, and J. Bird, *Transport in nanostructures*, 2nd ed. (Cambridge University Press, Cambridge, 2009).

[93] J. C. Cuevas and E. Scheer, *Molecular electronics: An introduction to theory and experiment*, World Scientific Series in Nanoscience and Nanotechnology, Vol. 1 (World Scientific, Singapore, 2010).

[94] S. Tarucha, D. Austing, Y. Tokura, W. van der Wiel, and L. Kouwenhoven, *Direct coulomb and exchange interaction in artificial atoms,* Phys. Rev. Lett. **84**, 2485 (2000).

[95] T. H. Oosterkamp, T. Fujisawa, W. G. Van Der Wiel, K. Ishibashi, R. V. Hijman, S. Tarucha, and L. P. Kouwenhoven, *Microwave spectroscopy of a quantum-dot molecule,* Nature **395**, 873 (1998).

[96] P. A. Maksym, H. Imamura, G. P. Mallon, and H. Aoki, *Molecular aspects of electron correlation in quantum dots,* J. Phys.: Condens. Matter **12**, R299 (2000).

[97] T. Fujisawa, D. G. Austing, Y. Tokura, Y. Hirayama, and S. Tarucha, *Allowed and forbidden transitions in artificial hydrogen and helium atoms,* Nature **419**, 278 (2002).

[98] G. Begemann, D. Darau, A. Donarini, and M. Grifoni, *Symmetry fingerprints of a benzene single-electron transistor: Interplay between coulomb interaction and orbital symmetry,* Phys. Rev. B **77**, 201406 (2008).

[99] W. G. van der Wiel, S. De Franceschi, J. M. Elzerman, T. Fujisawa, S. Tarucha, and L. P. Kouwenhoven, *Electron transport through double quantum dots,* Rev. Mod. Phys. **75**, 1 (2003).

[100] M. Misiorny, I. Weymann, and J. Barnaś, *Spin effects in transport through single-molecule magnets in the sequentail and cotunneling regimes,* Phys. Rev. B **79**, 224420 (2009).

[101] A. McCaskey, Y. Yamamoto, M. Warnock, E. Burzurí, H. S. J. van der Zant, and K. Park, *Electron-vibron coupling effects on electron transport via a single-molecule magnet,* Phys. Rev. B **91**, 125419 (2015).

[102] R. Vincent, S. Klyatskaya, M. Ruben, W. Wernsdorfer, and B. F., *Electronic read-out of a single nuclear spin using a molecular spin transistor,* Nature **488**, 357 (2012).

[103] M. Ganzhorn, S. Klyatskaya, M. Ruben, and W. Wernsdorfer, *Strong spin-phonon coupling between a*

single-molecule magnet and a carbon nanotube nanoelectromechanical system, Nature Nanotechn. **8**, 165 (2013).

[104] S. Thiele, R. Vincent, M. Holzmann, S. Klyatskaya, M. Ruben, F. Balestro, and W. Wernsdorfer, *Electrical readout of individual nuclear spin trajectories in a single-molecule magnet spin transistor,* Phys. Rev. Lett. **111**, 037203 (2013).

[105] D. Cobden, M. Bockrath, P. McEuen, A. Rinzler, and R. Smalley, *Spin splitting and even-odd effects in carbon nanotubes,* Phys. Rev. Lett. **81**, 681 (1998).

[106] T. S. Jespersen, K. Grove-Rasmussen, K. Flensberg, J. Paaske, K. Muraki, T. Fujisawa, and J. Nygård, *Gate-dependent orbital magnetic moments in carbon nanotubes,* Phys. Rev. Lett. **107**, 186802 (2011).

[107] P. Weber, H. L. Calvo, J. Bohle, K. Goß, C. Meyer, M. R. Wegewijs, and C. Stampfer, *Switchable coupling of vibrations to two-electron carbon-nanotube quantum dot states,* Nano Lett. **15**, 4417 (2015).

[108] P. G. Piva, G. A. DiLabio, J. L. Pitters, J. Zikovsky, M. Rezeq, S. Dogel, W. A. Hofer, and R. A. Wolkow, *Field regulation of single-molecule conductivity by a charged surface atom,* Nature **435**, 658 (2005).

[109] C. A. Martin, J. M. van Ruitenbeek, and H. S. J. van der Zant, *Sandwich-type gated mechanical break junctions,* Nanotechnology **21** (2010), Artn 265201 10.1088/0957-4484/21/26/265201.

[110] R. Temirov, A. Lassise, F. B. Anders, and F. S. Tautz, *Kondo effect by controlled cleavage of a single-molecule contact,* Nanotechnology **19**, 065401 (2008).

[111] C. Toher, R. Temirov, A. Greuling, F. Pump, M. Kaczmarski, G. Cuniberti, M. Rohlfing, and F. S. Tautz, *Electrical transport through a mechanically gated molecular wire,* Physical Review B **83**, 155402 (2011).

[112] A. Greuling, M. Rohlfing, R. Temirov, F. S. Tautz, and F. B. Anders, *Ab initio study of a mechanically gated molecule: From weak to strong correlation,* Physical Review B **84**, 125413 (2011).

[113] A. Greuling, R. Temirov, B. Lechtenberg, F. B. Anders, M. Rohlfing, and F. S. Tautz, *Spectral properties of a molecular wire in the Kondo regime,* Physica Status Solidi (b) **250**, 2386 (2013).

[114] C. Wagner and R. Temirov, *Tunnelling junctions with additional degrees of freedom: An extended toolbox of scanning probe microscopy,* Progress in Surface Science **90**, 194 (2015).

[115] M. J. Yoo, T. A. Fulton, H. F. Hess, R. L. Willett, L. N. Dunkleberger, R. J. Chichester, L. N. Pfeiffer, and K. W. West, *Scanning single-electron transistor microscopy: Imaging individual charges,* Science **276**, 579 (1997).

[116] C. Wagner, M. F. B. Green, P. Leinen, T. Deilmann, P. Krüger, M. Rohlfing, R. Temirov, and F. S. Tautz, *Scanning quantum dot microscopy,* Phys. Rev. Lett. **115**, 026101 (2015).

[117] H. Bruus and K. Flensberg, *Many-body quantum theory in condesed matter physics*, Oxford Graduate Texts (Oxford University Press, Oxford, 2004).

[118] J. Koch and F. von Oppen, *Franck-Condon blockade and giant Fano factors in transport through single molecules,* Phys. Rev. Lett. **94**, 206804 (2005).

[119] J. Koch, F. von Oppen, and A. V. Andreev, *Theory of the Franck-Condon blockade regime,* Phys. Rev. B **74**, 205438 (2006).

[120] F. Reckermann, M. Leijnse, M. R. Wegewijs, and H. Schoeller, *Transport signature of pseudo jahn-teller dynamics in a single-molecule transistor,* Europhys. Lett. **83**, 58001 (2008).

[121] F. Reckermann, M. Leijnse, and M. R. Wegewijs, *Vibrational detection and control of spin in mixed-valence molecular transistors,* Phys. Rev. B **79**, 075313 (2009).

[122] C. W. J. Beenakker, *Theory of Coulomb-blockade oscillations in the conductance of a quantum dot,* Phys. Rev. B **44**, 1646 (1991).

[123] K. Kaasbjerg and K. Flensberg, *Image charge effects in single-molecule junctions: Breaking of symmetries and negative-differential resistance in a benzene single-electron transistor,* Phys. Rev. B **84**, 115457 (2011).

[124] J. Lambe and R. C. Jaklevic, *Molecular vibration spectra by inelastic electron tunneling,* Phys. Rev. **165**, 821 (1968).

[125] A. A. Khajetoorians, J. Wiebe, B. Chilian, S. Lounis, S. Blügel, and R. Wiesendanger, *Atom-by-atom engineering and magnetometry of tailored nanomagnets,* Nature Phys. **8**, 497 (2012).

[126] J. Brede and R. Wiesendanger, *Spin-resolved characterization of single cobalt phthalocyanine molecules on a ferromagnetic support,* Phys. Rev. B **86**, 184423 (2012).

[127] A. A. Khajetoorians, B. Baxevanis, C. Hübner, T. Schlenk, S. Krause, T. O. Wehling, S. Lounis, A. Lichtenstein, D. Pfannkuche, J. Wiebe, and R. Wiesendanger, *Current-driven spin dynamics of artificially constructed quantum magnets,* Science **339**, 55 (2013).

[128] B. Bryant, A. Spinelli, J. J. T. Wagenaar, M. Gerrits, and A. F. Otte, *Local control of single atom magnetocrystalline anisotropy,* Phys. Rev. Lett. **111**, 127203 (2013).

[129] I. G. Rau, S. Baumann, S. Rusponi, F. Donati, S. Stepanow, L. Gragnaniello, J. Dreiser, C. Piamonteze, F. Nolting, S. Gangopadhyay, O. R. Albertini, R. M. Macfarlane, C. P. Lutz, B. A. Jones, P. Gambardella,

A. J. Heinrich, and H. Brune, *Reaching the magnetic anisotropy limit of a 3d metal atom,* Science **344**, 988 (2014).

[130] P. Hapala, G. Kichin, C. Wagner, F. S. Tautz, R. Temirov, and P. Jelínek, *Mechanism of high-resolution stm/afm imaging with functionalized tips,* Phys. Rev. B **90**, 085421 (2014).

[131] C. Wagner, N. Fournier, V. G. Ruiz, C. Li, K. Müllen, M. Rohlfing, A. Tkatchenko, R. Temirov, and F. S. Tautz, *Non-additivity of molecule-surface van der waals potentials from force measurements,* Nature Commun. **5**, 5568 (2014).

[132] M. Bazarnik, B. Bugenhagen, M. Elsebach, E. Sierda, A. Frank, M. H. Prosenc, and R. Wiesendanger, *Toward tailored all-spin molecular devices,* Nano Lett. **16**, 577 (2016).

[133] C. Hirjibehedin, C. Lutz, and A. Heinrich, *Spin coupling in engineered atomic structures,* Science **312**, 1021 (2006).

[134] C. Hirjibehedin, C. Lin, A. Otte, M. Ternes, C. Lutz, B. Jones, and A. Heinrich, *Large magnetic anisotropy of a single atomic spin embedded in a surface molecular network,* Science **317**, 1199 (2007).

[135] D. Serrate, P. Ferriani, Y. Yoshida, S.-W. Hla, M. Menzel, K. von Bergmann, S. Heinze, A. Kubetzka, and R. Wiesendanger, *Imaging and manipulating the spin direction of individual atoms,* Nature Nanotech. **5**, 350 (2010).

[136] S. Baumann, F. Donati, S. Stepanow, S. Rusponi, W. Paul, S. Gangopadhyay, I. G. Rau, G. E. Pacchioni, L. Gragnaniello, M. Pivetta, J. Dreiser, C. Piamonteze, C. P. Lutz, R. M. Macfarlane, B. A. Jones, P. Gambardella, A. J. Heinrich, and H. Brune, *Origin of perpendicular magnetic anisotropy and large orbital moment in Fe atoms on MgO,* Phys. Rev. Lett. **115**, 237202 (2015).

[137] C. Weiss, C. Wagner, C. Kleimann, M. Rohlfing, F. S. Tautz, and R. Temirov, *Imaging pauli repulsion in scanning tunneling microscopy,* Phys. Rev. Lett. **105**, 086103 (2010).

[138] T. Esat, T. Deilmann, B. Lechtenberg, C. Wagner, P. Krüger, R. Temirov, F. B. Anders, M. Rohlfing, and F. S. Tautz, *Transfering spin into an extended π orbital of a large molecule,* Phys. Rev. B **91**, 144415 (2015).

[139] N. Atodiresei, V. Caciuc, P. Lazić, and S. Blügel, *Chemical versus van der waals interaction: The role of the heteroatom in the flat absorption of aromatic molecules C_6H_6, C_5NH_5, and $C_4N_2H_4$ on the Cu(110) surface,* Phys. Rev. Lett. **102**, 136809 (2009).

[140] S. Loth, K. von Bergmann, M. Ternes, A. Otte, C. Lutz, and A. Heinrich, *Controlling the state of quantum spins with electric currents,* Nature Phys. **6**, 340 (2010).

[141] A. A. Khajetoorians, S. Lounis, B. Chilian, A. T. Costa, L. Zhou, D. L. Mills, J. Wiebe, and R. Wiesendanger, *Itinerant nature of atom-magnetization excitation by tunneling electrons,* Phys. Rev. Lett. **106**, 037205 (2011).

[142] S. Yan, D.-J. Choi, J. A. J. Burgess, S. Rolf-Pissarczyk, and S. Loth, *Three-dimensional mapping of single-atom magnetic anisotropy,* Nano Lett. **15**, 1938 (2015).

[143] S. Yan, D.-J. Choi, J. A. J. Burgess, S. Rolf-Pissarczyk, and S. Loth, *Control of quantum magnets by atomic exchange bias,* Nature Nanotechnol. **10**, 40 (2015).

[144] A. A. Khajetoorians, M. Steinbrecher, M. Ternes, M. Bouhassoune, M. dos Santos Dias, S. Lounis, J. Wiebe, and R. Wiesendanger, *Tailoring the chiral magnetic interaction between two individual atoms,* Nature Commun. **7**, 10620 (2016).

[145] M. Steinbrecher, A. Sonntag, M. dos Santos Dias, M. Bouhassoune, S. Lounis, J. Wiebe, R. Wiesendanger, and A. A. Khajetoorians, *Absence of a spin-signature from a single ho adatom as probed by spin-sensitive tunneling,* Nature Commun. **7**, 10454 (2016).

[146] A. Otte, M. Ternes, K. von Bergmann, S. Loth, H. Brune, C. Lutz, C. Hirjibehedin, and A. Heinrich, *The role of magnetic anisotropy in the Kondo effect,* Nature Phys. **4**, 847 (2008).

[147] S. Loth, C. Lutz, and A. Heinrich, *Spin-polarized spin excitation spectroscopy,* New J. Phys. **12**, 125021 (2010).

[148] *Recent advances in scanning tunneling microscopy and spectroscopy,* C. F. Hirjibehedin and Y. Wang, eds., special section in J. Physc.: Condens. Matter **26**, 394001–394010 (2014).

[149] S. De Franceschi, S. Sasaki, J. Elzerman, W. van der Wiel, S. Tarucha, and L. Kouwenhoven, *Electron cotunneling in a semiconductor quantum dot,* Phys. Rev. Lett. **86**, 878 (2001).

[150] D. M. Zumbühl, C. M. Marcus, M. P. Hanson, and A. C. Gossard, *Cotunneling spectroscopy in few-electron quantum dots,* Phys. Rev. Lett. **93**, 256801 (2004).

[151] G. Katsaros, P. Spathis, M. Stoffel, F. Fournel, M. Mongillo, V. Bouchiat, F. Lefloch, A. Rastelli, O. G. Schmidt, and S. De Franceschi, *Hybrid superconductor-semiconductor devices made from self-assembled sige nanocrystals on silicon,* Nature Nanotechnology **5**, 458 (2010).

[152] M. R. Wegewijs and Y. V. Nazarov, *Inelastic co-tunneling through an excited state of a quantum dot,* arXiv:cond-mat/0103579 (2001).

[153] U. Hartmann and F. K. Wilhelm, *Nonlinear cotunneling through an artificial molecule,* Phys. Rev. B **67**, 161307 (2003).
[154] D. V. Averin and Y. V. Nazarov, *Virtual electron diffusion during quantum tunneling of the electric charge,* Phys. Rev. Lett. **65**, 2446 (1990).
[155] H. Grabert and M. H. Devoret, eds., *Single charge tunneling: Coulomb blockade phenomena in nanostructures,* NATO Advanced Science Institutes Series, Vol. 294 (Springer Science & Business Media, New York, 1992).
[156] B. C. Stipe, M. A. Rezaei, and W. Ho, *Single-molecule vibrational spectroscopy and microscopy,* Science **280**, 1732 (1998).
[157] L. H. Yu, Z. K. Keane, J. W. Ciszek, L. Cheng, M. P. Stewart, J. M. Tour, and D. Natelson, *Inelastic electron tunneling via molecular vibrations in single-molecule transistors,* Phys. Rev. Lett. **93**, 266802 (2004).
[158] Y. Kim, H. Song, F. Strigl, H.-F. Pernau, T. Lee, and E. Scheer, *Conductance and vibrational states of single-molecule junctions controlled by mechanical stretching and material variation,* Phys. Rev. Lett. **106**, 196804 (2011).
[159] M. Bürkle, J. K. Viljas, T. J. Hellmuth, E. Scheer, F. Weigend, G. Schön, and F. Pauly, *Influence of vibrations on electron transport through nanoscale contacts,* Phys. Status Solidi B **250**, 2468 (2013).
[160] T. Böhler, A. Edtbauer, and E. Scheer, *Conductance of individual C_{60} molecules measured with controllable gold electrodes,* Phys. Rev. B **76**, 125432 (2007).
[161] M. Herz and E. Scheer, *Force-noise spectroscopy by tunneling current deflection sensing,* Appl. Phys. Lett. **108**, 023103 (2016).
[162] J. König, H. Schoeller, and G. Schön, *Cotunneling at resonance for the single-electron transistor,* Phys. Rev. Lett. **78**, 4482 (1997).
[163] S. Schmaus, V. Koerting, J. Paaske, T. S. Jespersen, J. Nygård, and P. Wölfle, *Nonequilibrium cotunneling through a three-level quantum dot,* Phys. Rev. B **79**, 045105 (2009).
[164] J. Paaske, A. Rosch, P. Wolfle, N. Mason, C. M. Marcus, and J. Nygard, *Non-equilibrium singlet-triplet kondo effect in carbon nanotubes,* Nature Phys. **2**, 460 (2006).
[165] M. Wagner, *Unitary transformations in solid state physics,* Modern problems in condensed matter sciences, Vol. 15 (North-Holland Physics Publishing, Amsterdam, 1986).
[166] J. Appelbaum, *"sd" exchange model of zero-bias tunneling anomalies,* Phys. Rev. Lett. **17**, 91 (1966).
[167] J. Appelbaum, *Exchange model of zero-bias tunneling anomalies,* Phys. Rev. **154**, 633 (1967).
[168] J. R. Schrieffer and P. A. Wolff, *Relation between the Anderson and Kondo hamiltonians,* Phys. Rev. **149**, 491 (1966).
[169] J. Schrieffer, *The Kondo effect—The link between magnetic and nonmagnetic impurities in metals?* J. Appl. Phys. **38**, 1143 (1967).
[170] S. Bravyi, D. P. DiVincenzo, and D. Loss, *Schrieffer–Wolff transformation for quantum many-body systems,* Ann. Phys. **326**, 2793 (2011).
[171] K. Kikoin, M. Kiselev, and Y. Avishai, *Dynamical symmetries in Nanophysics,* Nanophysics, Nanoclusters and Nanodevices (NOVA Science Publisher, New York USA, 2006).
[172] L. Hirst, *Theory of the coupling between conduction electrons and moments of 3d and 4f ions in metals,* Advances in Physics **27**, 231 (1978).
[173] M. Eto and Y. V. Nazarov, *Enhancement of kondo effect in quantum dots with an even number of electrons,* Phys. Rev. Lett. **85**, 1306 (2000).
[174] B. Sothmann and J. König, *Nonequilibrium current and noise in inelastic tunneling through a magnetic atom,* New J. Phys. **12**, 083028 (2010).
[175] A. Hurley, N. Baadji, and S. Sanvito, *Perturbative approach to the kondo effect in magnetic atoms on nonmagnetic substrates,* Physical Review B **84** (2011), ARTN 115435 10.1103/PhysRevB.84.115435.
[176] A. Hurley, N. Baadji, and S. Sanvito, *Bias asymmetry in the conductance profile of magnetic ions on surfaces probed by scanning tunneling microscopy,* Phys. Rev. B **86**, 125411 (2012).
[177] B. Schweflinghaus, M. dos Santos Dias, A. T. Costa, and S. Lounis, *Renormalization of electron self-energies via their interaction with spin excitations: A first principles investigation,* Phys. Rev. B **89**, 235439 (2014).
[178] A. Rosch, J. Paaske, J. Kroha, and P. Wölfle, *Nonequilibrium transport through a kondo dot in a magnetic field: perturbation theory and poor man's scaling,* Phys. Rev. Lett. **90**, 076804 (2003).
[179] J. Paaske, A. Rosch, and P. Wölfle, *Nonequilibrium transport through a kondo dot in a magnetic field: Perturbation theory,* Phys. Rev. B **69**, 155330 (2004).
[180] H. Schoeller and F. Reininghaus, *Real-time renormalization group in frequency space: A 2-loop analysis of the nonequilibrium anisotropic kondo model at finite magnetic field,* Phys. Rev. B **80**, 045117 (2009).

[181] R. Saptsov and M. Wegewijs, *Fermionic superoperators for zero-temperature nonlinear transport: Real-time perturbation theory and renormalization group for Anderson quantum dots,* Phys. Rev. B **86**, 235432 (2012).

[182] I. L. Aleiner, P. W. Brouwer, and L. I. Glazman, *Quantum effects in coulomb blockade,* Phys. Rep. **358**, 309 (2002).

[183] M. Pustilnik and L. I. Glazman, *Kondo effect in quantum dots,* J. Phys.: Condens. Matter **16**, R513 (2004).

[184] L. I. Glazman and M. Pustilnik, *Low temperature transport through a quantum dot,* in *Nanophysics: Coherence and Transport*, École de Physique des Les Houches, Vol. 81, edited by H. Bouchiat, Y. Gefen, S. Guéron, G. Montambaux, and J. Dalibard (Elsevier, Amsterdam, 2005) pp. 427–478.

[185] H. Schoeller, *A perturbative nonequilibrium renormalization group method for dissipative quantum mechanics,* Euro. Phys. J. Special Topics **168**, 179 (2009).

[186] P. Fritsch and S. Kehrein, *Non-equilibrium scaling analysis of the kondo model with voltage bias,* Ann. Phys. **324**, 1105 (2009).

[187] J. Eckel, F. Heidrich-Meisner, S. G. Jakobs, M. Thorwart, M. Pletyukhov, and R. Egger, *Comparative study of theoretical methods for non-equilibrium quantum transport,* New Journal of Physics **12** (2010), Artn 043042 10.1088/1367-2630/12/4/043042.

[188] J. Paaske, A. Rosch, J. Kroha, and P. Wöllfle, *Nonequilibrium transport through a kondo dot: Decoherence effects,* Phys. Rev. B **70**, 155301 (2004).

[189] H. B. Heersche, Z. de Groot, J. A. Folk, L. P. Kouwenhoven, H. S. J. van der Zant, A. A. Houck, J. Labaziewicz, and I. L. Chuang, *Kondo effect in the presence of magnetic impurities,* Phys. Rev. Lett. **96**, 017205 (2006).

[190] G. D. Scott and D. Natelson, *Kondo resonances in molecular devices,* ACS Nano **4**, 3560 (2010).

[191] T. Komeda, H. Isshiki, J. Liu, Y.-F. Zhang, N. Lorente, K. Katoh, B. K. Breedlove, and M. Yamashita, *Observation and electric current control of a local spin in a single-molecule magnet,* Nature Commun. **2**, 217 (2011).

[192] C. Romeike, M. R. Wegewijs, W. Hofstetter, and H. Schoeller, *Quantum-tunneling-induced Kondo effect in single molecular magnets,* Phys. Rev. Lett. **96**, 196601 (2006).

[193] M. N. Leuenberger and E. R. Mucciolo, *Berry-phase oscillations of the Kondo effect in single-molecule magnets,* Phys. Rev. Lett. **97**, 126601 (2006).

[194] C. Romeike, M. R. Wegewijs, W. Hofstetter, and H. Schoeller, *Erratum: Kondo-transport spectroscopy of single molecule magnets [Phys. Rev. Lett. 97, 206601 (2006)],* Phys. Rev. Lett. **106**, 019902 (2011).

[195] M. R. Wegewijs, C. Romeike, H. Schoeller, and W. Hofstetter, *Corrigendum: Magneto-transport through single-molecule magnets: Kondo-peaks, zero-bias dips, molecular symmetry and berry's phase [new. j. phys. 9:344 (2007)],* New Journal of Physics **13**, 079501 (2011), work done by F. May.

[196] R. Žitko, R. Peters, and T. Pruschke, *Properties of anisotropic magnetic impurities on surfaces,* Phys. Rev. B **78**, 224404 (2008).

[197] R. Žitko, R. Peters, and T. Pruschke, *Splitting of the Kondo resonance in anisotropic magnetic impurities on surfaces,* New J. Phys. **11**, 053003 (2009).

[198] J. Fernández-Rossier, *Theory of single-spin inelastic tunneling spectroscopy,* Phys. Rev. Lett. **102**, 256802 (2009).

[199] R. Žitko and T. Pruschke, *Many-particle effects in adsorbed magnetic atoms with easy-axis anisotropy: the case of Fe on the CuN/Cu (100) surface,* New J. Phys. **12**, 063040 (2010).

[200] F. Elste and C. Timm, *Resonant and Kondo tunneling through molecular magnets,* Phys. Rev. B **81**, 24421 (2010).

[201] M. Misiorny, I. Weymann, and J. Barnaś, *Interplay of the Kondo effect and spin-polarized transport in magnetic molecules, adatoms, and quantum dots,* Phys. Rev. Lett. **106**, 126602 (2011).

[202] M. Misiorny, I. Weymann, and J. Barnaś, *Influence of magnetic anisotropy on the Kondo effect and spin-polarized transport through magnetic molecules, adatoms, and quantum dots,* Phys. Rev. B **84**, 035445 (2011).

[203] F. Delgado and J. Fernández-Rossier, *Cotunneling theory of atomic spin inelastic electron tunneling spectropy,* Phys. Rev. B **84**, 045439 (2011).

[204] M. Misiorny and I. Weymann, *Transverse anisotropy effects on spin-resolved transport through large-spin molecules,* Phys. Rev. B **90**, 235409 (2014).

[205] M. Ternes, A. Heinrich, and W.-D. Schneider, *Spectroscopic manifestations of the Kondo effect on single adatoms,* J. Phys.: Condens. Matter **21**, 053001 (2009).

[206] H. Brune and P. Gambardella, *Magnetism of individual atoms adsorbed on surfaces,* Surf. Sci. **603**, 1812 (2009).

[207] S. Lounis, B. Schweflinghaus, M. dos Santos Dias, M. Bouhassoune, R. B. Muniz, and A. T. Costa,

Theoretical probing of inelastic spin-excitations in adatoms on surfaces, Surf. Science **630**, 317 (2014).

[208] G. Begemann, S. Koller, M. Grifoni, and J. Paaske, *Inelastic cotunneling in quantum dots and molecules with weakly broken degeneracies,* Physical Review B **82** (2010).

[209] S. Koller, M. Grifoni, M. Leijnse, and M. R. Wegewijs, *Density-operator approaches to transport through interacting quantum dots: Simplifications in fourth-order perturbation theory,* Phys. Rev. B **82**, 235307 (2010).

[210] M. Turek and K. A. Matveev, Phys. Rev. B **65**, 115332 (2002).

[211] C. Timm, *Tunneling through molecules and quantum dots: Master-equation approaches,* Phys. Rev. B **77**, 195416 (2008).

[212] C. Timm, *Time-convolutionless master equation for quantum dots: Perturbative expansion to arbitrary order,* Phys. Rev. B **83**, 115416 (2011).

[213] J. König, J. Schmid, H. Schoeller, and G. Schön, *Resonant tunneling through ultrasmall quantum dots: Zero-bias anomalies, magnetic-field dependence, and boson-assisted transport,* Phys. Rev. B **54**, 16820 (1996).

[214] J. König, H. Schoeller, and G. Schön, *Cotunneling and renormalization effects for the single-electron transistor,* Phys. Rev. B **58**, 7882 (1998).

[215] N. Gergs, R. Saptsov, M. R. Wegewijs, and D. Schuricht, In preparation (2017).

[216] E. A. Osorio, K. Moth-Poulsen, H. van der Zant, J. Paaske, P. Hedegård, K. Flensberg, J. Bendix, and T. Bjørnholm, *Electrical manipulation of spin states in a single electrostatically gated transition-metal complex,* Nano Lett. **10**, 105 (2010).

[217] A. Eliasen, J. Paaske, K. Flensberg, S. Smerat, M. Leijnse, M. R. Wegewijs, H. I. Jørgensen, M. Monthioux, and J. Nygård, *Transport via coupled states in a c_{60} peapod quantum dot,* Phys. Rev. B **81**, 155431 (2010).

[218] C. Stevanato, M. Leijnse, K. Flensberg, and J. Paaske, *Finite-bias conductance anomalies at a singlet-triplet crossing,* Phys. Rev. B **86**, 165427 (2012).

[219] M. Leijnse, M. R. Wegewijs, and M. H. Hettler, *Pair tunneling resonance in the single-electron transport regime,* Phys. Rev. Lett. **103**, 156803 (2009).

[220] F. D. M. Haldane, *Hartree-fock study of the anderson model coupled to a boson field; mixed valence states,* Phys. Rev. B **15**, 281 (1977).

[221] J. Koch, M. E. Raikh, and F. von Oppen, *Pair tunneling through single molecules,* Phys. Rev. Lett. **96**, 056803 (2006).

[222] M.-J. Hwang, M.-S. Choi, and R. López, *Pair tunneling and shot noise through a single molecule in a strong electron-phonon coupling regime,* Phys. Rev. B **76**, 165312 (2007).

[223] J. Koch, E. Sela, Y. Oreg, and F. von Oppen, *Nonequilibrium charge-kondo transport through negative-u molecules,* Phys. Rev. B **75**, 195402 (2007).

[224] E. Sela, H.-S. Sim, Y. Oreg, M. E. Raikh, and F. von Oppen, *Electron-pair resonance in the coulomb blockade,* Phys. Rev. Lett. **100**, 056809 (2008).

[225] D. H. Evans and M. W. Lehmann, *Two-electron reactions in organic and organometallic electrochemistry,* Acta Chemica Scandinavica **53**, 765 (1999).

[226] G. L. Cheng, M. Tomczyk, S. C. Lu, J. P. Veazey, M. C. Huang, P. Irvin, S. Ryu, H. Lee, C. B. Eom, C. S. Hellberg, and J. Levy, *Electron pairing without superconductivity,* Nature **521**, 196 (2015).

[227] A. Hamo, A. Benyamini, I. Shapir, I. Khivrich, J. Waissman, K. Kaasbjerg, Y. Oreg, F. von Oppen, and S. Ilani, *Electron attraction mediated by coulomb repulsion,* Nature **535**, 395 (2016).

[228] M. Nilsson, L. Namazi, S. Lehmann, M. Leijnse, K. A. Dick, and C. Thelander, *Electron-hole interactions in coupled inas-gasb quantum dots based on nanowire crystal phase templates,* Phys. Rev. B **94**, 115313 (2016).

[229] B. Sothmann and J. König, *Transport through quantum-dot spin valves containing magnetic impurities,* Phys. Rev. B **82**, 245319 (2010).

[230] M. Misiorny, M. Hell, and M. R. Wegewijs, *Spintronic magnetic anisotropy,* Nature Phys. **9**, 801 (2013).

[231] M. Braun, J. König, and J. Martinek, *Theory of transport through quantum-dot spin valves in the weak-coupling regime,* Phys. Rev. B **70**, 195345 (2004).

[232] J. König and Y. Gefen, *Coherence and partial coherence in interacting electron systems,* Phys. Rev. Lett. **86**, 3855 (2001).

[233] B. Wunsch, M. Braun, J. König, and D. Pfannkuche, *Probing level renormalization by sequential transport through double quantum dots,* Phys. Rev. B **72**, 205319 (2005).

[234] A. Donarini, M. Grifoni, and K. Richter, *Dynamical symmetry breaking in transport through molecules,* Phys. Rev. Lett. **97**, 166801 (2006).

[235] R. Härtle and A. J. Millis, *Formation of nonequilibrium steady states in interacting double quantum dots: When coherences dominate the charge distribution,* Phys. Rev. B **90**, 245426 (2014).

[236] S. Wenderoth, J. Bätge, and R. Härtle, *Sharp peaks in the conductance of a double quantum dot and a quantum-dot spin valve at high temperatures: A hierarchical quantum master equation approach,* Phys. Rev. B **94**, 121303 (2016).

[237] A. Donarini, B. Siegert, S. Sobczyk, and M. Grifoni, *Topographical fingerprints of many-body interference in stm junctions on thin insulating films,* Phys. Rev. B **86**, 155451 (2012).

[238] A. Donarini, G. Begemann, and M. Grifoni, *All-electric spin control in interference single electron transistors,* Nano Lett. **9**, 2897 (2009).

[239] A. Donarini, G. Begemann, and M. Grifoni, *Interference effects in the coulomb blockade regime: Current blocking and spin preparation in symmetric nanojunctions,* Phys. Rev. B **82**, 125451 (2010).

[240] M. M. E. Baumgärtel, M. Hell, S. Das, and M. R. Wegewijs, *Transport and accumulation of spin anisotropy,* Phys. Rev. Lett. **107**, 087202 (2011).

[241] M. Misiorny, I. Weymann, and J. Barnaś, *Underscreened Kondo effect in $S = 1$ magnetic quantum dots: Exchange, anisotropy and temperature effects,* Phys. Rev. B **86**, 245415 (2012).

[242] J. C. Oberg, M. R. Calvo, F. Delgado, M. Moro-Lagares, D. Serrate, D. Jacob, J. Fernández-Rossier, and C. F. Hirjibehedin, *Control of single-spin magnetic anisotropy by exchange coupling,* Nature Nanotechnol. **9**, 64 (2014).

[243] F. Delgado, C. F. Hirjibehedin, and J. Fernández-Rossier, *Consequences of kondo exchange on quantum spins,* Surf. Sci. **630**, 337 (2014).

[244] P. Jacobson, T. Herden, M. Muenks, G. Laskin, O. Brovko, V. Stepanyuk, M. Ternes, and K. Kern, *Quantum engineering of spin and anisotropy in magnetic molecular junctions,* Nature Commun. **6**, 8536 (2015).

[245] M. Hell, B. Sothmann, M. Leijnse, M. Wegewijs, and J. König, *Spin resonance without spin splitting,* Phys. Rev. B **91**, 195404 (2015).

[246] S. Accorsi, A. L. Barra, A. Caneschi, G. Chastanet, A. Cornia, A. C. Fabretti, D. Gatteschi, C. Mortalo, E. Olivieri, F. Parenti, P. Rosa, R. Sessoli, L. Sorace, W. Wernsdorfer, and L. Zobbi, *Tuning anisotropy barriers in a family of tetrairon(iii) single-molecule magnets with an s=5 ground state,* Journal of the American Chemical Society **128**, 4742 (2006).

[247] R. Gaudenzi, E. Burzurí, D. Reta, I. d. P. R. Moreira, S. T. Bromley, C. Rovira, J. Veciana, and H. S. J. van der Zant, *Exchange Coupling Inversion in a High-Spin Organic Triradical Molecule.* Nano Lett. **16**, 2066 (2016).

[248] E. A. Osorio, K. O'Neill, M. R. Wegewijs, N. Stuhr-Hansen, J. Paaske, T. Bjørnholm, and H. S. van der Zant, *Electronic excitations of a single molecule contacted in a three-terminal configuration,* Nano Lett. **7**, 3336 (2007).

[249] A. K. Hüttel, H. Qin, A. W. Holleitner, R. H. Blick, K. Neumaier, D. Weinmann, K. Eberl, and J. P. Kotthaus, *Spin blockade in ground-state resonance of a quantum dot,* Europhys. Lett. **62**, 712 (2003).

[250] M. Ciorga, A. S. Sachrajda, P. Hawrylak, C. Gould, P. Zawadzki, S. Jullian, Y. Feng, and Z. Wasilewski, *Addition spectrum of a lateral dot from coulomb and spin-blockade spectroscopy,* Phys. Rev. B **61**, R16315 (2000).

[251] A. C. Johnson, J. R. Petta, C. M. Marcus, M. P. Hanson, and A. C. Gossard, *Singlet-triplet spin blockade and charge sensing in a few-electron double quantum dot,* Phys. Rev. B **72**, 165308 (2005).

[252] D. Weinmann, W. Häusler, W. Pfaff, B. Kramer, and U. Weiss, *Spin blockade in non-linear transport through quantum dots,* Europhys. Lett. **26**, 467 (1994).

[253] D. Weinmann, W. Häusler, and B. Kramer, *Spin blockades in linear and nonlinear transport through quantum dots,* Phys. Rev. Lett. **74**, 984 (1995).

[254] D. Weinmann, *Spin blockades in the transport through quantum dots,* Lect. Notes Phys. **630**, 289 (2003).

[255] C. Romeike, M. R. Wegewijs, and H. Schoeller, *Spin quantum tunneling in single molecular magnets: Fingerprints in transport spectroscopy of current and noise,* Phys. Rev. Lett. **96**, 196805 (2006).

[256] C. Romeike, M. R. Wegewijs, M. Ruben, W. Wenzel, and H. Schoeller, *Charge-switchable molecular magnet and spin blockade of tunneling,* Phys. Rev. B **75**, 064404 (2007).

[257] K. O'Neill, E. A. Osorio, and H. S. J. van der Zant, *Self-breaking in planar few-atom au constrictions for nanometer-spaced electrodes,* Appl. Phys. Lett. **90**, 133109 (2007).

[258] R. Gaudenzi, J. O. Island, J. de Bruijckere, E. Burzurí, T. M. Klapwijk, and H. S. J. van der Zant, *Superconducting molybdenum-rhenium electrodes for single-molecule transport studies,* Applied Physics Letters **106**, 222602 (2015).

[259] R. Frisenda and H. S. J. van der Zant, *Transition from strong to weak electronic coupling in a single-molecule junction,* Phys. Rev. Lett. **117**, 126804 (2016).

[260] F. Haque, M. Langhirt, E. Del Barco, T. Taguchi, and G. Christou, *Magnetic field dependent transport through a mn4 single-molecule magnet,* J. Appl. Phys. **109**, 07B112 (2011).
[261] J. J. Henderson, C. M. Ramsey, E. del Barco, A. Mishra, and G. Christou, *Fabrication of nanogapped single-electron transistors for transport studies of individual single-molecule magnets,* J. Appl. Phys. **101**, 09E102 (2007).
[262] M.-H. Jo, J. Grose, K. Baheti, M. Deshmukh, J. Sokol, E. Rumberger, D. Hendrickson, R. Jeffrey, H. Park, and D. Ralph, *Signatures of molecular magnetism in single-molecule transport spectroscopy,* Nano Lett. **6**, 2014 (2006).
[263] A. Candini, S. Klyatskaya, M. Ruben, W. Wernsdorfer, and M. Affronte, *Graphene spintronic devices with molecular nanomagnets,* Nano Lett. **11**, 2634 (2011).
[264] M. Urdampilleta, S. Klyatskaya, J. Cleuziou, M. Ruben, and W. Wernsdorfer, *Supramolecular spin valves,* Nature Mater. **10**, 502 (2011).
[265] S. Voss, M. Fonin, L. Burova, M. Burgert, Y. S. Dedkov, A. B. Preobrajenski, E. Goering, U. Groth, A. R. Kaul, and U. Ruediger, *Investigation of the stability of mn12 single molecule magnets,* Appl. Phys. A **94** (2009).
[266] B. W. Heinrich, L. Braun, J. I. Pascual, and K. J. Franke, *Protection of excited spin states by a superconducting energy gap,* Nature Physics **9**, 765 (2013).
[267] N. Roch, S. Florens, T. A. Costi, W. Wernsdorfer, and F. Balestro, *Observation of the underscreened kondo effect in a molecular transistor,* Phys. Rev. Lett. **103**, 197202 (2009).
[268] T. Esat, B. Lechtenberg, T. Deilmann, C. Wagner, P. Kruger, R. Temirov, M. Rohlfing, F. B. Anders, and F. S. Tautz, *A chemically driven quantum phase transition in a two-molecule kondo system,* Nature Physics **12**, 867 (2016).
[269] S. Sasaki, S. De Franceschi, J. Elzerman, W. van der Wiel, M. Eto, S. Tarucha, and L. Kouwenhoven, *Kondo effect in an integer-spin quantum dot,* Nature **405**, 764 (2000).
[270] In a renormalization group (RG) treatment of the master equation the broadening arises naturally. First, in uniform way as the sum of all tunnel rates in the discrete RG approximation. Then during a continuous RG flow the broadening is corrected in an energy dependent way.
[271] The nonperturbative hierarchical density-operator approach (HQME) can also deal with the broadening, as demonstrated both for SET and COSET resonances in the cited reference.
[272] C. Schinabeck, A. Erpenbeck, R. Härtle, and M. Thoss, *Hierarchical quantum master equation approach to electronic-vibrational coupling in nonequilibrium transport through nanosystems,* Phys. Rev. B **94**, 201407 (2016).
[273] N. M. Gergs, C. B. M. Hörig, M. R. Wegewijs, and D. Schuricht, *Charge fluctuations in nonlinear heat transport,* Phys. Rev. B **91**, 201107 (2015).
[274] G. E. W. Bauer, E. Saitoh, and B. J. van Wees, *Spin caloritronics,* Nature Mater. **11**, 391 (2012).
[275] M. Gomberg, *An instance of trivalent carbon triphenylmethyl,* J. Am. Chem. Soc. **22**, 757 (1900).
[276] R. G. Hicks, *Stable Radicals: Fundamentals and Applied Aspects of Odd-Electron Compounds* (John Wiley and Sons, Ltd, 2010).
[277] I. Ratera and J. Veciana, *Playing with organic radicals as building blocks for functional molecular materials,* Chem. Soc. Rev. **41**, 303 (2012).
[278] A. R. Rocha, V. M. Garcia-Suarez, S. W. Bailey, C. J. Lambert, J. Ferrer, and S. Sanvito, *Towards molecular spintronics,* Nat. Mater. **4**, 335 (2005).
[279] M. Mas-Torrent, N. Crivillers, C. Rovira, and J. Veciana, *Attaching persistent organic free radicals to surfaces: How and why,* Chem. Rev. **112**, 2506 (2012).
[280] N. Crivillers, C. Munuera, M. Mas-Torrent, C. Simao, S. T. Bromley, C. Ocal, C. Rovira, and J. Veciana, *Dramatic influence of the electronic structure on the conductivity through open- and closed-shell molecules,* Adv. Mater. **21**, 1177 (2009).
[281] N. Crivillers, M. Paradinas, M. Mas-Torrent, S. T. Bromley, C. Rovira, C. Ocal, and J. Veciana, *Negative differential resistance (ndr) in similar molecules with distinct redox behaviour,* Chem. Commun. **47**, 4664 (2011).
[282] C. Simao, M. Mas-Torrent, N. Crivillers, V. Lloveras, J. M. Artes, P. Gorostiza, J. Veciana, and C. Rovira, *A robust molecular platform for non-volatile memory devices with optical and magnetic responses,* Nat. Chem. **3**, 359 (2011).
[283] J. Liu, H. Isshiki, K. Katoh, T. Morita, B. K. Breedlove, M. Yamashita, and T. Komeda, *First observation of a kondo resonance for a stable neutral pure organic radical, 1,3,5-triphenyl-6-oxoverdazyl, adsorbed on the au(111) surface,* J. Am. Chem. Soc. **135**, 651 (2013).
[284] Y.-h. Zhang, S. Kahle, T. Herden, C. Stroh, M. Mayor, U. Schlickum, M. Ternes, P. Wahl, and K. Kern, *Temperature and magnetic field dependence of a kondo system in the weak coupling regime.* Nat. Commun. **4**, 2110 (2013).

[285] S. Müllegger, M. Rashidi, M. Fattinger, and R. Koch, *Surface-Supported Hydrocarbon π Radicals Show Kondo Behavior.* J. Phys. Chem. C. Nanomater. Interfaces **117**, 5718 (2013).

[286] J. J. Parks, A. R. Champagne, T. A. Costi, W. W. Shum, A. N. Pasupathy, E. Neuscamman, S. Flores-Torres, P. S. Cornaglia, A. A. Aligia, C. A. Balseiro, G. K. L. Chan, H. D. Abruna, and D. C. Ralph, *Mechanical control of spin states in spin-1 molecules and the underscreened kondo effect,* Science **328**, 1370 (2010).

[287] J. Kondo, *Resistance minimum in dilute magnetic alloys,* Progr. Theor. Phys. **32**, 37 (1964).

[288] D. Goldhaber-Gordon, H. Shtrikman, D. Mahalu, D. Abusch-Magder, U. Meirav, and M. A. Kastner, *Kondo effect in a single-electron transistor,* Nature **391**, 156 (1998).

[289] J. J. Parks, A. R. Champagne, G. R. Hutchison, S. Flores-Torres, H. D. Abruna, and D. C. Ralph, *Tuning the kondo effect with a mechanically controllable break junction,* Phys. Rev. Lett. **99**, 026601 (2007).

[290] L. H. Yu and D. Natelson, *The kondo effect in c_{60} single-molecule transistors,* Nano Lett. **4**, 79 (2004).

[291] G. D. Scott and D. Natelson, *Kondo resonances in molecular devices,* ACS Nano **4**, 3560 (2010).

[292] G. D. Scott, D. Natelson, S. Kirchner, and E. Munoz, *Transport characterization of kondo-correlated single-molecule devices,* Phys. Rev. B **87**, 241104(R) (2013).

[293] W. Liang, M. P. Shores, M. Bockrath, J. R. Long, and H. Park, *Kondo resonance in a single-molecule transistor,* Nature **417**, 725 (2002).

[294] S. Wagner, F. Kisslinger, S. Ballmann, F. Schramm, R. Chandrasekar, T. Bodenstein, O. Fuhr, D. Secker, K. Fink, M. Ruben, and H. B. Weber, *Switching of a coupled spin pair in a single-molecule junction,* Nat. Nanotech. **8**, 575 (2013).

[295] O. Armet, J. Veciana, C. Rovira, J. Riera, J. Castaner, E. Molins, J. Rius, C. Miravitlles, S. Olivella, and J. Brichfeus, *Inert carbon free-radicals .8. polychlorotriphenylmethyl radicals - synthesis, structure, and spin-density distribution,* J. Phys. Chem. **91**, 5608 (1987).

[296] H. Hakkinen, *The gold-sulfur interface at the nanoscale,* Nat. Chem. **4**, 443 (2012).

[297] M. Ratner, *A brief history of molecular electronics,* Nat. Nanotech. **8**, 378 (2013).

[298] L. de la Vega, A. Martin-Rodero, N. Agrait, and A. L. Yeyati, *Universal features of electron-phonon interactions in atomic wires,* Phys. Rev. B **73**, 075428 (2006).

[299] W. H. A. Thijssen, D. Djukic, A. F. Otte, R. H. Bremmer, and J. M. van Ruitenbeek, *Vibrationally induced two-level systems in single-molecule junctions,* Phys. Rev. Lett. **97**, 226806 (2006).

[300] D. Goldhaber-Gordon, J. Gores, M. A. Kastner, H. Shtrikman, D. Mahalu, and U. Meirav, *From the kondo regime to the mixed-valence regime in a single-electron transistor,* Phys. Rev. Lett. **81**, 5225 (1998).

[301] K. Nagaoka, T. Jamneala, M. Grobis, and M. F. Crommie, *Temperature dependence of a single kondo impurity,* Phys. Rev. Lett. **88**, 077205 (2002).

[302] T. A. Costi, *Kondo effect in a magnetic field and the magnetoresistivity of kondo alloys,* Phys. Rev. Lett. **85**, 1504 (2000).

[303] J. M. van Ruitenbeek, A. Alvarez, I. Pineyro, C. Grahmann, P. Joyez, M. H. Devoret, D. Esteve, and C. Urbina, *Adjustable nanofabricated atomic size contacts,* Rev. Sci. Instrum. **67**, 108 (1996).

[304] C. A. Martin, R. H. M. Smit, R. v. Egmond, H. S. J. van der Zant, and J. M. van Ruitenbeek, *A versatile low-temperature setup for the electrical characterization of single-molecule junctions,* Rev. Sci. Instrum. **82**, 053907 (2011).

[305] E. Burzurí, R. Gaudenzi, and H. S. J. van der Zant, *Observing Magnetic Anisotropy in Electronic Transport through Individual Single-Molecule Magnets.* J. Phys. Condens. Matter **27**, 113202 (2015).

[306] M. J. Frisch, G. W. Trucks, H. B. Schlegel, G. E. Scuseria, M. A. Robb, J. R. Cheeseman, G. Scalmani, V. Barone, B. Mennucci, G. A. Petersson, H. Nakatsuji, M. Caricato, X. Li, H. P. Hratchian, A. F. Izmaylov, J. Bloino, G. Zheng, J. L. Sonnenberg, M. Hada, M. Ehara, K. Toyota, R. Fukuda, J. Hasegawa, M. Ishida, T. Nakajima, Y. Honda, O. Kitao, H. Nakai, T. Vreven, J. Montgomery, J. A., J. E. Peralta, F. Ogliaro, M. Bearpark, J. J. Heyd, E. Brothers, K. N. Kudin, V. N. Staroverov, R. Kobayashi, J. Normand, K. Raghavachari, A. Rendell, J. C. Burant, S. S. Iyengar, J. Tomasi, M. Cossi, N. Rega, J. M. Millam, M. Klene, J. E. Knox, J. B. Cross, V. Bakken, C. Adamo, J. Jaramillo, R. Gomperts, R. E. Stratmann, O. Yazyev, A. J. Austin, R. Cammi, C. Pomelli, J. W. Ochterski, R. L. Martin, K. Morokuma, V. G. Zakrzewski, G. A. Voth, P. Salvador, J. J. Dannenberg, S. Dapprich, A. D. Daniels, Ö. Farkas, J. B. Foresman, J. V. Ortiz, J. Cioslowski, and D. J. Fox, *Gaussian 09, Revision D.01,* (2009).

[307] P. J. Stephens, F. J. Devlin, C. F. Chabalowski, and M. J. Frisch, *Ab-initio calculation of vibrational absorption and circular-dichroism spectra using density-functional force-fields,* J. Phys. Chem. **98**, 11623 (1994).

[308] S. Grimme, *Semiempirical gga-type density functional constructed with a long-range dispersion correction,* J. Comput. Chem. **27**, 1787 (2006).

[309] J. C. Scheer, E.; Cuevas, *Molecular Electronics: an introduction to theory and experiments* (World

Scientific, 2010).

[310] S. a. Wolf, D. D. Awschalom, R. Buhrman, J. M. Daughton, S. von Molnár, M. L. Roukes, A. Y. Chtchelkanova, and D. M. Treger, *Spintronics: a Spin-Based Electronics Vision for the Future.* Science **294**, 1488 (2001).

[311] S. Sanvito, *Molecular Spintronics,* Chem. Soc. Rev. **40**, 3336 (2011).

[312] M. Urdampilleta, S. Klyatskaya, J.-P. Cleuziou, M. Ruben, and W. Wernsdorfer, *Supramolecular Spin Valves,* Nat. Mater. **10**, 502 (2011).

[313] L. Bogani and W. Wernsdorfer, *Molecular Spintronics using Single-Molecule Magnets.* Nat. Mater. **7**, 179 (2008).

[314] R. Vincent, S. Klyatskaya, M. Ruben, W. Wernsdorfer, and F. Balestro, *Electronic Read-Out of a Single Nuclear Spin using a Molecular Spin Transistor,* Nature **488**, 357 (2012).

[315] S. Thiele, F. Balestro, R. Ballou, S. Klyatskaya, M. Ruben, and W. Wernsdorfer, *Electrically Driven Nuclear Spin Resonance in Single-Molecule Magnets,* Science **344**, 1135 (2014).

[316] J. Lehmann, A. Gaita-Ariño, E. Coronado, and D. Loss, *Quantum Computing with Molecular Spin Systems,* J. Mater. Chem. **19**, 1672 (2009).

[317] F. Troiani, M. Affronte, A. Candini, A. Ghirri, R. Biagi, U. del Pennino, S. Carretta, E. Garlatti, P. Santini, G. Amoretti, G. Timco, R. E. P. Winpenny, M. Affronte, M. Nakahara, H. Hara, P. Carl, P. Höfer, and T. Takui, *Molecular Spins for Quantum Information Technologies,* Chem. Soc. Rev. **40**, 3119 (2011).

[318] J. Ferrando-Soria, S. A. Magee, A. Chiesa, S. Carretta, P. Santini, I. J. Vitorica-Yrezabal, F. Tuna, G. F. Whitehead, S. Sproules, K. M. Lancaster, A.-L. Barra, G. A. Timco, E. J. McInnes, and R. E. Winpenny, *Switchable Interaction in Molecular Double Qubits,* Chem **1**, 727 (2016).

[319] J. Ferrando-Soria, E. Moreno Pineda, A. Chiesa, A. Fernandez, S. A. Magee, S. Carretta, P. Santini, I. J. Vitorica-Yrezabal, F. Tuna, G. A. Timco, E. J. McInnes, and R. E. Winpenny, *A Modular Design of Molecular Qubits to Implement Universal Quantum Gates,* Nat. Commun. **7**, 11377 (2016).

[320] M. Trif, F. Troiani, D. Stepanenko, and D. Loss, *Spin-Electric Coupling in Molecular Magnets,* Phys. Rev. Lett. **101**, 217201 (2008).

[321] E. A. Osorio, K. Moth-Poulsen, H. S. J. van der Zant, J. Paaske, P. Hedegård, K. Flensberg, J. Bendix, and T. Bjørnholm, *Electrical Manipulation of Spin States in a Single Electrostatically Gated Transition-Metal Complex,* Nano Lett. **10**, 105 (2010).

[322] M. Trif, F. Troiani, D. Stepanenko, and D. Loss, *Spin Electric Effects in Molecular Antiferromagnets,* Phys. Rev. B **82**, 045429 (2010).

[323] M. F. Islam, J. F. Nossa, C. M. Canali, and M. Pederson, *First-Principles Study of Spin-Electric Coupling in a { Cu 3 } Single Molecular Magnet,* Phys. Rev. B **82**, 155446 (2010).

[324] S. Florens, A. Freyn, N. Roch, W. Wernsdorfer, F. Balestro, P. Roura-Bas, and A. A. Aligia, *Universal Transport Signatures in Two-Electron Molecular Quantum Dots: Gate-Tunable Hund's Rule, Underscreened Kondo Effect and Quantum Phase Transitions,* J. Phys. Condens. Matter **23**, 243202 (2011).

[325] A. Palii, J. M. Clemente-Juan, B. Tsukerblat, and E. Coronado, *Electric field control of the optical properties in magnetic mixed-valence molecules,* Chemical Science **5**, 3598 (2014).

[326] S. Cardona-Serra, J. M. Clemente-Juan, E. Coronado, A. Gaita-Ariño, N. Suaud, O. Svoboda, R. Bastardis, N. Guihéry, and J. J. Palacios, *Electrically switchable magnetic molecules: Inducing a magnetic coupling by means of an external electric field in a mixed-valence polyoxovanadate cluster,* Chemistry–A European Journal **21**, 763 (2015).

[327] E. Burzurí, A. S. Zyazin, A. Cornia, and H. S. J. van der Zant, *Direct Observation of Magnetic Anisotropy in an Individual Fe 4 Single-Molecule Magnet,* Phys. Rev. Lett. **109**, 147203 (2012).

[328] J. F. Nossa, M. F. Islam, C. M. Canali, and M. R. Pederson, *Electric Control of a { Fe 4 } Single-Molecule Magnet in a Single-Electron Transistor,* Phys. Rev. B **88**, 224423 (2013).

[329] M. Misiorny, E. Burzurí, R. Gaudenzi, K. Park, M. Leijnse, M. R. Wegewijs, J. Paaske, A. Cornia, and H. S. J. van der Zant, *Probing Transverse Magnetic Anisotropy by Electronic Transport through a Single-Molecule Magnet,* Phys. Rev. B **91**, 035442 (2015).

[330] M. Scarrozza, P. Barone, R. Sessoli, S. Picozzi, M. Barry, A. Doran, M. P. Cruz, Y. H. Chu, C. Ederer, N. A. Spaldin, R. R. Das, D. M. Kim, S. H. Baek, C. B. Eom, and R. Ramesh, *Magnetoelectric Coupling and Spin-Induced Electrical Polarization in Metal–Organic Magnetic Chains,* J. Mater. Chem. C **4**, 4176 (2016).

[331] A. Rajca, J. Wongsriratanakul, and S. Rajca, *Magnetic Ordering in an Organic Polymer,* Science **294**, 1503 (2001).

[332] T. Li, G. Tan, D. Shao, J. Li, Z. Zhang, Y. Song, Y. Sui, S. Chen, Y. Fang, and X. Wang, *Magnetic Bistability in a Discrete Organic Radical,* J. Am. Chem. Soc. **138**, 10092 (2016).

[333] M. Mas-Torrent, N. Crivillers, V. Mugnaini, I. Ratera, C. Rovira, J. Veciana, C. Wöll, S. Prato, P. Pittana,

Y. Manassen, and D. N. Reinhoudt, *Organic Radicals on Surfaces: Towards Molecular Spintronics,* J. Mater. Chem. **19**, 1691 (2009).

[334] J. Lehmann, A. Gaita-Ariño, E. Coronado, and D. Loss, *Spin Qubits with Electrically Gated Polyoxometalate Molecules,* Nat. Nanotechnol. **2**, 312 (2007).

[335] F. Luis, A. Repollés, M. J. Martínez-Pérez, D. Aguilà, O. Roubeau, D. Zueco, P. J. Alonso, M. Evangelisti, A. Camón, J. Sesé, L. A. Barrios, and G. Aromí, *Molecular Prototypes for Spin-Based CNOT and SWAP Quantum Gates,* Phys. Rev. Lett. **107**, 117203 (2011).

[336] J. Veciana, C. Rovira, N. Ventosa, M. I. Crespo, and F. Palacio, *Stable polyradicals with high-spin ground states. 2. Synthesis and characterization of a complete series of polyradicals derived from 2,4,6-trichloro-.alpha.,.alpha.,.alpha.',.alpha.',.alpha.",.alpha."-hexakis(pentachlorophenyl)mesitylene with S = 1/2, ,* J. Am. Chem. Soc. **115**, 57 (1993).

[337] M. L. Perrin, E. Burzurí, and H. S. J. van der Zant, *Single-Molecule Transistors.* Chem. Soc. Rev. **44**, 902 (2015).

[338] M. Ternes, *Spin Excitations and Correlations in Scanning Tunneling Spectroscopy,* New J. Phys. **17**, 063016 (2015).

[339] M. Souto, V. Lloveras, S. Vela, M. Fumanal, I. Ratera, and J. Veciana, *Three Redox States of a Diradical Acceptor-Donor-Acceptor Triad: Gating the Magnetic Coupling and the Electron Delocalization,* J. Phys. Chem. Lett. **7**, 2234 (2016).

[340] J. Paaske, A. Rosch, P. Wölfle, N. Mason, C. M. Marcus, and J. Nygård, *Non-equilibrium singlet–triplet Kondo effect in carbon nanotubes,* Nat. Phys. **2**, 460 (2006).

[341] A. D. Becke, *Density-Functional Thermochemistry. III. The Role of Exact Exchange,* J. Chem. Phys. **98**, 5648 (1993).

[342] W. J. Hehre, R. Ditchfield, and J. A. Pople, *Self—Consistent Molecular Orbital Methods. XII. Further Extensions of Gaussian—Type Basis Sets for Use in Molecular Orbital Studies of Organic Molecules,* J. Chem. Phys. **56**, 2257 (1972).

[343] J. D. Dill and J. A. Pople, *Self-consistent molecular orbital methods. XV. Extended Gaussian-type basis sets for lithium, beryllium, and boron,* J. Chem. Phys. **62**, 2921 (1975).

[344] M. M. Francl, W. J. Pietro, W. J. Hehre, J. S. Binkley, M. S. Gordon, D. J. DeFrees, and J. A. Pople, *Self-consistent molecular orbital methods. XXIII. A polarization-type basis set for second-row elements,* J. Chem. Phys. **77**, 3654 (1982).

[345] K. Yamaguchi, Y. Takahara, T. Fueno, and K. Nasu, *Ab Initio MO Calculations of Effective Exchange Integrals between Transition-Metal Ions via Oxygen Dianions: Nature of the Copper-Oxygen Bonds and Superconductivity,* Jpn. J. Appl. Phys. **26**, L1362 (1987).

[346] K. Yamaguchi, F. Jensen, A. Dorigo, and K. Houk, *A spin correction procedure for unrestricted Hartree-Fock and Møller-Plesset wavefunctions for singlet diradicals and polyradicals,* Chem. Phys. Lett. **149**, 537 (1988).

[347] K. Yamaguchi, Y. Takahara, T. Fueno, and K. N. Houk, *Extended Hartree-Fock (EHF) theory of chemical reactions,* Theor. Chim. Acta **73**, 337 (1988).

[348] L. Noodleman, *Valence bond description of antiferromagnetic coupling in transition metal dimers,* J. Chem. Phys. **74**, 5737 (1981).

[349] L. Noodleman and E. R. Davidson, *Ligand spin polarization and antiferromagnetic coupling in transition metal dimers,* Chem. Phys. **109**, 131 (1986).

[350] L. Noodleman, C. Peng, D. Case, and J.-M. Mouesca, *Orbital interactions, electron delocalization and spin coupling in iron-sulfur clusters,* Coord. Chem. Rev. **144**, 199 (1995).

[351] W. Kabsch, *A solution for the best rotation to relate two sets of vectors,* Acta Crystallogr. Sect. A **32**, 922 (1976).

[352] W. Kabsch, *A discussion of the solution for the best rotation to relate two sets of vectors,* Acta Crystallogr. Sect. A **34**, 827 (1978).

[353] J. C. Kroman and A. Bratholm, *GitHub: Calculate RMSD for two XYZ structures http://github.com/charnley/rmsd.* .

[354] B. W. Heinrich, G. Ahmadi, V. L. Müller, L. Braun, J. I. Pascual, and K. J. Franke, *Change of the magnetic coupling of a metal-organic complex with the substrate by a stepwise ligand reaction.* Nano Lett. **13**, 4840 (2013).

[355] O. Kahn and B. Briat, *Exchange interaction in polynuclear complexes. Part 1.?Principles, model and application to the binuclear complexes of chromium(III),* J. Chem. Soc. Faraday Trans. 2 **72**, 268 (1976).

[356] B. Bryant, A. Spinelli, J. J. T. Wagenaar, M. Gerrits, and A. F. Otte, *Local Control of Single Atom Magnetocrystalline Anisotropy,* Phys. Rev. Lett. **111**, 127203 (2013).

[357] P. Grünberg, R. Schreiber, Y. Pang, M. B. Brodsky, and H. Sowers, *Layered Magnetic Structures: Ev-*

idence for Antiferromagnetic Coupling of Fe Layers across Cr Interlayers, Phys. Rev. Lett. **57**, 2442 (1986).

[358] A. Fert, P. Grünberg, A. Barthélémy, F. Petroff, and W. Zinn, *Layered magnetic structures: interlayer exchange coupling and giant magnetoresistance,* J. Magn. Magn. Mater. **140-144**, 1 (1995).

[359] J. Sedó, N. Ventosa, D. Ruiz-Molina, M. Mas, E. Molins, C. Rovira, and J. Veciana, *Crystal Structures of Chiral Diastereoisomers of a Carbon-Based High-Spin Molecule,* Angew. Chemie Int. Ed. **37**, 330 (1998).

[360] H. C. Longuet-Higgins, *Some Studies in Molecular Orbital Theory I. Resonance Structures and Molecular Orbitals in Unsaturated Hydrocarbons,* J. Chem. Phys. **18**, 265 (1950).

[361] A. A. Ovchinnikov, *Multiplicity of the ground state of large alternant organic molecules with conjugated bonds,* Theor. Chim. Acta **47**, 297 (1978).

[362] W. T. Borden and E. R. Davidson, *Effects of electron repulsion in conjugated hydrocarbon diradicals,* J. Am. Chem. Soc. **99**, 4587 (1977).

[363] D. Reta Mañeru, R. Costa, M. Guix Márquez, I. d. P. R. Moreira, and F. Illas, *Handling Magnetic Coupling in Trinuclear Cu(II) Complexes,* J. Chem. Theory Comput. **11**, 3650 (2015).

[364] I. d. P. R. Moreira and F. Illas, *A unified view of the theoretical description of magnetic coupling in molecular chemistry and solid state physics.* Phys. Chem. Chem. Phys. **8**, 1645 (2006).

[365] P. C. Hariharan and J. A. Pople, *The influence of polarization functions on molecular orbital hydrogenation energies,* Theor. Chim. Acta **28**, 213 (1973).

[366] W. Heisenberg, *Zur Theorie des Ferromagnetismus,* Zeitschrift für Phys. **49**, 619 (1928).

[367] P. A. M. Dirac, *Quantum Mechanics of Many-Electron Systems,* Proc. R. Soc. A Math. Phys. Eng. Sci. **123**, 714 (1929).

[368] J. H. Van Vleck, *The theory of electric and magnetic susceptibilities* (Oxford University Press, Oxford, 1932).

[369] P. A. M. Dirac, *Principles of Quantum Mechanics* (Clarendon Press, Oxford, 1958).

[370] E. Sinn, *Magnetic exchange in polynuclear metal complexes,* Coord. Chem. Rev. **5**, 313 (1970).

[371] E. Ising, *Beitrag zur Theorie des Ferromagnetismus,* Zeitschrift für Phys. **31**, 253 (1925).

[372] R. Landauer, *Irreversibility and heat generation in the computing process,* IBM Journal of Research and Development **5**, 183 (1961).

[373] C. H. Bennett, *The thermodynamics of computation - a review,* International Journal of Theoretical Physics **21**, 905 (1982).

[374] C. H. Bennett, *Notes on the history of reversible computation,* IBM Journal of Research and Development **32**, 16 (1988).

[375] H. Leff and A. Rex, *Maxwell's demon: Information, entropy, computing,* A Hilger and Princeton Univ. Press, Europe/USA (1990).

[376] B. Lambson, D. Carlton, and J. Bokor, *Exploring the thermodynamic limits of computation in integrated systems: Magnetic memory, nanomagnetic logic, and the landauer limit,* Phys. Rev. Lett. **107**, 010604 (2011).

[377] L. Gammaitoni, D. Chiuchiu, M. Madami, and G. Carlotti, *Towards zero-power ict,* Nanotechnology **26**, 222001 (2015).

[378] T. Gerrits, H. A. M. van den Berg, J. Hohlfeld, L. Bar, and T. Rasing, *Ultrafast precessional magnetization reversal by picosecond magnetic field pulse shaping,* Nature **418**, 509 (2002).

[379] I. Žutić, J. Fabian, and S. Das Sarma, *Spintronics: Fundamentals and applications,* Rev. Mod. Phys. **76**, 323 (2004).

[380] T. A. Ostler, J. Barker, R. F. L. Evans, R. W. Chantrell, U. Atxitia, O. Chubykalo-Fesenko, S. El Moussaoui, L. Le Guyader, E. Mengotti, L. J. Heyderman, F. Nolting, A. Tsukamoto, A. Itoh, D. Afanasiev, B. A. Ivanov, A. M. Kalashnikova, K. Vahaplar, J. Mentink, A. Kirilyuk, T. Rasing, and A. V. Kimel, *Ultrafast heating as a sufficient stimulus for magnetization reversal in a ferrimagnet,* Nature Communications **3**, 666 (2012).

[381] Y. Yang, R. Wilson, J. Gorchon, C.-H. Lambert, S. Salahuddin, and J. Bokor, *Ultrafast magnetization reversal by picosecond electrical pulses,* arXiv preprint arXiv:1609.06392 (2016).

[382] Y. Jun, M. Gavrilov, and J. Bechhoefer, *High-precision test of landauer's principle in a feedback trap,* Phys. Rev. Lett. **113**, 190601 (2014).

[383] A. Berut, A. Arakelyan, A. Petrosyan, S. Ciliberto, R. Dillenschneider, and E. Lutz, *Experimental verification of landauer principle linking information and thermodynamics,* Nature **483**, 187 (2012).

[384] J. Hong, B. Lambson, S. Dhuey, and J. Bokor, *Experimental test of landauer principle in single-bit operations on nanomagnetic memory bits,* Science advances **2**, 1501492 (2016).

[385] E. Burzurí, F. Luis, B. Barbara, R. Ballou, E. Ressouche, O. Montero, J. Campo, and S. Maegawa, *Magnetic dipolar ordering and quantum phase transition in an* fe_8 *molecular magnet,* Phys. Rev.

Lett. **107**, 097203 (2011).
[386] D. Gatteschi, R. Sessoli, and J. Villain, *Molecular Nanomagnets* (Oxford University Press, 2006) p. 408.
[387] C. Sangregorio, T. Ohm, C. Paulsen, R. Sessoli, and D. Gatteschi, *Quantum tunneling of the magnetization in an iron cluster nanomagnet,* Phys. Rev. Lett. **78**, 4645 (1997).
[388] E. Burzurí, F. Luis, O. Montero, B. Barbara, R. Ballou, and S. Maegawa, *Quantum interference oscillations of the superparamagnetic blocking in an* fe_8 *molecular nanomagnet,* Phys. Rev. Lett. **111**, 057201 (2013).
[389] F. Luis, J. Bartolome, and J. F. Fernandez, *Resonant magnetic quantum tunneling through thermally activated states,* Physical Review B **57**, 505 (1998).
[390] N. Margolus and L. B. Levitin, *The maximum speed of dynamical evolution,* Physica D **120**, 188 (1998).
[391] S. Lloyd, *Ultimate physical limits to computation,* Nature **406**, 1047 (2000).
[392] Y. Aharonov and D. Bohm, *Time in the quantum theory and the uncertainty relation for time and energy,* Phys. Rev. **122**, 1649 (1961).
[393] J. Anandan and Y. Aharonov, *Geometry of quantum evolution,* Phys. Rev. Lett. **65**, 1697 (1990).
[394] S. Deffner and E. Lutz, *Energy-time uncertainty relation for driven quantum systems,* Journal of Physics a-Mathematical and Theoretical **46** (2013).
[395] S. Campbell and S. Deffner, *Trade-off between speed and cost in shortcuts to adiabaticity,* Physical Review Letters **118** (2017).
[396] G. E. Blonder, M. Tinkham, and T. M. Klapwijk, *Transition from metallic to tunneling regimes in superconducting micro-constrictions - excess current, charge imbalance, and super-current conversion,* Physical Review B **25**, 4515 (1982).
[397] T. Soda, T. Matsuura, and Y. Nagaoka, *S-d exchange interaction in a superconductor,* Progress of Theoretical Physics **38**, 551 (1967).
[398] H. Shiba and T. Soda, *Superconducting tunneling through barrier with paramagnetic impurities,* Progress of Theoretical Physics **41**, 25 (1969).
[399] H. Shiba, *Classical spins in superconductors,* Progress of Theoretical Physics **40**, 435 (1968).
[400] A. I. Rusinov, *Anisotropy of critical current for surface superconductivity near field strength hc3,* Soviet Physics Jetp-Ussr **29**, 772 (1969).
[401] E. Scheer, P. Joyez, D. Esteve, C. Urbina, and M. H. Devoret, *Conduction channel transmissions of atomic-size aluminum contacts,* Physical Review Letters **78**, 3535 (1997).
[402] V. Koerting, B. M. Andersen, K. Flensberg, and J. Paaske, *Nonequilibrium transport via spin-induced subgap states in superconductor/quantum dot/normal metal cotunnel junctions,* Physical Review B **82** (2010).
[403] B. M. Andersen, K. Flensberg, V. Koerting, and J. Paaske, *Nonequilibrium transport through a spinful quantum dot with superconducting leads,* Physical Review Letters **107** (2011).
[404] I. A. Sadovskyy, D. Chevallier, T. Jonckheere, M. Lee, S. Kawabata, and T. Martin, *Josephson effect through an anisotropic magnetic molecule,* Physical Review B **84** (2011).
[405] M. Lee, T. Jonckheere, and T. Martin, *Josephson effect through an isotropic magnetic molecule,* Physical Review Letters **101** (2008).
[406] J. Bauer, J. I. Pascual, and K. J. Franke, *Microscopic resolution of the interplay of kondo screening and superconducting pairing: Mn-phthalocyanine molecules adsorbed on superconducting pb(111),* Physical Review B **87** (2013).
[407] A. Y. Kasumov, K. Tsukagoshi, M. Kawamura, T. Kobayashi, Y. Aoyagi, K. Senba, T. Kodama, H. Nishikawa, I. Ikemoto, K. Kikuchi, V. T. Volkov, Y. A. Kasumov, R. Deblock, S. Gueron, and H. Bouchiat, *Proximity effect in a superconductor-metallofullerene-superconductor molecular junction,* Physical Review B **72**, 033414 (2005).
[408] C. B. Winkelmann, N. Roch, W. Wernsdorfer, V. Bouchiat, and F. Balestro, *Superconductivity in a single-c-60 transistor,* Nature Physics **5**, 876 (2009).
[409] E. Scheer, W. Belzig, Y. Naveh, M. H. Devoret, D. Esteve, and C. Urbina, *Proximity effect and multiple andreev reflections in gold atomic contacts,* Physical Review Letters **86**, 284 (2001).
[410] M. R. Buitelaar, T. Nussbaumer, and C. Schonenberger, *Quantum dot in the kondo regime coupled to superconductors,* Physical Review Letters **89**, 256801 (2002).
[411] S. De Franceschi, L. Kouwenhoven, C. Schonenberger, and W. Wernsdorfer, *Hybrid superconductor-quantum dot devices,* Nature Nanotechnology **5**, 703 (2010).
[412] J. Talvacchio, M. A. Janocko, and J. Greggi, *Properties of evaporated mo-re thin-film superconductors,* Journal of Low Temperature Physics **64**, 397 (1986).
[413] T. M. Klapwijk, *Proximity effect from an andreev perspective,* Journal of Superconductivity **17**, 593

(2004).

[414] S. Gueron, H. Pothier, N. O. Birge, D. Esteve, and M. H. Devoret, *Superconducting proximity effect probed on a mesoscopic length scale,* Physical Review Letters **77**, 3025 (1996).

[415] A. A. Golubov, E. P. Houwman, J. G. Gijsbertsen, V. M. Krasnov, J. Flokstra, H. Rogalla, and M. Y. Kupriyanov, *Proximity effect in superconductor-insulator-superconductor josephson tunnel-junctions - theory and experiment,* Physical Review B **51**, 1073 (1995).

[416] W. Belzig, C. Bruder, and G. Schon, *Local density of states in a dirty normal metal connected to a superconductor,* Physical Review B **54**, 9443 (1996).

[417] K. D. Usadel, *Generalized diffusion equation for superconducting alloys,* Physical Review Letters **25**, 507 (1970).

[418] L. I. Glazman and K. A. Matveev, *Resonant josephson current through kondo impurities in a tunnel barrier,* Jetp Letters **49**, 659 (1989).

[419] A. K. Mitchell, T. F. Jarrold, and D. E. Logan, *Quantum phase transition in quantum dot trimers,* Physical Review B **79**, 085124 (2009).

[420] A. K. Mitchell, T. F. Jarrold, M. R. Galpin, and D. E. Logan, *Local moment formation and kondo screening in impurity trimers,* The Journal of Physical Chemistry B **117**, 12777 (2013).

[421] P. P. Baruselli, R. Requist, M. Fabrizio, and E. Tosatti, *Ferromagnetic kondo effect in a triple quantum dot system,* Physical review letters **111**, 047201 (2013).

[422] J. de Bruijckere, *Superconducting transport through Fe_4 single-molecule magnets,* Master thesis, TU Delft (2015).

[423] D. Chatzopoulos, *Superconducting nanodevices for single-molecule transport studies: Experiments and simulations,* Master thesis, TU Delft (2017).

[424] S. Takahashi, I. Tupitsyn, J. Van Tol, C. Beedle, D. Hendrickson, and P. Stamp, *Decoherence in crystals of quantum molecular magnets,* Nature **476**, 76 (2011).

[425] N. Jones, *The quantum company,* Nature **498**, 286 (2013).

[426] T. F. Rønnow, Z. Wang, J. Job, S. Boixo, S. V. Isakov, D. Wecker, J. M. Martinis, D. A. Lidar, and M. Troyer, *Defining and detecting quantum speedup,* Science **345**, 420 (2014).

[427] J. Brooke, D. Bitko, T. Rosenbaum, and G. Aeppli, *Quantum annealing of a disordered magnet,* Science **284**, 779 (1999).

[428] K. Bader, D. Dengler, S. Lenz, B. Endeward, S.-D. Jiang, P. Neugebauer, and J. van Slageren, *Room Temperature Quantum Coherence in a Potential Molecular Qubit,* Nat. Commun. **5**, 5304 (2014).

[429] M. Shiddiq, D. Komijani, Y. Duan, A. Gaita-Ariño, E. Coronado, and S. Hill, *Enhancing coherence in molecular spin qubits via atomic clock transitions,* Nature **531**, 348 (2016).

[430] K. Bader, S. Schlindwein, D. Gudat, and J. van Slageren, *Molecular qubits based on potentially nuclear-spin-free nickel ions,* Physical Chemistry Chemical Physics , 2525 (2017).

[431] R. M. Brown, A. M. Tyryshkin, K. Porfyrakis, E. M. Gauger, B. W. Lovett, A. Ardavan, S. A. Lyon, G. A. D. Briggs, and J. J. L. Morton, *Coherent state transfer between an electron and nuclear spin in* $^{15}\mathbf{N@c_{60}}$, Phys. Rev. Lett. **106**, 110504 (2011).

[432] J. E. Green, J. W. Choi, A. Boukai, Y. Bunimovich, E. Johnston-Halperin, E. DeIonno, Y. Luo, B. A. Sheriff, K. Xu, Y. S. Shin, *et al.*, *A 160-kilobit molecular electronic memory patterned at 1011 bits per square centimetre,* Nature **445**, 414 (2007).

CURRICULUM VITÆ

Rocco GAUDENZI

12-12-1987 Born in Bologna, Italy.

EDUCATION

2001–2006 High School
Liceo Classico Statale *'Terenzio Mamiani'*
Pesaro, Italy

2006–2009 Bachelor of Science in Physics *(cum laude)*
Università di Roma Tre, Rome, Italy
Thesis: The Aharonov-Bohm effect
Supervisors: Prof. dr. R. Raimondi

2010–2012 Master of Science in Physics
ETH Zürich, Zürich, Switzerland
Thesis: Scanning gate microscopy in the integer and fractional quantum Hall regimes
Supervisors: Prof. dr. T. Ihn

2012 Internship
Paul Schrerrer Institute (PSI), Villigen, Switzerland

2013–2017 Ph.D. in Applied Physics
Delft University of Technology, Delft, the Netherlands

Thesis: Quantum transport phenomena in magnetic molecules
Supervisors: Prof. dr. ir. H.S.J. van der Zant

LIST OF PUBLICATIONS

[10] **R. Gaudenzi**, E. Burzurí, S. Maegawa, H.S.J. van der Zant, F. Luis, *Quantum-enhanced Landauer erasure and storage,* arXiv:1703.04607 (in review, Nature Physics).

[9] A. M. Monteiro, D. J. Groenendijk, I. Groen, J. de Bruijckere, **R. Gaudenzi**, H.S.J. van der Zant, A. D. Caviglia, *Two-dimensional superconductivity at the (111) $LaAlO_3/SrTiO_3$ interface*, arXiv:1703.04742 (submitted to Phys. Rev. B).

[8] **R. Gaudenzi**, J. de Bruijckere, D. Reta, I. de P.R. Moreira, C. Rovira, J. Veciana, H.S.J. van der Zant, E. Burzurí, *Redox-induced gating of the exchange interactions in a single organic diradical*, Accepted (ACS Nano, DOI: 10.1021/acsnano.7b01578).

[7] J. O. Island, **R. Gaudenzi**, J. de Bruijckere, E. Burzurí, C. Franco, M. Mas-Torrent, C. Rovira, J. Veciana, T. M. Klapwijk, R. Aguado, H.S.J. van der Zant, *Proximity-induced Shiba states in a molecular junction*, Phys. Rev. Lett. **118**, 117001 (2017).

[6] **R. Gaudenzi**, M. Misiorny, E. Burzurí, M. R. Wegewijs, H.S.J. van der Zant, *Transport mirages in single-molecule devices*, J. Chem. Phys. **146**, 092330 (2017).

[5] **R. Gaudenzi**, E. Burzurí, D. Reta, I. de P.R. Moreira, S. Bromley, C. Rovira, J. Veciana, H.S.J. van der Zant, *Exchange coupling inversion in a high-spin organic triradical molecule*, Nano Letters **16**, 2066 – 2071 (2016).

[4] **R. Gaudenzi**, J. O. Island, J. de Bruijckere, E. Burzurí, T. M. Klapwijk, H.S.J. van der Zant, *Superconducting molybdenum-rhenium electrodes for single-molecule transport studies*, Appl. Phys. Lett. **106**, 222602 (2015).

[3] E. Burzurí, **R. Gaudenzi**, H.S.J. van der Zant *Observing magnetic anisotropy in electronic transport through individual single-molecule magnets*, J. Phys. Cond. Matter **27**, 113202 (2015).

[2] R. Frisenda*, **R. Gaudenzi***, C. Franco, M. Mas-Torrent, C. Rovira, J. Veciana, I. Alcon, S. Bromley, E. Burzurí, H.S.J. van der Zant, *Kondo effect in a neutral and stable all organic radical single molecule break junction*, Nano Letters **15**, 3109 – 3114 (2015).

[1] M. Misiorny, E. Burzurí, **R. Gaudenzi**, K. Park, M. Leijnse, M. R. Wegewijs, J. Paaske, A. Cornia, H.S.J. van der Zant, *Probing transverse magnetic anisotropy by electronic transport through a single-molecule magnet*, Phys. Rev. B **91** 035442 (2015).

* These two authors contributed equally

ACKNOWLEDGEMENTS

To make a revolution
you should, above all, never grow tired to repeat

Anonymous from Pesaro

I interpret these acknowledgements as a confession, a tribute. The title of a forgotten and beautiful jazz song goes: "For those I never knew". And, in fact, they symbolise to me the uncharted territory, forever reign of the could-have-been – only quantum particles do not need to choose –, which has forever slipped to us. The essence of this we call 'growing up': second after second reducing the potentially knowable, restricting the cone of causal influence of the Universe on us; our light-cone tentacles. As the mist evaporates of the future ahead of us, we do morph the magic of the not-yet-unfolded into mundane realizations and lifeless list of achievements. The angle of our vision is inexorably eroded, one degree after the other, and the list lengthens of the forever unknowable ones. Yes, we do accumulate wisdom in the weights of our past, but as much as we silently lose the whimsical mobility of feathers. And the souls of those who we will never know will be flocking and dancing, innumerable, in the dark side of our light-cone. To those this work is dedicated, paradoxically, in the guise of a joke to allude to the power of the written published word in stretching into the space and time of our life's limited possibilities, by throwing a stone where the spoken word can not stretch. And some of these stones have rolled a long way here, in space and time, so it happens that we can have, here and now, Henri Poincaré, Giuseppe Ungaretti, Lao-Tzu and Cornelius Tacitus and Saint Augustine from a couple of millennia ago. I will thus commence by thanking them.

Let us come now to the ones I have known.
In force of the total freedom that this section grants me, for now let me declare the "H" the first letter of the alphabet and, in order to spare the brain of the unattached reader, I will mark the inside jokes with an asterisk. Now, please, a bow of reverence and respect. Silence. For our *Eccelentissimus et Illustrissimus* Gran Maestro Professor Dottor Ir. Herre S. J. van der Zant[10], in Italy also known as The Honorable Duca Robbe de la Sabbia. Beyond the eminent titles, you will find a person, after all, who is simply known among us as Herre (phonetic central Macedonian Ǧ'h'ere*). His office adjacent to the lab, a pair of elegant shoes left suffering in a corner, contorted and unevenly pointing, piles of papers on the table; hanging on the right side of the entrance, forgotten, a suit and a white shirt: when we first met, this I saw and made up my mind, for the scientist and the person. An invaluable mingle of caringness and carelessness, with a grain of Dutch folly and an attention for the *other*. In common language, we call this *humanity* and, as much as it is connatural to each of us, it is

[10]The meaning of some of these letters is still shrouded in mystery.

sometimes so buried under layers of folds that you wonder how it possibly sank so deep. But the sagacity of the master truly emerges where the disciple's lacks: I remember Herre entering the lab and asking "Are you happy?" In the midst of a lab crisis, confronted with the question, I would reply, poorly masking my gloominess: "Eeh, Eeh[11]... I don't know Herre, here... (unspoken: it's a mess!)" Few minutes later he would have solved the riddle with a twist, sometimes just by letting me see where I stand, what I am seeing and where we are heading. What were the words and the exact dynamics of this spell, dear reader, still escapes my poor mind of physicist. What I am sure of is that it had been, once again, the scientist *and* the person.

Walking on the dim corridor of the laboratories, the day I came to meet Herre, I remember vividly too, I met what would become my faithful companion of scientific wanderings. In time, he would explain to me all the art and science of measuring molecules, hocus-pocus of low temperatures and nanofabrication, attending at my mistakes, storms of questions and actions with an inborn gentleness, with the humility yet self-assuredness of someone who knows, but never imposes his knowledge. The conferences of molecular magnetism with all the spin-ups and spin-downs*of Mr. Masahiro luckily took us also to wander in the surreal light of the white nights of Saint Petersburg, discussing at length about the world and its characters, by the Neva; they took us to Como lake, Ascona and Zaragoza respectively along the *Lago Maggiore* and the Ebro, as if all these waters were there to support the ambulating thoughts. Yes, you know whom I am thinking about.

When it comes to press the "submit" button, my mind inevitably goes to a campfire late night. Except for the fact that we were *not* playing a guitar and we were *not* on a beach, but in the meeting room of the university. The deadline on the next day, finally all the cards are in the right place: "Maarten, I actually just know realize that... did you check that? I thought you had done it" "No, I thought you would do that. Don't tell me that now... ". Great humour, great stories of seasonal workers*: decades ago, they were humble, southern and low-educated, now it is the highly-skilled theoreticians which have to peregrinate in search for good data to chew.

It is now the turn of the 'T', for Teun Klapwijk: one for the science and one for the philosophy. A dear memory I will conserve sees the two of us sitting at the desk, carefully answering a referee report. It is through the simple actions that you get the character of a person and I, there, got a glimpse of what I believe it was old-school science: a vital attention to the details and less of that political correctness nowadays so much in vogue. You see, with Teun I also found myself discussing about the nature of physical laws or the Hellenists' scientific development, when me, and him, had casually walked into the common room only for a coffee or a print, and I can assure that my merit, if any, had been only in provoking him properly.

'F' for Fernando Luis who has enthusiastically believed in the "Landauer", his special passion for science, his dedication. It is not flattering, as you might think, but simply witnessing. I remember that he just could not leave that underground lab in Zaragoza where we were measuring the Landauer erasure. Despite his wife calling, the late hour, the hunger and having repeatedly expressed to himself and us his *actual* will of going, the invisible thread of curiosity was tying him (and us) to the dilution refrigerator and to that last-and-then-I-go data point like a curb, deferring

[11] Ask Herre for a faithful live reproduction.

his leave to an undefined moment. A special tribute to this man.

It is time to get to the peers now. The session has to be opened with the letters D&G. No, I am not referring to the couple that gives the name to the fashion brand, but rather to the couple – they are only friends – Dejan-Giordano whose whole muscular and intellectual prowess of Riace Bronzes you can admire only if you read these lines in due time, i.e. before the official defence of the present dissertation. The two paranymphs committed to defend me in case the questions from the German Wing would take an unexpected turn. Should I thank them? They should thank me for having the privilege. You see, dear reader, there is no need to say: through action and logic you should deduce, from the very fact that they will stand like pillars at my sides, all you need to know about their importance to me. Since any spoken recount would hardly transfer even the gist of my relation with these adventurous gentlemen, I concede myself only a small description. To you, too curious reader, is left to infer on the rest.

Dejan (aka Dejan Davidovich Scapone*, Mr. KJ*, chiefly Macedonian* "Solnze" in particularly intimate circumstances), awarded of the internationally renowned prize "Host of The Year 2015 and 2016" for clear merits. Ooh (sigh), our Macedonian "Great Gatsby" implanted in the Netherlands – yes, he can't wait to dispose of his present passport. What should I do to redeem this man? You see, if it were not for his indulgence in sexual jokes and his socialist, therefore blasphemous, Yugoslavian passport, Dante would certainly place him in the third and last section of the *Divina Commedia*, i.e. the Paradise. His generosity is unsurpassed – that is also what the clerk of his bank keeps telling him*– and if there is something he can do for you, he will do it[12]. He is one of the few who is able to feel nothing but joy at other's fortunes and only for this, I tell you, he would deserve Heaven. Dante wrote me that he actually is not going to promote him up there because he speaks too long on the phone, then he added: "If only he would employ a fraction of his time to focus on a written page, – something we ancient called *reading* –, he would sit between the hot Beatrice Portinari[13] and King Solomon". I ask you, dear reader, what should *I* do with this man?

Giordano (phonetic central Macedonian Giovan(n)i*, in Holland known as George Baksteen*) is a bit like a brother to me, someone with whom I felt inexplicably close to from the start: silence between us has never been uncomfortable. You might know the feeling with these younger brothers who are more gifted, smarter and faster than you: the only thing you can possibly instil into them is a grain of wisdom, about life and knowledge. In the attempt of doing this, against a proverbial stubbornness, I spent the long evenings with him. This partly earned me the appellative "the Preacher", which has had viral success ever since. An extraordinarily critical listener he is, to the point that if an idea, by any chance, sneaks through his tight sieve, you'd better run to the patent office.

Probably in his past or future life, I was told, he was or will be a jester. You see, what we sometimes fail to understand is that a jester is a physiological element of any human organization whose very existence bespeaks the plurality of views which I refer to at the end of the introduction; a sign of sanity of any system of power. In the medieval era, the kings themselves were appointing jesters in order to be poignantly criticised and derided at and stung as much as governments were by the satirists,

[12] So, please, think before asking.

[13] Maddalena, don't get angry, we are talking about life after death.

in the Roman and Greek societies. Santiago (Carta-miele, cartamilozzo Bueno or, in special circumstances, Buenissimo; the "albanian director" Giacomo (Calzebianche) di Pietro)*laurea *honoris causa* in mathematics of intrigues and paranoid theories – a new branch of theoretical physics – and next in line for a PhD in physics. Despite all that, I held him in great esteem, not certainly for his fine taste in clothing, but for his audacity, boldness and idealism. If I only had half the talent this man has for... In these years we have built a sound friendship and, possibly, we will be partners in crime.

An acute rational mind I had the pleasure to recognize in that of a glorious compatriot. And not only, also a vast knowledge of the sciences of alchemy and botany and of the mighty powers of the herbs. Ruthlessly honest and firm with his principles, this character has granted me the honour of being born exactly one year after him and the use of four letters of his name to compose my own. With the Gran Maestro as the head, Enrique, him and the undersigned are the founder of the Knight Order of the Radicals which, as the name might suggest, is a masonic organization with the plan of subverting the world's order – I am not sure I should say this – and therefore change, as a by-product, also the destiny of science. Details are not clear yet. In order to be part of this big underhand plan, the postulant has to have shown sufficient proof of a measurement on a radical species – for which one of the members of my illustrious committee would already be eligible –, preferably one of those in Chapters 2, 3 or 4 (superconducting leads are not allowed). We cannot conceal our predilection for the extreme rare species[14] whose triangular mighty powers are not fully known yet. Unanimous agreement between the vertices has so far been reached only on the inversion of the exchange coupling constant.

There is a man who unfortunately has lost the use of vocals: he calls but finds them nowhere, nor in his throat, nor in his guts. This does not diminish his valour whatsoever, rather it augments it to the point that the Balkans tremble at his utterances, compact as bullets and penetrating as spears. The legends wants him born in the midst of Central Anatolia. Abandoned there by Allah and subsequently found by transhumant pastors on their way to Europe, this child grows into what you all know now as the charming (O)ttom(a)n, the eight-handed, the sultan. Behind his adamantine and austere manners, result of the rude upbringing, a gentle and romantic heart nonetheless conceals, which I have witnessed with my own eyes. He is endowed with that sense of prophetic wisdom that inexplicably seem to accompany the long-bearded – I am not claiming a causality here, I can only testify a correlation. It would take you only a small leap of imagination to picture how this son of Mohammed and the Preacher could speculate limitlessly about life and celestial love, and argue about the nature of spirituality seamlessly indulging, at times, in discussions on more profane passions.

There was a time when only two individuals, like souls in torment, would meet in the otherwise practically desolated corridors of a dormant university. Some Huang somewhere in the central wing of the building, an annoying night guard and these two individuals:

"Dotto', anche Lei qui? Si misura?"

"Sempre, Michi, sempre. E tu?"

[14]The only powder exemplar left is stored in a safe whose location I cannot disclose, for obvious reasons.

"Anch'io come vedi. Dai, fa'mose 'na pizza, va!"

"San Marco?"

Despite the language, you might recognize the universal word "pizza" and thus figuring the two of them sitting at a wooden table eating a *Raffaele* – it is the best: Margherita base with sun-dried tomatoes and rucola –, over there, in a corner. To this indefatigable and emotional friend I would confess the troubled relationships of the time. He would recount me, in return, of the lab and Herre and the comradeship with the long-gone fellows and the time he used to live alone in a garret somewhere close to the lab, with a tip of nostalgia. We shared the *saudade* for the sea, the sailing and our towns. Thank god, we shared also some hand-made ravioli later on.

His brain never ceases to think, pondering, reasoning, weighing, reconsidering. Of Nikos (Ni-kos-pa-pa-do-pou-los, stadium choir style) I love what I would call the *problematic* flow: the attitude of ruminating events, psychological processes, life choices as well as experiments, is truly that of a philosopher; a Greek philosopher to whom I can confess, with inexplicable lightness, all my hesitancies. Regardless of whether we caress our beards or our bellies to stimulate thinking, it is probably because we two sense, in decisions, the burden of irreversibility and we would never want to take one for good.

There is also a guy, whom I have never seen actually working. Yes, he did graduate and I kept seeing papers and calculations and setup construction and programming and image processing and helping you with all the previous and happening to take a casual stroll on the *Mont Blanche* – he kept saying despised, as it is use among the French, that the southern face of *our* Monte Bianco he did not appreciated. This mysterious character, I was saying, I have *never* seen working. They say he has a twin, isn't perhaps the twin whom I saw once in the canteen and did not answer to my petulant waving, the *éminence grise* who does the job? Who is Mickael? Who is that who cloaks his identity under the variegated appellatives Mickeal, Mikcheal, Michel, Mickaël or Perrino? I actually would have an idea, but it is out of the scope of the present dissertation and will be subject of further investigation. (next dissertation).

My goodness, there was another character producing papers as if they were continuations of his hands. I had to prevent once his impulse of warming up a sample that could still yield some juice*. Board-gamers among us, show me your wits, I will give you another hint: his is a Jewish name of a famous character of the Old-testament. "Not much help!" you might say. Of the few times he was granting us of his presence – righteously despising the fun of us youngsters – I remember one, when I questioned him on what he would want ultimately from doing science, beyond the ephemeral sake of it. He told me he would, most of all, want to leave a tangible *trace* of his presence in this world. I appreciated that.

Just past my first year, a Russian girl was put to work with me. I was consequently instructed to teach her the basics of the dilution refrigerator, the molecule deposition and so on. Well, I could not restrain from admit to her, while soldering a pin of the sample holder, my true love for Russian culture and literature. She frowned with her typical frown. Asking the reason for the unexpected turn, I remember her replying that – here I report a poetical paraphrase of it – "reading the darkness I could not find light". I maintained that it was exactly the opposite, in my modest opinion, as the Dostoevskian character through the evil come to choose the good and that good is then truly authentically wanted, as a result of free will. I told: "After all, Dostoevskij

in one of his letters wrote that *Beauty will save the world* and that is a clear message". In the face of her incredulity, I proposed a bet on the trustworthiness on the source. I won that bet.

For sure what has impressed my mind for good is what I would name, in a stroke of genius, "the gymnastic with headphones". Fortunately, the practitioners of this sport left on the planet are few. My dear officemate Massimo Carbone (short and kind for "Massimiliano sfiga Carbone", here who knows, knows*) is one of those. A song from Paolo Conte goes: "Max, *era* Max, più tranquillo che mai...". Well put (note the use of the past)! The one that *has been a man once* is now Max(ima) and "walks between the kitchen and the bed". Massimo was a good partner in many scientific discussion and not rarely, to my uttermost joy, has illuminated me with his multi-folded practical philosophy. To him and his partner I wish *ogni bene*.

I have observed from afar Messer Giacomo Digaverde slowly growing from the callow student – coauthoring Nat. Comm. publications – into the honourable man that such a name demands. At the time when he still was in his former phase, he came to consult me on a certain matter[15]. To witness his scientific puberty, I have seen the sparse stalks on his face growing into disconnected patches at first and forming an uninterrupted layer then, with time. The admission among the "beardful" – in that respect Andrea has still some way to go – was conceded without further proof. Together with the other *enfants prodige* of our cheerful brigade – Giordano, Dejan and Joeri – they belong to this class of people that consistently beat me at board games, as any other, after all. What these gentlemen fail to grasp is that I take pride in other things. "Who's lucky at games is unlucky in love", that is why I let them win.

Shun, our clean-room samurai, is what John von Neumann would have called "the man of the hidden variables": a similar argument he used when justifying the epistemic incompleteness of quantum theory. Entanglement, for instance, would result of a hidden connection which we do not see. I had the honour to get to know some of these hidden variables on his vision of life and work and relationships which I exhort him to change, but I keenly respect. I also deeply revere the extreme humility and the profoundly different sense of aesthetic which I heard once condensing in an *haiku*.

E quel matto di Alessandro Bruno... the only difference between him and the other Bruno is that the former is not a philosopher and will not be roasted on a barbecue – given the legends running on supervisors over there, you may never know. The craziness, and the diabolic laughter, are doubtlessly the same. Here is a character whose inherited motto, I know, is "Stay hungry, stay foolish". You see, Neaples is not Italy, it is an enclave of unpredictable and creative jesters whose laughter is both mocking and benevolent. I spent several nights on Alessandro's couch with his cats messing up with my preposterous dreams. These days I hardly see him, but I keep an eye... you never know.... I might need to intervene.

The first time I heard one of her manifestation of joy, I could not believe human mouth could speak so fully. This most likely is already enough of a hint. If it were not, I add that her speech combines with a perceptible rocking of the head, left and right, which substantially differs from the one of our Greek representative in that it keeps the shoulders absolutely still. I feel a great affection to her, which the troubled waters

[15] Unfortunately, my professional secret requires total reserve on the content.

have not changed, and her partner. Very intelligent – though still a bit too stubborn and convinced –, her speech goes so fast that sometimes prevents her from listening. There have been and will be progresses in that which will allow the volcanic flow to enter the right rail.

I am not sure I can say that I discovered a talent, but I can certainly say I witnessed a fraction of his growth, in the role of supervisor. Normally I am lucky – I should be careful in stating that – and I was even luckier that the only master student I had is one of the *prodiges* belonging now to our scientific brigade. I remember with great pleasure the discussions we had on the interpretation of the Usadel formalism in an effort to come to a physical picture and I hope to have shaped his intellect, even a little, in emulation of or contrast to some of my idiosyncrasies. By then, we had spent so much time on reasoning and weighing that my stream of consciousness had become audible. There I discovered the patient listener and great interlocutor that still he is to me. His knowledge disposition and accuracy are, in my opinion, truly that of a scientific mind. His spiritual side I have not know. I hope there will be a chance.

"They have no corresponding power to endure hard work and exertion, and have little capacity to bear thirst and heat; but their climate and soil have taught them to bear cold and hunger. [...] To that strength of limb and size of body which excite our admiration. [...] The young men are slow to mate, and their powers, therefore, are never exhausted." These are only few excerpts detailing how the southern Romans regarded the Germans through Cornelius Tacitus's scientific eye. Now I finally understand how our valorous German – whose surname indeed testifies not a droplet of Latin heritage – could dub the pouring rain on his smooth head as "a refreshing bless" or why I would always see him in the lab, indefatigably pondering or frowning at an instrument until late hours. In other circumstances, I also understand why, if you properly feed him with a "juice they extract from barley or grain", "lasting a day and a night, is not considered [among them] in any way disgraceful." In fact, "graceful" long nights in a pub or in the company of a guitar we have spent. And, at times, in a mixture of admiration and scorn, he would utter a "Ooh, you Italians!" All in all, you see, a line still exists.

A tribute to Floris, our Lord of the Ring, tireless manipulator of vacancies, for his outdated and aristocratic beauty; a tribute to Vera for the temperament of a combatant; to Ignacio for interesting confrontations and the breathtaking equilibrist performances; to Julien for the contorted mind, the uncompromising principles and all the complots; to Gabriele&Maria ...pause... with you it is pure joy of time; to Wilbert for his exquisite restlessness; to Magdalena for *such a host* cannot exist without *such a hostess*; to Anna for the icastic Roman jargon and skirmishes with Ronald; to Ronald for skirmishing with Anna; to Laura&Roberto for the the good time and the humanitarian adventures; to Ranko for constantly teasing me; to Davide for his softness; to Ana Mafalda\todo{look up middle names}*for that vigorous laughter and the Portuguese charm; to Mark for his faith in the resurrection of Italy; to Joao for his openness; to Gary for his questions and contempt for molecules; to Sal for his madness; to Diana for the secrets stories about Herre; to Tino for enabling my irresponsible mechanisms; to Sander for the limpidness and kind spirit; to Maureen for an invisible thread; to Andrea Caviglia for his knowledge, jokes and unconditional appreciation; to Nicoletta for being uncatchable; to Maciek for his meticulousness; to Simon

for his subtle noble disdain; to Ludovica for having existed in my life; to Peter for his serenity, imperturbability and for fruitful provocations on Landauer; to Richard for his smile; to Marios for having finally joined the right party; to Andrea Cornia for his always perspicacious comments and the molecules; to Yaroslav for his peripatetic walks; to the *through-legend* Yuly; to Daniel Reta for the patience; to Jaume and Concepio for being the mighty couple of the radicals; to Herre, again and again, for having directed this gigantic orchestra.

Out of the academic bubble, there is a someone – believe it or not – on this planet who *actually* possesses the superhuman abilities to listen to my annoying lucubrations *for hours* and be ready to give sharp and inspiring answers in return, at any given moment. The beauty and sweetness and profoundness and untameableness of this character I could not resist. The first time I met this dark-haired angel, she fended me off like you do with an insect. The second time, years later, somehow I managed.

A tribute to those without whom *technically* I could not be here; to my mother for the loving-kindness, extreme care, inflexibility and to my father for the incredible intuition, knowledge and organic intelligence. My parents whose qualities have, hopefully, managed to creep through. A non-payable debt to my sister for the universal connection, to my brother for his playing completely out of any scheme, to Take for having absolved at times the role of a father and at times that of a second brother to all of us. And the mentors: my uncle Paolo and Roberto Marchionni, for having laid the *foundations* and much else; Mastro for the irony; Andre for the courage and the mighty time; Sim for being my perfect complement; Prof. Luisi, that of approaching you... a *bifurcation* point; Okan for the physical and metaphysical travels; my aunt Silvia; Thomas Ihn; Jens Eller and Aleksey Kosikov for the immeasurable care.

Nino perchè è Nino e nessun vuole che non sia altro che Nino; Antonio, il mio corrispondente "dal mondo" che mi da tutte le gioie del viaggio risparmiandomene la fatica; e le feste e la bella musica e mettiamoci pure la Carlofortina.

Per praticamente *tutto* il resto di ciò che ho detto sopra, sono grato, da ultimo, alla delegazione italiana composta da Coni, Mello, Giachi e Bellu, Muletto Racing Team anesso, e a quella Italo-Belga ad unico ed illustre rappresentante Monsieur Alàn Cappellì, che se vicino o lontano comunque invariabilmente importante, per essere pronta a rispondere alle domande della commissione europea (a maggioranza tedesca) nel caso esse risultassero, diciamo, poco diplomatiche.

Quoting from the last slide of our French thoroughbred's (Julien's) talks: "I thank the Earth with all its elements and you for your attention". Without these two essentials, the "Earth" and the "Other", *all* this could not be happening. Nothing is ours, we only *borrow* from the world. Recall this, every once in a while.

Any resemblance to real events and/or to real persons, living or dead, is NOT purely coincidental.

Rotterdam, 02:43 AM, 23.05.2017